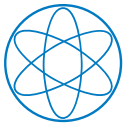

# Dissertation

## Searches for Higgs Boson Decays to Muon Pairs in the Standard Model and in its Minimal Supersymmetric Extension with the ATLAS Detector


von

Sebastian Stern


eingereicht an der

Fakultät für Physik

der

Technischen Universität München

erstellt am

Max–Planck–Institut für Physik

(Werner–Heisenberg–Institut)

München

Juli 2013

MAX-PLANCK-GESELLSCHAFT

TECHNISCHE UNIVERSITÄT MÜNCHEN

Max–Planck–Institut für Physik
(Werner–Heisenberg–Institut)

# Searches for Higgs Boson Decays to Muon Pairs in the Standard Model and in its Minimal Supersymmetric Extension with the ATLAS Detector

Sebastian Stern

Vollständiger Abdruck der von der Fakultät für Physik der Technischen Universität München zur Erlangung des akademischen Grades eines

Doktors der Naturwissenschaften (Dr. rer. nat.)

genehmigten Dissertation.

Vorsitzender: Univ.–Prof. Dr. N. Kaiser
Prüfer der Dissertation:
1. Priv.–Doz. Dr. H. Kroha
2. Univ.–Prof. Dr. L. Oberauer

Die Dissertation wurde am 16.07.2013 bei der Technischen Universität München eingereicht und durch die Fakultät für Physik am 23.07.2013 angenommen.

# Abstract

Two studies of Higgs boson decays to two oppositely charged muons in the Standard Model and in its minimal supersymmetric extension with the ATLAS experiment at the Large Hadron Collider (LHC) at CERN are presented.

The search for the decays of the neutral Higgs bosons, $h$, $A$ and $H$, of the Minimal Supersymmetric Extension of the Standard Model (MSSM) to $\mu^+\mu^-$ is performed in proton-proton collisions at a centre-of-mass energy of 7 TeV based on the data recorded in 2011 which correspond to an integrated luminosity of $4.8\,\text{fb}^{-1}$. The branching fraction for the $h/A/H \to \mu^+\mu^-$ decay is about 300 times smaller compared to the most sensitive $h/A/H \to \tau^+\tau^-$ decay channel. But due to the very high experimental $\mu^+\mu^-$ mass resolution, the signal appears as narrow resonances in the $\mu^+\mu^-$ invariant mass distribution on top of a continuous background. Motivated by the two Higgs boson production modes, via gluon fusion and in association with $b$ quarks, the search is performed in two complementary event categories either without or with at least one reconstructed $b$ jet in the selected $\mu^+\mu^-$ events. The two event categories have different signal–to–background ratios and their statistical combination improves the sensitivity of the search. Signal and background are parametrised by analytic functions. The total background contribution is estimated directly from the data. No significant excess of events above the Standard Model background is observed. Exclusion limits are derived for the MSSM $m_h^{\text{max}}$ benchmark scenario with positive Higgs mixing parameter as a function of the free parameters $m_A$ and $\tan\beta$. In addition, less model–dependent exclusion limits are set on the production cross section times branching fraction of a generic Higgs boson, $\phi$, produced in either gluon fusion or in association with $b$ quarks as a function its mass, $m_\phi$.

The second study evaluates the physics potential of the ATLAS experiment for the search for the rare decay of the Standard Model Higgs boson with a mass of 125 GeV to $\mu^+\mu^-$. The study uses Monte Carlo simulations of the proton–proton collisions at a centre-of-mass energy of 14 TeV with simplified description of the detector response. The sensitivity is evaluated for two benchmark scenarios with integrated luminosities of $300\,\text{fb}^{-1}$ and $3000\,\text{fb}^{-1}$ which are expected to be reached after two stages of luminosity upgrades of the LHC machine. The prospects are expressed in terms of expected exclusion limits and signal significances and contribute to the combined Higgs boson coupling measurement. With the proposed data set of $3000\,\text{fb}^{-1}$, decays of the Standard Model Higgs boson with mass of 125 GeV to $\mu^+\mu^-$ are expected to be discovered with a significance of more than 6 standard deviations. Higgs boson couplings to the second–generation leptons can be determined with an accuracy of about 25 % relative to the third–generation lepton couplings.

# Acknowledgements

I devote this page to all the people who went along with me during the past more than three years and supported me and my work in many different ways. Looking back now, I feel deeply grateful to these many helping hands.

I am indebted to Dr. Hubert Kroha for being my thesis advisor, for guiding me through the quite busy last weeks with much patience and for giving me plenty of valuable advice.

I want to express my deepest gratitude to Dr. Sandra Kortner for offering me a PhD position in the ATLAS Minerva group at MPI and for giving me the possibility to participate in interesting schools, workshops and conferences all over the world. Most important, I thank her for always showing much patience with me, being available for my questions and the following fruitful discussions even though she had also a pretty busy time during these years. Many thanks for all the support, especially during the last months while I was compiling this thesis.

For the time I was working on the muon data quality monitoring I would like to thank Dr. Dominique Fortin and the muon combined performance group conveners by that time, Dr. Oliver Kortner and Dr. Wolfgang Liebig for introducing me to the data quality business and Athena code development and for supporting my work.

Related to my work on the neutral MSSM Higgs boson search I would like to thank again Oliver for providing me with countless valuable information especially on the field of fitting. I also want to thank Dr. Trevor Vickey who was the Higgs sub–group convener my analysis was associated to for supporting the $h/A/H \to \mu^+\mu^-$ one–man–show and for giving me the chance to publish this work. Concerning the work on the publication itself, I would like to thank my fellow editors, Julian Glatzer, John Stakely Keller, Nikos Rompotis, Holger von Radziewski and again Trevor. It took us fairly long to get this out but it was a great experience and I've learned a lot from you guys.

I thank all my colleagues at MPI Munich who came and went during my years here. Thanks for the very pleasant atmosphere, especially during the not so busy days — yes, there were some — when we've managed to go out for some drinks. I have to say that I was in very good company.

I want to thank Dr. Jörg Dubbert for being always an excellent host when I came to CERN, for the epic Armagetron battles and for his help in proofreading my thesis.

My very special and biggest thanks go to Philipp Schwegler and my office mate Maximilian Emanuel Goblirsch–Kolb, better known as Max Power, for making the days at MPI as pleasant as possible. I thank you for the entertaining coffee breaks and BBs, for collecting a remarkable browsing history and for the excellent atmosphere we always had in the office.

Finally, I would like to thank a couple of very special fellows in my life outside physics. My family and long–time friends, Mum and Dad, Claudia, Moni, Luci, Carola and Jeff, Vaddi, Hatze, Piffe, Aldi, Leuke and Gierle. My deepest thanks for all the support throughout the years, for the time I could spend with you, for distracting me from physics and most important, for just being there.

# Contents

# Chapter 1

# Introduction

The Standard Model of Particle Physics developed in the second half of the last century has been thoroughly tested over the past decades and turned out to be extremely successful. Based on the principle of local gauge invariance, it describes with per–mille accuracy the elementary constituents of matter, the spin–1/2 fermions, and their interactions by the electromagnetic, weak and strong forces mediated by spin–1 gauge bosons. Electroweak gauge invariance in the Standard Model requires all elementary particles to be massless — in obvious contradiction to the observations — unless there is the phenomenon of spontaneous electroweak symmetry breaking. A solution to this problem is provided by introducing an additional complex scalar field coupling to weak gauge bosons and fermions and giving them masses. The mechanism of spontaneous symmetry breaking gives rise to a new scalar particle, the Higgs boson. Being the last missing particle predicted by the Standard Model, the Higgs boson has been extensively searched for during the last decades.

In July 2012, a breakthrough in the search for the Standard Model Higgs boson was made with the discovery of a new boson with a mass of $125.5 \pm 0.2(\text{stat})^{+0.5}_{-0.6}(\text{syst})$ GeV by the ATLAS and CMS collaborations at the Large Hadron Collider (LHC) at CERN. Measurements of its spin, CP and coupling properties show good compatibility with the predictions of the Standard Model. More data are needed to finally pin down the nature of the new boson and discriminate whether it is the Standard Model Higgs boson or it belongs to a more complex Higgs sector of an extension of the Standard Model.

It is widely believed that the Standard Model is an effective theory valid only up to a certain energy scale and that it needs to be extended to describe the physics phenomena at the very high energy scales. Supersymmetry provides attractive solutions to several intrinsic problems of the Standard Model. The simplest supersymmetric extension of the Standard Model is the Minimal Supersymmetric Standard Model (MSSM). In addition to supersymmetric partners for every Standard Model particle, the MSSM Higgs sector predicts five physical Higgs bosons. Three of them are electrically neutral while the other two have positive and negative electric charges. Two of the neutral MSSM Higgs bosons

are scalar particles with even CP quantum number. The remaining neutral boson is a pseudoscalar with odd CP quantum number. The new particle discovered at the LHC can also be interpreted as one of the CP–even MSSM Higgs bosons.

An introduction to the theoretical framework of the Standard Model and of its minimal supersymmetric extension is given in Chapter 2. An overview of the phenomenological consequences of the Higgs sector in the Standard Model and the MSSM is given in Chapter 3 including a summary of the current status of the experimental searches and constraints.

The LHC is the world's most powerful accelerator in terms of centre–of–mass energy and luminosity. It started its physics programme in 2009 and will explore physics phenomena at the TeV scale in the next decades. After the start with proton–proton collisions at a centre–of–mass energy of $\sqrt{s} = 7\,\text{TeV}$ in 2010, the LHC was raised to $\sqrt{s} = 8\,\text{TeV}$ in 2012 and will reach a centre–of–mass energy of close to $\sqrt{s} = 14\,\text{TeV}$ after the two–year shut down in 2013/2014. The design luminosity of $10^{34}\,\text{cm}^{-2}\text{s}^{-1}$ is expected to be reached shortly after the 2013/2014 shut down. Proposed high–luminosity upgrades of the LHC (HL–LHC) can reach peak luminosities of 5 to $7 \cdot 10^{34}\,\text{cm}^{-2}\text{s}^{-1}$ after the year 2022.

Four major experiments are studying the collisions of proton or lead beams provided by the LHC: ATLAS, ALICE, CMS and LHCb. While ALICE and LHCb are specialised to study mainly lead–lead collisions and physics with $b$ quarks, respectively, ATLAS and CMS are multi–purpose detectors designed for the search for the Higgs boson and a wide range of new physics phenomena. This thesis is performed in the framework of the ATLAS experiment. The LHC and the ATLAS detector are discussed in Chapter 4 together with the LHC upgrade plans.

Efficient muon identification and precise muon momentum measurement are key requirements for the ATLAS detector in order of efficiently exploit the physics potential at the LHC. Muons provide important signatures for the triggering and identification of interesting physics events. High muon reconstruction efficiency and excellent momentum resolution are particularly important for the analyses presented in this thesis. During data taking and during the offline event reconstruction, the performance of the detector systems and of the reconstruction algorithms need to be continuously monitored. In the context of this thesis, the data quality monitoring procedures of the muon trigger and of the muon reconstruction have been improved. The results of the muon data quality monitoring for the 2011 data are presented in Chapter 5 together with an overview of the ATLAS muon reconstruction.

The main topic of this thesis is the search for the neutral MSSM Higgs bosons in decays to muon pairs. These decays have very small branching fraction but offer excellent Higgs boson mass resolution. The signal of the three neutral MSSM Higgs bosons is expected to appear as narrow resonances in the $\mu^+\mu^-$ invariant mass on top of a continuous background from Standard Model processes. Since the signal–to–background ratio is expected to be small, precise estimation of the background contribution is essential. The search for the

neutral MSSM Higgs bosons in decays to two muons in 2011 ATLAS data at $\sqrt{s} = 7\,\text{TeV}$ is presented in Chapter 6.

The $\mu^+\mu^-$ decay channel providing high mass resolution is also interesting for the study of the properties of the newly discovered boson. The study of this rare Higgs boson decay requires large integrated luminosity at the highest centre–of–mass energy. Chapter 7 describes the study of the physics potential of the ATLAS experiment for the measurement of the Standard Model Higgs boson decays to $\mu^+\mu^-$ and the determination of its couplings at high–luminosity upgrades of the LHC.

# Chapter 2

# Higgs Bosons in the Standard Model and the MSSM

This chapter introduces the theoretical background of the experimental searches for the Standard Model Higgs boson and the neutral MSSM Higgs bosons presented in this thesis. The Standard Model of Particle Physics and its minimal supersymmetric extension, the Minimal Supersymmetric Standard Model (MSSM), are outlined. Section 2.1 describes the Standard Model based on References [1, 2]. An introduction to the MSSM with focus on the Higgs sector is given in Section 2.2 based on References [3, 4].

## 2.1 The Standard Model of Particle Physics

The Standard Model of particle physics (SM) describes our current understanding of the elementary constituents of matter — the spin–1/2 fermions — and of their interactions with the exception of gravitation. The fundamental interactions mediated by spin–1 gauge bosons are described by quantum field theories. Their dynamics is determined in a consistent framework by the principle of local gauge invariance. The Standard Model is a Yang–Mills theory [5] based on the direct product of the three simplest unitary Lie groups: $SU(3)_C \times SU(2)_L \times U(1)_Y$. The electromagnetic and weak interactions are determined by the $SU(2)_L \times U(1)_Y$ symmetry group of the electroweak gauge theory [6–8] and the strong interactions are described by the $SU(3)_C$ colour symmetry group of quantum chromodynamics (QCD) [9]. The field equations are the Euler–Lagrange equations derived according to Hamilton's principle of least action [10] with the classical Lagrange function replaced by the integral of the Lagrange density, the so–called Lagrangian $\mathfrak{L}$. The gauge structure of the Standard Model Lagrangian is introduced in Section 2.1.1. At low energies the Standard Model gauge symmetry is spontaneously broken by the vacuum

to $SU(3)_C \times U(1)_Q$ leading to the prediction of the Standard Model Higgs boson. The mechanism describing the electroweak symmetry breaking is discussed in Section 2.1.2. Section 2.1.3 summarises theoretical constraints on the Higgs boson mass.

### 2.1.1 The Gauge Structure of the Standard Model

The local gauge symmetry of the Standard Model determines the electroweak and the strong interactions via minimal gauge invariant couplings of the gauge fields to the matter fields. The structure of the fields and coupling terms is briefly outlined in the following. More information is given in References [1, 2] and references therein.

#### The Matter Fields

The elementary fermion states of the Standard Model are assigned to the multiplets of the fundamental representations of the gauge symmetry groups.

The weak interaction maximally violates parity [11]. Left–handed and right–handed quarks and leptons, $f_{L,R} = \frac{1}{2}(1 \mp \gamma_5)f$ with the product of the four Dirac matrices, $\gamma_5 = i\gamma_0\gamma_1\gamma_2\gamma_3$, couple differently to the weak gauge bosons. In the fundamental representation of the electroweak symmetry group $SU(2)_L \times U(1)_Y$ the left–handed fermions and quarks are assigned to three generations of weak isospin doublets,

$$\begin{aligned} L_1 &= \begin{pmatrix} \nu_e \\ e^- \end{pmatrix}_L, \; L_2 = \begin{pmatrix} \nu_\mu \\ \mu^- \end{pmatrix}_L, \; L_3 = \begin{pmatrix} \nu_\tau \\ \tau^- \end{pmatrix}_L, \\ Q_1 &= \begin{pmatrix} u \\ d \end{pmatrix}_L, \; Q_2 = \begin{pmatrix} c \\ s \end{pmatrix}_L, \; Q_3 = \begin{pmatrix} t \\ b \end{pmatrix}_L, \end{aligned} \tag{2.1}$$

where $L_{1,2,3}$ represent the lepton and $Q_{1,2,3}$ the quark generations and the members of the doublets are distinguished by their quantum numbers, $I_f^{3,L} = \pm\frac{1}{2}$, the third component of the weak isospin. The right–handed fermions are weak isosinglets under $SU(2)_L$,

$$\begin{aligned} e_{R_1} &= e_R^-, \quad e_{R_2} = \mu_R^-, \quad e_{R_3} = \tau_R^-, \\ u_{R_1} &= u_R, \quad u_{R_2} = c_R, \quad u_{R_3} = t_R, \\ d_{R_1} &= d_R, \quad d_{R_2} = s_R, \quad d_{R_3} = b_R, \end{aligned} \tag{2.2}$$

with $I_f^{3,R} = 0$. The neutrinos are considered massless in the original version of the Standard Model and only have left–handed components. The $U(1)_Y$ symmetry adds another quantum number to the left– and right–handed fermions, the weak hypercharge, defined as

$$Y_f = 2Q_f - 2I_f^3 \tag{2.3}$$

with the electric charge quantum number $Q_f$.

In the representation of the $SU(3)_C$ symmetry group of quantum chromodynamics, the quarks appear in three colour triplet states,

$$q = \begin{pmatrix} q_r \\ q_g \\ q_b \end{pmatrix}, \tag{2.4}$$

with $q = u, d, s, c, t, b$ and the three colour quantum numbers $r$, $g$ and $b$. Leptons are colour singlets under $SU(3)_C$ and have no colour charge.

The non–observation of coloured particles motivates the colour confinement hypothesis. It forbids the existence of free coloured states and requires that quarks and gluons are bound in colourless singlets, the baryons and mesons. Charged pions, for example, have the colour components

$$\pi^+ = \frac{1}{\sqrt{3}} \left( u_r \bar{d}_{\bar{r}} + u_g \bar{d}_{\bar{g}} + u_b \bar{d}_{\bar{b}} \right). \tag{2.5}$$

On the other hand, at the short distances within the bound colourless states, the quarks behave as free particles. This so–called asymptotic freedom is confirmed experimentally by the measurements of the running of the strong coupling constant, $\alpha_s(Q^2)$, with the energy scale $Q^2$ [12].

### The Gauge Fields

The gauge symmetry groups determine the properties of the interactions. Their generators correspond to quantum mechanical observables, the charges of the interactions. The interactions are mediated by the exchange of vector bosons with spin 1, corresponding to the gauge fields.

The electroweak symmetry group $SU(2)_L \times U(1)_Y$ has one generator, $Y$, corresponding to the weak hypercharge and three generators, $T^a_{SU(2)}$ $(a = 1, 2, 3)$, corresponding to the weak isospin. These generators obey the relations

$$\begin{aligned} [Y, T^a_{SU(2)}] &= 0 \\ [T^a_{SU(2)}, T^b_{SU(2)}] &= i\epsilon^{abc} T_{c\,SU(2)} \\ T^a_{SU(2)} &= \frac{1}{2}\tau^a \end{aligned} \tag{2.6}$$

where $\tau^a$ are the $2 \times 2$ Pauli matrices and $\epsilon^{abc}$ is the totally antisymmetric tensor. The gauge vector fields $W^{1,2,3}_\mu$ of the $SU(2)_L$ symmetry group form a weak isospin triplet. The weak isospin singlet field $B_\mu$ is the gauge field of the $U(1)_Y$ group.

The $SU(3)_C$ symmetry group has eight generators $T^a_{SU(3)}$ $(a = 1, ..., 8)$ fulfilling the

relations

$$\begin{aligned}[T^a_{SU(3)}, T^b_{SU(3)}] &= if^{abc}T_{c\,SU(3)} \\ T^a_{SU(3)} &= \frac{1}{2}\lambda^a,\end{aligned} \tag{2.7}$$

where $f^{abc}$ are the structure constants of $SU(3)$ and $\lambda^a$ are the $3 \times 3$ Gell–Mann matrices. The $SU(3)_C$ gauge fields are the gluon fields, $G^{1,\ldots,8}_\mu$, which are assigned to a colour octet.

The field strength tensors of the strong, weak and electromagnetic gauge fields are given by

$$\begin{aligned}G^a_{\mu\nu} &= \partial_\mu G^a_\nu - \partial_\nu G^a_\mu + g_3 f^{abc} G^b_\mu G^c_\nu, \\ W^a_{\mu\nu} &= \partial_\mu W^a_\nu - \partial_\nu W^a_\mu + g_2 \epsilon^{abc} W^b_\mu W^c_\nu \quad \text{and} \\ B_{\mu\nu} &= \partial_\mu B_\nu - \partial_\nu B_\mu,\end{aligned} \tag{2.8}$$

respectively, where $g_2$ and $g_3$ are the coupling constants of $SU(2)_L$ and $SU(3)_C$. The generators of the non–abelian symmetry groups $SU(2)_L$ and $SU(3)_C$ do not commute with each other. This leads to self–coupling terms for the gluon and the weak vector boson fields.

### Matter–Gauge Field Coupling

To satisfy the requirement of local gauge invariance of the Standard Model Lagrangian, the ordinary derivative is replaced by the covariant derivative defined as

$$D_\mu \psi = \left(\partial_\mu - ig_3 \frac{\lambda_a}{2} G^a_\mu - ig_2 \frac{\tau_a}{2} W^a_\mu - ig_1 \frac{Y_f}{2} B_\mu\right) \psi, \tag{2.9}$$

where $\psi$ are the matter fields defined in Equations 2.1, 2.2 and 2.4 and $g_1$ is the coupling constant of $U(1)_Y$.

The complete Lagrangian of the SM before electroweak symmetry breaking is given by

$$\begin{aligned}\mathfrak{L}_{SM} = &-\frac{1}{4} G^a_{\mu\nu} G^{\mu\nu}_a - \frac{1}{4} W^a_{\mu\nu} W^{\mu\nu}_a - \frac{1}{4} B_{\mu\nu} B^{\mu\nu} + \\ &+ \bar{L}_i i D_\mu \gamma^\mu L_i + \bar{e}_{R_i} i D_\mu \gamma^\mu e_{R_i} + \bar{Q}_i i D_\mu \gamma^\mu Q_i + \\ &+ \bar{u}_{R_i} i D_\mu \gamma^\mu u_{R_i} + \bar{d}_{R_i} i D_\mu \gamma^\mu d_{R_i},\end{aligned} \tag{2.10}$$

with $i = 1, 2, 3$ for the three fermion generations. Inserting Equations 2.8 into the first line results in the kinetic terms of the gauge fields and the terms describing the self–interaction of the non–abelian gauge fields. Inserting Equation 2.9 into the second and third lines of Equation 2.10 gives the kinetic terms of the matter fields and the matter–gauge field

couplings. The $SU(2)_L$ term in Equation 2.9,

$$-ig_2\frac{\tau_a}{2}W_\mu^a = -i\frac{g_2}{2}\begin{pmatrix} W_\mu^3 & W_\mu^1 + iW_\mu^2 \\ W_\mu^1 - iW_\mu^2 & -W_\mu^3 \end{pmatrix}, \tag{2.11}$$

can be written in terms of the physical gauge bosons

$$W^\pm = \frac{1}{\sqrt{2}}\left(W_\mu^1 \mp iW_\mu^2\right), \tag{2.12}$$

mediating the charged–current interactions and of $W_\mu^3$. The electrically neutral gauge fields of the electroweak sector, $W_\mu^3$ and $B_\mu$, are related to the neutral weak gauge field, $Z_\mu^0$, mediating the neutral–current interactions and to the electromagnetic field, $A_\mu$, by a rotation,

$$\begin{pmatrix} A_\mu \\ Z_\mu^0 \end{pmatrix} = \begin{pmatrix} \cos\theta_W & \sin\theta_W \\ -\sin\theta_W & \cos\theta_W \end{pmatrix}\begin{pmatrix} B_\mu \\ W_\mu^3 \end{pmatrix}, \tag{2.13}$$

with the Weinberg angle $\theta_W$ which is chosen such that the coupling of the neutrino to the photon field is zero:

$$\begin{aligned} \cos\theta_W &= \frac{g_2}{\sqrt{g_2^2 + g_1^2}}, \\ \sin\theta_W &= \frac{g_1}{\sqrt{g_2^2 + g_1^2}}. \end{aligned} \tag{2.14}$$

The full Lagrangian in Equation 2.10 satisfies the requirement of local gauge invariance under $SU(3)_C \times SU(2)_L \times U(1)_Y$, describes the strong, weak and electromagnetic interactions and incorporates all observed elementary fermions and vector bosons. However, it does not contain mass terms for the weak gauge bosons and the fermions which is in contradiction to the observations. Adding Klein–Gordon mass terms of the form $-\frac{1}{2}m_W^2 W_\mu^+ W^{-\mu}$ and $-\frac{1}{2}m_Z^2 Z_\mu^0 Z^{0\mu}$ for massive weak gauge bosons to the Lagrangian violates the local $SU(2)_L$ gauge invariance. While Dirac mass terms for fermions, $-m_f\bar{\psi}\psi$, do not break $SU(3)_C$, they violate the global $SU(2)_L$ gauge symmetry because left– and right–handed matter fields transform differently under $SU(2)_L$.

A solution for incorporating massive $W^\pm$ and $Z$ gauge bosons while preserving the local $SU(2)_L$ gauge symmetry has been proposed by P.W. Higgs, F. Englert, R. Brout and G.S. Guralnik, C.R. Hagen and T.W.B. Kibble [13–18]. This solution allows also for the introduction of fermion mass terms without violating global $SU(2)_L$ gauge symmetry. It is commonly referred to as the Higgs mechanism and is introduced in the following section.

### 2.1.2 The Higgs Mechanism

The Higgs mechanism extends the Standard Model by a complex scalar field, $\Phi$, which gives additional longitudinal polarisation degrees of freedom to the weak gauge bosons. In its minimal realisation in the Standard Model [8] one scalar $SU(2)_L$ doublet,

$$\Phi = \begin{pmatrix} \phi^+ \\ \phi^0 \end{pmatrix} = \frac{1}{\sqrt{2}} \begin{pmatrix} \phi_3 + i\phi_4 \\ \phi_1 + i\phi_2 \end{pmatrix}, \tag{2.15}$$

with four degrees of freedom and weak hypercharge $Y = +1$ is introduced.

The Lagrangian of the scalar field,

$$\mathfrak{L}_S = (D^\mu \Phi)^\dagger (D_\mu \Phi) - V(\Phi), \tag{2.16}$$

contains the Higgs potential,

$$V(\Phi) = \mu^2 \Phi^\dagger \Phi + \lambda (\Phi^\dagger \Phi)^2, \tag{2.17}$$

with the mass parameter, $\mu$, and the self–coupling parameter, $\lambda$. The scalar Lagrangian is invariant under local $SU(2)_L \times U(1)_Y$ transformations. While the Higgs potential is bounded from below only for $\lambda > 0$, there is no a priori preference for the sign of $\mu^2$. For $\mu^2 > 0$, the scalar potential has a minimum at $\Phi_0^2 = 0$ but for $\mu^2 < 0$ the scalar field develops an infinite set of degenerate ground states with non–zero field strength,

$$\Phi_0^2 = -\frac{\mu^2}{2\lambda} \neq 0. \tag{2.18}$$

As the $U(1)_Q$ symmetry of the electromagnetic interaction must remain unbroken according to the observation of a single massless photon, the non–zero vacuum expectation value, $v = \sqrt{\frac{-\mu^2}{2\lambda}}$, of the scalar field is chosen for the neutral component of the scalar field,

$$\langle \Phi \rangle_0 = \begin{pmatrix} 0 \\ \frac{v}{\sqrt{2}} \end{pmatrix}. \tag{2.19}$$

By choosing this particular ground state, the $SU(2)_L \times U(1)_Y$ symmetry is spontaneously broken with the electromagnetic gauge symmetry $U(1)_Q$ remaining as a symmetry of the ground state.

Field excitations from the ground state can be parametrised as

$$\Phi(x) = \exp\left[ i \frac{\zeta_a(x) \tau^a}{v} \right] \begin{pmatrix} 0 \\ \frac{1}{\sqrt{2}}(v + H(x)) \end{pmatrix} \tag{2.20}$$

with four real scalar fields, $\zeta_a(x)$ $(a = 1, 2, 3)$ and $H(x)$. The fields $\zeta_a(x)$ correspond to

massless Goldstone bosons arising according to the Goldstone theorem [19] and can be eliminated by a local $SU(2)_L$ gauge transformation into the unitary gauge defined by $\zeta_a(x) = 0$. A physical massive scalar field, $H(x)$, remains which corresponds to the Higgs boson, $H$.

The scalar Lagrangian after spontaneous symmetry breaking in the unitary gauge is obtained by inserting Equation 2.20 in Equation 2.16 with $\zeta_a(x) = 0$ as well as the electroweak part of the covariant derivative of Equation 2.9,

$$\begin{aligned}\mathfrak{L}_S =& \frac{1}{2}\left(\partial^\mu H \partial_\mu H - m_H^2 H^2\right) - \lambda v H^3 - \frac{\lambda}{4} H^4 \\ &+ \frac{g^2}{4}(H^2 + 2vH)\left(W_\mu^+ W^{\mu,-} + \frac{1}{2\cos^2\theta_W} Z_\mu^0 Z^{\mu,0}\right) \\ &+ \frac{1}{2} m_W^2 \left(W_\mu^+ W^{\mu,+} + W_\mu^- W^{\mu,-}\right) + \frac{1}{2} m_Z^2 Z_\mu^2 Z^{\mu,0}.\end{aligned} \tag{2.21}$$

Here the gauge fields are substituted by the physical fields using Equations 2.12, 2.13 and 2.14. In Equation 2.21 the masses of the weak gauge bosons and of the Higgs boson are given by the relations

$$\begin{aligned} m_W &= \frac{gv}{2}, \\ m_Z &= \frac{m_W}{\cos\theta_W}, \\ m_H &= \sqrt{2\lambda v^2}. \end{aligned} \tag{2.22}$$

Finally, also masses for the fermions can be generated via Yukawa couplings to the same scalar field, $\Phi$. The Lagrangian for the Yukawa couplings of the fermions of the first generation (the terms for the other two generations are analogous) has the form

$$\mathfrak{L}_F = -\lambda_e \bar{L}_1 \Phi e_{R1} - \lambda_{d1} \bar{Q}_1 \Phi d_{R1} - \lambda_u \bar{Q}_1 \tilde{\Phi} u_{R1} + h.c. \tag{2.23}$$

where $\tilde{\Phi} = i\tau_2 \Phi^*$ is the $SU(2)_L$ doublet conjugate to $\Phi$ with weak hypercharge $Y = -1$. In the unitary gauge, the mass terms for the fermions, $f$, in this Lagrangian are given by

$$m_f = \frac{\lambda_f v}{\sqrt{2}}, \tag{2.24}$$

where $\lambda_f$ are the suitably chosen Yukawa coupling constants.

In summary, with the introduction of an additional complex scalar field, $\Phi$, with negative squared mass parameter, $\mu^2 < 0$, the masses for the weak gauge bosons and the fermions are generated in a consistent way without violating the electroweak local gauge invariance of the Lagrangian. The Higgs self–coupling constant, $\lambda$, and thus $m_H$, are free parameters and need to be determined by experiment. The vacuum expectation value, $v$, is determined by

the Fermi coupling constant, $G_{\mathrm{F}}$, using the relation $v = (\sqrt{2}G_{\mathrm{F}})^{-1/2}$ [2]. In the presented minimal version of the Higgs mechanism, the fermion couplings to the Higgs field are determined by the fermion masses (see Equation 2.24).

It has been shown that the Standard Model with the Higgs mechanism satisfies the requirement for renormalisability [20] and unitarity [21, 22]. The complete Standard Model Lagrangian is given as the sum of Equations 2.10, 2.21 and 2.23 and is invariant under local $SU(3)_C \times SU(2)_L \times U(1)_Y$ symmetry transformations.

### 2.1.3 Theoretical Constraints on the Higgs Boson Mass

Although the Higgs boson mass, $m_H$, is a free parameter in the Standard Model, constraints on its value can be derived from the requirements of unitarity of scattering amplitudes and from the assumption on the energy scale up to which the Standard Model is supposed to be valid [23]. This energy cut–off parameter, $\Lambda_C$, marks the scale at which perturbation theory of the Standard Model breaks down and new physics should appear. Values of $\Lambda_C$ up to the Planck scale, $10^{19}\,\mathrm{GeV}$, are considered. At that energy scale at the latest the Standard Model has to be extended since gravitation becomes as strong as the fundamental interactions of the Standard Model and needs to be incorporated in a unified quantum theory.

**The Unitarity Bound** Unitarity is an essential self–consistency requirement of all quantum field theories [21, 22]. In di–boson scattering processes the amplitudes for the longitudinal components of the gauge bosons grow proportional to the energy and violate unitarity at a certain energy scale if there is no sufficiently light Higgs boson [24]. By requiring that the amplitudes for the scattering processes $W^{\pm}W^{\mp}$, $ZZ$, $HH$, $ZH$ and $W^{\pm}H$ satisfy the unitarity condition, one obtains an upper bound on the Higgs boson mass of

$$m_H \leq 780\,\mathrm{GeV}\ [25]. \tag{2.25}$$

**The Triviality and Vacuum Stability Bounds** Tighter bounds on the Higgs boson mass are derived from the evolution of the Higgs boson quartic self–coupling, $\lambda$, with the squared momentum transfer, $Q^2$ [1, 26].

Contributions from Higgs boson loops drive $\lambda$ to infinity as energy increases while it tends to zero with decreasing energy. To ensure that the theory remains perturbative and non–trivial, i.e. $\lambda$ is non–zero, the quartic self–coupling is required to remain finite, $0 < \lambda(Q^2) < \infty$, for $Q^2 < \Lambda_C$ which sets an upper bound on the Higgs boson mass.

In addition, contributions from top–quark loops to the quartic self–coupling become dominant for small $\lambda$, potentially driving it to negative values. In this case the Higgs potential, $V$, shown in Equation 2.17 is no longer bounded from below and the vacuum

becomes unstable. The requirement that $\lambda$ remain positive at all scales up to $\Lambda_C$ ensures that the electroweak vacuum develops a stable ground state setting a lower bound on the Higgs boson mass.

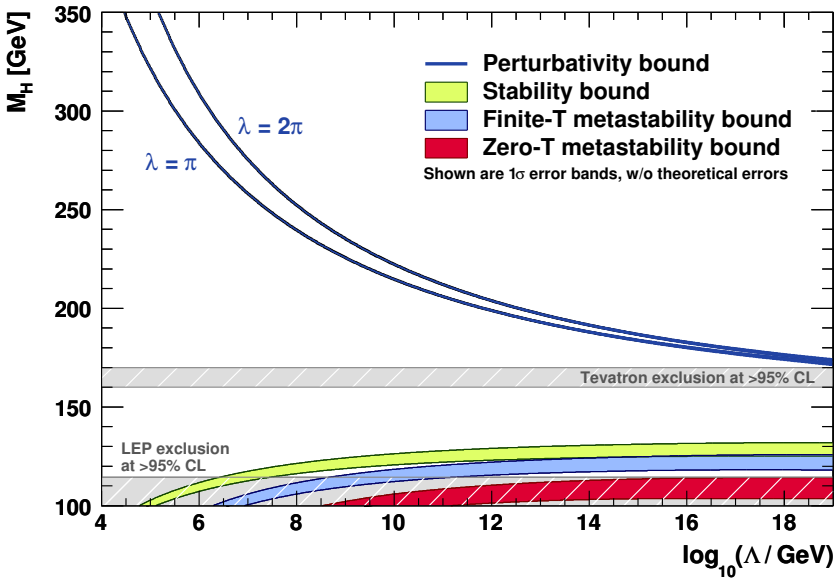


**Figure 2.1:** Triviality (perturbativity) and vacuum stability bounds on the Standard Model Higgs boson mass as a function of the energy scale, $\Lambda$, up to which the Standard Model is assumed to be valid [27]. The triviality bound is shown for $\lambda = \pi$ (lower bold blue line) and $\lambda = 2\pi$ (upper bold blue line); their difference indicates the theoretical uncertainty in this bound. The absolute vacuum stability bound (light shaded green) and the less restrictive finite–temperature (light shaded blue) and zero–temperature (dark shaded red) bounds are shown with their $1\,\sigma$ uncertainty bands from the measurement uncertainty of the top quark mass and the strong coupling constant, $\alpha_s$. Theoretical uncertainties are not included in the bands.

The triviality and vacuum stability bounds on the Higgs boson mass as functions of the energy scale $\Lambda$ obtained from renormalisation group equation (RGE) calculations of $\Lambda(Q^2)$ [27] are shown in Figure 2.1. The upper bold blue pair of lines shows the triviality bound (also called perturbativity bound) obtained from the critical values of $\lambda = \pi$ and $\lambda = 2\pi$ for which the one–loop and two–loop corrections to $\lambda$, respectively, become sizeable. For Higgs boson masses above these lines, the Higgs self interaction cannot be treated perturbatively or new physics has to appear. The stability bound is shown as the light shaded green band. For Higgs boson masses below this bound, the electroweak vacuum is no longer an absolute but at most a local minimum. A second deeper minimum appears which leads to an instability of the electroweak vacuum. Below the stability bound, metastable regions are indicated for which the electroweak vacuum has a lifetime longer than the age of the Universe. The transitions to the deeper ground state take place either via zero–temperature quantum fluctuations below the dark shaded red

band or via thermal fluctuations already below the light shaded blue band. The widths of the triviality, stability and metastability bounds indicate the $1\,\sigma$ uncertainties in the input parameters from the top quark mass, $m_t$, and the strong coupling constant, $\alpha_s$. Theoretical uncertainties from missing higher order corrections are not shown but can be found in the original documentation [27]. The calculations show that Higgs boson masses in the range of approximately 129 GeV to 175 GeV preserve the perturbativity of the Standard Model up to the Planck scale. The uncertainties in these mass bounds are on the order of 1 to 3 GeV.

For completeness it is noted here that an additional constraint on $m_H$ is induced by the fine tuning problem which will be discussed in Section 2.2.1.

## 2.2 The Minimal Supersymmetric Standard Model

The Minimal Supersymmetric Standard Model (MSSM) is the simplest effective low–energy supersymmetric extension of the Standard Model [28, 29]. In the MSSM, global supersymmetry is introduced in the most minimal way, i.e. adding a minimum number of new parameters. In this section the MSSM is introduced based on the References [3, 4]. Section 2.2.1 briefly recalls the successful precision tests of the Standard Model and outlines open questions of the theory which motivate supersymmetric models. Section 2.2.2 introduces basic concepts of supersymmetry. The structure of the MSSM is introduced in Section 2.2.3. Particular attention is paid to the MSSM Higgs sector which is discussed in Section 2.2.4. Constraints on the large MSSM parameter space relevant for this thesis are discussed in Sections 2.2.5 and 2.2.6.

### 2.2.1 Successes and Limitations of the Standard Model

#### Precision Tests of the Standard Model

The Standard Model has withstood a vast number of experimental tests during the last decades. Highly accurate theoretical predictions of electroweak observables including radiative corrections provide predictions with per–mille level precision [30]. These predictions have been confirmed experimentally mainly at LEP, SLC and the Tevatron [31, 32]. Except for the Higgs boson mass and self–coupling constant, all parameters of the Standard Model have been determined. Figure 2.2 shows a comparison of the world–average of the measurements of the $W$ boson and top quark masses, $m_W$ and $m_t$, with indirect determinations from the global fit of all Standard Model parameters to the electroweak precision measurements except $m_W$ and $m_t$ [33] under different assumptions on the Higgs boson mass range. The predicted relationship of the $W$ boson and top quark masses are also shown for different Higgs boson mass scenarios.

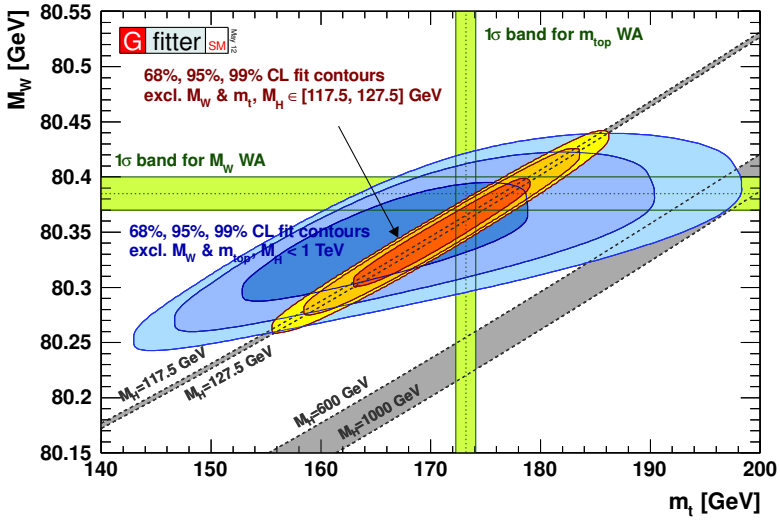


**Figure 2.2:** Comparison of the world–average of the measurements of $m_W$ and $m_t$ (green bands) and the indirect determinations from the global fit to the electroweak precision measurements expect $m_W$ and $m_t$ for two assumptions on the Higgs boson mass, $m_H < 1$ TeV (blue area) and $117.5\,\text{GeV} < m_H < 127.5\,\text{GeV}$ (red/yellow area). Also shown is the Standard Model prediction for the relationship of the masses $m_W$ and $m_t$, for the two Higgs boson mass scenarios, $117.5\,\text{GeV} < m_H < 127.5\,\text{GeV}$ and $600\,\text{GeV} < m_H < 1000\,\text{GeV}$ (grey bands) [33].

Figure 2.3 shows the pulls of the measured values of individual electroweak observables compared to the corresponding values obtained from the electroweak global fit [34]. The measured values agree with the results of the global fit within two standard deviations, except for the forward–backward asymmetry, $A_{fb}^{0,b}$, of $b$ quarks where the two values differ by three standard deviations.

### Limitations of the Standard Model

Although the Standard Model is well established by precision tests as a theory describing the known elementary particles and their fundamental interactions at presently accessible energies, there are several open questions which suggest that this model may be only an effective low–energy approximation of a more general theory involving new physics phenomena.

**Neutrino Masses** In the Standard Model discussed in Section 2.1 it is assumed that neutrinos are massless. However, the observation of neutrino oscillations [35] requires finite neutrino masses. Even in simple extensions of the Standard Model which incorporate neutrino masses [36] there is no explanation why neutrinos are much lighter than the other fermions.

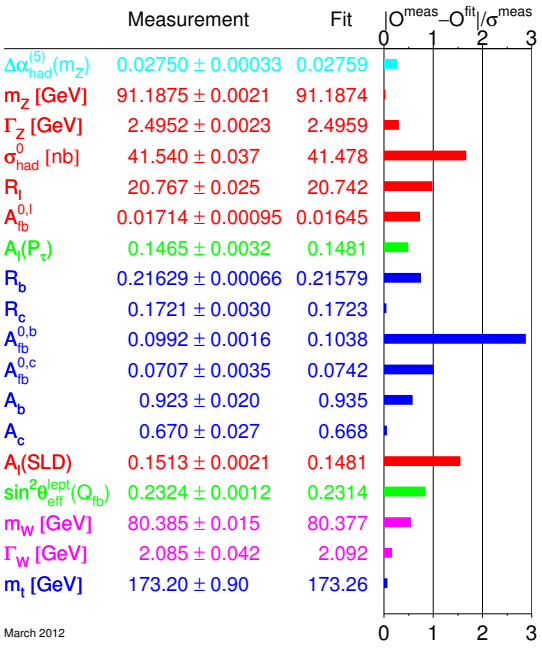


**Figure 2.3:** Measured values of electroweak observables compared to the corresponding results of the electroweak global fit [34].

**Gravitation** The Standard Model does not incorporate the fourth fundamental interaction in nature, gravitation. At presently accessible energies, gravitational forces between elementary particles are about 30 orders of magnitude weaker than the other interactions. However, they increase with the energy scale and at latest at the Planck scale, $\Lambda_{\text{Planck}} = 10^{19}\,\text{GeV}$, gravitation becomes as strong as the other fundamental interactions and needs to be included in a unified theory.

**Cold Dark Matter** Several cosmological observations point to the existence of non–baryonic cold dark matter [37, 38] which contributes with approximately 23 % to the total energy density of the Universe [39]. The Standard Model does not contain candidates for dark matter particles with the required properties of being stable, massive and only very weakly interacting.

**Unification Problem** Electromagnetic and weak interactions are unified to the electroweak interaction [6–8] and it can be shown that their coupling strengths meet at high energies (see Figure 2.4). However, there is no unification with the strong interaction. Considering the successful unification of the electroweak interaction, the unification of all gauge interactions of the Standard Model in a Grand Unified Theory (GUT) with a single gauge group has been suggested [40, 41] which predicts the unification of all three gauge

coupling strengths at the GUT energy scale, $\Lambda_{\rm GUT} \approx 10^{16}\,\text{GeV}$.

**Fine–Tuning and Hierarchy Problems** Radiative corrections to the bare Higgs boson mass squared diverge quadratically with the cut–off energy scale, $\Lambda$. Assuming the validity of the Standard Model up to the GUT scale, the correction terms to the Higgs boson mass are well beyond 1 TeV and thus exceeding the unitarity and triviality bounds unless the bare Higgs boson mass is adjusted to cancel the radiative corrections with an unnaturally high precision of $\mathcal{O}(10^{-30})$. This is known as the fine–tuning problem [42–44]. In other words, the question is why $m_H$ is so much lighter than $\Lambda_{\rm GUT}$ or $\Lambda_{\rm Planck}$ which is know as the hierarchy problem. Related to this issue is the question why the weak interaction is $10^{32}$ times stronger than gravitation although radiative corrections evolve the Fermi coupling constant close to Newton's gravitation constant at $\Lambda_{\rm Planck}$.

### 2.2.2 Supersymmetry

Several of the limitations of the Standard Model can be resolved in a rather natural way by introducing supersymmetry [45], a symmetry relating fermions and bosons. The generator, $\mathcal{Q}$, of the supersymmetry algebra transforms fermionic and bosonic states into each other,

$$\begin{aligned} \mathcal{Q}|\text{Fermion}\rangle &= |\text{Boson}\rangle, \\ \mathcal{Q}|\text{Boson}\rangle &= |\text{Fermion}\rangle, \end{aligned} \tag{2.26}$$

and, consequently, alters the spin by $\frac{1}{2}$. Supersymmetry is not an internal symmetry, like the local gauge symmetries of the Standard Model. The transformations of the operators $\mathcal{Q}$ define non–trivial extensions of the Poincaré group [46,47]. The particle states transformed into each other are called superpartners and are assigned to multiplets of the fundamental representations of the supersymmetry algebra, the supermultiplets. Except for their spin, the superpartners have equal quantum numbers and equal masses if supersymmetry is an exact symmetry. Since superpartners of the Standard Model particles have not been observed they must be heavier than presently achievable energies at particle accelerators. Therefore supersymmetry has to be broken.

If supersymmetry is a local symmetry it includes gravitation [48]. If the baryon and lepton numbers are conserved, supersymmetry provides a good candidate for cold dark matter in the Universe [49, 50]: the lightest supersymmetric particle (LSP) is then absolutely stable and in many scenarios the LSP is the lightest neutralino which is electrically neutral and weakly interacting. In addition, the extended particle spectrum modifies the running of the gauge couplings such that they meet at $M_{\rm GUT} \approx 10^{16}\,\text{GeV}$ [51, 52] as illustrated in Figure 2.4. Most important, supersymmetry can solve the fine–tuning and hierarchy problems [53]. Loop contributions of Standard Model particles to $m_H^2$ which cause quadratically divergent radiative corrections are compensated by loop contributions

of their corresponding superpartners as indicated in Figure 2.5. If supersymmetry is an exact symmetry all radiative corrections to the Higgs mass cancel exactly to zero. For a "soft" supersymmetry (see below) only the logarithmically divergent terms remain and quadratic divergencies still cancel. This cancellation stabilises the hierarchy between the GUT and the electroweak scale without the need for unnatural fine–tuning of the Higgs boson mass.

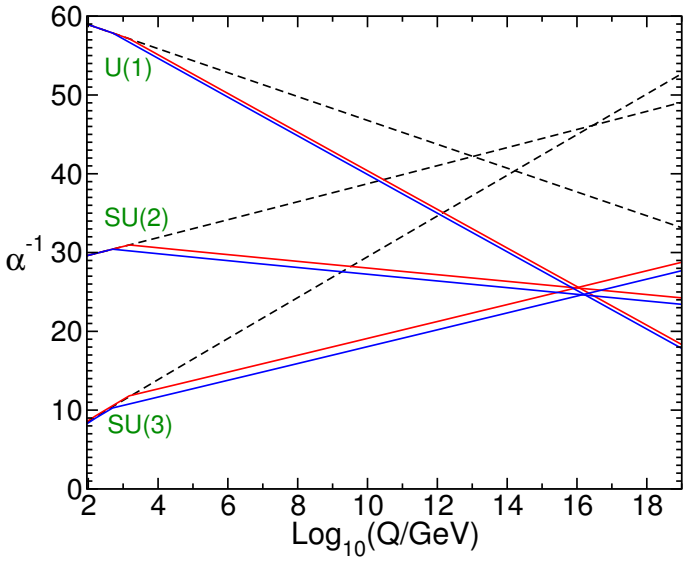


**Figure 2.4:** Running of the inverse gauge couplings of the electromagnetic ($U(1)$), weak ($SU(2)$) and strong ($SU(3)$) interactions in the Standard Model (dashed lines) and in the MSSM (solid lines) [4]. The upper (red) and lower (blue) lines indicate variations of the sparticle mass scale and of $\alpha_s$.

As mentioned above, supersymmetry has to be broken and supersymmetric particles are heavier than their Standard Model partners. Broken supersymmetry can only solve the unification, fine–tuning and hierarchy problems discussed above if the supersymmetric particles are not too heavy. This can only be achieved with the so–called "soft" supersymmetry breaking. In this case the effective Lagrangian is

$$\mathfrak{L} = \mathfrak{L}_{\mathrm{SUSY}} + \mathfrak{L}_{\mathrm{soft}}, \tag{2.27}$$

where $\mathfrak{L}_{\mathrm{SUSY}}$ describes the gauge and Yukawa interactions and preserves supersymmetry and the supersymmetry–breaking term $\mathfrak{L}_{\mathrm{soft}}$ contains only mass terms and coupling parameters with positive mass dimensions. The associated mass scale, $m_{\mathrm{soft}}$, of superpartners contributes to the radiative corrections to $m_H^2$. If this contribution is small enough in order not to reintroduce an unnatural fine–tuning, the masses of the superpartners do not differ from each other by more than about one order of magnitude. Therefore, the masses of the lightest superpartners should be not much larger than 1 TeV.

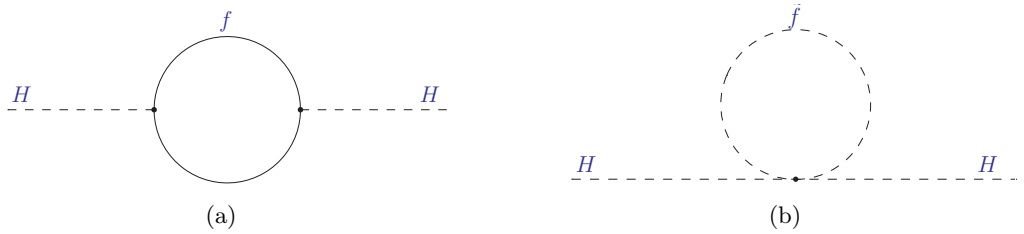


**Figure 2.5:** One–loop radiative corrections to the Higgs boson mass squared. Contributions from Dirac fermions (a) lead to quadratically divergent terms in $m_H^2$ in the Standard Model which are cancelled by contributions from scalar superpartners (b) in supersymmetric extensions of the Standard Model.

### 2.2.3 The Gauge Structure of the Minimal Supersymmetric Standard Model

In the Minimal Supersymmetric Standard Model, supersymmetry is introduced with minimum modifications to the Standard Model. In this section the minimal requirements for the gauge symmetries, the particle content and $R$–parity conservation (see below) are discussed. The MSSM superpotential and the MSSM Lagrangian are outlined briefly.

**The Minimal Gauge Symmetry Group** The gauge symmetry group of the MSSM, $SU(3)_C \times SU(2)_L \times U(1)_Y$, is the same as for the Standard Model. Each spin–1 gauge field gets a spin–1/2 superpartner: eight gluinos corresponding to $SU(3)_C$, three winos corresponding to $SU(2)_L$ and the bino corresponding to $U(1)_Y$. Gauge bosons and gauginos are assigned to the gauge supermultiplets as shown in Table 2.1.

**Table 2.1:** Gauge supermultiplets and superpartners in the MSSM and their quantum numbers [3, 4]. The superpartners here are eigenstates of the gauge symmetries. The spinor (vector) fields corresponding to the gauginos (gauge bosons) are labelled Spin 1/2 (Spin 1).

| Supermultiplets | Superpartners | Spin 1/2 | Spin 1 | $SU(3)_C$,$SU(2)_L$,$U(1)_Y$ |
|---|---|---|---|---|
| $\hat{G}_a$ $(a = 1, ..., 8)$ | gluinos, gluons | $\tilde{G}_a$ | $G_a^\mu$ | (**8**,**1**,0) |
| $\hat{W}_a$ $(a = 1, 2, 3)$ | winos, $W$ bosons | $\tilde{W}_a$ | $W_a^\mu$ | (**1**,**3**,0) |
| $\hat{B}$ | bino, $B$ boson | $\tilde{B}$ | $B^\mu$ | (**1**,**1**,0) |

**The Minimal Particle Content** The fermionic states of the Standard Model are assigned to chiral supermultiplets because the left– and right–handed states transform differently under $SU(2)_L$. The superpartners of the spin–1/2 Standard Model matter fields are spin–0 sfermion fields. Each left– and right–handed quark and lepton state in

the representation by separate two–component Weyl spinors has its own complex scalar superpartner.

As will be discussed in Section 2.2.4, as a minimum two complex scalar Higgs doublets, $H_u$ and $H_d$, are needed which give masses separately to the up–type and down–type fermions. The two spin–0 Higgs doublets together with their superpartners, the spin–1/2 higgsinos, form two chiral supermultiplets.

The fermion and Higgs supermultiplets are shown in Table 2.2. The notation follows the standard convention [4] that all chiral supermultiplets are defined in terms of left–handed Weyl spinors and the left–handed conjugate states are used for the $SU(2)_L$ singlet fields.

**Table 2.2:** Chiral supermultiplets and superpartners in the MSSM and their quantum numbers. Only the first generation of quark and lepton supermultiplets is shown here. The spin–0 fields are complex scalars and the spin–1/2 fields are two–component Weyl spinors [4].

| Supermultiplets | Superpartners | spin 0 | spin 1/2 | $SU(3)_C$, $SU(2)_L$, $U(1)_Y$ |
|---|---|---|---|---|
| $\hat{Q}$ | squarks, quarks | $(\tilde{u}_L\ \tilde{d}_L)$ | $(u_L\ d_L)$ | $(\mathbf{3}, \mathbf{2}, \frac{1}{3})$ |
| $\hat{u}^c$ | ($1^{st}$ family) | $\tilde{u}^*_R$ | $u^\dagger_R$ | $(\bar{\mathbf{3}}, \mathbf{1}, -\frac{4}{3})$ |
| $\hat{d}^c$ | | $\tilde{u}^*_R$ | $d^\dagger_R$ | $(\bar{\mathbf{3}}, \mathbf{1}, \frac{2}{3})$ |
| $\hat{L}$ | sleptons, leptons | $(\tilde{\nu}_L\ \tilde{e}_L)$ | $(\nu_L\ e_L)$ | $(\mathbf{1}, \mathbf{2}, -1)$ |
| $\hat{e}^c$ | ($1^{st}$ family) | $\tilde{e}^*_R$ | $e^\dagger_R$ | $(\mathbf{1}, \mathbf{1}, 2)$ |
| $\hat{H}_u$ | Higgs, higgsinos | $(H^+_u\ H^0_u)$ | $(\tilde{H}^+_u\ \tilde{H}^0_u)$ | $(\mathbf{1}, \mathbf{2}, +1)$ |
| $\hat{H}_d$ | | $(H^0_d\ H^-_d)$ | $(\tilde{H}^0_d\ \tilde{H}^-_d)$ | $(\mathbf{1}, \mathbf{2}, -1)$ |

***R*–parity Conservation** In most general supersymmetric theories, baryon and lepton number conservation is violated leading in many cases to an unstable proton with a decay life–time shorter than the experimental lower limit. To enforce the conservation of these quantum numbers, a new symmetry, called $R$–parity, is introduced. $R$–parity is defined by

$$P_R = (-1)^{2s+3B+L} \tag{2.28}$$

where $L$ and $B$ are the lepton and baryon quantum numbers and $s$ is the spin quantum number. With this definition, the Standard Model particles have $P_R = +1$ and their superpartners have $P_R = -1$. With conserved $R$–parity, supersymmetric particles and their anti–particles are produced in pairs and the lightest supersymmetric particle (LSP) is stable and therefore provides a good candidate for cold dark matter in the Universe.

**The MSSM Superpotential** The minimal gauge group and particle content together with $R$–parity conservation allow to build a globally supersymmetric Lagrangian using the

superpotential which gives the form of the scalar potential, $V$, and the Yukawa interactions between fermion and scalar fields [3],

$$\begin{aligned} W_{\text{MSSM}} = &+ \hat{u}^{c\,ia}\,(\boldsymbol{y_u})^j_i\,\hat{Q}_{j\alpha a}\left(\hat{H}_u\right)_\beta \epsilon^{\alpha\beta} \\ &- \hat{d}^{c\,ia}\,(\boldsymbol{y_d})^j_i\,\hat{Q}_{j\alpha a}\left(\hat{H}_d\right)_\beta \epsilon^{\alpha\beta} \\ &- \hat{e}^{c\,ia}\,(\boldsymbol{y_e})^j_i\,\hat{L}_{j\alpha a}\left(\hat{H}_d\right)_\beta \epsilon^{\alpha\beta} \\ &+ \mu\left(\hat{H}_u\right)_\alpha\left(\hat{H}_d\right)_\beta \epsilon^{\alpha\beta}, \end{aligned} \tag{2.29}$$

with family indices $i, j = 1, 2, 3$, the colour index $a = 1, 2, 3$, the weak isospin $\alpha, \beta = 1, 2$ and the totally antisymmetric tensor, $\epsilon^{\alpha\beta}$. The objects $\hat{H}_{u,d}$, $\hat{Q}$, $\hat{L}$, $\hat{u}^c$,$\hat{d}^c$, $\hat{e}^c$ are the chiral supermultiplets in Table 2.2 and $\boldsymbol{y_{u,d,e}}$ are the generalised $3 \times 3$ Yukawa coupling matrices which determine the masses and CKM mixing angles after electroweak symmetry breaking. The last term in Equation 2.29 is the so–called $\mu$ term, the globally supersymmetric Higgs mass term with the Higgs mixing parameter, $\mu$.

The Lagrangian of the MSSM is given by

$$\mathfrak{L}_{\text{MSSM}} = \mathfrak{L}_{\text{chiral}} + \mathfrak{L}_{\text{gauge}}. \tag{2.30}$$

The chiral part of the Lagrangian is

$$\mathfrak{L}_{\text{chiral}} = -D^\mu \phi^{*i} D_\mu \phi_i + i\psi^{\dagger i}(-1)\sigma^\mu D_\mu \psi_i - \frac{1}{2}\left(W^{ij}\psi_i\psi_j + W^*_{ij}\psi^{\dagger i}\psi^{\dagger j}\right) - W^i W^*_i, \tag{2.31}$$

with the complex scalar fields, $\phi_i$, and left–handed Weyl fermion fields, $\psi_j$, of the supermultiplets listed in Table 2.2 and the Pauli matrices, $\sigma^\mu$, as well as the total derivatives,

$$W^i = \frac{\delta W}{\delta \phi_i} \tag{2.32}$$

and

$$W^{ij} = \frac{\delta^2 W}{\delta\phi_i \delta\phi_j}, \tag{2.33}$$

of the superpotential, $W$, with the indices, $i$ and $j$, running over all gauge and flavour degrees of freedom. The Lagrangian for each of the gauge supermultiplets ($\hat{G}_a$, $\hat{W}_a$ and $\hat{B}$) is

$$\mathfrak{L}_{\text{gauge}} = -\frac{1}{4}F^a_{\mu\nu}F^{\mu\nu a} + i\lambda^{\dagger a}\bar{\sigma}^\mu D_\mu \lambda^a + \frac{1}{2}g^2\left(\phi^* T^a \phi\right)^2, \tag{2.34}$$

with the field strength tensor,

$$F^a_{\mu\nu} = \partial_\mu A^a_\nu - \partial_\nu A^a_\mu + g f^{abc} A^b_\mu A^c_\nu, \tag{2.35}$$

and the covariant derivative,

$$D_\mu \lambda^a = \partial_\mu \lambda^a + g f^{abc} A^b_\mu \lambda^c \tag{2.36}$$

of the two–component Weyl gaugino fields, $\lambda^a$, with the massless gauge boson fields, $A^a_\mu$, and the structure constant, $f^{abc}$, of the respective gauge group. In Equation 2.34, $T^a$ are the generators of the gauge group and $g$ is the respective coupling constant. For the three gauge supermultiplets in the MSSM, the index $a$ runs over $a = 1, ..., 8$ for the $SU(3)_C$ gauge group, $a = 1, 2, 3$ for the $SU(2)_L$ gauge group and $a = 1$ for $U(1)_Y$.

**Minimal Soft Supersymmetry Breaking** To finalise the MSSM, supersymmetry has to be softly broken as discussed above. The specific mechanism of supersymmetry breaking is not known so far. Instead the effects of spontaneous supersymmetry breaking are parametrised by adding by hand the most general soft supersymmetry breaking terms to the MSSM Lagrangian:

$$\begin{aligned}
\mathfrak{L}^{\text{MSSM}}_{\text{soft}} = & -\frac{1}{2}\left(M_3 \tilde{G}^a \tilde{G}_a + M_2 \tilde{W}^b \tilde{W}_b + M_1 \tilde{B}\tilde{B} + c.c.\right) \\
& - \left(\tilde{\bar{u}} \boldsymbol{a_u} \tilde{Q} H_u - \tilde{\bar{d}} \boldsymbol{a_d} \tilde{Q} H_d - \tilde{\bar{e}} \boldsymbol{a_e} \tilde{L} H_d + c.c\right) \\
& - \tilde{Q}^\dagger \boldsymbol{m^2_Q} \tilde{Q} - \tilde{L}^\dagger \boldsymbol{m^2_L} \tilde{L} - \tilde{\bar{u}} \boldsymbol{m^2_{\bar{u}}} \tilde{\bar{u}}^\dagger - \tilde{\bar{d}} \boldsymbol{m^2_{\bar{d}}} \tilde{\bar{d}}^\dagger - \tilde{\bar{e}} \boldsymbol{m^2_{\bar{e}}} \tilde{\bar{e}}^\dagger \\
& - m^2_{H_u} H^*_u H_u - m^2_{H_d} H^*_d H_d - (B\mu\, H_u H_d + c.c.)\,,
\end{aligned} \tag{2.37}$$

with the indices $a = 1, ..., 8$ and $b = 1, 2, 3$. $M_{1,2,3}$ are the bino, wino and gluino mass terms, $\boldsymbol{a_{u,d,e}}$ are complex $3 \times 3$ matrices in family space which correspond to the Yukawa matrices, $\boldsymbol{y_{u,d,e}}$, of the superpotential such that the matrix elements are given by $a^{ij}_{u,d,l} = A^{ij}_{u,d,l}\, y^{ij}_{u,d,l}$ with the trilinear sfermion–Higgs couplings, $A^{ij}_{u,d,l}$. The objects $\boldsymbol{m^2_{Q,L,\bar{u},\bar{d},\bar{e}}}$ are $3 \times 3$ mass matrices in family space for squarks and sleptons. The last line in Equation 2.37 contains the squared Higgs mass parameters, $m^2_{H_u}$ and $m^2_{H_d}$, the Higgs mixing parameter, $\mu$, and the supersymmetry breaking bilinear Higgs coupling term, $B$, for the two Higgs doublets $H_u$ and $H_d$.

The soft supersymmetry breaking terms in Equation 2.37 introduce 105 free parameters in addition to the 19 free parameters of the Standard Model. Without restrictions on any of these parameters, the model is called the unconstrained MSSM.

**Gauge Versus Mass Eigenstates** The superpartners listed in Tables 2.1 and 2.2 are the gauge eigenstates of the MSSM which are not necessarily mass eigenstates. Effects from electroweak and supersymmetry breaking can introduce a mixing between the charged and neutral gauge eigenstates of the electroweak gauginos and higgsinos and also among sfermions and Higgs scalars to form the mass eigenstates of the MSSM given in Table 2.3. In the notation of Table 2.3, the sfermion mixing occurs in all three generations but it

is convention to neglect the mixing of first and second generation sfermions. Note that gluinos and electroweak goldstinos do not mix with any other state because there are none with the same quantum numbers.

**Table 2.3:** Gauge eigenstates of MSSM particles and their corresponding mass eigenstates [4]. For squarks and sleptons only the first generation is shown, the second and third generations behave equivalently. First and second generation sfermion mixing is often assumed to be negligible. Spin and $R$–parity, $P_R$, quantum numbers are also shown.

| Particles | Spin | $P_R$ | Gauge Eigenstates | Mass Eigenstates |
|---|---|---|---|---|
| Higgs bosons | 0 | +1 | $H_u^0$, $H_d^0$, $H_u^+$, $H_d^-$ | $h$, $H$, $A$, $H^\pm$ |
| squarks | 0 | −1 | $\tilde{u}_L$, $\tilde{u}_R$, $\tilde{d}_L$, $\tilde{d}_R$ | $\tilde{u}_1$, $\tilde{u}_2$, $\tilde{d}_1$, $\tilde{d}_2$ |
| sleptons | 0 | −1 | $\tilde{e}_L$, $\tilde{e}_R$, $\tilde{\nu}_e$ | $\tilde{e}_1$, $\tilde{e}_2$, $\tilde{\nu}_e$ |
| neutralinos | 1/2 | −1 | $\tilde{B}^0$, $\tilde{W}^0$, $\tilde{H}_1^0$, $\tilde{H}_2^0$ | $\tilde{\chi}_1^0$, $\tilde{\chi}_2^0$, $\tilde{\chi}_3^0$, $\tilde{\chi}_4^0$ |
| charginos | 1/2 | −1 | $\tilde{W}^\pm$, $\tilde{H}_u^+$, $\tilde{H}_d^-$ | $\tilde{\chi}_1^\pm$, $\tilde{\chi}_2^\pm$ |
| gluino | 1/2 | −1 | $\tilde{G}$ | $\tilde{G}$ |
| goldstino | 1/2 | −1 | $\tilde{g}$ | $\tilde{g}$ |

### 2.2.4 The Higgs Sector of the MSSM

To break the electroweak symmetry in the framework of the MSSM two doublets of complex scalar fields are needed due to the following reasons.

In the Standard Model, chiral anomalies which spoil the renormalisability of the theory are cancelled because the sum of hypercharges, $Y$, and isospin, $I^3$, quantum numbers of the left–handed fermions, i.e. of the electric charges in each generation is zero, $\mathrm{Tr}[Y_f] = \mathrm{Tr}[Q_f] = 0$. In the MSSM the Higgs fields are members of chiral supermultiplets in which their fermionic superpartners are weak isodoublets with hypercharge $Y = 1$ or $-1$. If there is only one Higgs doublet the traces of $Q$ and $Y$ are no longer zero and chiral anomalies are not cancelled. To preserve these cancellations, two chiral Higgs supermultiplets are needed with weak hypercharges $Y = \pm 1$, respectively.

A second reason for two Higgs doublets is the generation of the masses for up– and down–type fermions. In the Standard Model this is achieved by Yukawa couplings of the field $\Phi$ and its conjugate $\tilde{\Phi}$. In a supersymmetric theory, the superpotential is only a function of the superfields and not of their conjugates (see Equation 2.29). Therefore, two separate scalar fields with hypercharges $Y = \pm 1$ are needed to give masses individually to the up– and down–type fermions.

With the two Higgs doublets introduced in Section 2.2.3,

$$H_u = \begin{pmatrix} H_u^+ \\ H_u^0 \end{pmatrix}, \quad H_d = \begin{pmatrix} H_d^0 \\ H_d^- \end{pmatrix}, \tag{2.38}$$

the corresponding classical scalar Higgs potential is given by

$$\begin{aligned} V_H = &\left(|\mu|^2 + m_{H_u}^2\right)\left(|H_u^0|^2 + |H_u^+|^2\right) + \left(|\mu|^2 + m_{H_d}^2\right)\left(|H_d^0|^2 + |H_d^-|^2\right) \\ &+ \left[B\mu\left(H_u^+ H_d^- - H_u^0 H_d^0\right) + c.c.\right] \\ &+ \frac{1}{8}\left(g_1^2 + g_2^2\right)\left(|H_u^0|^2 + |H_u^+|^2 - |H_d^0|^2 - |H_d^-|^2\right)^2 \\ &+ \frac{1}{2} g_2^2 |H_u^+ H_d^{0*} + H_u^0 H_d^{-*}|^2, \end{aligned} \tag{2.39}$$

where terms proportional to $|\mu|^2$ come from the last term in the superpotential in Equation 2.29 and terms proportional to $g_1^2$ and $g_2^2$ come from the last term in the gauge part of the MSSM Lagrangian given in Equation 2.34. The terms proportional to $m_{H_u}^2$, $m_{H_d}^2$ and $B\mu$ correspond to the fourth line of the soft supersymmetry breaking Lagrangian in Equation 2.37. Additional terms in the complete scalar potential involving sfermion fields are not included here because they do not contribute to electroweak symmetry breaking. The minimum of the potential $V_H$ needs to break $SU(2)_L \times U(1)_Y$ symmetry while preserving $U(1)_Q$. This is achieved by choosing the vacuum expectation value of $H_u^+$ to be zero which requires the vacuum expectation value of $H_d^-$ to be zero as well. The scalar potential is bounded from below if

$$2B\mu < 2|\mu|^2 + m_{H_u}^2 + m_{H_d}^2. \tag{2.40}$$

To break the electroweak symmetry, a linear combination of $H_u^0$ and $H_d^0$ has to acquire a negative value of the mass parameter squared, which requires

$$(B\mu)^2 > \left(|\mu|^2 + m_{H_u}^2\right)\left(|\mu|^2 + m_{H_d}^2\right). \tag{2.41}$$

Both conditions can only be satisfied simultaneously if $m_{H_d}^2 \neq m_{H_u}^2$ which means that the electroweak symmetry can only be broken if supersymmetry is broken.

In models with minimal supergravity [54, 55] or in gauge mediated supersymmetry breaking models [56, 57], $m_{H_d}^2 = m_{H_u}^2$ is satisfied at tree level at high energy scales. But heavy fermion and sfermion contributions to the running of $m_{H_{u,d}}^2$ break this mass degeneracy at the electroweak scale. This mechanism is called radiative electroweak symmetry breaking [58] and provides a mechanism for the electroweak phase transition.

### The MSSM Higgs Bosons

The vacuum expectation values of the two Higgs doublets,

$$v_u = \langle H_u^0 \rangle, \quad v_d = \langle H_d^0 \rangle, \tag{2.42}$$

are chosen to be real and positive and their ratio is written as

$$\tan\beta = \frac{v_u}{v_d}. \tag{2.43}$$

The two complex scalar doublets in Equation 2.38 have eight real degrees of freedom. The mass eigenstates of the Higgs fields (see Table 2.3) are obtained from rotations,

$$\begin{pmatrix} H_u^0 \\ H_d^0 \end{pmatrix} = \begin{pmatrix} v_u \\ v_d \end{pmatrix} + \frac{1}{\sqrt{2}} \begin{pmatrix} \cos\alpha & \sin\alpha \\ \sin\alpha & \cos\alpha \end{pmatrix} \begin{pmatrix} h \\ H \end{pmatrix} + \frac{i}{\sqrt{2}} \begin{pmatrix} \sin\beta & \cos\beta \\ \cos\beta & \sin\beta \end{pmatrix} \begin{pmatrix} G \\ A \end{pmatrix} \tag{2.44}$$

and

$$\begin{pmatrix} H_u^+ \\ H_d^{-*} \end{pmatrix} = \begin{pmatrix} \sin\beta & \cos\beta \\ \cos\beta & \sin\beta \end{pmatrix} \begin{pmatrix} G^+ \\ H^+ \end{pmatrix}, \tag{2.45}$$

with the angles $\alpha$ and $\beta$ chosen such that the quadratic part of the scalar potential is transformed into diagonal mass terms. The scalars $G^+$ and $H^+$ have electric charge $+1$, their conjugates $G^- = G^{+*}$ and $H^- = H^{+*}$ have charge $-1$. The scalars $h$ and $H$ are electrically neutral and CP–even while the scalars $A$ and $G$ are neutral and CP–odd. As in the Standard Model, the massless neutral and charged Goldstone bosons $G$, $G^\pm$ become the longitudinal modes of the massive gauge bosons, $Z$ and $W^\pm$, after a suitable gauge transformation. The masses of the MSSM Higgs bosons are then given by

$$\begin{aligned} m_A^2 &= 2B\mu/\sin(2\beta) = 2|\mu|^2 + m_{H_u}^2 + m_{H_d}^2, \\ m_{h,H}^2 &= \frac{1}{2}\left(m_A^2 + m_Z^2 \mp \sqrt{\left(m_A^2 - m_Z^2\right)^2 4 m_Z^2 m_A^2 \sin^2(2\beta)}\right), \\ m_{H^\pm}^2 &= m_A^2 + m_W^2. \end{aligned} \tag{2.46}$$

At tree level, the mixing angle $\alpha$ is given by

$$\alpha = \frac{1}{2}\arctan\left(\tan(2\beta)\frac{m_A^2 + m_Z^2}{m_A^2 - m_Z^2}\right), \quad -\frac{\pi}{2} < \alpha < 0. \tag{2.47}$$

As can be seen from Equations 2.46, the masses of $A$, $H$ and $H^\pm$ can have arbitrary values, but the mass of $h$ is bounded from above. At tree level, $m_h$ is constrained to be

$$m_h < m_Z |\cos(2\beta)|, \tag{2.48}$$

but radiative corrections, in particular from top quark and squark contributions, can weaken this bound notably as discussed in Section 2.2.5.

### 2.2.5 The $m_h^{\text{max}}$ Scenario

Equations 2.46 show that at tree level the MSSM Higgs boson masses are determined by two free parameters — usually by convention chosen as $m_A$ and $\tan\beta$ — and by the $W$ and $Z$ boson masses. However, radiative corrections contribute significantly to the Higgs masses [59]. At one–loop level, the main corrections arise from the top–stop quark sector, for large values of $\tan\beta$ also from the bottom–sbottom quark sector. Assuming that the stop and sbottom masses are degenerate and equal to the supersymmetry breaking scale, $M_{\text{SUSY}}$, the relevant parameters are $m_b$, $m_t$ and $M_{\text{SUSY}}$, the trilinear Higgs–stop and Higgs–sbottom Yukawa couplings $A_{t,b}$ and the Higgs mixing parameter, $\mu$. Additional corrections are determined by the electroweak gaugino mass parameters, $M_{1,2}$, with $M_1 = \frac{5}{3}\frac{\sin^2\theta_W}{\cos^2\theta_w} \cdot M_2$. At two–loop level, also the gluino mass parameter, $M_3$, becomes relevant. This leads to in total 9 additional free parameters specifying the MSSM Higgs sector. In order to reduce the parameter space, the $m_h^{\text{max}}$ benchmark scenario has been proposed [60] where the parameters contributing to the radiative corrections are fixed such that the mass, $m_h$, of the light CP–even Higgs boson becomes maximal under variation of $m_A$ and $\tan\beta$. For the fixed parameters given in Table 2.4, the maximum possible value of $m_h \lesssim 135\,\text{GeV}$ for all values of $\tan\beta$ is obtained for the maximum allowed value of the CP–odd Higgs boson mass in this scenario, $m_A = 1\,\text{TeV}$.

**Table 2.4:** Parameters contributing to higher order corrections of the MSSM Higgs boson properties, with values defined according to the $m_h^{\text{max}}$ scenario [60]. The parameters $m_b$ and $\alpha_s$ are evaluated at energy scales corresponding to the bottom quark and the $Z$ boson mass, respectively. The stop mixing parameter $X_t$ is given by $X_t = A_t - \mu/\tan\beta$.

| $m_t$ | $m_b(m_b)$ | $\alpha_s(m_z)$ | $M_{\text{SUSY}}$ | $\mu$ | $M_2$ | $M_3$ | $X_t$ | $A_b$ |
|---|---|---|---|---|---|---|---|---|
| 174.3 GeV | 4.213 GeV | 0.119 | 1 TeV | 200 GeV | 200 GeV | 800 GeV | 2 TeV | $A_t$ |

The $m_h^{\text{max}}$ scenario allows to set conservative bounds on $\tan\beta$ and is used throughout this thesis with the parameters in Table 2.4 except for the top mass which is set to a more recent world average of $m_t = 172.5\,\text{GeV}$ [61]. In the $m_h^{\text{max}}$ scenario all parameters of the Higgs sector except for $m_A$ and $\tan\beta$ are fixed and the masses, $m_h$, $m_H$ and $m_{H^\pm}$, of the remaining Higgs bosons are derived depending on $m_A$ and $\tan\beta$ as shown in Figure 2.6. Especially for large values of $\tan\beta$ two of the three neutral Higgs bosons are closely degenerate in mass such that for light CP–odd Higgs masses, $m_A \lesssim 130\,\text{GeV}$, the light CP–even and the CP–odd Higgs bosons are degenerated, $m_h \simeq m_A$, and the heavy CP–even Higgs boson is $m_H \simeq 130\,\text{GeV}$. For $m_A \gtrsim 130\,\text{GeV}$ the heavy CP–even Higgs boson is degenerate in mass with the CP–odd Higgs boson, $m_H \simeq m_A$, and $m_h$ reaches its maximum value.

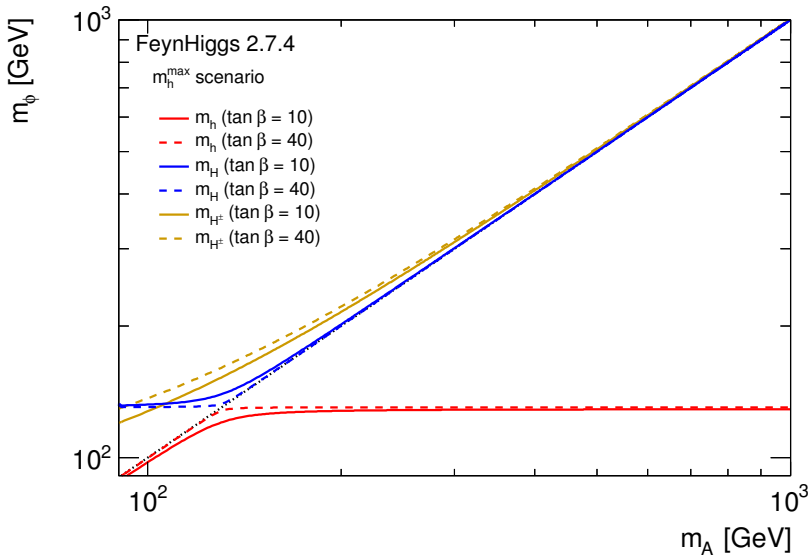


**Figure 2.6:** Masses of the MSSM Higgs bosons in the $m_h^{\max}$ scenario as a function of the mass, $m_A$, of the CP–odd Higgs boson for $\tan\beta = 10$ and 40 calculated with the FeynHiggs 2.7.4 programme [59, 62–64].

### 2.2.6 Theoretical Constraints on the MSSM Higgs Sector

In the MSSM, $\tan\beta$ is a free parameter. The couplings of the pseudoscalar and charged MSSM Higgs bosons, as well as the coupling of the $h$ ($H$) boson for small (large) values of $m_A$, to up– and down–type fermions are proportional to $\cot\beta$ and $\tan\beta$, respectively, as can be seen from Table 3.1 using Equation 2.47. The requirement that the couplings should remain in the perturbative regime puts constraints on $\tan\beta$. In the most general MSSM scenarios, the resulting bound is rather loose, $\tan\beta \lesssim 150$, but in models with universal boundary conditions at the GUT scale, perturbation theory breaks down unless $\tan\beta$ is within the range of $0.5 \leq \tan\beta \leq \frac{m_t}{m_b} \simeq 60$ [65] for $M_{\text{SUSY}} \sim 1\,\text{TeV}$.

# Chapter 3

# Higgs Boson Phenomenology

This chapter reviews phenomenological aspects of the Standard Model Higgs boson and of the neutral MSSM Higgs bosons relevant for the two experimental searches in the decay channel to two oppositely charged muons performed in the context of this thesis. Section 3.1 outlines the phenomenology of proton–proton collisions based on Reference [66]. Production mechanisms and decay channels of the Standard Model Higgs boson at the Large Hadron Collider (LHC) are discussed in Section 3.2 based on Reference [1]. Section 3.3 summarises the production modes and decay channels of neutral MSSM Higgs bosons at the LHC based on Reference [3]. Section 3.4 gives an overview of the current status of Higgs boson searches at hadron colliders.

## 3.1 Phenomenology of Proton–Proton Collisions

Scattering processes at hadron colliders can be classified in hard and soft processes. The hard processes, like Higgs boson production, occur at high momentum transfer, $Q^2$, and can be precisely predicted by perturbative QCD calculations, while the properties of the soft processes are dominated by non–perturbative QCD effects. In proton–proton collisions at high energy, the hard process is accompanied by soft interactions like initial and final state gluon radiation and interactions of the proton remnants which lead to final state particles generally referred to as the underlying event.

The hadronic cross section of, for instance, Higgs boson production in collisions of two protons $A$ and $B$, $\sigma_{AB\to HX}$, where $H$ is the Higgs boson and $X$ are hadronic remnants from soft interactions, can be calculated using the QCD factorisation theorem [67]. This concept was first introduced in the calculation of the Drell–Yan process [68]. Higher order corrections involving virtual and real gluon emissions, in general cannot be determined

perturbatively but rather can be split off from the hard process and absorbed in the parton distribution functions (PDF) of the protons [66]. The parton distribution function, $f_{q|A}(x, Q^2)$, is the probability density function of the momentum fraction $x$ of a parton $q$ in the proton $A$ in a process with momentum transfer $Q^2$. The resulting separation of the short–distance part of the interaction calculated perturbatively and the long–distance part described by the parton distribution functions is called factorisation.

A generic hadronic interaction is illustrated in Figure 3.1. According to the factorisation theorem, the hadronic cross section is obtained by weighting the cross section, $\hat{\sigma}_{ab\to H}$, for the hard interaction of the partons $a$ and $b$ in the protons $A$ and $B$, respectively with the parton distribution functions of the two protons, $f_{a|A(x,\mu_F^2)}$ and $f_{b|B(x,\mu_F^2)}$:

$$\sigma_{AB\to HX} = \iint dx_a dx_b f_{a|A(x_a,\mu_F^2)} f_{b|B(x_b,\mu_F^2)} \hat{\sigma}_{ab\to H}(\alpha_s(\mu_R^2)), \tag{3.1}$$

where the so–called factorisation scale, $\mu_F$, is the energy scale at which the short–distance part of the interaction is separated from the long–distance part. The cross section for the hard process is calculated perturbatively with radiative corrections in powers of the running strong coupling constant $\alpha_s(\mu_R^2)$ which is evaluated at the renormalisation scale, $\mu_R$.

Figure 3.2 shows the predictions for hadronic cross sections of Standard Model processes in $pp$ and $p\bar{p}$ collisions as a function of the centre–of–mass energy calculated in next–to–leading order perturbation theory using the factorisation formalism [66].

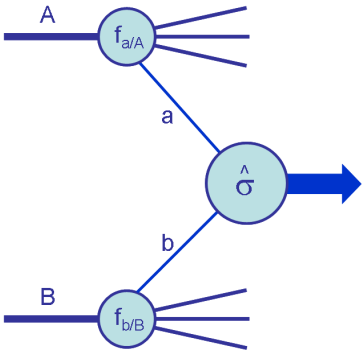


**Figure 3.1:** Schematic diagram of a generic hard scattering process between two hadrons [66].

## 3.2 Standard Model Higgs Boson Production at the LHC

The properties of the Standard Model Higgs boson, such as the production cross sections, the decay rates to fermions and gauge bosons, and the total decay width are completely determined when the Higgs boson mass is known.

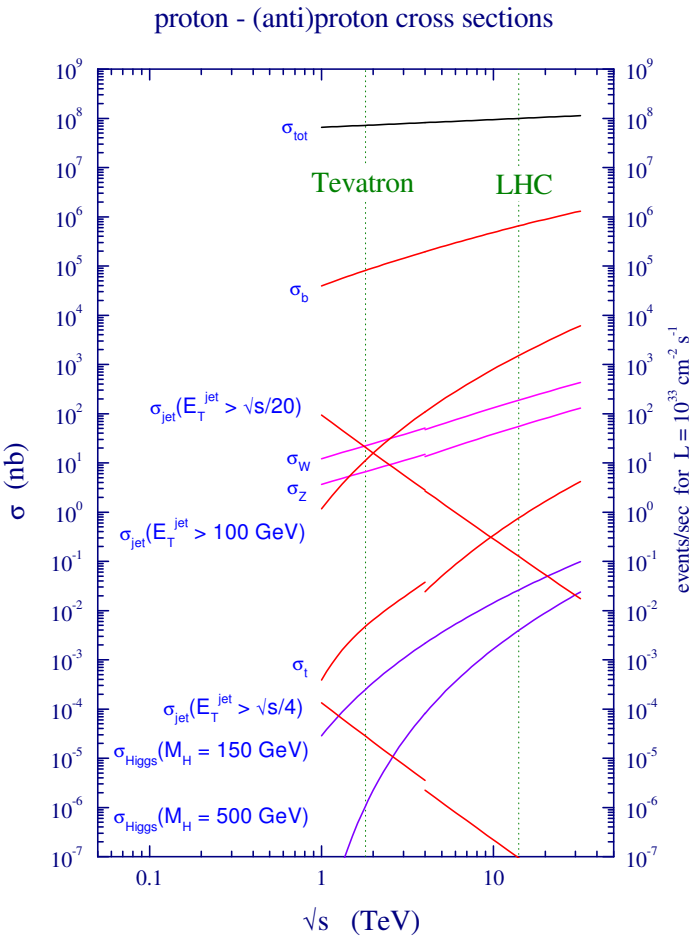


**Figure 3.2:** Cross sections of Standard Model processes in $p\bar{p}$ and $pp$ collisions as a function of the centre–of–mass energy, $\sqrt{s}$, calculated in next–to–leading order perturbation theory [66]. The design centre–of–mass energies of the Tevatron (1.96 TeV) and the LHC (14 TeV) are indicated.

The Standard Model Higgs boson is produced through several production modes in proton–proton collisions as illustrated by the tree–level Feynman diagrams in Figure 3.3. The cross sections of these processes are shown in Figure 3.4(a) as a function of the Higgs boson mass calculated for the LHC design centre–of–mass energy of $\sqrt{s} = 14\,\text{TeV}$. The dominant production mode is the gluon fusion process, followed by the vector boson fusion process. The latter is approximately one order of magnitude lower in cross section, but the characteristic high–energy forward jets allow for an efficient suppression of background processes. The associated vector boson and associated top quark pair production modes have significantly lower cross sections than the vector boson fusion, but provide signatures for exclusive searches for experimentally challenging Higgs boson decays. For example, $H \to b\bar{b}$ decays are only detectable at the LHC if the Higgs boson is produced in association

with top quark pairs or vector bosons which can be used to reduce the large background from $b\bar{b}$ production at the LHC. The production cross sections for the Standard Model Higgs boson in proton–proton collisions increases with the centre–of-mass energy as can be seen in Figure 3.2. The total production cross section for the LHC centre–of-mass energies of $\sqrt{s} = 7\,\text{TeV}$, $8\,\text{TeV}$ and $14\,\text{TeV}$ are shown in Figure 3.4(b). The former two centre–of–mass energies correspond to the LHC operation in the years 2011 and 2012.

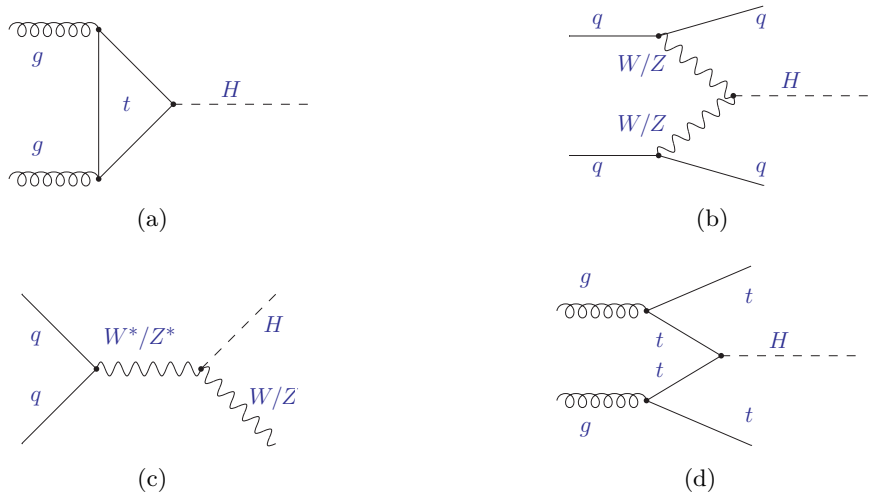


**Figure 3.3:** Tree–level Feynman diagrams for the dominant production modes of the Standard Model Higgs boson in $pp$ collisions at the LHC: the gluon fusion process (a), vector boson fusion (b), associated production with $W$ or $Z$ bosons (c) and associated production with top quark pairs (d). Particles and anti–particles are labelled the same, $q$ refers to all quark flavours.

The calculations of the cross sections for the different Higgs boson production processes as well as the parton distribution functions, factorisation and normalisation scales and corresponding uncertainties used for the calculations are reported in References [69, 70] and references therein. The cross section for the gluon fusion process is calculated in next–to–next–to–leading order (NNLO) QCD including next–to–leading order (NLO) electroweak (EW) corrections and QCD soft–gluon resummation in next–to–next–to–leading logarithm (NNLL) approximation assuming the factorisation of QCD and EW corrections. For Higgs boson production in vector boson fusion, the cross section is calculated with full NLO QCD and EW corrections and approximate NNLO QCD corrections. The cross sections for Higgs boson production in association with vector bosons are calculated including NNLO QCD and NLO EW corrections. For Higgs boson production in association with top quark pairs, the cross section is estimated in NLO QCD. The Higgs boson decay branching fractions are computed with the programmes HDECAY [71] and PROPHECY4F [72, 73].

The Standard Model Higgs boson decays predominantly to the heaviest fermions and

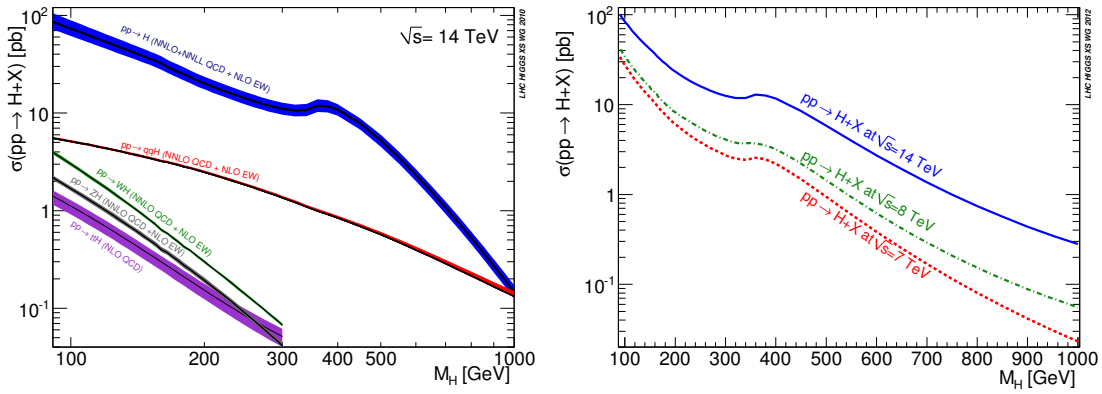


(a) (b)

**Figure 3.4:** Cross sections for the production of the Standard Model Higgs boson in $pp$ collisions at the nominal LHC centre–of–mass energy of $\sqrt{s} = 14\,\text{TeV}$ via gluon fusion ($pp \to H$), vector boson fusion ($pp \to qqH$) and productions in association with $W$ bosons ($pp \to WH$), $Z$ bosons ($pp \to ZH$) and top quark pairs ($pp \to ttH$) (a) and total Higgs boson production cross section for $pp$ collisions at centre–of–mass energies of $\sqrt{s} = 7\,\text{TeV}$ and $8\,\text{TeV}$ corresponding to the LHC running in 2011 and 2012 compared to the nominal LHC centre–of–mass energy of $\sqrt{s} = 14\,\text{TeV}$ (b) as functions of the Higgs boson mass, $M_H$ [69].

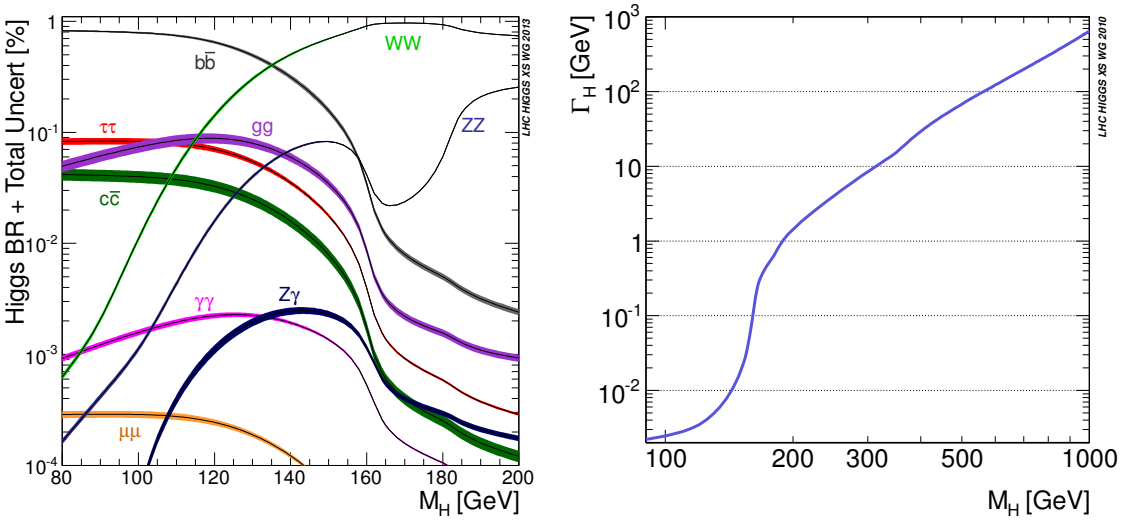


(a) (b)

**Figure 3.5:** Decay branching fractions (a) and total width (b) of the Standard Model Higgs boson as a function of its mass, $M_H$ [69].

gauge bosons allowed by phase space. The branching fractions of the Standard Model Higgs boson decays are shown in Figure 3.5(a) as a function of its mass. The Higgs boson

decay to two oppositely charged muons, $H \to \mu^+\mu^-$, which is studied in Chapter 7 has a very low branching fraction of about 10 times smaller than for the $H \to \gamma\gamma$ decay for a Higgs boson mass of about 125 GeV. Figure 3.5(b) shows the natural width of the Standard Model Higgs boson as a function of its mass. For Higgs boson masses below about 200 GeV, the natural width becomes too small to be resolved experimentally.

## 3.3 Neutral MSSM Higgs Boson Production at the LHC

In contrast to the Standard Model Higgs boson, the properties of the neutral MSSM Higgs bosons such as production cross sections, branching fractions and natural widths are not fully determined once their masses are known. At tree level, the Higgs boson properties depend on the mass, $m_A$, of the CP–odd Higgs boson and on $\tan\beta$. Additional parameters introduced by higher order corrections are fixed in the $m_h^{\max}$ scenario discussed in Section 2.2.5. The couplings of the neutral MSSM Higgs bosons to up– and down–type fermions and to gauge bosons can be expressed relative to the Standard Model Higgs boson couplings in terms of the MSSM angles $\alpha$ and $\beta$ as shown in Table 3.1. The couplings of the CP–odd Higgs boson, $A$, as well as the CP–even Higgs boson, $h$ ($H$), for small (large) values of $m_A$ to up– and down–type fermions are proportional to $\cot\beta$ and $\tan\beta$, respectively. The coupling to gauge bosons is suppressed for the CP–even Higgs bosons, $h$ and $H$, and is non–existent for the CP–odd Higgs boson, $A$.

**Table 3.1:** Couplings of the neutral MSSM Higgs bosons to up– and down–type fermions and to gauge bosons relative to the couplings of the Standard Model Higgs boson [3].

| $\phi$ | $CP$ | $g_{\phi\bar{u}u}$ | $g_{\phi\bar{d}d}$ | $g_{\phi VV}$ |
|---|---|---|---|---|
| SM $H$ | *even* | 1 | 1 | 1 |
| $h$ | *even* | $\cos\alpha/\sin\beta$ | $-\sin\alpha/\cos\beta$ | $\sin(\beta-\alpha)$ |
| $H$ | *even* | $\sin\alpha/\sin\beta$ | $\cos\alpha/\cos\beta$ | $\cos(\beta-\alpha)$ |
| $A$ | *odd* | $\cot\beta$ | $\tan\beta$ | 0 |

In proton–proton collisions at the LHC, there are two dominant production mechanisms for neutral MSSM Higgs bosons. The tree–level Feynman diagrams of these processes are shown in Figure 3.6 and the corresponding production cross sections in proton–proton collisions at a centre–of–mass energy of $\sqrt{s} = 7\,\text{TeV}$ are shown in Figure 3.7 as functions of the CP–odd Higgs boson mass, $m_A$, and $\tan\beta$. In contrast to the Standard Model, the gluon fusion process in addition to the top quark loop has a significant contribution from the $b$ quark loop. Additional stop and sbottom loop contributions only play a role in the case of small squark masses. The $b$ quark contribution is particularly important for large values of $\tan\beta$ where the couplings to down–type fermions are strongly enhanced. For the same reason the $b$–quark associated production is the second major production

mode. At tree–level, the Higgs bosons are accompanied by up to two $b$ quarks in the final state. Higher order effects increase the number of the final state $b$ quarks. This is in particular important for the bottom quark annihilation process predicting at tree–level no $b$ quarks in the final state. The accompanying $b$ quarks in the associated production allow for an efficient suppression of background process. The cross sections for gluon fusion and $b$–quark associated production both increase with $\tan\beta$ and the latter becomes dominant for $\tan\beta \gtrsim 8$. The cross section for the gluon fusion process is calculated with the HIGLU [74] and ggh@nnlo [75, 76] programmes in next–to–next–to–leading order (NNLO) QCD. For the $b$–quark associated production, a matching scheme [77] is used to combine the cross section calculations at NNLO QCD using the four–flavour [78, 79] and five–flavour [80] schemes. The branching fractions of the neutral MSSM Higgs boson decays discussed below are calculated with FeynHiggs 2.7.4 [59, 62–64]. The details for the calculations and their uncertainties due to the value of the running strong coupling constant, $\alpha_s$, as well as the parton distribution functions and factorisation and renormalisation scales are reported in References [69, 70].

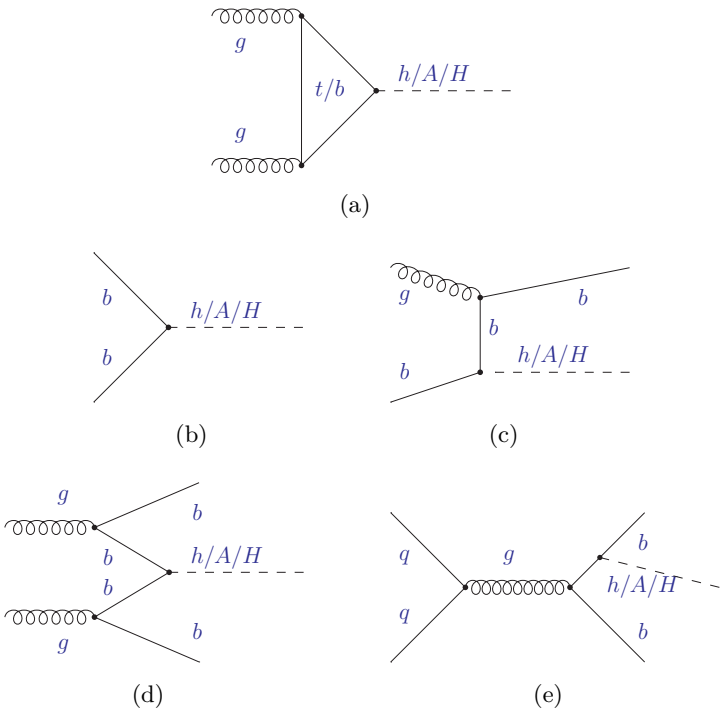


**Figure 3.6:** Tree–level Feynman diagrams for the dominant production modes of neutral MSSM Higgs bosons in $pp$ collisions at the LHC: the gluon fusion process (a) and the production in association with $b$ quarks (b,c,d,e). Particles and anti–particles are labelled the same, $q$ refers to all quark flavours.

The experimentally most important decays of the neutral MSSM Higgs bosons are to

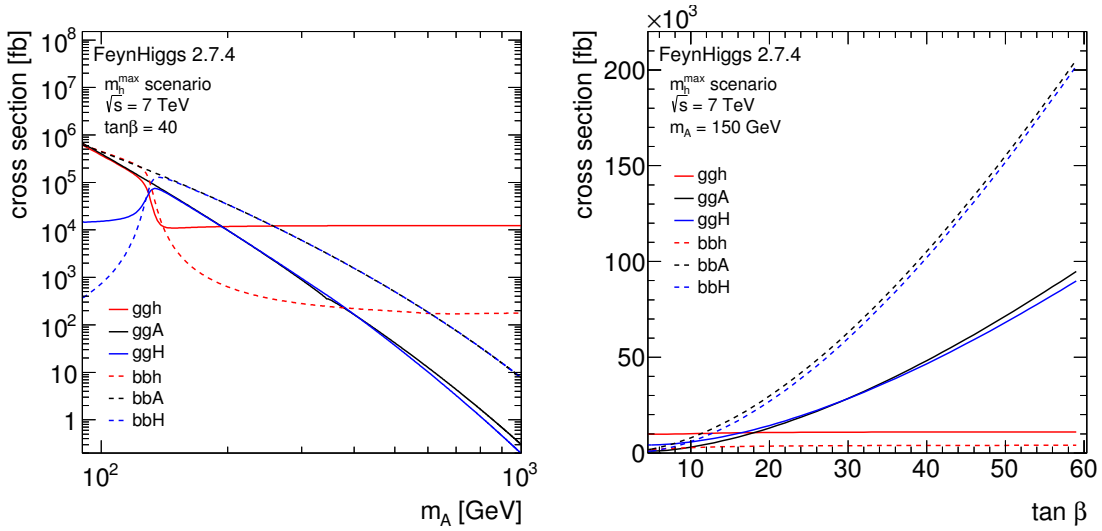


(a) (b)

**Figure 3.7:** Cross sections for the production of the three neutral MSSM Higgs bosons, $h$, $A$ and $H$, in $pp$ collisions at a centre–of–mass energy of $\sqrt{s} = 7\,\text{TeV}$ via gluon fusion or in association with $b$ quarks as a function of the CP–odd Higgs boson mass, $m_A$, for $\tan\beta = 40$ (a) and of $\tan\beta$ for $m_A = 150\,\text{GeV}$ (b) calculated in the $m_h^{\text{max}}$ scenario with FeynHiggs 2.7.4 [59, 62–64].

Standard Model particles. In particular in the $m_h^{\text{max}}$ scenario where all supersymmetric particles are assumed to be very heavy, the Higgs sector is decoupled from the supersymmetric particle spectrum. In a wide range of the allowed $m_h^{\text{max}}$ parameter space, the neutral MSSM Higgs bosons have significantly different dominant decay modes than the Standard Model Higgs boson. Decays to gauge bosons are suppressed for $h$ and $H$ bosons and do not exist for the $A$ boson. Thus, decays to fermions dominate. Especially for high values of $\tan\beta$, the decays to down–type fermions are strongly enhanced. Experimentally interesting channels are therefore decays to $b\bar{b}$, $\tau^+\tau^-$ and $\mu^+\mu^-$. The branching fractions of these processes are shown in Figure 3.8(a). The $h/A/H \to b\bar{b}$ decay dominates with a branching fraction of about 90 %, followed by the $h/A/H \to \tau^+\tau^-$ decay with a branching fraction of about 10 %. The branching fraction of the $h/A/H \to \mu^+\mu^-$ decay amounts to about $4 \cdot 10^{-4}$. The dependence of this branching fraction on $\tan\beta$ is shown in Figure 3.8(b) for $m_A = 150\,\text{GeV}$.

The natural widths of the neutral MSSM Higgs bosons are shown in Figure 3.9 as functions of $m_A$ and $\tan\beta$. It can be seen, that the natural widths of the $A$ and $H$ bosons increase significantly with $\tan\beta$. For high values of $\tan\beta$, these widths can be resolved experimentally in the search channel $h/A/H \to \mu^+\mu^-$ studied in Chapter 6 which provides high experimental mass resolution.

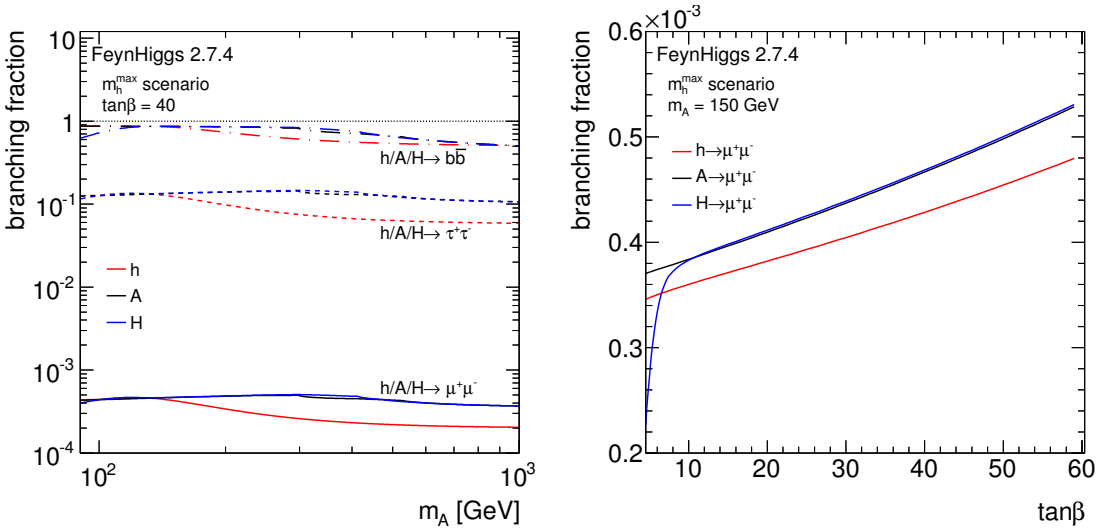


(a) (b)

**Figure 3.8:** Branching fractions of the experimentally interesting decays of neutral MSSM Higgs bosons as a function of the CP–odd Higgs boson mass, $m_A$, for $\tan\beta = 40$ (a) and the branching fractions of the $h/A/H \to \mu^+\mu^-$ decays as a function of $\tan\beta$ for $m_A = 150\,\text{GeV}$ (b) calculated in the $m_h^{\text{max}}$ scenario with FeynHiggs 2.7.4 [59, 62–64].

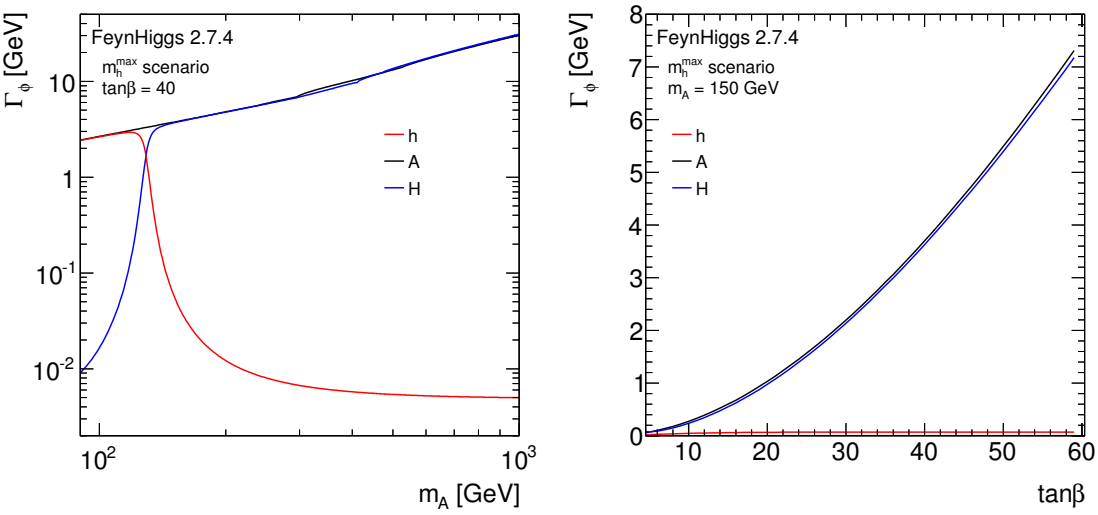


(a) (b)

**Figure 3.9:** Natural widths of the neutral MSSM Higgs bosons as a function of the mass of the CP–odd Higgs boson, $m_A$, for $\tan\beta = 40$ (a) and as a function of $\tan\beta$ for $m_A = 150\,\text{GeV}$ (b) calculated in the $m_h^{\text{max}}$ scenario with FeynHiggs 2.7.4 [59, 62–64].

It is noted that there is one special case where all MSSM Higgs bosons except for the light CP–even one are very heavy and degenerate in mass, i.e. $m_A \simeq m_H \simeq m_{H^\pm} \gg m_Z$. In this regime the heavy Higgs bosons decouple and the light CP–even MSSM Higgs boson has very similar properties as the Standard Model Higgs boson [3]. This so–called decoupling regime is of particular interest in Section 3.4.

## 3.4 Status of the Searches for the Standard Model Higgs Boson

A breakthrough in the search for the Standard Model Higgs boson has been reached in July 2012. The ATLAS and CMS collaborations at the LHC independently discovered a new boson with a mass of about 125.5 GeV and properties compatible with the Standard Model Higgs boson [81,82]. In addition, the CDF and DØ collaborations at the Tevatron observed an excess of events in data at the level of 2.5 standard deviations above the Standard Model background expectation around the mass of 120 GeV [83]. In the following, the ATLAS results are summarised. They are in agreement with the results from CMS.

The Higgs boson searches at the ATLAS experiment were performed with $pp$ collision data sets recorded in 2011 at a centre–of–mass energy of $\sqrt{s} = 7\,\text{TeV}$ corresponding to an integrated luminosity of up to $4.8\,\text{fb}^{-1}$ and in 2012 at $\sqrt{s} = 8\,\text{TeV}$ corresponding to up to $20.7\,\text{fb}^{-1}$. The decay modes to $\gamma\gamma$, $ZZ^*$, $W^+W^-$, $\tau^+\tau^-$ and $b\bar{b}$ were considered.

Combined exclusion limits have been set at the 95 % confidence level as shown in Figure 3.10(a) for the 2011 and only part of the 2012 data set covering already the whole allowed mass range of the Higgs boson. The upper limit on the signal strength parameter, $\mu$, i.e. the signal cross section relative to the Standard Model prediction, is shown as a function of the Higgs boson mass, $m_H$. Under the background–only hypothesis, i.e. assuming there is no Higgs boson at a given mass, $m_H$, the expected exclusion limit at 95 % CL ranges from 110 GeV to 582 GeV. The observed exclusion ranges from 111 GeV to 122 GeV and from 131 GeV to 559 GeV.

At a mass of about 125.5 GeV, a new boson was discovered with an observed signal significance of about $10\,\sigma$ for the combination of all search channels using the complete 2011 and 2012 data sets [84] as shown in Figure 3.10(b). The excess of events over the expected Standard Model background contribution in the data is found in a narrow mass window in the decay channels $H \to \gamma\gamma$ [85] and $H \to ZZ^* \to 4\ell$ [86] with a high mass resolution corresponding to an observed (expected) signal significance of $7.46\,\sigma$ ($4.1\,\sigma$) and $6.6\,\sigma$ ($4.4\,\sigma$), respectively. The observation is confirmed in the $H \to W^+W^- \to \ell\nu\ell\nu$ [87] channel, which in contrast has a low mass resolution, with a significance of $3.8\,\sigma$ with the corresponding expected significance of $3.7\,\sigma$ for the Standard Model Higgs boson hypothesis.

The mass of the new resonance is measured in the two high–resolution channels $H \to \gamma\gamma$ and $H \to ZZ^* \to 4\ell$ resulting in a combined value of $m_H = 125.5 \pm 0.2(\text{stat})$

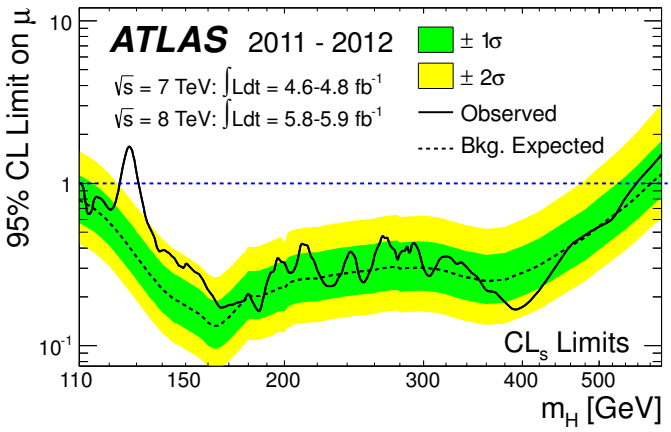


(a)

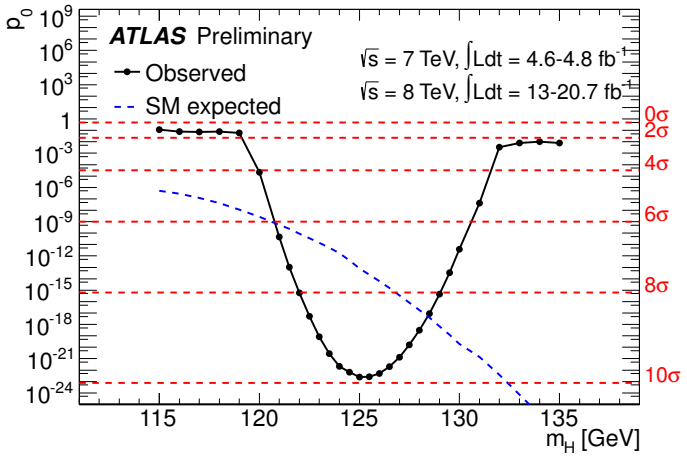


(b)

**Figure 3.10:** Combined search results for the Standard Model Higgs boson at the ATLAS experiment: Observed exclusion limit at the 95 % confidence level as a function of the Higgs boson mass, $m_H$, (solid line) compared to the expectation under the background–only hypothesis (dashed line) with $\pm 1\,\sigma$ (green) and $\pm 2\,\sigma$ (yellow) uncertainty bands for the expectation [81] (a). The observed $p_0$–value as a function of $m_H$ (solid line) compared to the expected $p_0$–value (dashed line) for a Standard Model Higgs boson signal hypothesis at a given mass, $m_H$ [84] (b). The $p_0$–value is the probability of a background fluctuation creating an excess of events at least as high as the one observed in the data.

$^{+0.5}_{-0.6}$(syst) GeV [88]. The measured signal strengths at that mass value are shown in Figure 3.11(a) for the individual search channels. The combined signal strength, $\mu = 1.30 \pm 0.13(\text{stat}) \pm 0.14(\text{syst})$ [84], is compatible with the Standard Model prediction, $\mu = 1$.

The signal strengths for the different Higgs boson production modes also have been

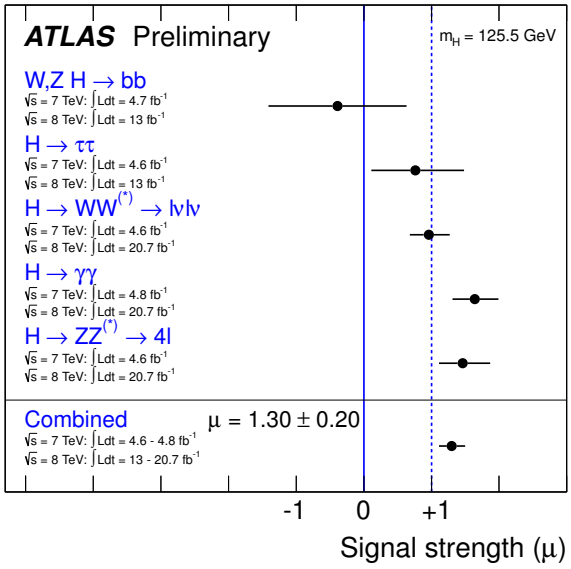


(a)

**Figure 3.11:** Signal strength parameter, $\mu$, for a Standard Model Higgs boson with $m_H = 125.5\,\text{GeV}$ measured in individual decay channels and for their combination [84].

studied in the different decay channels [84]. The four different production modes are grouped into two signal strength parameters according to the underlying couplings. Gluon fusion (ggF) and top–quark–associated production (ttH) are grouped together as they scale with the Higgs coupling to top quarks. Similarly, vector boson fusion (VBF) and vector–boson–associated production (VH) are combined since they scale with the Higgs boson coupling to the vector bosons. The contours of the profile likelihood ratio in the $\mu_{\text{ggF+ttH}}$–$\mu_{\text{VBF+VH}}$ plane of the two signal strength parameters multiplied by the respective measured branching fraction normalised to the Standard Model predictions are shown in Figure 3.12(a). The data agrees with the Standard Model predictions for the Higgs boson production.

The spin of the Higgs boson candidate has been studied in the decay channels $H \to \gamma\gamma$, $H \to ZZ^* \to 4\ell$ and $H \to W^+W^- \to \ell\nu\ell\nu$. The combined results [89] favour a CP–even spin–0 particle ($J^P = 0^+$). An alternative hypothesis with $J^P = 2^+$ has been excluded with a confidence level of 99.9 %.

**Interpretation within the MSSM** The resonance observed by the ATLAS and CMS collaborations is consistent with the Standard Model Higgs boson [81, 84, 88, 89] as summarised above but can also be interpreted within the MSSM as either the light or the heavy CP–even Higgs boson. The fact that a Standard Model Higgs–like boson has been observed at a mass of about 125.5 GeV is remarkable since the MSSM would have been

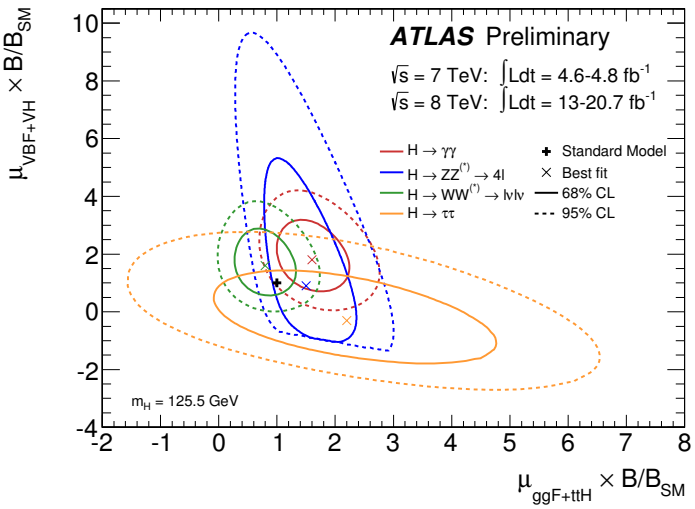


(a)

**Figure 3.12:** Likelihood contours in the $\mu_{\mathrm{ggF+ttH}}$–$\mu_{\mathrm{VBF+VH}}$ signal strength parameter plane for the different decay channels including the branching ratios, $B$, relative to the Standard Model prediction, $B_{\mathrm{SM}}$. The best fit to the data ($\times$) in each decay channel and the Standard Model expectation ($+$) are also shown [84].

ruled out with the observation of such a particle at a mass greater than $m_h \simeq 135\,\mathrm{GeV}$. The new observed particle cannot be the CP–odd MSSM Higgs boson, $A$, since it decays to weak gauge bosons.

Since no evidence for MSSM Higgs bosons has been observed in direct searches, yet (see Chapter 6), such interpretations are useful also because they can help to reduce the allowed MSSM parameter space to interesting regions favoured by the experimental data. The direct search for the neutral MSSM Higgs boson decays to $\mu^+\mu^-$ is subject of this thesis. Therefore, the current status of the direct searches is discussed in Chapter 6.

Since the $h/A/H \to \mu^+\mu^-$ search is performed in the context of the $m_h^{\mathrm{max}}$ scenario, the interpretation of the new particle within this MSSM benchmark scenario [90] is summarised in the following. More recent general interpretations are briefly outlined further below.

Figure 3.13 shows the experimental constraints in the $m_A$–$\tan\beta$ parameter plane of the MSSM Higgs sector in the $m_h^{\mathrm{max}}$ scenario. The regions excluded by LEP and the LHC/Tevatron shown in blue and dark red, respectively, are determined using the Higgs-Bounds [91, 92] programme. The most stringent limits from hadron colliders come from the $h/A/H \to \tau^+\tau^-$ searches with the CMS detector based on a $pp$ collision data with $1.6\,\mathrm{fb}^{-1}$ at $\sqrt{s} = 7\,\mathrm{TeV}$ [93]. The grey area shows the allowed region without taking into account the observation of the new boson. Superimposed on the grey area is the green region in Figure 3.13(a) which is allowed if there is a light CP–even Higgs boson, $h$, in the

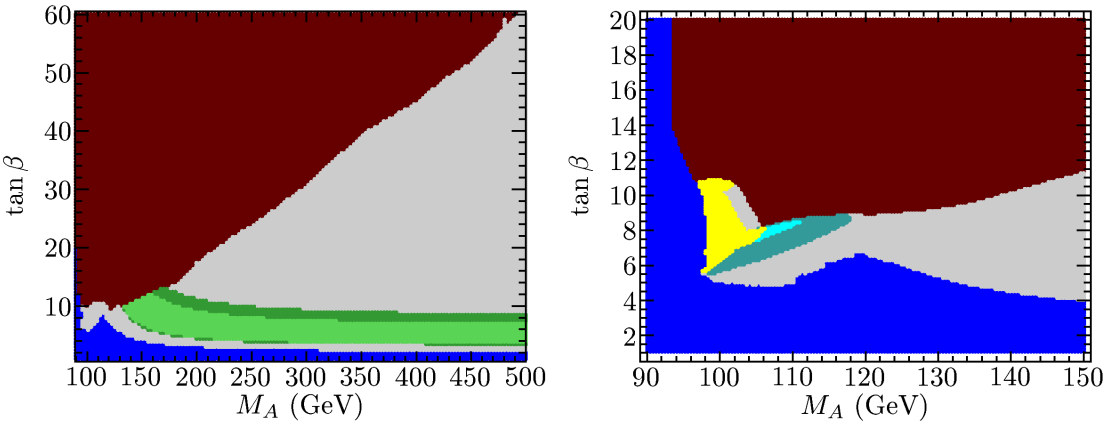


(a) (b)

**Figure 3.13:** Constraints on the $m_A$–$\tan\beta$ parameter space of the MSSM Higgs sector in the $m_h^{\text{max}}$ scenario [90]. The dark–red areas are excluded by LHC/Tevatron, the blue area is excluded by LEP measurements. The grey area is still allowed without taking into account the Standard Model Higgs boson searches at the LHC. The light–green band shows the allowed region for a light CP–even Higgs boson, $h$, in the mass range $122 < m_h < 128\,\text{GeV}$, the dark green band takes into account the $\pm 1\,\sigma$ uncertainty in the top quark mass (a). The yellow and cyan areas show the allowed region for a heavy CP–even Higgs boson, $H$, in the above mass range (b). Due to the small allowed region for a heavy CP–even Higgs boson, only the low mass region is shown in the right–hand side figure.

mass range $122 < m_h < 128\,\text{GeV}$. The mass range is defined by a Standard–Model–like Higgs boson with a mass of 125 GeV measured with an uncertainty of $\pm 1\,\text{GeV}$ and the theoretical uncertainty in the prediction of the lightest MSSM Higgs boson mass due missing higher–order calculations of about $\pm 2\,\text{GeV}$ added linearly. The assumed mass of the Higgs–like state at $125 \pm 1\,\text{GeV}$ accounts for the excesses at 126 GeV and 124 GeV reported by ATLAS [94] and CMS [95] in $\sqrt{s} = 7\,\text{TeV}$ $pp$ collisions with up to $4.9\,\text{fb}^{-1}$ and up to $4.7\,\text{fb}^{-1}$, respectively. The dark green band indicates the effect from the uncertainty in the top quark mass. Figure 3.13(b) shows in cyan and yellow the allowed $m_A$–$\tan\beta$ region if there is a heavy CP–even Higgs boson, $H$, in the mass range of $122 < m_H < 128\,\text{GeV}$. Only the yellow region is allowed if the decay rate for $H \to \gamma\gamma$ is at least 90 % of predicted rate for the Standard Model Higgs boson.

It can be seen that especially the interpretation of the new boson in terms of the light CP–even Higgs boson leads to a rather unconstrained parameter space in $m_A$ while $\tan\beta$ is constrained to a narrow range, $2 \lesssim \tan\beta \lesssim 10$. For a heavy CP–even Higgs boson with $m_H \approx 125\,\text{GeV}$, only a very small region in the parameter space is not yet excluded experimentally. But in this case, $m_h$ would always be below the LEP limit of

$m_h \geq 114.4\,\text{GeV}$ [96].

In addition to interpreting the new boson in terms of one particular model like the $m_h^{\text{max}}$ scenario, it is interesting to investigate the regions in the unconstrained MSSM parameter space which are favoured by the experimental results. For this purpose a scan of the whole MSSM parameter space needs to be performed. As mentioned in Section 2.2.3, the unconstrained MSSM has 105 free parameters. A scan over of such a large parameter set is not feasible and the experimental uncertainties are too large to simultaneously constrain so many model parameters. Therefore, more constrained models are used for such interpretations.

A large effort was made after the discovery of the new particle to interpret the Higgs boson candidate in phenomenological MSSM (pMSSM) models [97] with up to 19 free parameters considering the new boson to be either the light or the heavy CP–even MSSM Higgs boson. A series of publications of such studies is available (see for example Reference [98] and references therein).

The most recent studies take into account the measured signal rates of direct Higgs boson searches in $\sqrt{s} = 7$ and 8 TeV data with ATLAS and CMS and direct Higgs boson search results from the Tevatron as well as the averaged mass of the new boson measured by ATLAS and CMS [98]. Additional input from LEP, Tevatron and LHC exclusion limits and low energy observables, for instance from heavy flavour physics (e.g. $\text{BR}(B_s \to \mu^+\mu^-)$) and from the anomalous magnetic moment of the muon are considered. It should be noted that systematic uncertainties and correlations among the separate measurements are not always fully taken into account in these studies. Under these conditions the results mostly show that the allowed MSSM parameter space can be significantly reduced to regions favoured by the data and that certain MSSM configurations can reproduce the observed signal rates. Nevertheless, due to the good compatibility of the direct search results with the Standard Model Higgs boson prediction no final conclusion can be drawn from these studies.

The impact of the results of the MSSM Higgs boson search presented in this thesis are discussed in Section 6.13.

In addition to the direct searches for MSSM Higgs bosons (see Chapter 6) and the above interpretations of the discovered Higgs boson candidate in the light of the MSSM, precision observables provide powerful measures to test the Standard Model (see also Section 2.2.1) and its extensions like the MSSM.

In both the Standard Model and the MSSM, for example the relations of the $W$ boson mass, $m_W$, and the top quark mass, $m_t$, can be calculated [99] including radiative corrections from various other model parameters such as the masses of the $Z$ or Higgs bosons or supersymmetric particles in the MSSM case. Comparisons with precision measurements of $m_W$ and $m_t$ allow to interpret the compatibility of the data with the Standard Model and

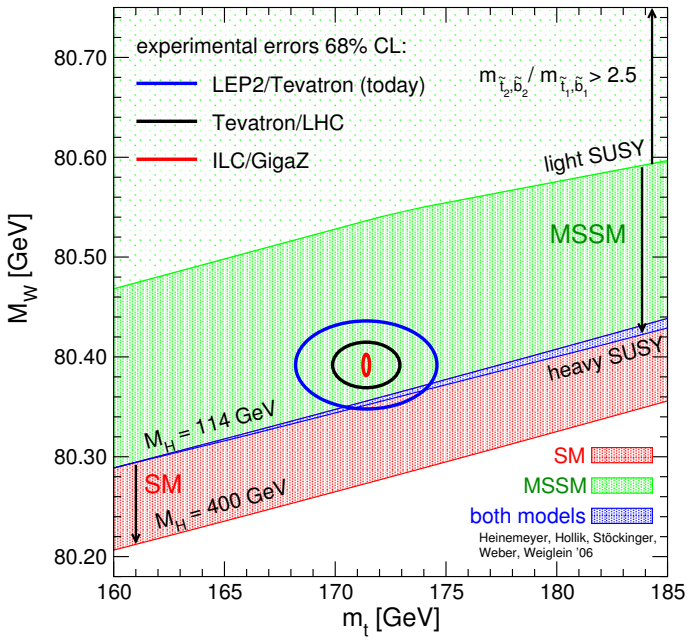


**Figure 3.14:** Comparison of the 68 % confidence level contour for the measurements of $m_W$ and $m_t$ performed at LEP and the Tevatron (blue line) and expected for the LHC (black line) and the future ILC (red line) with theoretical predictions for the Standard Model (red shaded) and the MSSM (green/light shaded) [99]. The overlap of both models is indicated by the blue shaded area. The Standard Model prediction is shown for Higgs boson masses in the range of 114 GeV to 400 GeV. The MSSM prediction is shown for variations of the squark and slepton masses in the range of 100 GeV to 2000 GeV, of the trilinear bottom and top quark couplings as well as Higgs mixing parameter in the range of −2000 GeV and 2000 GeV and $m_A$ in the range of 90 GeV to 1000 GeV. The light shaded area indicates possible predictions of the MSSM with at least one of the ratios $m_{\tilde{t}_2}/m_{\tilde{t}_1}$ or $m_{\tilde{b}_2}/m_{\tilde{b}_1}$ exceeding 2.5, while the green shaded region these ratios are unconstrained.

the MSSM and to exclude large regions in the parameter space.

Figure 3.14 compares the 68 % confidence level contour of the combined LEP and Tevatron measurements of $m_W$ and $m_t$ with the theoretical prediction of the relation of $m_W$ and $m_t$ within the Standard Model and the MSSM [99]. Expected measurement accuracies for the LHC and a future international linear collider (ILC) are shown as well. The dependence of the theoretical predictions for the two models on additional parameters result in bands in the $m_t$–$m_W$ plane having a small overlap region indicated by the blue area. The MSSM band is divided into two regions for different assumptions of stop and sbottom mass ratios. The experimental results from LEP and the Tevatron are compatible with both, the Standard Model and the MSSM, while slightly favouring the MSSM in the case of no restriction on the squark mass ratios. In addition, the experimental results allow for a strong reduction of the allowed parameter space.

# Chapter 4

# The ATLAS Experiment at the LHC

This chapter introduces the Large Hadron Collider (LHC) and the ATLAS experiment. An overview on the LHC design and performance is given in Section 4.1 based on Reference [100]. Section 4.2 summarises the detector requirements for the physics programme of the ATLAS experiment and introduces the detector design based on Reference [101]. In Section 4.3 the LHC proton beam conditions and ATLAS data taking performance during the run period in the year 2011 are summarised defining the data set used for the MSSM Higgs boson search presented in Chapter 6. The corresponding performance in the year 2012 is briefly discussed after which a short summary of future data taking plans at the nominal centre–of–mass energy of $\sqrt{s} = 14\,\text{TeV}$ are also given. These plans are setting the stage for the study of prospects for the Standard Model Higgs boson search in the $\mu^+\mu^-$ decay channel which is presented in Chapter 7.

## 4.1 The Large Hadron Collider

The Large Hadron Collider (LHC) [100] at CERN is a superconducting hadron accelerator and storage ring installed in the tunnel which housed the Large Electron Positron Collider (LEP) before its decommissioning in the year 2000. The tunnel has a circumference of 26.7 km and is 45 m to 170 m below surface. It is designed as a quasi–ring having eight straight sections equipped with accelerating radio frequency (RF) cavities and other machine utilities. The nominal beam crossing points are located in the middle of these straight sections. In practice not all of the nominal beam crossing points are used by

experiments. The straight sections are connected by eight arc sectors where the particle beams are bent in magnetic dipole fields.

The LHC is a particle–particle collider in contrast to particle–antiparticle colliders like LEP and the Tevatron. Therefore two vacuum pipes are needed to house the counter–rotating beams. With the compact design chosen for the LHC, the two separate vacuum pipes are integrated into the superconducting dipole magnets which bend the two proton beams sharing the yoke and the cryostat. The superconducting bending magnets operate at a temperature of 1.9 K and provide a design–magnetic field strength of 8.33 T which defines the maximum beam energy. The LHC can be operated in three modes, colliding protons with protons ($pp$), lead ions with lead ions ($PbPb$) or protons with lead ions ($pPb$). At the nominal magnetic dipole field the design proton beam energy is 7 TeV while fully ionised lead nuclei ($^{208}Pb^{82+}$) have an energy of 2.76 TeV/nucleon resulting in a total $Pb$ beam energy of 1.15 PeV.

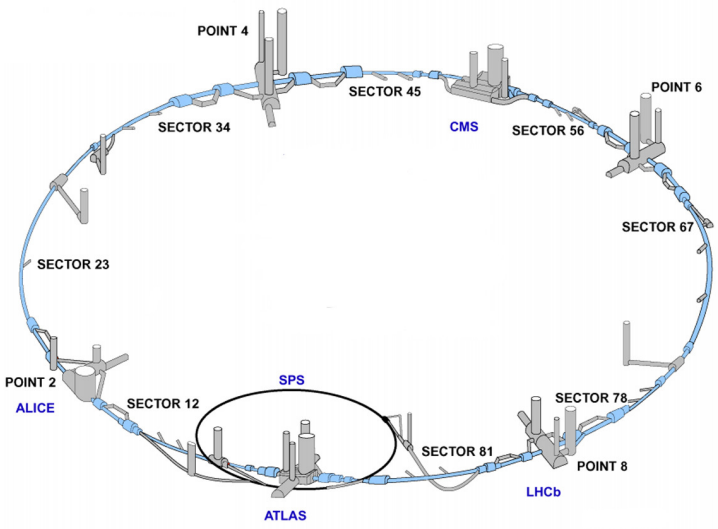


**Figure 4.1:** Schematic layout of the LHC accelerator [102]. Eight straight sections contain the nominal interaction points, labelled Point 1 to 8. The main experiments ATLAS, ALICE, CMS and LHCb are located at the beam crossing points 1, 2, 5 and 8, respectively. The accelerating unit is at Point 4. Points 3 and 7 allocate beam cleaning collimators and the beam dumping system is located at Point 6. Between the straight sections there are eight arc sectors where the beams are bent in the magnetic field of superconducting dipoles. The arc sectors, labelled Sector $XY$, connect the straight sections corresponding to Points $X$ and $Y$.

A schematic overview of the LHC and the last stage of the pre–accelerator chain, the Super Proton Synchrotron (SPS), are shown in Figure 4.1. The interaction regions in four of the straight sections where the beams cross and the particles are brought to collision are

allocated to the main experiments ATLAS [101], ALICE [103], CMS [104] and LHCb [105]. Three smaller experiments, LHCf [106], MoEDAL [107] and TOTEM [108], are located at some distance to the interaction points in the straight sections of the ATLAS, LHCb and CMS experiments, respectively. Close to the interaction points, magnetic beam optics focus the beams to a small interaction region of typically 30 µm diameter transverse to the beam axis. In one of the four other straight sections the superconducting RF cavities are installed providing the accelerating electric field. In two other straight sections movable collimator devices are installed which clean the beam halo which builds up with time due to repulsive space charge effects and scattering of the protons in the bunches at each other or at residual gas molecules in the evacuated beam pipes. The last straight section is used for the beam dumping system which can quickly extract the beams, which have a total stored energy of about 360 MJ at design operating conditions, from the rings into a 700 m straight evacuated pipe and deposits them in carbon absorber blocks.

**Luminosity and Pileup** The interaction rate of a physics process at a particle collider is given by

$$\frac{dN}{dt} = L \cdot \sigma(\sqrt{s}), \tag{4.1}$$

where $L$ is the instantaneous luminosity and $\sigma(\sqrt{s})$ the cross section for a given process at centre–of–mass energy $\sqrt{s}$. The luminosity is determined by the beam parameters and is for symmetric beams given by

$$L = \frac{f_{\mathrm{rev}}\, n_{\mathrm{b}}\, N_{\mathrm{b}}^2\, \gamma}{4\, \epsilon_{\mathrm{n}}\, \beta^*} \cdot F \tag{4.2}$$

where $f_{\mathrm{rev}}$ is the revolution frequency, $n_{\mathrm{b}}$ the number of bunches per beam, $N_{\mathrm{b}}$ the number of particles per bunch and $\gamma$ the relativistic gamma factor of the particles. The parameter $\epsilon_{\mathrm{n}}$ denotes the normalised transverse beam emittance, which at the LHC is mainly determined by the beam injection system, $\beta^*$ is the envelope of the betatron oscillations at the interaction point and $F$ the geometric reduction factor due to a beam crossing angle. The integral of the instantaneous luminosity,

$$\mathcal{L} = \int dt\, L, \tag{4.3}$$

over a certain time period is the integrated luminosity which is a measure of the amount of interactions per unit cross section.

At the design operating the LHC collides 2808 bunches with $1.15 \cdot 10^{11}$ protons each resulting in an instantaneous luminosity of $10^{34}\mathrm{cm}^{-2}\mathrm{s}^{-1}$. This implies bunch crossings every 25 ns at the interaction points. With a total inelastic proton–proton cross section of about 80 mb at a centre–of–mass energy of 14 TeV, on average 23 inelastic proton–proton collisions are expected per bunch crossing. This means that a potentially interesting hard–

scattering physics event is on average accompanied by 23 predominantly soft interactions, so–called pileup events.

## 4.2 The ATLAS Experiment

The ATLAS detector is a multi–purpose detector designed to exploit a wide range of physics topics. The physics programme of the ATLAS experiment ranges from precision measurements of known Standard Model processes to the search for a large variety of new physics phenomena accessible at the LHC.

The unprecedented centre–of–mass energy and the high luminosity of the LHC allow for precise measurements of electroweak and heavy flavour physics and of QCD processes. In particular, the high production rate of top quarks allows for the precise determination of the top quark properties. One major goal of the ATLAS experiment is the discovery of the Higgs boson and the study of the origin of electroweak symmetry breaking. The detector is designed to be sensitive to the Standard Model Higgs boson production in the entire allowed mass range up to $m_H \simeq 1\,\text{TeV}$. Supersymmetry is the most favoured extension of the Standard Model (see Section 2.2). The search for supersymmetric particles is therefore another important goal of the ATLAS experiment. Apart from supersymmetry, more exotic physics scenarios beyond the Standard Model are searched for. Heavy gauge bosons, $W'$ and $Z'$, and quark compositeness can be probed up to energy scales of about 10 TeV. Flavour changing neutral current processes and effects of extra dimensions and of microscopic black holes are further possible phenomena studied by the ATLAS experiment.

The production cross sections of the interesting new physics processes are small even at the design collision energy. To observe such processes at a sufficient rate high luminosity is needed. In hard proton–proton interactions at the LHC the production of dijet events dominates. The high collision rate and the capability of discriminating interesting events from the large dijet background imposes tight demands on the detector design, data aquisition and trigger system, as well as the particle identification. The design bunch crossing rate of 40 MHz with the production of on average 1000 particles per bunch crossing require fast, highly granular and radiation–hard detector technologies and electronics. Hermetic calorimetry is essential for accurate jet and missing transverse momentum measurements. A highly selective and efficient trigger system is needed to strongly reduce the event rate while minimising the loss of interesting physics events.

The ATLAS detector design developed to satisfy the tight requirements outlined above is summarised in the following based on Reference [101]. A schematic view on the ATLAS detector is shown in Figure 4.2. ATLAS has a design typical for collider experiments with a forward–backward symmetry with respect to the collision point and dedicated sub–systems built cylindrically around the beam pipe. The innermost system is the inner detector operating in a solenoidal magnetic field and providing tracking as well as momentum and

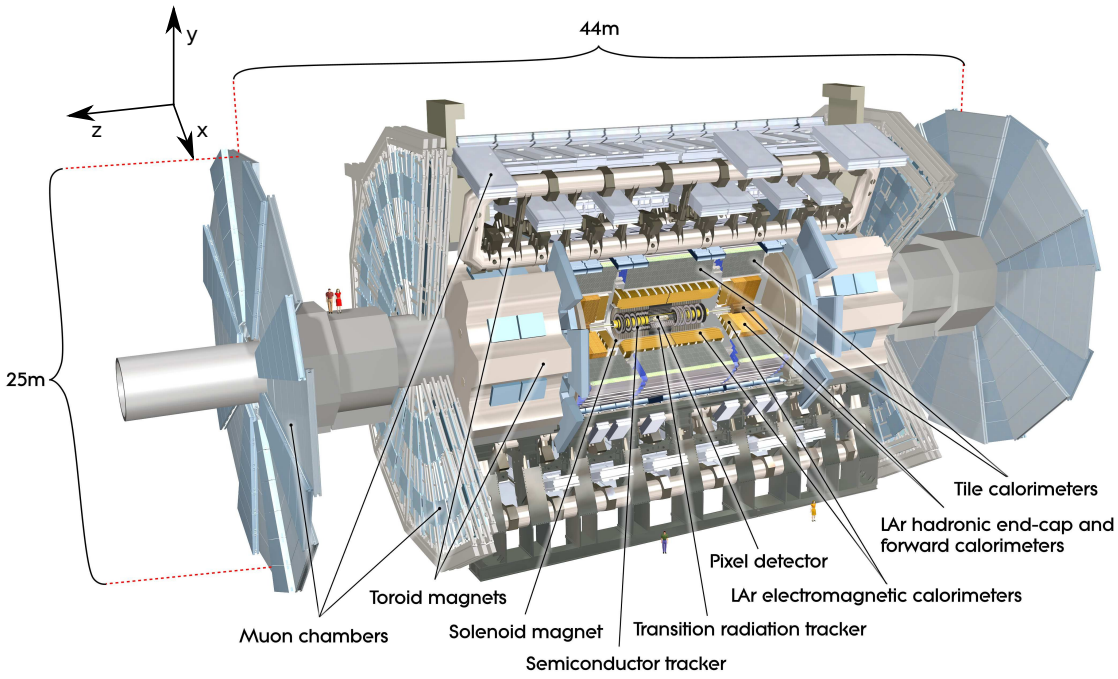


**Figure 4.2:** Cut–away overview of the ATLAS detector with its sub–systems and overall size labelled [101]. The right–handed ATLAS coordinate system is also indicated.

charge measurement of charged particles. Outside the inner detector the calorimeter system is placed providing identification and energy measurement of electromagnetic and hadronic interacting particles. The outermost sub–system, the muon spectrometer, operates in a toroidal magnetic field and provides tracking, identification and stand–alone momentum and charge measurement of muons. The general performance goals of the individual sub–systems are summarised in Table 4.1, their design is outlined in the following sections.

Separate from the ATLAS sub–detectors there are three additional smaller detectors which cover the very forward region. Closest to ATLAS is LUCID [109] with distances of $\pm 17\,\mathrm{m}$ from the interaction point. It detects inelastic $pp$ scattering in the very forward direction and allows for the online monitoring of the relative instantaneous luminosity for the data recorded by the ATLAS detector. A second luminosity detector, ALFA [109], is $\pm 240\,\mathrm{m}$ away from the interaction point and measures the absolute instantaneous luminosity. The zero–degree calorimeter, ZDC [110], located $\pm 140\,\mathrm{m}$ from the interaction point where the beam pipe is re–separated into two pipes. The ZDC is of main interest for the ATLAS heavy ion physics programme as it determines the centrality in those collisions.

**Table 4.1:** Design performance goals for energy ($E$) and transverse momentum ($p_{\mathrm{T}}$) resolution and $\eta$ coverage of the different sub–systems of the ATLAS detector [101]. The $\eta$ coverage in parentheses corresponds to the required trigger coverage. The units for $E$ and $p_{\mathrm{T}}$ are in GeV. The ATLAS coordinate system is defined in Section 4.2.1

| Subsystem | Energy/Momentum Resolution | $\eta$ Coverage (Trigger) |
|---|---|---|
| Inner tracker | $\sigma_{p_{\mathrm{T}}}/p_{\mathrm{T}} = 0.05\,\% \oplus 1\,\%$ | $\pm 2.5$ |
| EM calorimeter | $\sigma_E/E = 10\,\%/\sqrt{E} \oplus 0.7\,\%$ | $\pm 3.2$ ($\pm 2.5$) |
| Hadronic calorimeter | | |
| barrel/end–cap | $\sigma_E/E = 50\,\%/\sqrt{E} \oplus 3\,\%$ | $\pm 3.2$ |
| forward | $\sigma_E/E = 100\,\%/\sqrt{E} \oplus 10\,\%$ | $3.1 < \lvert\eta\rvert < 4.9$ |
| Muon spectrometer | $\sigma_{p_{\mathrm{T}}}/p_{\mathrm{T}} = 10\,\%$ for $p_{\mathrm{T}} = 1\,\mathrm{TeV}$ | $\pm 2.7$ ($\pm 2.4$) |

### 4.2.1 The ATLAS Coordinate System

The coordinate system of the ATLAS detector is introduced first as it is used throughout this and the following Chapters. The ATLAS detector and the particles emerging from the collisions are described in a right–handed coordinate system with the origin in the nominal interaction point. The $x$–axis points from the interaction point to the centre of the LHC ring and the $y$–axis points upwards. The $z$–axis is defined in beam direction and points counter–clockwise. Positive values of $z$ define the A–side of the detector whereas negative values define the C–side. Transverse particle momenta and energies are measured in the $x$–$y$ plane. The azimuthal angle, $\phi$, is measured around the beam axis with respect to the positive $x$–axis. The polar angle, $\theta$, measured from the positive $z$–axis is typically expressed by the pseudorapidity defined as $\eta = -\ln\tan(\theta/2)$. Distances of particles and tracks are conventionally expressed in the pseudorapidity–azimuthal angle space defined as $\Delta R = \sqrt{\Delta\eta^2 + \Delta\phi^2}$.

### 4.2.2 The Magnet System

To measure the charge and momentum of charged particles the ATLAS detector is equipped with a large superconducting magnet system. Liquid helium is used to cool the magnet coils to their operating temperatur of 4.5 K. The ATLAS magnet system consists of one superconducting solenoid providing a 2 T magnetic field in beam direction for the inner detector and three large superconducting toroids separated in a barrel and two end–cap systems providing a bending power of 1.0 Tm to 7.5 Tm. In total the magnetic energy stored in the whole system is 1.6 GJ. A schematic view of the ATLAS magnet system is shown in Figure 4.3.

The central solenoid is placed between the inner detector and the calorimeters. In order to keep the amount of dead material in front of the calorimeters as low as possible the solenoid has one thin single–layer coil and shares the vacuum vessel with the liquid argon

calorimeter. This results in approximately 0.66 radiation lengths of the total solenoid assembly. The solenoid measures 5.8 m in length and only 2.46 m to 2.56 m in diameter. The magnetic flux of the solenoid is returned by the steel structure of the ATLAS hadronic calorimeter.

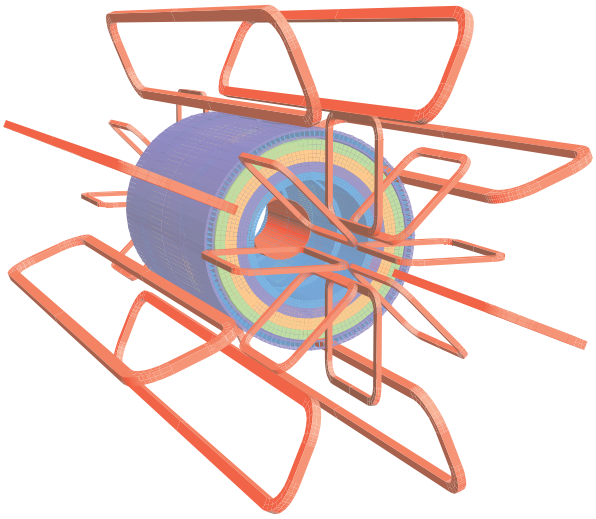

**Figure 4.3:** Schematic view of the ATLAS magnet system [101]. The separate barrel and end–cap toroid coils are shown. The solenoid coil is visible inside the calorimeter volume. The tile calorimeter serving as the return yoke for the solenoid is shown in five different colors indicating different magnetic properties.

The ATLAS toroid magnet system provides a large volume magnetic field of approximately 12000 $m^3$ in which the muon spectrometer is embedded. The barrel toroid consists of eight coils in individual vacuum vessels and has a total size of 25.3 m in length with inner and outer diameters of 9.4 m and 20.1 m, respectively. The two end–cap toroids optimise the magnetic field in the forward regions of the muon spectrometer. Each end–cap toroid consists of eight coils sharing one common vacuum vessel which is placed in front of the calorimeter end–caps inside the barrel toroid. The end–cap toroid coils are rotated by 22.5° with respect to the barrel toroid to provide an optimal overlap of the magnetic fields. The total size of the end–cap toroids is 5 m in length and 10.7 m (1.65 m) in outer (inner) diameter. Due to the air–core design of the toroid magnets with a missing massive yoke, multiple scattering of muons traversing the muon spectrometer is significantly reduced.

### 4.2.3 Inner Detector

The ATLAS inner detector (ID) is a highly granular tracking detector composed of three different technologies. It is operating in a 2 T solenoidal magnetic field and provides robust pattern recognition, high–precision tracking and accurate momentum and charge

measurement of charged particles. A schematic view of the ATLAS inner detector is shown in Figure 4.4.

The innermost part of the ID is made of silicon pixels arranged in three cylindric layers around the beam axis in the barrel part of the detector and three discs perpendicular to the beam axis in each end–cap region. The pixel detector offers highest granularity with approximately 80.4 million read–out channels and measures both track coordinates in the transverse plane with high precision. It is placed very close to the interaction point — the innermost pixel layer has a distance of 50.5 mm from the beam — allowing for precise secondary vertex measurements. Typically three pixel layers are crossed by each track emerging from the interaction point.

The second system of the ID with a minimum distance of 300 mm from the interaction point is the semiconductor tracker, SCT. Each track crosses typically eight silicon strip layers which are arranged pair–wise at small angle to measure both coordinates of the track hit. The four stereo layers are arranged in concentric cylinders around the beam axis in the barrel part and in discs on each end–cap side of the detector. The SCT has lower granularity compared to the pixel detector with approximately 6.3 million read–out channels but provides four space points for each track and a larger length of the measured track.

The complete silicon tracking detector — pixel and SCT — has a pseudorapidity coverage of $|\eta| < 2.5$ with a total diameter of $\sim 1$ m and a length of $\sim 5.4$ m.

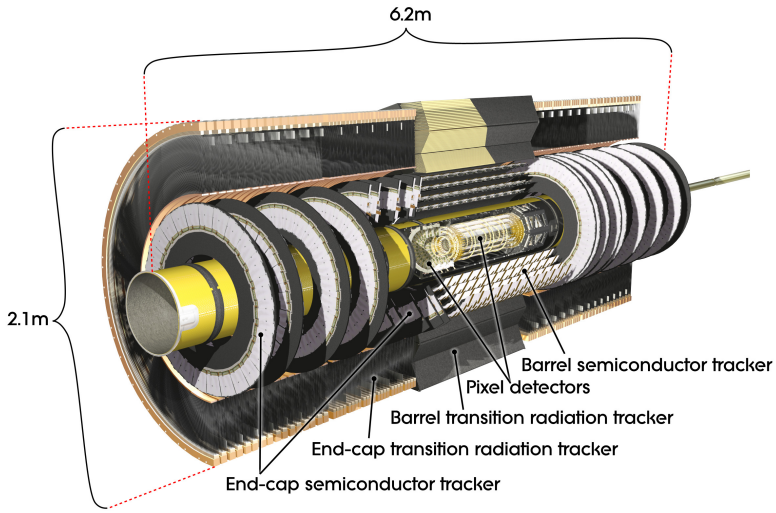


**Figure 4.4:** Cut–away view of the ATLAS inner detector [101]. The different detector components, pixel, SCT and TRT, which are divided in barrel and end–cap parts are labelled.

Outside the SCT, the transition radiation tracker, TRT, is placed which has a diameter of $\sim 2.1$ m and a length of $\sim 6.2$ m. It consists of approximately 351000 straw tubes with a 4 mm diameter providing typically 36 hits per track. The straw tubes are arranged in

parallel to the beam axis in the barrel part and radially in the wheels in the end–cap region of the detector. This allows track following with a large number of hits up to $|\eta| = 2.0$. The TRT has a lower precision of the single track point measurements but with the large number of hits and length of the measured track it contributes significantly to the momentum measurement of the inner detector. The straw tubes of the TRT are filled with a $Xe/CO_2/O_2$ gas mixture and are interleaved with transition radiation material. In addition to the tracking the Xe–based gas allows to detect the low–energy transition radiation photons which provides electron identification complementary to the calorimeter–based identification.

### 4.2.4 Calorimeters

The ATLAS sampling calorimeters provide high–resolution energy measurements of electromagnetic and hadronic interacting particles and robust particle identification. The calorimeter system is separated into the electromagnetic and the hadronic calorimeters comprising different granularity, pseudorapidity coverage and detector technologies. In particular the choice of the absorbers is dedicated to either electromagnetic or hadronic interactions. The complete calorimeter system covers a pseudorapidity range of $|\eta| < 4.9$ and provides a good containment of electromagnetic and hadronic showers with more than 22 interaction lengths of the electromagnetic calorimeter and approximately 10 interaction lengths of the hadronic calorimeter. A schematic view of the different calorimeter sub–systems is shown in Figure 4.5.

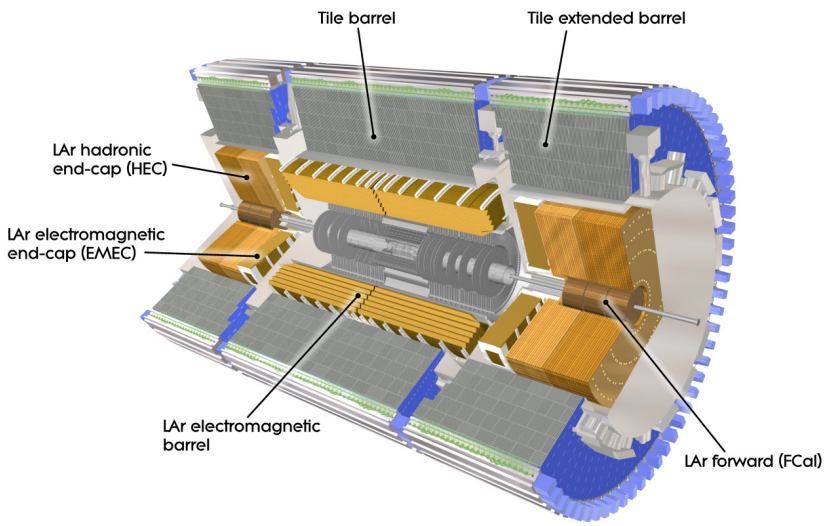


**Figure 4.5:** Cut–away view of the ATLAS calorimeter system [101]. The different calorimeter concepts dedicated to the reconstruction of electromagnetic and hadronic showers are labelled.

**Electromagnetic Calorimeter** The electromagnetic (EM) calorimeter is a high–granularity sampling calorimeter consisting of lead absorber plates and liquid argon (LAr) as active material. The absorbers and electrodes are accordion shaped providing an optimal $\phi$ symmetry without azimuthal cracks. The EM calorimeter is divided into a barrel part with $|\eta| < 1.475$ and two end–caps with $1.375 < |\eta| < 3.2$ each in their own cryostat. The barrel EM calorimeter shares its vacuum vessel with the central solenoid to minimise dead material and optimise the calorimeter performance. In the pseudorapidity region dedicated for high precision physics measurements, $|\eta| < 2.5$, the EM calorimeter has its highest granularity and three sampling layers in the barrel and end–cap parts and four layers in the transition region. For higher pseudorapidities a coarser granularity is sufficient. In the region of the central solenoid, $|\eta| < 1.8$, the EM calorimeter is equipped with a presampler consisting of an active LAr layer to correct for energy losses of electrons and photons in front of the calorimeter. In total the EM calorimeter has approximately 173000 read–out channels.

**Hadronic Calorimeter** The hadronic calorimeter comprises two different technologies. The central part is the tile calorimeter surrounding the EM calorimeter. It is separated into a barrel and two extended–barrel parts covering the pseudorapidity ranges of $|\eta| < 1.0$ and $0.8 < |\eta| < 1.7$, respectively. The tile calorimeter is a sampling calorimeter consisting of steel absorber plates and scintillating tiles as active material. It has three sampling layers in both the barrel and extended–barrel regions and in total approximately 9900 read–out channels.

The hadronic end–cap calorimeter (HEC) is located directly behind the EM calorimeter end–cap on each side of the detector. Similarly to the EM calorimeter it uses liquid argon technology, while its absorber plates arranged in four layers perpendicular to the beam axis are made of copper. The HEC covers a pseudorapidity range of $1.5 < |\eta| < 3.2$ and has approximately 5600 read–out channels.

The hadronic calorimeter is completed at high pseudorapidities by the forward calorimeter (FCal). It shares the cryostat with the HEC and covers a pseudorapidity range of $3.1 < |\eta| < 4.9$. The FCal is separated in three layers. In the first layer the absorber material is copper providing good electromagnetic shower measurements, the second and third layers are made of tungsten to measure predominantly hadronic showers. The FCal absorbers build a matrix of longitudinal channels parallel to the beam axis filled with the electrodes and the active material, LAr. In total, the FCal has approximately 3500 read–out channels.

### 4.2.5 Muon Spectrometer

The ATLAS muon spectrometer (MS) defines the overall size of the ATLAS detector of 44 m in length and 25 m in diameter. It is embedded in a large toroidal magnetic field.

The MS covers a pseudorapidity range of $|\eta| < 2.7$ with a barrel part at $|\eta| < 1.4$ and two end–caps covering $1.6 < |\eta| < 2.7$ with separate toroid magnets. In the transition regions, $1.4 < |\eta| < 1.6$, a combination of the overlapping magnetic fields bends the muon tracks. The toroidal field configuration is mainly orthogonal to the muon tracks up to the highest pseudorapidities. The air–core magnet design minimises degradation of the momentum resolution due to multiple scattering. The MS consists of three layers of muon chambers arranged in a cylindrical geometry in the barrel part and in so–called wheels perpendicular to the beam axis in the end–cap and transition regions. A schematic view of the ATLAS muon spectrometer is shown in Figure 4.6.

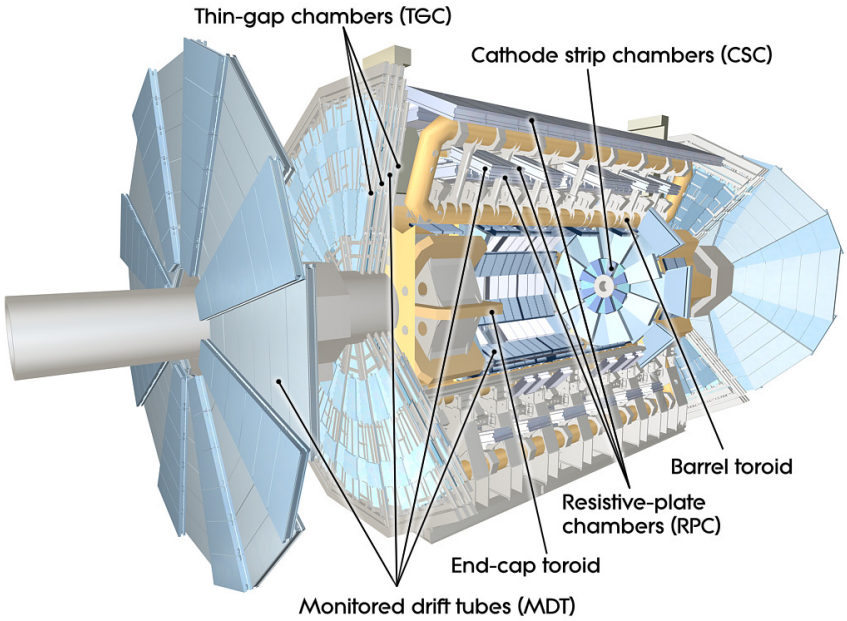


**Figure 4.6:** Cut–away view of the ATLAS muon spectrometer embedded in large air–core toroid magnets [101]. The muon spectrometer consists of different types of muon chambers labelled as well as the separate toroid magnet coils.

In the largest part of the MS, the measurement of the space points of muon tracks is performed by two types of chambers. The measurement of the track coordinates in the bending plane ($\eta$) is provided by precision tracking chambers while the measurement of the second coordinate ($\phi$) is performed with lower precision by the trigger chambers which also provide bunch crossing identification and a fast trigger decision based on coarse momentum measurements.

The precision measurement in the largest part of the pseudorapidity coverage is provided by monitored drift tube (MDT) chambers. In total 1088 MDT chambers are installed in the three layers of the barrel and the three wheels in each end–cap containing in total 339000 read–out channels. Only the region $2.0 < |\eta| < 2.7$ in the innermost wheels is

covered by 32 cathode strip chambers (CSC) which are multiwire proportional chambers with segmented cathode strip read–out providing the necessary higher rate capability in this detector region. The CSC chambers have approximately 31000 read–out channels.

Two types of chambers are used for the muon trigger system which covers a pseudorapidity range of $|\eta| < 2.4$. In total 544 resistive plate chambers (RPC) are used in the barrel part of the MS and 3588 thin gap chambers (TGC) in the end–caps. The RPCs and TGCs have 359000 and 318000 read–out channels, respectively.

**Muon Spectrometer Performance** The sensitivity of the searches for Higgs boson decays to $\mu^+\mu^-$, subject of this thesis, strongly depends on the performance of the ATLAS muon spectrometer. The design specifications of the MS allow for muon reconstruction with high momentum resolution and identification efficiency. For muons transverse momenta greater than 100 GeV (50 GeV) traversing the barrel (end–cap) region of the detector, the momentum resolution in the MS is better compared to the momentum resolution in the ID [111]. This is in particular important for the searches for heavy $\mu^+\mu^-$ resonances originating for example from heavy neutral gauge boson ($Z'$) or Higgs boson decays, since the experimental $\mu^+\mu^-$ invariant mass resolution is determined by the muon momentum resolution.

The high momentum resolution and identification efficiency is achieved by the combination of high resolution tracking MDT and CSC chambers, the air core toroid magnet design and the precision alignment of the in total 5200 individual trigger and tracking chambers.

The individual drift tubes of the MDT chambers measure the hits of the traversing muons with an intrinsic spatial resolution of about 80 µm and high hit efficiency [101]. Each MDT chamber consists of two multilayers with three or four layers of drift tubes each. This design, together with the optical in–plane alignment system which monitors internal chamber deformations, allows to reconstruct track segments in each chamber with a spatial resolution of about $35 - 40$ µm [101]. The CSC chambers provide similar spatial resolution and high hit efficiency.

To reconstruct the full muon tracks, the track segments are combined to curved tracks and the muon momentum is determined by the measurement of the track sagitta. Details on the muon reconstruction strategies are given in Section 5.1. The MS provides on average 20 hits per track allowing for a precise sagitta measurement [101]. The resolution of the track sagitta measurement depends in addition to the chamber resolution crucially on the exact knowledge of the magnetic field and on the alignment of the individual chambers with respect to each other and with respect to the other detector systems. The magnetic field is determined with 1800 Hall sensors distributed over the whole MS volume. The air core design of the toroid magnet system minimises the degradation of the momentum resolution due to multiple scattering of the muons traversing the solid structures of the detector. The relative chamber positions are monitored with an optical projective alignment system.

The global alignment of the MS relies on the reconstruction of straight and curved muon trajectories from known Standard Model processes.

With these specification, the resolution of the track sagitta measurement is better than 50 µm [101]. Muons with transverse momenta of 40 GeV can be reconstructed in the MS with a transverse momentum resolution of better than 4 % (5.5 %) in the barrel (end–cap) part of the MS [111]. For muons with transverse momenta of 1 TeV a resolution of better than 10 % is achieved [101].

### 4.2.6 Trigger and Data Acquisition

The ATLAS trigger and data acquisition (TDAQ) system is designed to reduce the event rate of initially 40 MHz down to a storable rate of approximately 200 Hz. Given the small production rates of the physics processes of interest the strong event reduction is required to be highly selective to ensure the minimal losses of these processes.

The ATLAS trigger system is divided into a three–fold level structure: Level–1 (L1), Level–2 (L2) and Event Filter (EF). The L1 trigger is fully hardware–based while the L2 and EF, forming together the high level trigger (HLT), are mainly software–based. The schematic view of the TDAQ system is shown in Figure 4.7, a brief overview of the main aspects of this system are given in the following.

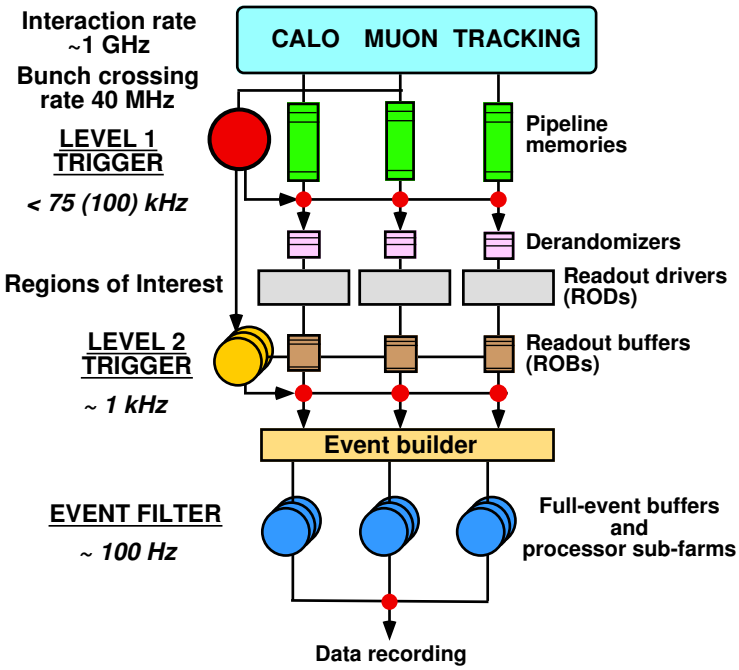


**Figure 4.7:** Simplified schematic overview of the ATLAS trigger and data acquisition system [112].

The L1 trigger is based on the muon trigger chambers RPC and TGC and reduced–granularity information from the calorimeter system. With precise timing the L1 determines the bunch crossing in which an event occurs and categorises each identified bunch crossing according to the bunch structure of the LHC beams. The L1 trigger is designed to search for muons, electrons/photons, jets and hadronically decaying $\tau$–leptons with high transverse momenta, as well as events having high total transverse momenta or high missing transverse momenta. The L1 trigger also defines regions of interest (RoI) containing the angular $\eta$–$\phi$–space of possible trigger objects and information about the passed trigger criteria. The L1 reduces the event rate from the initial bunch crossing rate of 40 MHz down to 75 kHz. The time for the L1 decision is limited to 2.5 µs due to limited front end buffer space. The individual decisions from muon and calorimeter systems are combined by the central trigger processor which accepts or rejects the event. If the event is accepted, the detector output which is buffered for the L1 trigger latency is transmitted off the detector to the DAQ system for further temporary storage.

The L2 trigger receives the event data associated to the RoI's from the detector read–out. It uses the full granularity information of the trigger object candidate defined by L1 plus additional information from the inner detector to refine the trigger decision. This reduces the accepted event rate from the L1 output rate down to the maximum output rate of 3.5 kHz with an average processing time of approximately 40 ms per event. The events passing the L2 trigger are transferred to the event building system which combines the complete read–out data of an event to one formatted data structure.

The DAQ system passes the fully–built events to the EF for the final trigger decision. The EF uses offline analysis algorithms and sends the accepted events to dedicated data streams, e.g. to the muon stream if it contains a muon HLT object. The EF processing time amounts to approximately four seconds and the selected events are passed to CERN's central data–recording facility with a rate of roughly 200 Hz. The final output rate depends on offline reconstruction speed and transfer bandwidth to the mass storage. These are extended with time so that the output rate is not a hard limit in the DAQ system.

### 4.2.7 Luminosity Measurement

ATLAS employs several systems for the measurement of the luminosity. Beam Condition Monitors (BCM), the minimum bias trigger scintillator disks (MBTS), LUCID and ZDC mentioned above and also the FCal have been used to determine the instantaneous luminosity in 2011 [113, 114]. The instantaneous luminosity in the LHC beams is degrading with time during ATLAS data taking as shown in Figure 4.8. The unit of time in which the luminosity is measured is called a luminosity block. The default length of a luminosity block for proton–proton collisions in 2011 was typically one minute. Within these time periods the luminosity is considered constant and the detector conditions discussed in Appendix A are not allowed to change. In case of a change in the trigger configuration or any other

issue affecting the detector conditions a new luminosity block is started immediately, even if the time period has still not expired. The measurements of the luminosity monitoring systems need to be calibrated. For this purpose three beam–separation scans, so–called van–der–Meer scans [115], were performed by the LHC in 2011 which allow for an absolute measurement of the luminosity from the beam geometry and beam current intensities. The resulting luminosity uncertainty for the 2011 data set amounts to 3.9 %, dominated by the uncertainty in the beam intensities.

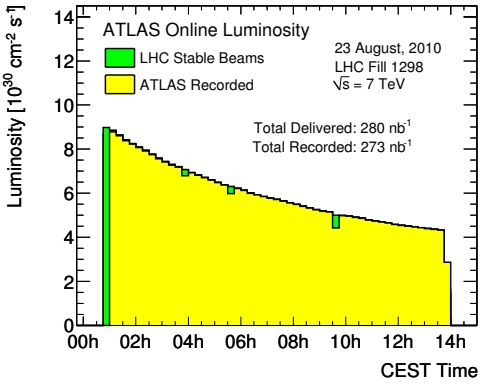


**Figure 4.8:** ATLAS instantaneous luminosity profiles as measured online for one representative LHC fill. The green shaded curve shows the delivered luminosity during stable beam condition allowing ATLAS to turn on their tracking devices, and the yellow shaded curve gives the recorded luminosity with the entire detector available. The luminosity values shown have been calibrated with van–der–Meer beam–separation scan data [116].

## 4.3 LHC Beam Conditions and ATLAS Data Taking

The LHC beam properties during the proton run in the year 2011 which is relevant for the data set used for the MSSM $h/A/H \to \mu^+\mu^-$ search presented in Chapter 6 have differed to some extent to the design specifications discussed in Section 4.1. In total, the ATLAS detector recorded an integrated luminosity of $5.25\,\text{fb}^{-1}$ throughout the year while the LHC delivered $5.61\,\text{fb}^{-1}$ of proton–proton collisions in stable beam conditions. This corresponds to a data taking efficiency of approximately 94 %. Inefficiencies arise from nominal detector operation procedures, as well as from read–out problems as discussed in Appendix A. As shown in the distribution of the instantaneous luminosity in Figure 4.9(a) the machine performance improved steadily over the year leading to optimised beam conditions for the physics programme of the LHC experiments.

The LHC beam energy was 3.5 TeV throughout the year leading to proton–proton collision at a centre–of–mass energy of $\sqrt{s} = 7\,\text{TeV}$. The number of bunches in each beam was increasing from 194 at the beginning of the data taking period to at maximum 1854

in October 2011. The number of protons per bunch was slightly increasing in middle of the year from $1.1 \cdot 10^{11}$ to roughly $1.4 \cdot 10^{11}$ already exceeding the design value. The corresponding cumulative distribution of the integrated luminosity over the year is shown in Figure 4.9(b). The intervals with no increase in the integrated luminosity indicate the four technical stops of the LHC in March, May, July and September 2011. The proton bunches in the beams are not homogeneously distributed over the ring but arranged in so–called bunch trains. The number of bunch trains increased from 9 to 12 during the 2011 run period. The distance of the proton bunches in the trains was reduced from 75 ns to 50 ns in the very beginning of the data taking.

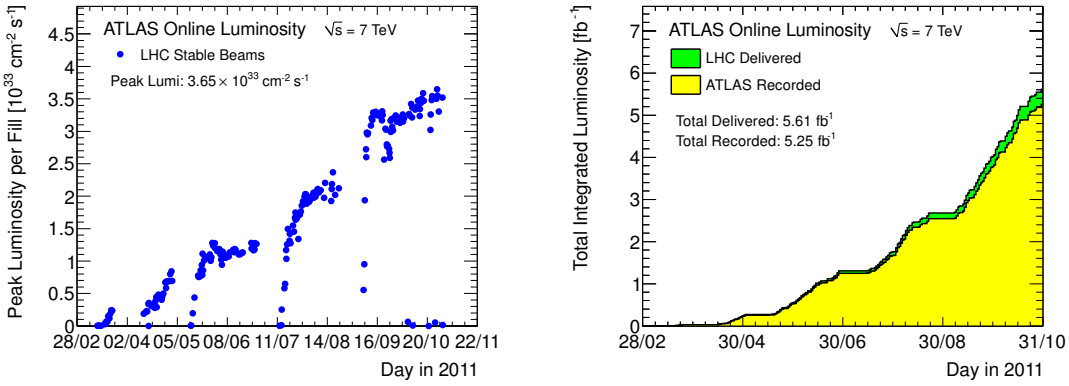


(a) (b)

**Figure 4.9:** (a) Distribution of the instantaneous luminosity increasing with improved LHC performance during the data taking period in the year 2011. (b) Cumulative distribution of the integrated luminosity delivered by the LHC and recorded by ATLAS for the data taking period in the year 2011 [116]. Gaps in the instantaneous luminosity and equivalent constant regions in the integrated luminosity indicate the four technical stops of the LHC in March, May, July and September 2011.

The increase in instantaneous luminosity is important to achieve a high rate of hard proton–proton interactions and therefore a high rate of possibly interesting physics processes. On the other hand it also leads to an increase in the number of simultaneous interactions occurring in one bunch crossing, i.e. an increase of pileup as discussed in Section 4.1. The amount of pileup can be characterised by the maximum and average number of interactions per bunch crossing shown in Figure 4.10(a). At the beginning of the 2011 data taking period, the maximum number of interactions per bunch crossing was roughly 10. By the end of the year this number grew to 24 where the biggest increase is due to the increase in the number of protons per bunch in July and the reduction of $\beta^*$ from 1.5 m to 1 m after the technical stop in September. The effect of pileup needs to be taken into account in physics analyses. The relevant quantity for the analyses is the average number of interactions per bunch crossing weighted with the integrated luminosity as shown in Figure 4.10(b). It can

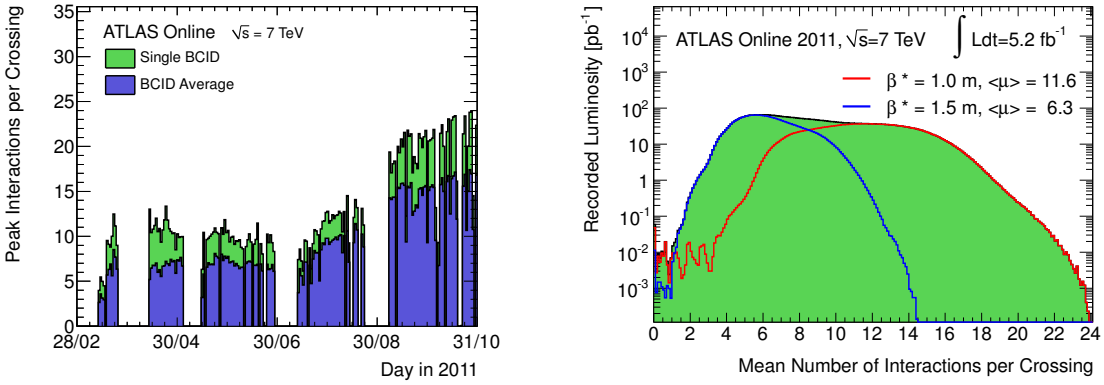


(a) (b)

**Figure 4.10:** (a) Maximum number of interactions per bunch crossing (green) and number of interactions averaged over the bunch crossings in one luminosity block (blue) in the data taking period in 2011. (b) Luminosity–weighted distribution of the mean number of interactions per bunch crossing in the year 2011. The blue and red curves show the distribution separately for the data taking periods before and after the technical stop in September where $\beta^*$ was reduced from 1.5 m to 1 m [116].

be seen that the average number of interactions per bunch crossing increased significantly with the reduction of $\beta^*$.

The increase in instantaneous luminosity affects also the TDAQ configuration of the ATLAS detector. The Event Filter output rate is kept at its maximum rate of approximately 200 Hz to record as many physics events as possible. However, with an increasing rate of interactions the trigger rate of the L1, L2 and EF increases and would overflow the buffers of the TDAQ system if no prescaling is applied on the triggers with too high rates. This means that only a certain fraction of events passing the respective trigger are recorded. Physics analyses like the MSSM $h/A/H \to \mu^+\mu^-$ search presented in Chapter 6 are typically performed on events passing unprescaled high level triggers.

The LHC configuration for the proton–proton run in the year 2012 was improved with respect to the parameters for the 2011 LHC run. The centre–of–mass energy was increased from $\sqrt{s} = 7$ TeV to 8 TeV while the bunch structure was equal to the configuration at the end of the 2011 run except for the number of protons per bunch which was increased to up to $2.2 \cdot 10^{11}$. The peak instantaneous luminosity reached a value of $7.73 \cdot 10^{33}\text{cm}^{-2}\text{s}^{-1}$ resulting in the maximum number of 45 pileup interactions per bunch crossing. The corresponding mean number of interactions per bunch crossing of approximately 20 was already exceeding the pileup condition expected for the design LHC parameters. By the end of the 2012 proton–proton run the LHC has delivered an integrated luminosity of $23\,\text{fb}^{-1}$ at $\sqrt{s} = 8$ TeV to the ATLAS experiment, roughly four times more than for the 7 TeV run in 2011.

### 4.3.1 LHC Upgrade Plans

The LHC baseline plan for the next 10 years foresees several upgrades and improvements of the machine in order to achieve the design parameters outlined in Section 4.1 and also reach significantly improved performance benchmarks [117, 118].

In early 2013, the LHC entered the first long shutdown, LS1, which is planned to take 18 months and in which the machine will be upgraded towards a centre–of–mass energy of 13 to 14 TeV, close to its design parameter. Shortly after the LHC re–start in 2015 the design luminosity of $10^{34}\text{cm}^{-2}\text{s}^{-1}$ will be reached.

After another long shutdown phase, LS2, planned for 2018, further improvements to the machine including new beam injectors are scheduled which will allow the LHC operation at twice the design luminosity. To cope with the upgraded LHC configuration also the experiments are planned to be upgraded during the LS1 and LS2 shutdowns.

By the end of 2021, the LHC is expected to deliver a total integrated luminosity of $300\,\text{fb}^{-1}$ at $\sqrt{s} = 14\,\text{TeV}$ to the ATLAS and CMS experiments. This benchmark represents the goal of the approved LHC physics programme.

After this period the statistical gain in running the LHC longer will be very small since the running time needed to halve the statistical error of the previous measurements will be more than 10 years [117]. To further exploit the physics potential of the LHC, significant upgrades either to the instantaneous luminosity or the centre–of–mass energy are necessary.

The current roadmap for the LHC foresees a third long shutdown, LS3, planned for 2022 to 2023 involving an upgrade to higher luminosities. In the upgraded configuration, called the high–luminosity LHC (HL–LHC) [117], nominal and peak luminosities of $5 \cdot 10^{34}\text{cm}^{-2}\text{s}^{-1}$ and $7 \cdot 10^{34}\text{cm}^{-2}\text{s}^{-1}$, respectively, are expected. The operation of the HL–LHC is planned for about 10 to 12 years and allows to reach the ultimate goal for the integrated luminosity of $3000\,\text{fb}^{-1}$ in 2030, marking the end of the LHC lifetime.

After the HL-LHC period a considerable extension of the physics programme involves the ambitious goal to upgrade the centre–of–mass energy to a maximum of $\sqrt{s} = 33\,\text{TeV}$. Essentially an entire new machine with dipole magnets providing a magnetic field of up to 16.5 T are necessary for the high–energy LHC (HE–LHC) [118]. Large efforts in design, R&D and construction set an earliest possible time scale for the start of the physics programme of the HE-LHC to later than 2035.

# Chapter 5

# Muon Identification and Data Quality Monitoring

This chapter gives an overview of the reconstruction and identification of muons with the ATLAS detector and presents the quality monitoring of the data produced by the muon identification algorithms. The reconstruction of charged particle tracks and the different muon identification algorithms are explained in Section 5.1 based on the Reference [119]. In Section 5.2, the data quality monitoring related to the performance of the muon identification is introduced and improvements implemented in the context of this thesis for the 2011 data taking are presented.

## 5.1 ATLAS Muon Reconstruction and Identification

Proton–proton collisions at LHC centre–of–mass energies result mainly in multijet events while only a small fraction of hard interactions produces physics processes of interest as discussed in Section 4.2. Muons, in particular with high transverse momenta, appear more likely in such rare events rather than in multijet background events and therefore provide important signatures for the triggering, identification and precise characterisation of these interesting events.

The ATLAS detector is designed to identify muons efficiently and provide precise measurements of their momenta and charge up to muon transverse momenta of 1 TeV [119]. Muon reconstruction in ATLAS relies on the reconstruction of charged particle trajectories in both the muon spectrometer and the inner detector. In addition, information from the calorimeter system is used to refine the performance of the muon identification and recover the acceptance holes in the muon spectrometer (see below). The basic tracking principles

are introduced in Section 5.1.1. Building on the reconstructed tracks, there are in total 9 algorithms dedicated to the muon identification in ATLAS. The muon identification strategies of these algorithms are introduced in Section 5.1.2.

### 5.1.1 Track Reconstruction

The reconstruction of charged particle trajectories is performed with the ATLAS inner detector and muon spectrometer. The track reconstruction software designed with high modularity [120] provides the track fitting and extrapolation in both detector systems taking into account the detector geometry and the distribution of active and passive materials. In addition, it allows for higher level reconstruction tasks like vertex finding.

The track reconstruction in the inner detector is divided in three steps [119]. First, in the pre–processing step the raw data of the inner detector components are transformed into hit clusters in the pixel and SCT layers and drift circles in the TRT. Second, in the track–finding step, a track seed from the three pixel layers and the inner SCT layer is extrapolated through the SCT. After an initial fit performed to reconstruct the track segment in the silicon detectors, several track quality cuts are applied and the track is extrapolated through the TRT. The final track is re–fitted using the full inner detector information. The track fitting employs global–$\chi^2$ and Kalman–based [121] fit routines as well as more specialised algorithms dedicated to particle identification after the track finding, e.g. Gaussian Sum Filters (GSF) [122] for the recovery of the Bremsstrahlung from electrons. In the final step, the post–processing, higher level tracking like primary and secondary vertex fitting and the reconstruction of the photon conversion are performed.

Track reconstruction in the muon spectrometer is performed as a part of the standalone muon identification algorithms and is therefore discussed in the respective section below.

### 5.1.2 Muon Identification

For the reconstruction and identification of muons four strategies are pursued in ATLAS [119]: standalone, combined, segment–tagged and calorimeter–tagged reconstruction. Two, or in the case of segment–tagged reconstruction, three independent algorithms are available for each strategy. The different algorithms for the standalone, combined and segment–tagged reconstruction are grouped in two families named Staco [123] and Muid [124]. The calorimeter–tagged algorithms are independent from these two families and provide a special collection of muons, referred to as CaloMuon collection in the following. All nine algorithms are used in a complementary way within the framework of the muon combined reconstruction and identification.

### Standalone Muon Reconstruction

The standalone muon reconstruction finds muon tracks using only the hits in the muon spectrometer and performs pattern recognition, track building and fitting complementary to the tracking in the inner detector outlined in Section 5.1.1. The standalone muon algorithms start with the hits in the muon stations, i.e. the three "layers" of the muon spectrometer consisting of RPC and TGC trigger chambers and single or pair–wise multilayers of MDT and CSC precision chambers. Straight track segments are built from the hits in the multilayers with the requirement to point roughly in the direction of the interaction point. Several stages of $\chi^2$–based track fits build the final muon spectrometer track accounting for the exact magnetic field configuration, detector geometry and multiple scattering. Finally, the muon spectrometer tracks are extrapolated back to the beam line accounting for multiple scattering and energy loss in the calorimeters.

As the standalone muon reconstruction operates independently from the inner detector acceptance it finds muon tracks in the whole pseudorapidity range of the muon spectrometer, $|\eta| < 2.7$, but suffers from acceptance holes at $|\eta| \approx 0$ and $|\eta| \approx 1.2$. The standalone muon reconstruction algorithms are also sensitive to non–prompt muons originating from pion and kaon decays in the calorimeter. These so–called "fake" muons are difficult to distinguish from prompt muons originating from the hard scattering processes in the proton–proton collisions if they point back to the interaction region.

The standalone algorithm from the Staco reconstruction package is called Muonboy [125], the equivalent from the Muid reconstruction package is called Moore [126]. Both algorithms differ mostly in the treatment of the energy loss in the calorimeter. Muonboy assigns a parametrised energy loss according to the amount of material crossed by a given muon track. The muon tracks reconstructed by the Moore algorithm are additionally corrected for the energy measurement in the calorimeter if the energy deposits are significantly larger than expected from parametrisation [127].

### Combined Muon Reconstruction

A better control of the fake muons from secondary interactions and pion and kaon decays in flight as well as a better transverse momentum resolution is provided by the combined reconstruction algorithms exploiting both tracking systems, the muon spectrometer and the inner detector. The combined muon algorithms are named after the reconstruction packages themselves, Staco combined (StacoCB) [123] and Muid combined (MuidCB) [124]. Combined muon tracks are reconstructed if the standalone muon tracks can be associated to the inner detector tracks.

The Staco combined algorithm performs a statistical combination of the tracks found in the inner detector and the muon spectrometer, accounting for the reconstructed track parameters and their covariance matrices.

The Muid combined algorithm performs a $\chi^2$–based re–fit of the combined track from the track parameters of the inner detector track and the standalone muon track extrapolated to the inner detector, accounting for their summed covariances.

### Segment–Tagged Muon Reconstruction

The third muon reconstruction strategy of the Staco and Muid reconstruction packages, called segment tagging, starts with an inner detector track which is extrapolated to the one or several stations of the muon spectrometer. This strategy aims particularly at muons with low momenta which do not penetrate all three stations of the muon spectrometer. Segment tagging also recovers muons in regions with incomplete coverage of the muon spectrometer or defect muon chambers.

The MuTag [123] segment tagging algorithm from the Staco package searches for track segments in the innermost layer and, for particular $\eta$–regions, also in the second layer of the muon spectrometer. To identify a tagged muon, a tag–$\chi^2$ is built from the difference of the track parameters from the muon spectrometer segment and the inner detector prediction. The MuTag algorithm operates fully complementary to the Muonboy and Staco combined algorithms as it is performed only on muon spectrometer segments not used by the standalone and combined algorithms.

The Muid package has two segment–tagging algorithms, named MuGirl [128] and MuTagIMO [129]. The MuGirl algorithm builds its own track segments from muon spectrometer hits in a $\eta$–$\phi$ road defined by the extrapolated inner detector track, accounting for energy losses in the calorimeters. The final discrimination between muon–like and fake–like candidates is performed by an artificial neutral network procedure using information from both the muon spectrometer hits and the built segments. The MuTagIMO algorithm extrapolates inner detector tracks and associates them with segments reconstructed by the Moore algorithm in any layer of the muon stations.

All three algorithms have in common that the momentum and charge measurement is performed by the inner detector and the muon spectrometer segments are only used for tagging the track as the muons.

### Calorimeter–Tagged Muon Reconstruction

The muon identification algorithms are complemented by two calorimeter–based algorithms. Both algorithms, called CaloMuonTag [119, 130] and CaloMuonLikelihood [119], start with inner detector tracks and search for associated signatures of minimal ionising particles in the calorimeter system. If an inner detector track matches the energy deposition pattern of a muon in the calorimeter the track is tagged as a muon. Calorimeter tagging particularly aims for muons with very low transverse momenta, $p_{\mathrm{T}} = 2 - 5\,\mathrm{GeV}$, and recovers the acceptance holes in the muon spectrometer, particularly at $|\eta| \approx 0$.

The CaloMuonTag algorithm extrapolates inner detector tracks through the calorimeters and measures the energy in the cell closest to the extrapolated track, separately for each sampling layer of the calorimeter. Minimum and maximum energy thresholds in the associated calorimeter cells, as well as the track quality criteria reduce the number of fake muons.

The CaloMuonLikelihood algorithm uses a likelihood ratio built from several energy ratios in different sampling layers of the calorimeters to discriminate muons from pion decays according to the structure of their energy deposits.

## 5.2 Muon Data Quality Monitoring

During data taking as well as during the reconstruction of the recorded data, numerous problems can appear, which might affect the physics measurements. The sources of such problems range from dead or noisy hardware channels and faulty power supply systems to false configurations of detector components, the trigger and the read–out of the different sub–systems of the ATLAS detector (see Section 4.2). The reconstruction of higher level physics objects, i.e. electrons, photons, muons, $\tau$ leptons and $b$ jets, can suffer from such problems or can produce poor–quality data itself due to problems in the reconstruction algorithms, in service tools or in databases which are needed for the particle reconstruction. As a consequence of such problems, affected sub–detectors or physics objects may not be usable in some physics analyses.

To assure the successful and efficient detector operation as well as precise physics measurements, the detector condition and the quality of the recorded and processed data is monitored. Problems are tracked and documented such that affected poor–quality data can be excluded from given analyses.

Important aspects of the ATLAS detector operation and data reconstruction relevant for the data quality assurance are described in Appendix A together with an overview of the online and offline data quality monitoring tools and the data quality assessment procedure. This section summarises the data quality monitoring related to the performance of the muon reconstruction and identification.

The ATLAS muon reconstruction introduced in Section 5.1 comprises in total nine different muon identification algorithms following different strategies and taking advantage of information from each sub–detector, the muon spectrometer, the inner detector and also the calorimeter system. In addition, the muon performance relies on the alignment and calibrations of different detector components, as well as several common reconstruction tools, like track extrapolators, fitting tools, tracking geometry and magnetic field services.

The primary goal of the muon data quality monitoring is to monitor the performance of the muon reconstruction algorithms. This implies checks for the proper setup of the reconstruction framework, for the operation of common service tools and for database

access. As a result, data quality assessments are made for each of the reconstruction algorithms indicating if the reconstructed muons in a particular run, i.e. an ATLAS data taking cycle (see Appendix A), can be used in physics analyses.

The operation of the sub–detector systems used by the muon reconstruction are monitored by dedicated data quality responsibles. This introduces a certain overlap with the muon data quality monitoring. Therefore, observed problems are first traced back to the sub–systems. Reconstructed muons are only excluded from physics measurements, if the problem is found to occur in the muon reconstruction itself.

In summary, the muon performance was operated very stable throughout the data taking periods. In the 2011 proton–proton run, which is relevant for this thesis, the muon reconstruction was affected in 2 of 267 runs by two problems originating from inner detector and muon spectrometer sub–systems. The muon trigger system was affected by a misconfiguration leading to a lower trigger efficiency in one sub–period (see Appendix A).

### 5.2.1 Monitoring of the Muon Reconstruction Algorithms

The monitoring of the muon reconstruction algorithms requires a certain amount of events since most useful data quality checks are performed on distributions of relevant variables. A selection of muon performance data quality monitoring histograms are discussed in the following. In these examples, the data taken in the ATLAS run 191715 is compared to the reference run 191190. Both runs have relatively high integrated luminosities of $49\,\mathrm{pb}^{-1}$ and $190\,\mathrm{pb}^{-1}$, respectively, providing sufficient amount of data for detailed comparisons. The histograms are normalised to the total number of events recorded in the monitored run 191715.

A first cross check inspects whether all reconstruction algorithms are fully operational. The nine different algorithms have different muon acceptances but the corresponding numbers of reconstructed muons relative to the total one should be approximately unchanged from one run to another. Figure 5.1(a) shows the number of muons in the run reconstructed with each of the nine muon reconstruction algorithms. A good agreement is observed with respect to the reference run indicating a reliable muon reconstruction. Furthermore, the number of muons produced in $pp$ collisions with positive and negative electric charge is expected to be very similar. Therefore, the distribution of the number of muons with positive and negative charges is used as a further data quality check. Figure 5.1(b) shows as example of such a histogram for muons reconstructed with the Staco combined algorithm.

The $p_{\mathrm{T}}$ spectrum of muons, as shown in Figure 5.2(a) for the Staco combined algorithm for example, is also expected to remain similar in different runs. The only acceptable exception is caused by the change in the trigger menu hardening the spectrum. The muon $p_{\mathrm{T}}$ spectrum is characterised by two rising edges. The first rising edge at $p_{\mathrm{T}} \approx 4\,\mathrm{GeV}$ marks the average energy a muon needs to penetrate all muon stations in the muon spectrometer. The second edge is located at the threshold value of the most efficient trigger in the trigger

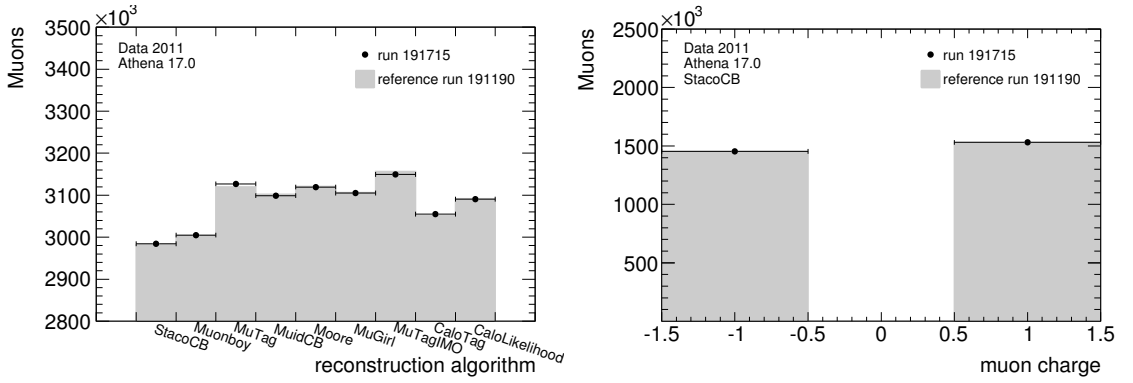


(a) (b)

**Figure 5.1:** Numbers of muons reconstructed with each of the nine muon reconstruction algorithms (a) and the number of muons with positive and negative electric charges found by the Staco combined algorithm (b) in the ATLAS run 191715 compared to the reference run 191190.

menu. In addition, with the raise of the trigger thresholds the fraction of $Z \to \mu^+\mu^-$ events in the recorded muon data increases, resulting in a more prominent "shoulder" in the $p_{\mathrm{T}}$ spectrum at about 40 GeV.

The monitoring of the occupancy of muon tracks in the $\eta$–$\phi$ plane, as shown in Figure 5.2(b), ensures the performance of the muon reconstruction in the entire angular acceptance range. This is sensitive mainly to the problems upstream the muon reconstruction, as for example dead detector regions in the muon spectrometer.

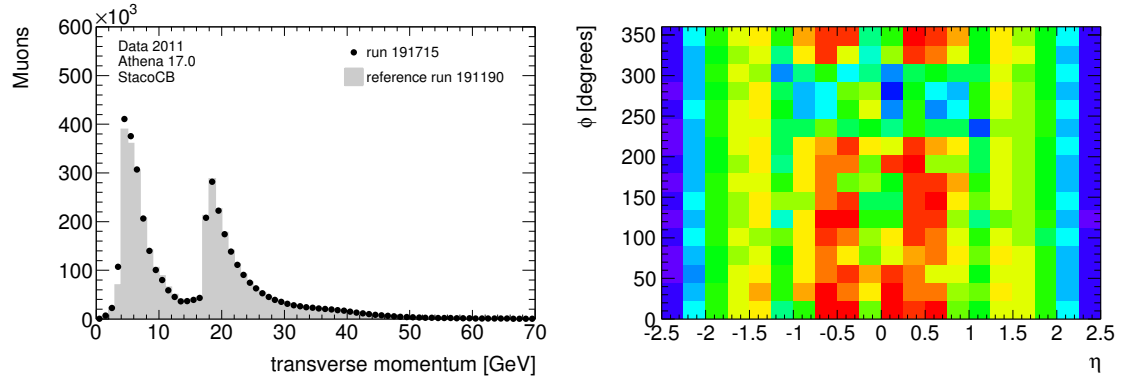


(a) (b)

**Figure 5.2:** The $p_{\mathrm{T}}$ spectrum (a) and the occupancy in the $\eta$–$\phi$ plane (b) for muons reconstructed with the Staco combined algorithm in ATLAS run 191715. In the $p_{\mathrm{T}}$ spectrum on the left–hand side is compared to the one from the reference run 191190.

More detailed information about specific features of the different muon reconstruction algorithms are obtained from various quantities like the number of hits in the muon spectrometer or the inner detector, comparisons of momenta reconstructed in the muon spectrometer with respect to the inner detector or information about the transverse and longitudinal impact parameters, $d_0$ and $z_0$. The transverse impact parameter, $d_0$, is the distance of closest approach of the track to the primary vertex point in the $r$–$\phi$ projection. The longitudinal impact parameter, $z_0$, is the $z$ coordinate of the track at the point of closest approach in $r$–$\phi$.

Using the example of the Staco combined algorithm which is performing a statistical combination of a muon spectrometer and an inner detector track, the pull distribution of the longitudinal impact parameters, $z_0^{\mathrm{MS}}$ and $z_0^{\mathrm{ID}}$, measured in the two sub–detectors allow for the monitoring of the quality of the combined track. The $z_0$ pull distribution is expected to have a mean compatible with zero and a width compatible with one, as for example shown in Figure 5.3(a).

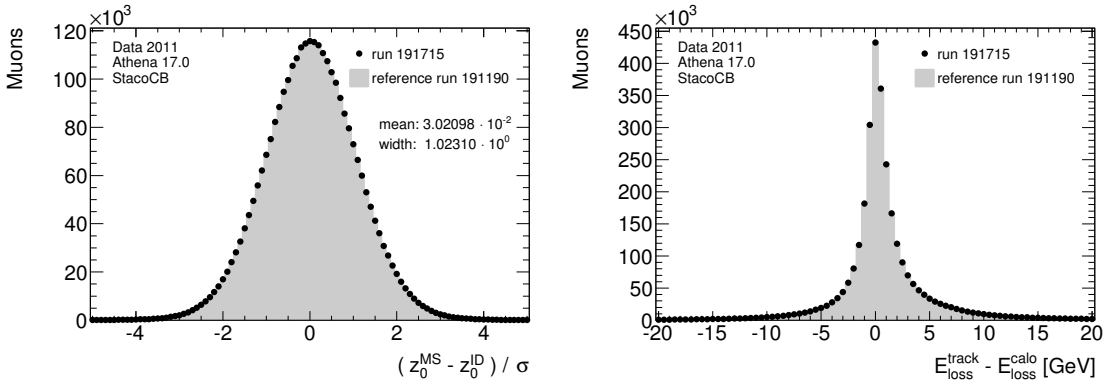


(a) (b)

**Figure 5.3:** Pull distribution of the longitudinal impact parameter, $z_0$, (a) and distribution of the muon energy loss in the calorimeter (b) shown for muons reconstructed with the Staco combined algorithm in ATLAS run 191715 compared to the reference run 191190.

The standalone algorithms perform an extrapolation of the standalone muon track back to the interaction point. This extrapolation takes into account the energy loss of the muons in the calorimeter. The energy loss correction can be monitored with combined muons comparing the measured momentum differences of the associated muon spectrometer and inner detector tracks with the assigned energy loss in the calorimeter. An example of such measurement obtained with the Staco combined algorithm is shown in Figure 5.3(b). In case of a correct energy loss parametrisation the distribution is expected to be narrow and peaking at zero.

### 5.2.2 Monitoring of Muon Identification and Trigger Efficiencies

With improved performance of the LHC accelerator the integrated luminosity of a single ATLAS run has increased significantly in 2011 compared to the data taking in 2010. Runs with integrated luminosities in the order of several $10\,\mathrm{pb}^{-1}$ allow for more detailed checks of the muon combined performance and the data quality monitoring was extended accordingly in late 2010. When monitoring reconstruction algorithms it is of great interest that these algorithms are operating efficiently and that the efficiency is stable over the data taking period. Therefore, a data–driven muon trigger and identification efficiency monitoring was introduced. The measurement is performed with $Z \to \mu^+\mu^-$ events selected by a so–called "tag–and–probe" method. The implementation of the efficiency monitoring into the data quality monitoring framework and the results obtained for the 2011 data are presented in the following.

#### Tag–and–Probe Method

The muon trigger and identification efficiencies are determined with the so–called "tag–and–probe" method [119] which allows for an unbiased measurement for muons originating from the $Z \to \mu^+\mu^-$ decay of the $Z$ boson. The method selects the events with two oppositely charged inner detector tracks with the invariant mass compatible with the $Z$ boson mass. One track is required to match a well reconstructed muon, i.e. the "tag muon". This implies that the second track should also be a muon. The matching of the second inner detector track to another reconstructed muon, i.e. the "probe muon", therefore allows to evaluate the identification efficiency of the probed muon relative to the inner detector tracking efficiency. In addition, if a probe muon is found it can be checked if this muon passes the requirements of a given muon trigger. This allows for the evaluation of the corresponding muon trigger efficiency. The tag–and–probe method is illustrated in Figure 5.4. The event selection of the described method as implemented within the muon performance data quality framework is presented in the following.

#### Event Selection

Events considered for the tag–and–probe method are required to pass the reference high–$p_\mathrm{T}$ single muon trigger with a transverse momentum threshold of 18 GeV. The method probes separately the muons reconstructed by the Staco and the Muid reconstruction packages as well as the calorimeter–tagged algorithms.

The $Z$ event selection requires a well reconstructed combined muon with a transverse momentum of $p_\mathrm{T} > 20\,\mathrm{GeV}$ and a pseudorapidity of $|\eta| < 2.5$. The combined track is required to be the best of all possible matches to a muon spectrometer track. This tag muon candidate is required to have triggered the event. Further quality criteria for the inner detector track associated to the tag muon candidate need to be fulfilled [131] as listed

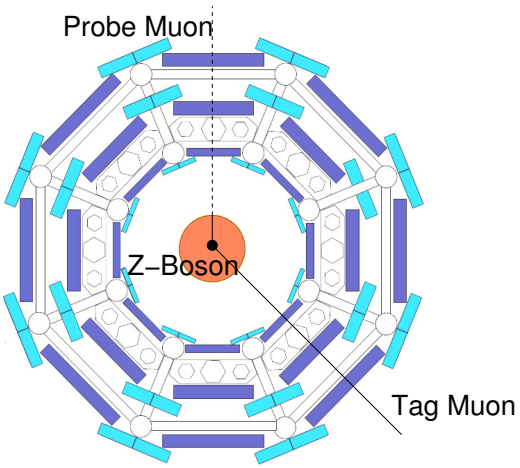


**Figure 5.4:** Schematic illustration of the tag–and–probe method showing a $Z$ boson decay to two muons in the transverse ATLAS detector plane. The inner detector (red), the muon stations (blue) and the toroid coils of the barrel muon spectrometer are shown as well. The tag muon with the corresponding inner detector track is well reconstructed indicated by the solid line. The second inner detector track (short solid line) serves as a probe to find a match to a corresponding second muon (probe muon), indicated by the dashed line. This allows for an efficiency determination relative to the inner detector tracking efficiency [119].

below. The inner detector track quality criteria account for the silicon detector conditions such that if a track passes a dead module or an uninstrumented area, a well detected hit in the corresponding system is counted.

- A hit of the muon inner detector track is required in the pixel $b$–layer (i.e. the innermost layer of the pixel detector) unless the extrapolated muon track passes an uninstrumented or dead area of the $b$–layer.
- The number of hits in the pixel detector summed with the number of crossed dead pixel sensors is required to be greater than 1.
- The number of hits in the SCT detector summed with the number of crossed dead SCT sensors is required to be greater than 5.
- The number of crossed operating pixel and SCT sensors not detecting a hit is required to be less than 3.
- If the inner detector track lies within the acceptance of the TRT detector it needs to be successfully extrapolated through the TRT. The relevant quantities for the extrapolation are the number of TRT hits on the track, $n_{\mathrm{TRT}}^{\mathrm{hits}}$, the number of TRT hits lying outside the extrapolated track, $n_{\mathrm{TRT}}^{\mathrm{outliers}}$, and the total number of TRT hits close to the extrapolated track, $n = n_{\mathrm{TRT}}^{\mathrm{hits}} + n_{\mathrm{TRT}}^{\mathrm{outliers}}$. The corresponding criteria are:

- For a track within $|\eta| \leq 1.9$ the number of TRT hits and outliers needs to be greater than 5, $n > 5$, and the number of outliers is constrained by $n_{\mathrm{TRT}}^{\mathrm{outliers}} < 0.9\,n$.
- For a track within $|\eta| > 1.9$ the number of outliers is constrained by $n_{\mathrm{TRT}}^{\mathrm{outliers}} < 0.9\,n$ only if there are more than 5 TRT hits, $n > 5$.

To increase the purity of the tag muons, the tag candidates are required to have a good quality match, $\chi^2_{\mathrm{match}}$, between the inner detector track and the muon spectrometer track and the activity in the calorimeter around the muon track should be low. The corresponding selection criteria are $\chi^2_{\mathrm{match}} < 150$ and $E_{\mathrm{T}}^{\mathrm{cone\ 0.4}} < 2\,\mathrm{GeV}$, where $E_{\mathrm{T}}^{\mathrm{cone\ 0.4}}$ is the calorimetric energy measured in a cone with radius parameter $\Delta R = 0.4$ around the muon track, excluding the energy associated to the muon itself.

The selection of the probe candidates starts from inner detector tracks with transverse momenta greater than $p_{\mathrm{T}} > 15\,\mathrm{GeV}$ and $|\eta| < 2.5$. Only well reconstructed tracks are taken into account, therefore the inner detector track quality criteria defined above are applied to the probe candidates and the $\chi^2$ value of the track fit is required to be $\chi^2_{\mathrm{fit}} < 150$. Finally, the probe track candidates are required to be isolated: the scalar sum of the transverse momenta of all tracks originating from the same vertex as the probe track, with $p_{\mathrm{T}} > 1\,\mathrm{GeV}$ and located within a cone of $\Delta R = 0.2$ around the probe track must be less than 20 % of the probe track transverse momentum, $p_{\mathrm{T}}^{\mathrm{cone\ 0.2}}/p_{\mathrm{T}} < 0.2$. The scalar sum is calculated excluding the transverse momentum of the probe track candidate itself.

A tag–and–probe pair is formed from each tag muon candidate and probe track candidate if both are originating from a $Z$ boson decay, i.e. the tag–and–probe candidates are required to have opposite electric charges and an invariant mass close to the $Z$ boson mass, $m_{\mathrm{tag\text{–}probe}} = m_Z \pm 15\,\mathrm{GeV}$. $Z$ boson decays tend to be balanced in the $r$–$\phi$ plane, therefore, the tag–and–probe candidates are required to be emitted back–to–back, i.e. $\cos\left(|\phi_{\mathrm{tag}} - \phi_{\mathrm{probe}}|\right) < -0.5$. To enhance the purity of the selected $Z$ events, both the tag–and–probe candidates are required to emerge from a common vertex. The differences in their transverse and longitudinal impact parameters are required to be small, i.e. $||d_0^{\mathrm{tag}}| - |d_0^{\mathrm{probe}}|| < 0.5$ and $||z_0^{\mathrm{tag}}| - |z_0^{\mathrm{probe}}|| < 1.0$. The purity of $Z \to \mu^+\mu^-$ events in the selected tag–and–probe candidates is estimated with simulated events. Considered processes are $Z$ boson production in association with jets with subsequent $Z$ boson decays to $\mu^+\mu^-$ and $\tau^+\tau^-$, as well as the production of top quark pairs and single top quarks, $b$ quark pairs, $W^+W^-$ di–bosons and $W$ bosons in association with jets. Accounting for misidentified tag–and–probe candidates from these processes the purty of $Z \to \mu^+\mu^-$ events is 99.87 %. Thus, the impact of the remaining 0.13 % of background processes on the measured muon trigger and identification efficiencies can be neglected.

The selected tag–and–probe pair corresponding to a $Z \to \mu^+\mu^-$ decay is then used for efficiency measurements on the probe side. The identification efficiency for a given muon reconstruction algorithm is evaluated with respect to the inner detector tracking efficiency

by counting the fraction of the probe tracks that can be matched to a muon reconstructed by the monitored algorithm. A probe muon with $p_{\mathrm{T}} > 15\,\mathrm{GeV}$ and $|\eta| < 2.5$ matches the inner detector track if the angular distance between track and muon is less than $\Delta R = 0.05$. Furthermore, if a probe muon is found the trigger efficiency is evaluated as the fraction of the probe muons that can be matched to a region of interest in the detector in which the given muon trigger has fired.

### Results

The tag–and–probe selection described above provides the muon identification and trigger efficiencies on a run–by–run basis. Muon identification efficiencies are obtained for each muon reconstruction algorithm as an overall value integrated over $p_{\mathrm{T}}$, $\eta$ and $\phi$ (for $p_{\mathrm{T}} > 20\,\mathrm{GeV}$) and in bins of $p_{\mathrm{T}}$ and $\eta$. Muon trigger efficiencies for the lowest unprescaled high–$p_{\mathrm{T}}$ single muon triggers are obtained as overall values integrated over $p_{\mathrm{T}}$, $\eta$ and $\phi$ (for $p_{\mathrm{T}}$ greater than the trigger threshold and $\eta$ within the acceptance of the trigger) and in bins of $p_{\mathrm{T}}$, $\eta$ and $\phi$. The $\eta$ and $\phi$ bins correspond to logical detector regions which helps spotting problems occurring in certain parts of the detector. The description of the logical detector regions in $\eta$ and $\phi$ are given in Appendix A.

For the initial 2011 data taking periods the transverse momentum threshold of the lowest unprescaled single muon trigger was set to $p_{\mathrm{T}} = 18\,\mathrm{GeV}$. For these data taking periods three trigger items are monitored: `EF_mu18`, `EF_mu18_MG` and `EF_mu40_MSonly_barrel`. `EF_mu18` is an "outside–in" trigger, i.e. the trigger algorithm at the event filter (EF) level starts from a muon spectrometer track and extrapolates to the inner detector to produce a combined track. For the "inside–out" trigger `EF_mu18_MG` the EF algorithm starts from an inner detector track and extrapolates and combines with the muon spectrometer tracks. `EF_mu40_MSonly_barrel` relies only on the standalone information from the muon spectrometer in the barrel region and has a transverse momentum threshold of $p_{\mathrm{T}} = 40\,\mathrm{GeV}$. All three triggers are seeded by the Level–1 (L1) trigger `L1_MU10` consisting of a two– (three–) station coincidence trigger in the barrel (end–cap) region with a $p_{\mathrm{T}}$ threshold of 10 GeV. For the later data taking periods starting in August 2011 the peak luminosity of the LHC reached $1.9 \cdot 10^{33}\mathrm{cm}^{-2}\mathrm{s}^{-1}$ and the `L1_MU10` trigger had to be prescaled. Therefore, for these data taking periods the single muon triggers were seeded by the `L1_MU11` trigger consisting of trigger coincidences from all three stations in both barrel and end–cap region. Consequently, muon performance data quality monitored the corresponding `L1_MU11` seeded trigger items `EF_mu18_medium`, `EF_mu18_MG_medium` and `EF_mu40_MSonly_barrel_medium`.

The results of the muon identification efficiency and trigger monitoring for the 2011 data taking periods shown in the following were evaluated for each run. For illustration purposes the runs contributing to the physics data taking are combined corresponding to several data taking periods (from period B to period M). The description of the individual data

taking periods defined by certain changes in the LHC beam or ATLAS detector conditions is given in Appendix A.

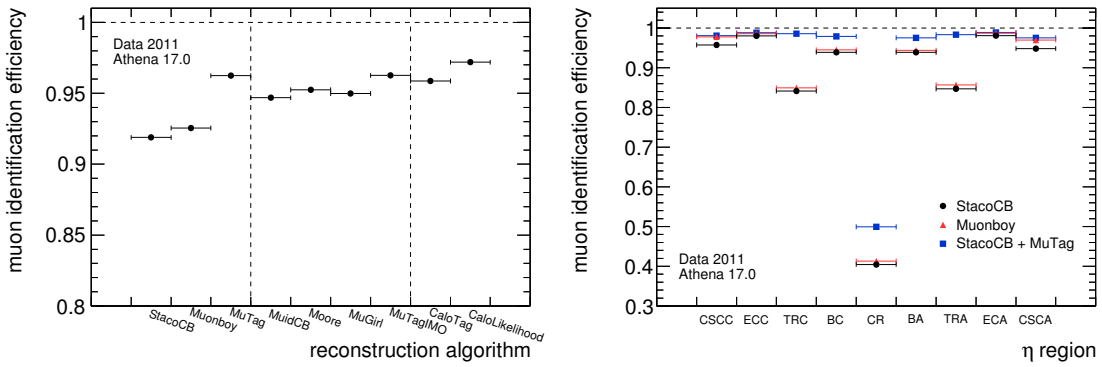


(a) (b)

**Figure 5.5:** Overall muon identification efficiencies for each ATLAS muon reconstruction algorithm evaluated using the full 2011 data set (a). The dashed vertical lines indicate the separation of the algorithms in the three families of reconstruction packages, Staco, Muid and calorimeter–tagged muons. Muon identification efficiencies for the three algorithms of the Staco reconstruction package in bins of $\eta$ corresponding to logical detector regions (b).

**Muon Identification Efficiencies** The overall efficiency for each of the nine muon reconstruction algorithms operational in ATLAS are shown in Figure 5.5(a) integrated over $p_{\mathrm{T}}$, $\eta$ and $\phi$ (for $p_{\mathrm{T}} > 20\,\mathrm{GeV}$). It can be seen that the segment–tagging and calorimeter–tagging algorithms have highest efficiencies followed by the standalone algorithms. The two combined algorithms, Staco combined and Muid combined, have the lowest identification efficiency which is compensated by a low contamination by fake muons and most precise momentum resolution. The efficiencies for the three algorithms of the Staco reconstruction package broken down into $\eta$ bins corresponding to logical detector regions (see Appendix A) are shown in Figure 5.5(b).

In addition to a generally higher efficiency over the whole acceptance range the segment–tagging algorithm performs in particular more efficiently in the transition regions (TRA, TRC) of the muon spectrometer. In these regions the muon tracks do not always cross all three stations of the muon spectrometer leading to a degraded efficiency of the standalone algorithms and consequently of the combined algorithms. Therefore, physics analyses relying on high muon efficiency, as the search for the neutral MSSM Higgs bosons decaying to $\mu^+\mu^-$ (see Chapter 6), typically use the segment–tagged muons in addition to the combined muons. If a muon is reconstructed by both algorithms, the combined muon track is used leading to high identification efficiency combined with a low fake rate and good momentum resolution.

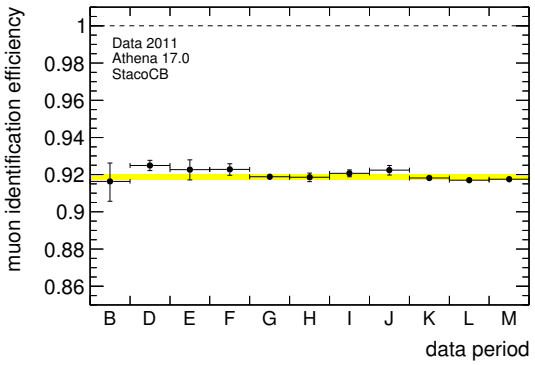


**Figure 5.6:** Stability of the muon identification efficiency for the Staco algorithms over the 2011 data taking shown for the 11 main data taking periods. The yellow band represents the 95 % confidence level band around the mean efficiency from the complete 2011 data set.

Figure 5.6 shows the overall muon identification efficiency for the Staco combined algorithm for the data taking periods of the 2011. The efficiencies in the individual periods are compatible showing the stable performance of the muon reconstruction.

The stability of the muon combined performance is also illustrated by the invariant mass distribution of the selected $\mu^+\mu^-$ pairs from $Z$ boson decays. The location of the peak of the $Z$ resonance is sensitive to the muon momentum scale. In addition, the reconstructed width of the resonance depends on the $\mu^+\mu^-$ mass resolution and therefore on the muon momentum resolution. To measure the location of the peak and the width of the $Z$ resonance the $\mu^+\mu^-$ invariant mass distributions for each data taking period are fitted with a Gaussian function in the invariant mass range of 87 GeV to 95 GeV. Mean and width of the fitted Gaussian functions are shown in Figures 5.7(a) and 5.7(b), respectively, in dependence of the data taking periods. In both cases, the fit results for the individual data taking periods are compatible proving the excellent stability of the muon reconstruction. The systematic shift of the mean value obtained from the Gaussian fit by approximately 0.3 GeV with respect to the world average value of the $Z$ boson mass [61] is due to final state radiation of the muons which is not corrected for. However, for the purpose of the data quality monitoring the exact position of the $Z$ resonance peak is less important than the variation in each run with respect to a reference run.

Figure 5.8 illustrates a problem monitored by muon performance data quality which occurred in the muon reconstruction in run 186877 in 2011. For a sequence of luminosity blocks one of five MDT read–out driver modules in the end–cap C of the muon spectrometer was busy. As a consequence, approximately 20 % of the muon system in this end–cap was effectively dead during this time and no muons were reconstructed in the affected detector region. Since at the same time the inner detector was fully operational this problem can be spotted as a degradation in the monitored muon identification efficiency. Figures 5.8(a)

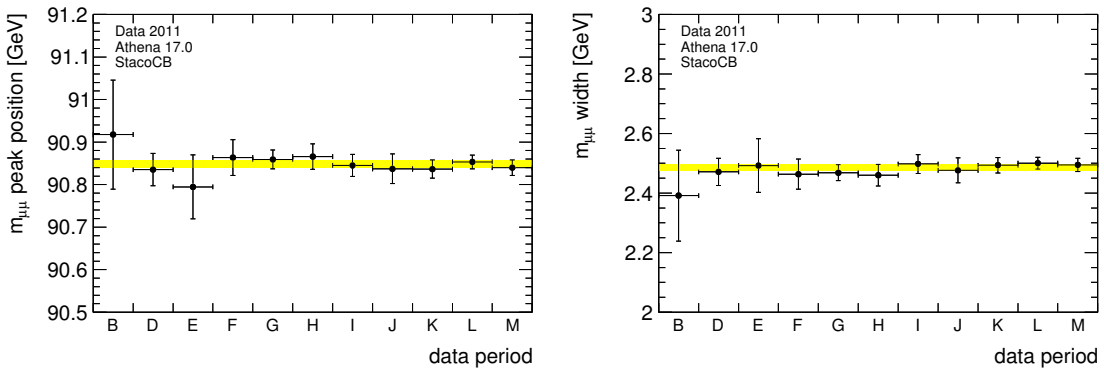


(a) (b)

**Figure 5.7:** Mean (a) and width (b) of the Gaussian functions fitted to the $\mu^+\mu^-$ invariant mass distributions, $m_{\mu\mu}$, of the selected $Z$ tag–and–probe events for each data taking period in the 2011 run. The yellow bands represent the 95 % confidence level band around the average values of the the mean and the width for the complete 2011 data set.

and 5.8(b) compare the muon efficiency measured in run 186877 with the efficiency for the whole corresponding data taking period. The efficiency is measured for the Staco combined algorithm in bins of $p_{\mathrm{T}}$ and $\eta$, respectively. The efficiency as a function of $p_{\mathrm{T}}$ is systematically shifted to lower values with respect to the reference in the whole $p_{\mathrm{T}}$ range. The origin of the problem is better understood looking at the efficiency as a function of $\eta$. The efficiency drops significantly in the detector regions CSCC and ECC corresponding to the end–cap C while in the remaining detector regions the measured efficiency is compatible with the reference. This is an example of the muon reconstruction suffering from non–operational parts of a sub–detector. The problem in this run is related to detector components in the muon spectrometer and was also monitored by the dedicated sub–system data quality monitoring which is an example for the successful interplay of the complementary data quality monitoring framework in ATLAS.

**Muon Trigger Efficiencies** The overall efficiencies integrated over $p_{\mathrm{T}}$, $\eta$ and $\phi$ (with muon $p_{\mathrm{T}}$ greater than the trigger threshold and $\eta$ within the acceptance of the trigger) for the six single muon triggers monitored during the 2011 physics data taking are shown in Figure 5.9. From data taking period B to I the `L1_MU10` seeded triggers `EF_mu18`, `EF_mu18_MG` and `EF_mu40_MSonly_barrel` were monitored. The total efficiencies for the `mu18` triggers are very similar at the level of $\sim 78\,\%$ for muon with transverse momenta greater than 18 GeV. A slightly higher efficiency is observed for the inside–out trigger `EF_mu18_MG`. The efficiency for the MS standalone trigger `EF_mu40_MSonly_barrel` operational in the barrel region is at about 70 % for muons in the barrel part with transverse momenta greater than 40 GeV. For the data taking periods J to M the muon triggers

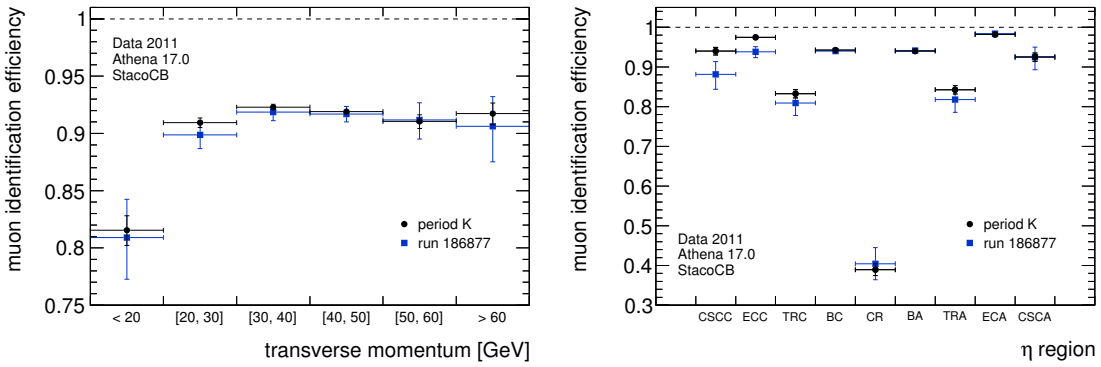


(a) (b)

**Figure 5.8:** Muon identification efficiency for the Staco combined algorithm as functions of $p_{\mathrm{T}}$ (a) and $\eta$ (b) shown for the reference data taking period K and for the run 186877 where part of the muon system in end–cap C was not operational for a certain fraction of the run.

`EF_mu18_medium`, `EF_mu18_MG_medium` and `EF_mu40_MSonly_barrel_medium` seeded by `L1_MU11` were monitored. Their total efficiencies are approximately $5 - 8\,\%$ lower than their `L1_MU10` seeded pendant.

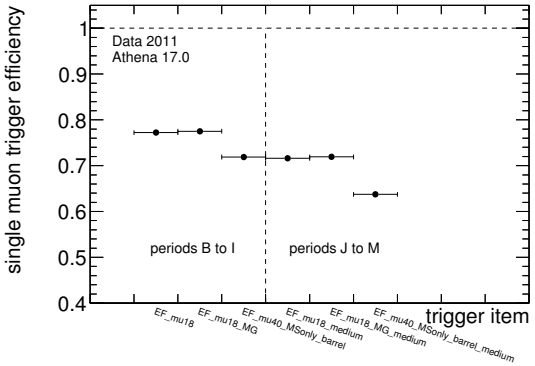


**Figure 5.9:** Overall trigger efficiencies for the three single muon triggers monitored in the 2011 physics data taking periods B to I and J to M, respectively.

The overall trigger efficiencies in Figure 5.9 are shown in Figure 5.10 broken down in bins of $p_{\mathrm{T}}$, $\eta$ and $\phi$, respectively. It can be seen that the trigger efficiencies are lowest in the central detector region and in the $\phi$–sectors corresponding to the detector feet region due to the limited coverage of muon trigger chambers in these particular regions. Furthermore, it can be seen that the trigger efficiencies are constant for muon transverse momenta above the trigger thresholds.

Similar as for the muon identification efficiencies, the stability of the trigger efficiencies can

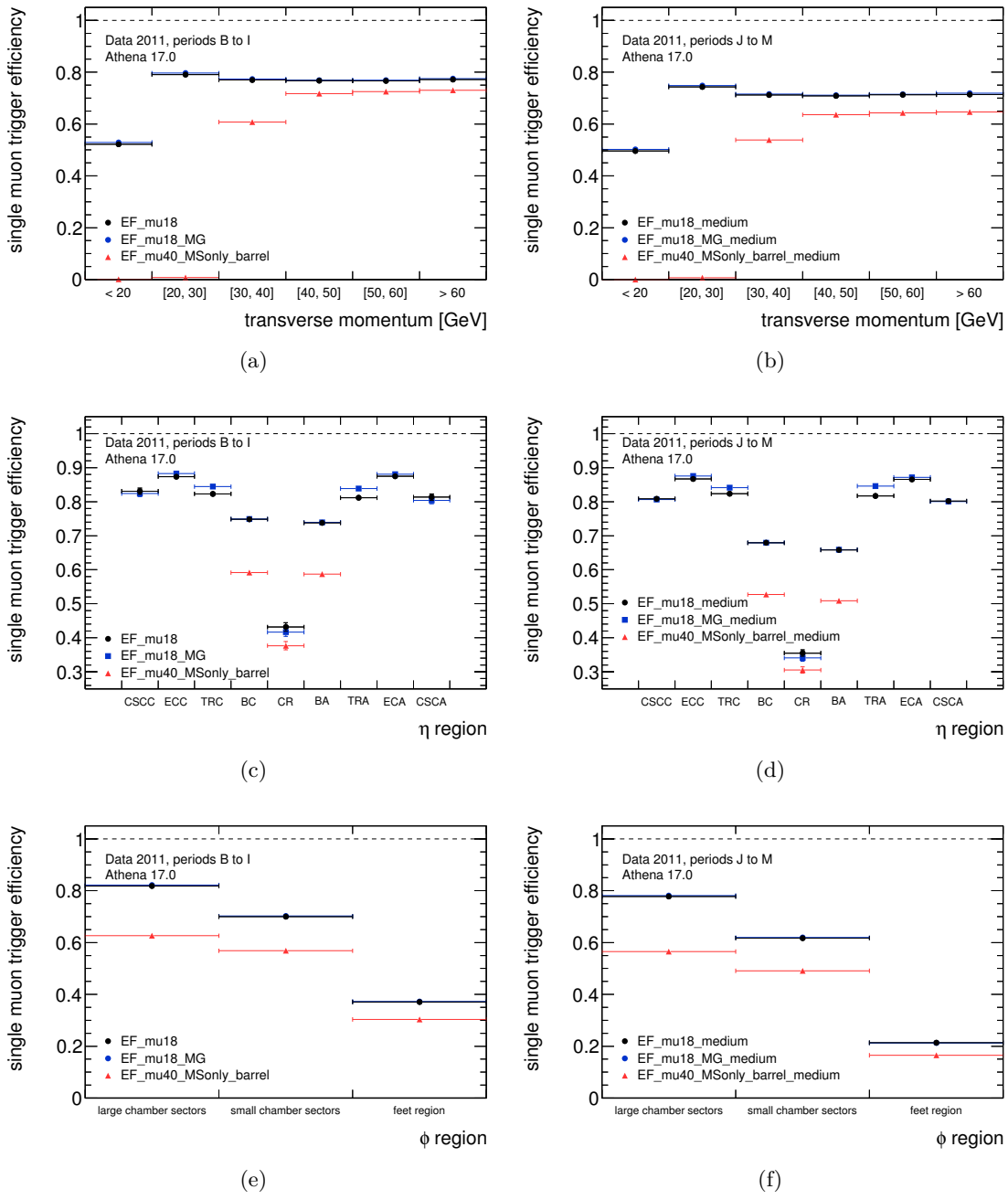


**Figure 5.10:** Single muon trigger efficiencies for the triggers `EF_mu18`, `EF_mu18_MG` and `EF_mu40_MSonly_barrel` (a, c, e) monitored in the 2011 data taking periods B to I and the triggers `EF_mu18_medium`, `EF_mu18_MG_medium` and `EF_mu40_MSonly_barrel_medium` (b, d, f) monitored in the periods J to M shown in bins of $p_{\mathrm{T}}$ (a, b), $\eta$ (c, d) and $\phi$ (e, f).

be tested over the data taking periods. Figure 5.11 shows the `EF_mu18` and `EF_mu18_medium` efficiencies for the corresponding data taking periods. The increase of the trigger efficiency with the beginning of period H is due to an update of the L1 muon trigger firmware (see Appendix A) with fixed misconfiguration of the trigger system on side A of the detector. The decrease in efficiency as of period J is due to the change in the muon trigger menu from `L1_MU10` seeded muon triggers to the `L1_MU11` seeded medium triggers as mentioned above. The trigger efficiencies in the single data taking periods are well compatible with the 95 % confidence level band around the average values in the period ranges B to G, H to I and J to M. The only exception is the significant drop of the `EF_mu18_medium` efficiency in period L which hints at a muon trigger problem in this period. The problem is traced to originate from a wrong RPC timing configuration of the `L1_MU11` trigger in the sub–periods L3 and L4 (see Appendix A) due to a faulty version of the read–out latencies and input pipeline delay. This problem cannot be recovered in a later data reprocessing campaign. Therefore, data analyses which use `L1_MU11`–seeded triggers need to account for the reduced trigger efficiency in the affected sub–periods when comparing the data to simulations.

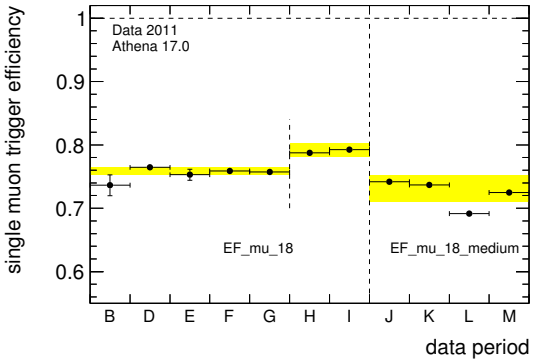


**Figure 5.11:** Stability of the muon trigger efficiencies for the single muon triggers `EF_mu18` for the 2011 data taking periods B to I and `EF_mu18_medium` for the data taking periods J to M. The dashed line between periods G and H indicates the efficiency gain due to a L1 muon trigger firmware update. The dashed line between periods I and J indicates the change in the muon trigger menu. The yellow bands represent the 95 % confidence level bands around the average value for the trigger efficiencies for the data taking periods B to G, I to J and J to M. The efficiency drop in period L is due to a wrong RPC trigger chamber timing configuration in the sub–periods L3 and L4.

# Chapter 6

# Search for neutral MSSM Higgs Bosons in $\mu^+\mu^-$ Decays

This chapter presents the search for neutral MSSM Higgs bosons decaying to two muons with the ATLAS detector at the LHC. The analysis is performed using $4.8\,\mathrm{fb}^{-1}$ of proton–proton collision data at a centre–of–mass energy of $\sqrt{s} = 7\,\mathrm{TeV}$ recorded in 2011. It is part of the ATLAS publication on the search for neutral MSSM Higgs bosons at $\sqrt{s} = 7\,\mathrm{TeV}$ [132]. The search for $h/A/H \to \mu^+\mu^-$ decays is motivated in Section 6.1 and the analysis strategy is outlined in Section 6.2. The signal signature and the relevant background processes are discussed in Section 6.3 followed by a description of the recorded data sample and of the Monte Carlo simulated event samples in Section 6.4. In Section 6.5 the reconstruction of the physics objects relevant for the analysis is described, followed by the description of the event selection criteria in Section 6.6. Depending on the number of reconstructed $b$ jets the events are divided into categories which have different signal and background contributions discussed in Section 6.7. The statistical procedure for the interpretation of the results is introduced in Section 6.8. The $\mu^+\mu^-$ background is estimated from the data by means of sideband fits to the $\mu^+\mu^-$ invariant mass distribution. In Sections 6.9 and 6.10 the signal and background parametrisations used for the statistical evaluation of the selected data are described. The systematic uncertainties are discussed in Section 6.11. Exclusion limits and local $p_0$–values in the framework of the MSSM are derived in Section 6.12. The combination of the search in the $\mu^+\mu^-$ final state with searches for $h/A/H \to \tau^+\tau^-$ decays [132] is presented in Section 6.13.

## 6.1 Motivation

One major goal of the LHC experiments is the understanding of the mechanism describing electroweak symmetry breaking. A Higgs–like particle has been discovered in 2012 by the ATLAS and CMS experiments. The properties of this particle are consistent with the Standard Model Higgs boson but also with one of the CP–even neutral MSSM Higgs bosons in certain model scenarios. In the MSSM case, the Higgs sector comprises five physical Higgs bosons of which three are neutral ($h$, $A$ and $H$) and two have positive and negative electric charges ($H^\pm$), as introduced in Section 2.2.4. Hints for more than one Higgs boson would be clear evidence for physics beyond the Standard Model. Searches for MSSM Higgs bosons have been performed previously at LEP [96], the Tevatron [133] and recently by ATLAS [132] and CMS [134, 135].

The production of the neutral MSSM Higgs bosons proceeds mainly through the gluon fusion process, $gg \to h/A/H$, and through the associated production with $b$ quarks, $pp \to b(b)h/A/H$, which becomes dominant for large values of $\tan\beta$. In contrast to the Standard Model Higgs boson, the decays to gauge boson pairs do not exist for the CP–odd Higgs boson, $A$, and are suppressed for the CP–even Higgs bosons, $h$ and $H$, (see Table 3.1). On the other hand, the branching fractions for decays to heavy down–type fermions are enhanced, particularly for large values of $\tan\beta$. This favours the decay modes to $b\bar{b}$ and $\tau^+\tau^-$. The former is very difficult to distinguish from the large background of $b\bar{b}$ production at the LHC. The $h/A/H \to \tau^+\tau^-$ decay with a branching fraction of about 10 % can be efficiently selected with high background discrimination such that this channel provides the highest sensitivity in the search for neutral MSSM Higgs bosons at the LHC. Due to the neutrinos in the $\tau$ decays the mass resolution in this channel, however, is rather low, at about $13 - 20$ % [136].

Compared to the $b\bar{b}$ and $\tau^+\tau^-$ decay modes, the direct decay $h/A/H \to \mu^+\mu^-$ has a substantially lower branching fraction of only about $4 \cdot 10^{-4}$ (see Figure 3.8). On the other hand, $\mu^+\mu^-$ events are very clean and can be selected with high efficiency and purity. Due to the absence of neutrinos and the precise muon momentum resolution, the $h/A/H \to \mu^+\mu^-$ decay channel offers the by far highest Higgs boson mass resolution among all MSSM search channels.

## 6.2 Analysis Strategy

Neutral MSSM $h/A/H \to \mu^+\mu^-$ decays are searched for in events with two oppositely charged muons with high transverse momenta which are isolated from additional activity in the detector. Background events arise mainly from $Z/\gamma^*$, $t\bar{t}$ and $W^+W^-$ production. The $Z/\gamma^*$ boson decays to two muons provide the dominant background contribution. The MSSM Higgs boson signal is searched for in the $\mu^+\mu^-$ invariant mass distribution above

the $Z$ boson mass peak. Due to the high experimental $\mu^+\mu^-$ mass resolution, the $h$, $A$ and $H$ signal contributions appear as narrow resonances on top of the continuously falling background.

Large part of the dominant $Z/\gamma^*$ background can be efficiently suppressed by requiring at least one reconstructed $b$ jet in the selected $\mu^+\mu^-$ events. This requirement, however, selects only signal events produced in association with $b$ quarks and rejects the part of the Higgs boson signal produced via gluon fusion. In addition, a fraction of signal events produced in association with $b$ quarks are lost due to limited $b$ jet identification efficiency. To recover the rejected signal events, the analysis is performed in two complementary event categories, with and without at least one reconstructed $b$ jet, having different signal–to–background ratios.

The $h/A/H \to \mu^+\mu^-$ search is performed in the MSSM $m_h^{\text{max}}$ benchmark scenario scanning the $m_A$–$\tan\beta$ plane in the ranges $120\,\text{GeV} \leq m_A \leq 300\,\text{GeV}$ and $5 \leq \tan\beta \leq 70$.

The shape and normalisation of the signal and total background invariant mass distributions are modelled with parametrised functions defined in the mass range of 110 GeV to 250 GeV (350 GeV) in the event category with (without) $b$ jets. The modelling of the signal mass distribution allows for interpolation of the signal predictions between few discrete points in the $m_A$–$\tan\beta$ parameter plane for which a full event simulation is used. To reduce the impact of systematic uncertainties on the sensitivity of the search, the background contribution in a given signal mass window is estimated from the data by means of sideband fits to the $\mu^+\mu^-$ invariant mass distribution. Monte Carlo predictions for the individual background contributions are only used for cross checks and do not enter the final results.

Systematic uncertainties taken into account arise from the uncertainty in the background estimation from data and from systematic uncertainties in the expected signal yield after the event selection. The latter is due to uncertainties in the prediction of the cross sections, in the description of the detector response and in the signal modelling procedure.

The results of this search are expressed in terms of observed and expected signal significances and exclusion limits. The compatibility of the measured invariant mass distribution with the signal and background model distributions normalised to the expected signal and background yields after the event selection is evaluated in terms of statistical hypothesis tests. The results are obtained by comparing the measured signal rate relative to the expectation depending on $m_A$ and $\tan\beta$.

The expected $3\,\sigma$–evidence and $5\,\sigma$–discovery contours for the MSSM $h/A/H \to \mu^+\mu^-$ signal predicted in the $m_h^{\text{max}}$ scenario are evaluated. In addition, the expected signal significances determined for each point in the scanned $m_A$–$\tan\beta$ parameter plane are compared to the observed values.

Exclusion limits are evaluated as a function of $m_A$ and $\tan\beta$ for the MSSM $m_h^{\text{max}}$ scenario with positive Higgs mixing parameter and, less model–dependent, on the cross section times branching fraction as a function of the mass, $m_\phi$, of a generic Higgs boson, $\phi$, for

the two MSSM Higgs boson production modes. The sign of the Higgs mixing parameter is in general not constrained, but a positive mixing parameter is favoured by measurements of the anomalous magnetic moment of the muon [137].

If not stated otherwise, all simulated signal distributions shown in the following are based on the predictions of the MSSM $m_h^{\text{max}}$ scenario for the $A$ boson with $m_A = 150\,\text{GeV}$ and $\tan\beta = 40$ and for the combination of the gluon fusion and $b$–quark associated production modes.

## 6.3 Signal and Background Processes

Independently of the Higgs boson production mode, the signature of the $h/A/H \to \mu^+\mu^-$ decay is a pair of isolated muons with high transverse momenta and opposite electric charges. In the gluon fusion production mode, no additional particles are present in the final state except for the underlying event. In the associated production one or two $b$ quarks with relatively low transverse momenta are present in addition. The reconstructed $b$ jets tag the $pp \to b(b)h/A/H$ production process allowing for strong background suppression. The tree–level Feynman diagrams for gluon fusion production and associated production with the subsequent decay $h/A/H \to \mu^+\mu^-$ are shown in Figure 6.1. Since the complete final state can be reconstructed, the missing transverse momentum, $E_{\text{T}}^{\text{miss}}$, in the signal events is small and related to the resolution of the $E_{\text{T}}^{\text{miss}}$ measurement [138].

There are several Standard Model background processes with signatures similar to the signal. The dominant background source is $Z/\gamma^*$ boson production either via the Drell–Yan process or in association with jets. The $Z/\gamma^*$ boson decays to muon pairs provide a largely irreducible background for the inclusive $h/A/H \to \mu^+\mu^-$ signal. Apart from the direct $Z/\gamma^* \to \mu^+\mu^-$ decays, the $Z/\gamma^*$ boson decays to $\tau$ lepton pairs with subsequent $\tau$ decays to muons and neutrinos contribute to the background, although the branching fraction for the decay of both $\tau$ leptons to muons is small. In addition, the presence of the neutrinos shifts the reconstructed $\mu^+\mu^-$ invariant mass to lower values which further reduces the contribution of this background in the mass range relevant for the $h/A/H \to \mu^+\mu^-$ search.

In addition to the $Z/\gamma^*$ boson background, the production of top, bottom and charm quark pair ($t\bar{t}$, $b\bar{b}$, $c\bar{c}$), $W$ boson pairs ($W^+W^-$), as well as $W$ bosons in association with jets and single top quarks have to be taken into account. The contribution of these processes becomes relevant once the $Z/\gamma^*$ background contribution is sufficiently suppressed. The tree–level Feynman diagrams for the dominant background processes are shown in Figure 6.2.

The production cross sections times branching fractions for decays to muon pairs for the background processes in proton–proton collisions at $\sqrt{s} = 7\,\text{TeV}$ are shown in Table 6.1 in comparison with the signal production cross sections for the benchmark parameters $m_A = 150\,\text{GeV}$ and $\tan\beta = 40$.

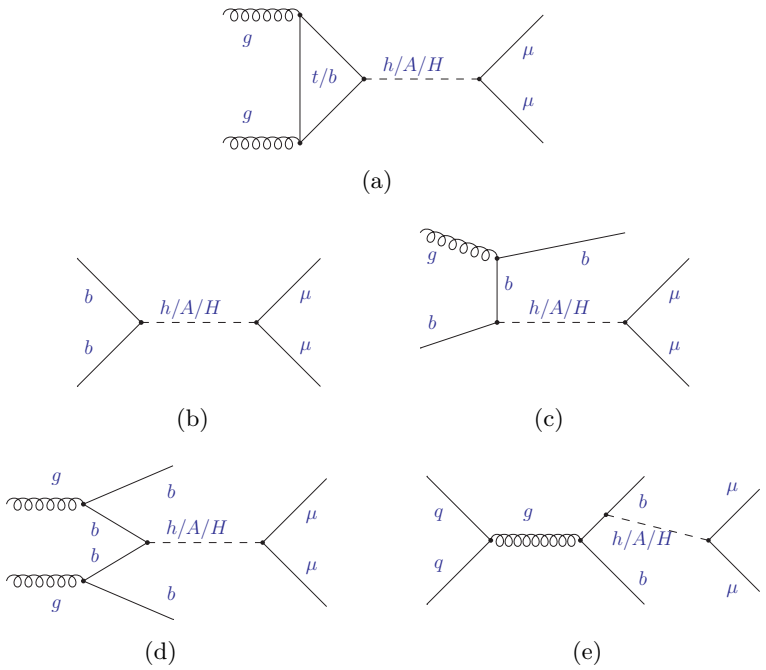


**Figure 6.1:** Tree–level Feynman diagrams for the dominant production modes of neutral MSSM Higgs bosons in proton–proton collisions at the LHC with subsequent decays to two muons: gluon fusion (a) and associated production with 0 (b), 1 (c) and 2 $b$ quarks (d, e) in the final state. Higher order processes introduce further $b$ quarks in the final state, in particular for $b$–quark annihilation (b). Particles and anti–particles are labelled the same, $q$ refers to all quark flavours.

## 6.4 Data and Monte Carlo Samples

The data sample used for the analysis consists of proton–proton collisions at a centre–of–mass energy of $\sqrt{s} = 7\,\text{TeV}$ delivered by the LHC. The data was recorded by the ATLAS detector between March and October 2011 and corresponds to an integrated luminosity of $4.8\,\text{fb}^{-1}$. Only events passing at least one of the muon high level triggers are considered for the analysis and only those events are analyzed for which all relevant components of the ATLAS detector were fully operational (see Appendix A). The list of good data runs requires in particular operational magnet system, muon detectors and muon reconstruction, inner detector tracking, vertex reconstruction, jet reconstruction, $b$–tagging and the reconstruction of the missing transverse momentum. For part of the 2011 data taking a part of the liquid Argon calorimeter was not operational because of a failure of the front–end electronics (see Appendix A). Events with energy deposits expected in this region are rejected in both data and simulation. For the latter the correct fraction of integrated luminosity corresponding to the affected data is taken into account.

To describe the expected signal and background processes discussed in Section 6.3, Monte

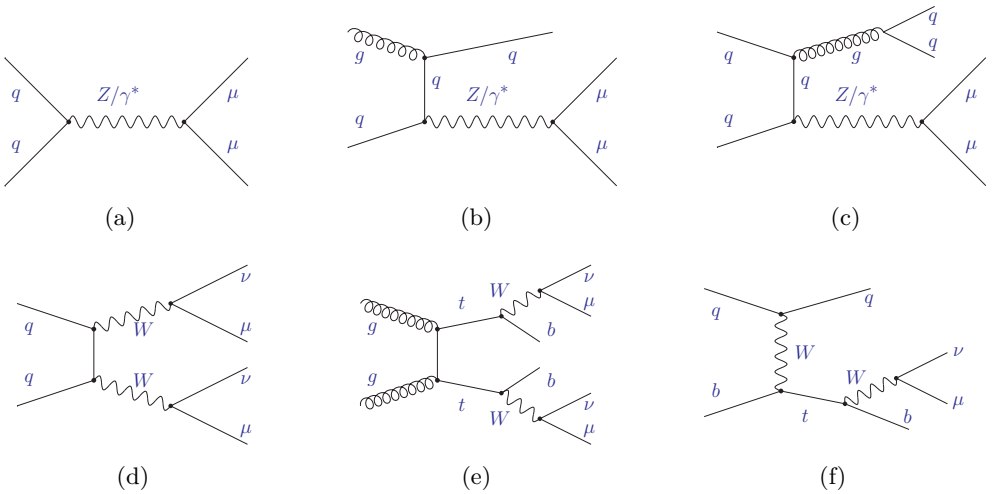


**Figure 6.2:** Tree–level Feynman diagrams for the dominant background processes in the search for the $h/A/H \to \mu^+\mu^-$ decay: Drell–Yan $Z/\gamma^*$ boson production (a), $Z/\gamma^*$ boson production in association with jets (b, c), $W^+W^-$ production (d), $t\bar{t}$ production (e) and single top quark production in the $t$–channel (f). Particles and anti–particles are labelled the same, $q$ refers to all quark flavours.

Carlo event samples with a dedicated simulation of the ATLAS detector response are used. The list of the Monte Carlo samples are given in Appendix B. Simulated background processes serve only for comparison with the data and as a cross–check of the background estimation from data and are not affecting the final analysis results.

**Signal Event Generation** The two neutral MSSM Higgs boson production modes were generated separately with subsequent direct decays to muon pairs. The cross sections, couplings, branching fractions and masses of the Higgs bosons are calculated for the $m_h^{\text{max}}$ scenario of the MSSM as described in Section 3.3. The gluon fusion samples were generated with the POWHEG event generator [139–141] interfaced with the PYTHIA programme [142] for the description of the underlying event. The signal samples for associated production with $b$ quarks were generated with the SHERPA event generator [143]. The signal samples contain only the CP–odd MSSM Higgs boson, $A$. The mass distributions of the corresponding $h$ and $H$ bosons are modelled from the $A$ boson samples as described in Section 6.9. For each production mode, seven samples were generated, for $\tan\beta = 40$ and for CP–odd Higgs boson masses in 20 GeV to 50 GeV steps in the range of $m_A = 110\,\text{GeV}$ to 300 GeV. For the modelling of the $\tan\beta$ dependence of the width of the $\mu^+\mu^-$ resonance, additional samples were generated for $m_A = 150\,\text{GeV}$ and 250 GeV with $\tan\beta = 20$, 40 and 60.

**Table 6.1:** Cross sections times branching fractions to $\mu^+\mu^-$ for the signal and background processes. NNLO calculations have been used for the signal and for $W$, $Z/\gamma^*$ and $W^+W^-$ production, NLO+NNLL for $t\bar{t}$ and LO for $b\bar{b}$ production. Signal cross sections are given separately for the $h$, $A$ and $H$ boson production. The cross sections for the signal processes are given in fb, the cross sections for the background processes in pb.

| Process | Cross Section × BR |
|---|---|
| Signal ($m_A = 150\,\text{GeV}$, $\tan\beta = 40$) | |
| $gg \to h/A/H$: $h/A/H \to \mu^+\mu^-$ | 4.7/22.5/21.8 |
| $pp \to b(b)h/A/H$: $h/A/H \to \mu^+\mu^-$ | 1.7/49.1/47.8 |
| Background | |
| $Z/\gamma^* \to \mu^+\mu^-$+ jets (10 GeV $< M_{\ell\ell} <$ 40 GeV) | 3990 |
| $Z/\gamma^* \to \mu^+\mu^-$+ jets ($M_{\ell\ell} >$ 40 GeV) | 1072 |
| $Z/\gamma^* \to \mu^+\mu^-$+ $b$ jets ($m_{\mu\mu} >$ 30 GeV) | 12.89 |
| $t\bar{t}$ | 164.6 |
| single top ($t$, $s$, $Wt$ channles) $\to \mu$ | 20.91/1.50/15.74 |
| $b\bar{b}/c\bar{c} \to \mu + \mu + X$ ($p_{\text{T}}^{\mu} >$ 10 GeV) | 8540 |
| $W^{\pm} \to \mu^{\pm}\nu$+ jets | 10483 |
| $W^+W^- \to \mu^+\nu\mu^-\nu$ | 4.554 |

**Background Event Generation** Events from $W$ and $Z/\gamma^*$ boson production in association with jets and Drell–Yan $Z/\gamma^*$ boson production were generated with the ALPGEN event generator [144]. Additional samples for the $Z/\gamma^*$ production in association with $b$ quarks are used to simulate the irreducible background for the $pp \to b(b)h/A/H$ signal contribution with high statistics. PYTHIA was used in addition for the generation of inclusive $Z/\gamma^*$ events to study the systematic effects of different parton distribution functions (see Appendix B). The $t\bar{t}$ and $W^+W^-$ production processes were generated with the next–to–leading order generator MC@NLO [145, 146] while the PythiaB interface [147, 148] was used for the production of the $b\bar{b}/c\bar{c}$ samples. Single top quark production in the $s$– and $t$–channels and in association with $W$ bosons were modelled with the AcerMC event generator [149]. For the inclusive $Z/\gamma^*$ production sample, the hadronisation process and the underlying event description were simulated with PYTHIA [150, 151]. For all other samples, the hadronisation process was simulated with the HERWIG generator [152] and the underlying event description was performed with the JIMMY package [153].

**Detector Simulation and Reconstruction** For the simulation of the response of the ATLAS detector to the generated particles, the Monte Carlo events are passed through the detailed GEANT4 detector simulation [154–156]. The only exception are the signal samples for the $\tan\beta$ modelling of the signal resonance width which are simulated with the faster, computationally less demanding ATLFAST–II simulation package [157] employing a parametrisation of the detector response. Good agreement of the detailed and fast

simulation has been demonstrated elsewhere [158]. The simulation is followed by the same event reconstruction applied to the data [159].

All simulated events are produced with the hard process overlaid with in–time and out–of–time pileup expected for the 50 ns LHC proton bunch train spacing in 2011 (see Section 4.3). To account for remaining differences between the expected amount of pileup and the one observed in data, the simulated events are reweighted according to the average numbers of interactions per bunch crossing as a function of the data taking periods.

The numbers of events in the Monte Carlo samples are scaled to the recorded integrated luminosity of $4.8\,\text{fb}^{-1}$. The actual sizes of the different simulated samples correspond to integrated luminosities which are typically larger than for the data (see Appendix B).

## 6.5 Identification of Physics Objects

For the selection of neutral MSSM Higgs boson candidate events, different physics objects are employed like muons, $b$ jets and missing transverse momentum. The reconstruction of muons has been discussed in Section 5.1 and only the selection cuts applied on the reconstructed muons are described in this section. For the remaining physics objects, a brief description of their reconstruction is given in addition to the applied selection criteria.

### 6.5.1 Trigger

Events considered in the analysis are required to pass a high–$p_{\text{T}}$ single muon trigger. To obtain the largest possible signal data sample, the least stringent unprescaled single muon triggers with transverse momentum thresholds of 18 GeV are employed (see Section 5.2.2). For the analysis, `EF_mu18` and `EF_mu18_medium` triggers are required for data recorded in periods B to I and J to M (see Appendix A), respectively. They are also emulated in the simulated Monte Carlo samples and are corrected for the trigger efficiencies measured in the data as discussed in Section 6.11.

### 6.5.2 Muon Identification

Muon tracks are reconstructed with the Staco package described in Section 5.1. Segment–tagged muons from the MuTag algorithm are used in addition to the combined muons from the StacoCB algorithm to cover the muon spectrometer transition region and obtain a uniform efficiency over the full pseudorapidity range (see Section 5.2.2). To reduce the number of fake muons found by the MuTag algorithm, only tight segment–tagged muons are accepted. These require at least two track segments in the barrel and one in the transition and end–cap regions of the muon spectrometer. Since the inner detector information is necessary for both combined and segment–tagged muons, the pseudorapidity range of the selected muons is limited to the inner detector coverage of $|\eta| < 2.5$. The associated inner

detector track has to fulfill the track quality requirements described in Section 5.2.2. The muons passing the above criteria are required to have transverse momenta $p_{\mathrm{T}} > 15\,\mathrm{GeV}$.

In addition, the muons are required to originate from the primary vertex by applying cuts on the longitudinal and transverse impact parameters. The primary vertex is defined as the vertex with the largest quadratic sum, $\sum p_{\mathrm{T}}^2$, of the transverse momenta of the associated tracks. The longitudinal impact parameter, $z_0$, is required to be smaller than 10 mm and the transverse impact parameter significance, $d_0/\sigma_{d_0}$, defined as the transverse impact parameter, $d_0$ divided by the uncertainty of the $d_0$ measurement, $\sigma_{d_0}$, is required to be smaller than 10.

The selected muons are required to be isolated using the track–based isolation criteria. The scalar sum, $p_{\mathrm{T}}^{\text{cone }0.2}$, of the transverse momenta of all tracks originating from the same vertex as the muon and located within a cone with radius parameter $\Delta R = 0.2$ around the muon must be smaller than 10 % of the muon transverse momentum, $p_{\mathrm{T}}^{\mu}$. Only tracks with $p_{\mathrm{T}} > 1\,\mathrm{GeV}$ are considered here and the scalar sum is calculated excluding the transverse momentum of the muon itself. The distribution of the isolation variable for the muons with the highest and with the next–to–highest transverse momenta passing the $\mu^+\mu^-$ selection (see Section 6.6) are shown in Figure 6.3. The isolation criteria serve mainly for the rejection of the top quark and multijet backgrounds.

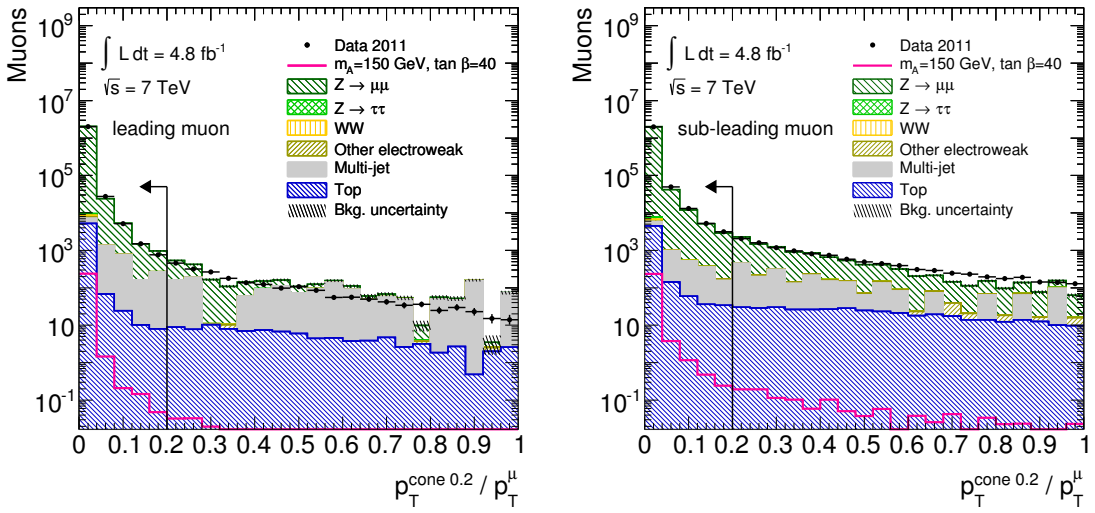


(a) (b)

**Figure 6.3:** Distributions of the track–based isolation variable, $p_{\mathrm{T}}^{\text{cone }0.2}/p_{\mathrm{T}}^{\mu}$, (see text) for leading (a) and sub–leading (b) muons for the data and Monte Carlo predictions for the signal ($m_A = 150\,\mathrm{GeV}$ and $\tan\beta = 40$) and backgrounds after the $\mu^+\mu^-$ selection (see Section 6.6).

### 6.5.3 Jet Reconstruction and *b*–Jet Tagging

Jets originating from the hadronisation of quarks and gluons are reconstructed with the anti–$k_T$ algorithm [160] with radius parameter $R = 0.4$ seeded by topological energy clusters [161] in the calorimeter.

Topological clusters are three–dimensional assemblies of energy deposits in calorimeter cells connected with each other. They are built from seed cells with high energy deposits above a certain threshold of the signal–to–noise ratio. Neighboring cells are added if they have energy deposits above a lower signal–to–noise threshold. The sum of the energy deposits of all associated cells gives the total cluster energy, $E$. According to the geometric region in the detector in which the cluster is reconstructed, a four–momentum vector with components $p_{\mathrm{T}}$, $\eta$, $\phi$ and $E$ is assigned to each cluster.

The anti–$k_T$ algorithm is a sequential recombination algorithm. For the reconstruction of jets it starts from the calorimeter clusters and assigns two "distance" parameters, $d_{ij}$ and $d_{iB}$, to each of them. The distance parameter $d_{ij}$ between two clusters is defined as

$$d_{ij} = \frac{1}{\max\left(p_{Ti}^2, p_{Tj}^2\right)} \frac{\Delta R_{ij}^2}{R^2}, \tag{6.1}$$

with the transverse momenta, $p_{Ti(j)}$, of the clusters $i$ ($j$), their angular distance, $R_{ij}$, and the radius parameter, $R$. The distance parameter $d_{iB}$ for an individual cluster is defined as

$$d_{iB} = \frac{1}{p_{Ti}^2}. \tag{6.2}$$

The minimum of all $d_{ij}$ and $d_{iB}$ is determined. In case the minimum is one of the distance parameters, $d_{ij}$, the two corresponding clusters are combined to one. If the minimum is one of the parameters, $d_{iB}$, the cluster $i$ is defined to be a jet and removed from the list of clusters. These jet finding steps are repeated with the updated list of clusters until all clusters are combined to jets.

The jet energy [162] is measured at the electromagnetic scale and corrected for the average additional energy due to pileup events obtained from minimum bias data. In addition, the direction of the jets measured in the calorimeter is corrected such that they originate from the primary vertex. Corrections for the hadronically interacting part of the jets are determined by simulations. The systematic uncertainty in the jet energy scale is obtained from experimental data. This employs measurements of the response to single charged pions in a test beam and measurements with proton–proton collision data using as constraints the transverse momenta of photons or of the sum of the transverse momenta of several low–$p_{\mathrm{T}}$ jets recoiling against a high–$p_{\mathrm{T}}$ jet. Jets considered in this analysis are required to have transverse energies $E_{\mathrm{T}} > 20\,\mathrm{GeV}$ and pseudorapidities $|\eta| < 4.5$.

Jets not originating from proton–proton collisions are rejected by quality requirements

on the energy deposits and the shape and timing of the electronic pulses of the calorimeter cells [162, 163]. So–called background jets can arise from the collisions of beam protons with residual gas in the beam pipe or from interactions of beam halo protons with beam collimators placed close to the ATLAS detector. In addition, background jets can be induced by cosmic ray muons which produce a shower in the calorimeter or by high calorimeter noise such as noise bursts in single cells or coherent noise in neighboring cells of the calorimeter.

In order to suppress jets from pileup events, the scalar sum of the transverse momenta of tracks associated to the jet and pointing back to the primary vertex has to be at least 75 % of the jet transverse momentum measured in the calorimeter.

***b*–Jet Tagging** To identify $b$ jets, i.e. the jets originating from the hadronisation of $b$ quarks, a multivariate method is used, the so–called MV1 $b$–tagging algorithm [164]. It combines measurements of displaced secondary vertices and three–dimensional impact parameters using a neural network [165]. The MV1 algorithm aims to identify $b$– and $c$–hadron decays inside the jet, assigning a weight to each reconstructed jet according to the probability that it is a $b$ jet. Jets with MV1–weight greater than 0.601713 are considered as $b$ jets in this analysis. This requirement corresponds to 70 % $b$–tagging efficiency in $t\bar{t}$ events with a purity of 91 % and light, $c$– and $\tau$–jet rejection factors of 134, 5 and 13, respectively. A $\tau$ jet is composed from the visible decay products of a hadronically decaying $\tau$ lepton. Light jets all jets initiated from the hadronisation of gluons or light $u$, $d$ and $s$ quarks.

The selected $b$ jets are required to have transverse momenta greater than 20 GeV and pseudorapidities $|\eta| < 2.5$.

### 6.5.4 Missing Transverse Momentum

The missing transverse momentum, $E_{\mathrm{T}}^{\mathrm{miss}}$, is defined as the negative sum of the transverse momenta of all visible particles in an event. The magnitude and direction of the missing transverse momentum are determined from the energy deposits in the calorimeter cells within a pseudorapidity range of $|\eta| < 4.9$ and from muon momenta in the pseudorapidity range of $|\eta| < 2.7$ [119]. The energy deposits in the calorimeter cells are calibrated according to the physics objects, i.e. electrons, photons, hadronic $\tau$ lepton decays and jets, to which they are associated, providing a high accuracy of the $E_{\mathrm{T}}^{\mathrm{miss}}$ reconstruction [138].

The muon contribution to the missing transverse momentum is determined using combined and segment–tagged muons for pseudorapidities $|\eta| < 2.5$ and standalone muons for $2.5 < |\eta| < 2.7$. The contributions from isolated and non–isolated muons are treated separately. The energy deposits in the calorimeter cells crossed by muon tracks are subtracted in order to avoid double counting of the muon energy loss.

Calorimeter cells which are not associated to a physics object are included in the $E_{\mathrm{T}}^{\mathrm{miss}}$ reconstruction individually as the so–called soft $E_{\mathrm{T}}^{\mathrm{miss}}$ contribution.

## 6.6 Event Selection

This section describes the selection of events with a topology characteristic for the $h/A/H \to \mu^+\mu^-$ signal discussed in Section 6.3. In addition to the general data quality criteria described in Section 6.4, an event is rejected if it contains a jet reconstructed in a noisy region of the calorimeter or a jet originating from non–collision background as discussed in Section 6.5.3. This is required in order to avoid deterioration of the missing transverse momentum measurement due to background jets. To select collision events, the reconstructed primary vertex in each collision candidate event is required to be compatible with the beamspot position and to have at least 3 associated tracks. After the selection, the events are divided into two categories without and with at least one reconstructed $b$ jet. The categorisation is motivated by the different event topologies for the two signal production modes leading to different signal–to–background ratios.

The selection requires that the event is triggered by the single muon trigger explained in Section 6.5.1. At least one reconstructed muon passing the selection in Section 6.5.2 is required to match the $\eta$–$\phi$ region of interest of the triggered object. To be safely in the plateau region of the `mu18` trigger efficiency as a function of $p_{\mathrm{T}}$ (see Figure 5.10), the transverse momentum of the matched muon has to be greater than 20 GeV. At least one additional muon with opposite electric charge and $p_{\mathrm{T}} > 15\,\mathrm{GeV}$ is required. The distributions of the transverse momenta for the leading and sub–leading muon after the $\mu^+\mu^-$ selection described in the following are shown in Figure 6.4 for simulated signal and background events. The applied $p_{\mathrm{T}}$ cuts are chosen relatively low compared to an average muon $p_{\mathrm{T}}$ in each signal sample in order to avoid strong dependence of the signal acceptance on the signal mass. The remaining dependence of the signal selection efficiency on the Higgs boson mass is discussed in Appendix B. Its effect on the signal modelling is addressed in Section 6.9.

Two muons with highest transverse momenta and opposite charges are combined to a $\mu^+\mu^-$ pair. Events with more than two muons are not rejected because of semi–leptonic $B$ hadron decays in signal events produced in association with $b$ quarks. The $t\bar{t}$ production and the $Z/\gamma^*$ boson production in association with $b$ quarks are simulated for $\mu^+\mu^-$ invariant masses greater than 60 GeV and 40 GeV, respectively. Therefore, invariant masses $m_{\mu\mu} > 70\,\mathrm{GeV}$ are required completing the $\mu^+\mu^-$ selection.

Finally, a missing transverse momentum cut of $E_{\mathrm{T}}^{\mathrm{miss}} < 40\,\mathrm{GeV}$ is applied. Since the signal as well as the $Z/\gamma^* \to \mu^+\mu^-$ background tend to have small missing transverse momentum, this cut rejects mainly the $t\bar{t}$ and $W^+W^-$ background. The $E_{\mathrm{T}}^{\mathrm{miss}}$ distribution after the $\mu^+\mu^-$ selection is shown in Figure 6.5 for the data and Monte Carlo signal and background

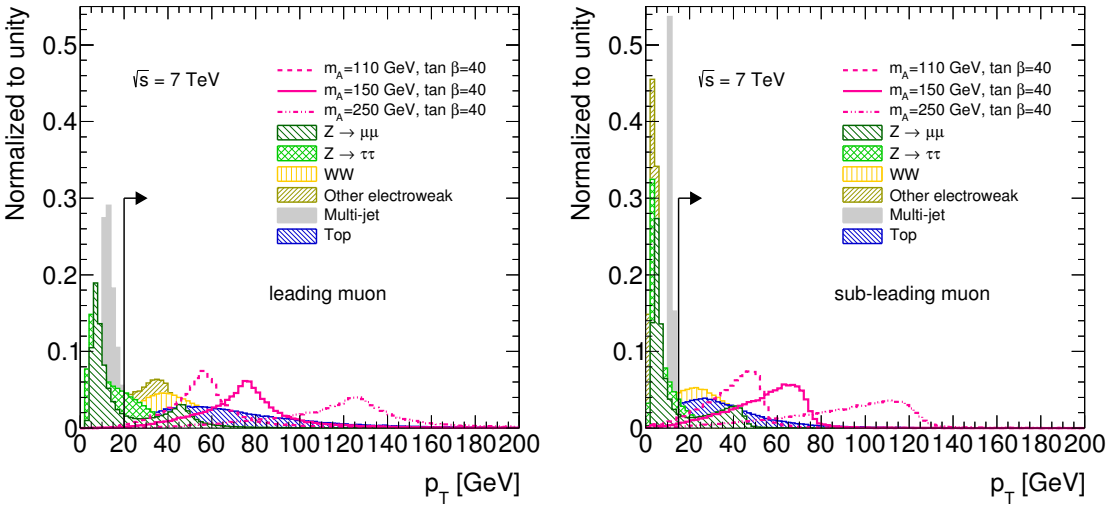


(a) (b)

**Figure 6.4:** Distributions of the transverse momenta of the leading (a) and sub–leading (b) muon in simulated events passing the $\mu^+\mu^-$ selection criteria without cuts on the muon transverse momenta for the relevant background processes and the sum of $pp \to b(b)A$ and $gg \to A$ signal processes expected for $\tan\beta = 40$ and $m_A = 110\,\text{GeV}$, $150\,\text{GeV}$ and $250\,\text{GeV}$. The $\mu^+\mu^-$ selection $p_\text{T}$ cuts are indicated. The enhancements in the $Z/\gamma^* \to \mu^+\mu^-$ and $Z/\gamma^* \to \tau^+\tau^-$ spectra at low $p_\text{T}$ arise from the $\gamma^*$ contribution in the $Z/\gamma^*$ processes.

contributions. The Monte Carlo $E_\text{T}^\text{miss}$ distribution is slightly shifted to higher values with respect to the data. The shift is within the systematic uncertainties in the missing transverse momentum measurement (see Section 6.11). The bin–by–bin significances of the deviations of the data from the expected background shown in Figure 6.5(b) and the following are evaluated using Equation 6.14 (see Section 6.8) where the $p_0$–value is the probability of observing at least $n_\text{D}$ data events while $n_\text{B}$ background events are expected from simulation. This probability is given by the tail integral of the Gamma–Poisson distribution [166], which takes into account the uncertainty, $\delta n_\text{B}$, on the expected number of background events.

The numbers of simulated events from the individual background processes passing each of the event selection criteria are shown in Table 6.2. The total number of background events compared to the number of expected simulated $A$ boson signal events and observed events in the data are shown in Table 6.3. At the stage of the $\mu^+\mu^-$ selection (i.e. before the cut on the $E_\text{T}^\text{miss}$) as well as after the event selection (i.e. after the cut on the $E_\text{T}^\text{miss}$) the agreement in the number of observed and simulated background events is better than 2 %.

**Table 6.2:** Numbers of simulated Monte Carlo background events passing each step of the event selection, normalised to an integrated luminosity of $4.8\,\mathrm{fb}^{-1}$. The selection criterion "MC weights" corresponds to the reweighting of events accounting for mismodelling of event generator and pileup predictions as well as the scaling factors which correct for mismodelling of the object reconstruction. The event selection criterion "DQ cuts" corresponds to the set of data taking quality cuts applied before the event selection (see text). The numbers in parentheses represent the statistical uncertainties in the last digit.

| Cut | $Z/\gamma^* \to \mu^+\mu^-$ ($m_{\mu\mu} > 40\,\mathrm{GeV}$ for $Z/\gamma^*$ + $b$ quarks) | $Z/\gamma^* \to \tau^+\tau^-$ | $W^+W^-$ | Other electroweak | Top ($m_{\mu\mu} > 60\,\mathrm{GeV}$ for $t\bar{t}$) | Multijet |
|---|---|---|---|---|---|---|
| No Cut | $2365[2]\cdot10^4$ | $2365[2]\cdot10^4$ | $3094[2]\cdot10^1$ | $10079[3]\cdot10^4$ | $2751[1]\cdot10^2$ | $4106[3]\cdot10^4$ |
| MC weights | $2440[2]\cdot10^4$ | $2440[2]\cdot10^4$ | $2189[2]\cdot10^1$ | $10078[3]\cdot10^4$ | $2419[1]\cdot10^2$ | $4105[3]\cdot10^4$ |
| DQ cuts | $2438[2]\cdot10^4$ | $2438[2]\cdot10^4$ | $2189[2]\cdot10^1$ | $9489[3]\cdot10^4$ | $2419[1]\cdot10^2$ | $4105[3]\cdot10^4$ |
| Vertex | $2437[2]\cdot10^4$ | $2437[2]\cdot10^4$ | $2183[2]\cdot10^1$ | $9486[3]\cdot10^4$ | $2397[1]\cdot10^2$ | $4093[3]\cdot10^4$ |
| Trigger | $3713[2]\cdot10^3$ | $2071[3]\cdot10^2$ | $744[1]\cdot10^1$ | $2153[1]\cdot10^4$ | $5439[7]\cdot10^1$ | $370[4]\cdot10^3$ |
| $\geq 2$ $\mu$ objects | $2233[1]\cdot10^3$ | $878[7]\cdot10^1$ | $1468[4]\cdot10^0$ | $33[9]\cdot10^1$ | $566[3]\cdot10^1$ | $91[8]\cdot10^2$ |
| $\mu^+\mu^-$ pair | $2233[1]\cdot10^3$ | $877[7]\cdot10^1$ | $1468[4]\cdot10^0$ | $24[7]\cdot10^1$ | $554[3]\cdot10^1$ | $81[8]\cdot10^2$ |
| $m_{\mu\mu} > 70$ GeV | $2058[1]\cdot10^3$ | $86[3]\cdot10^1$ | $929[3]\cdot10^0$ | $7[3]\cdot10^1$ | $455[2]\cdot10^1$ | $7[3]\cdot10^2$ |
| $E_{\mathrm{T}}^{\mathrm{miss}} < 40$ GeV | $1990[1]\cdot10^3$ | $79[3]\cdot10^1$ | $422[2]\cdot10^0$ | $4[2]\cdot10^1$ | $109[1]\cdot10^1$ | $6[3]\cdot10^2$ |

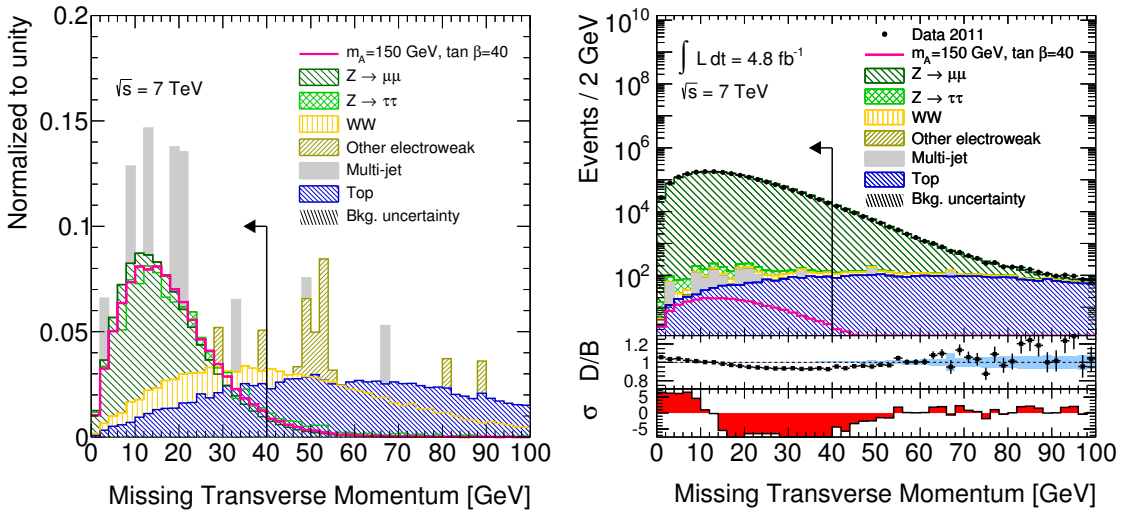


(a) (b)

**Figure 6.5:** Distributions of the missing transverse momentum, $E_{\mathrm{T}}^{\mathrm{miss}}$, in events passing the $\mu^+\mu^-$ selection for relevant background processes and the sum of expected $pp \to b(b)A$ and $gg \to A$ signal processes with $m_A = 150\,\mathrm{GeV}$ and $\tan\beta = 40$ normalised to unity (a) and normalised to the integrated luminosity with the backgrounds stacked in comparison with the data (b). The $E_{\mathrm{T}}^{\mathrm{miss}}$ selection cut is indicated. The ratio, $D/B$, of the data to the predicted background and the bin–by–bin significances, *sigma*, of the deviations of the data from the background prediction are also shown in (b).

## 6.7 Event Categorisation

The large background contribution from $Z/\gamma^*$ boson decays to two muons after the event selection (see for example Table 6.2 and Table 6.3) can be efficiently reduced by requiring that at least one $b$ jet is present in the final state. This, however, also results in a significant loss of signal. This is due to the fact that the signal events produced via gluon fusion are not accepted in this event category and that the $b$ quarks produced in association with the Higgs bosons have rather low energy. For an increasing cut on the $b$ jet transverse momentum the signal production cross section falls steeply [77–79]. This is illustrated in Figure 6.6 which shows the transverse momentum distributions of truth $b$ jets in simulated signal and background processes. A truth jet is a jet found by the jet reconstruction algorithm (see Section 6.5.3) from all generated visible particles arising from the hadronisation process of quarks and gluons (prior to the simulation of the detector response). A truth $b$ jet is a truth jet originating from the hadronisation of $b$ quarks. It can be seen in Figure 6.6 that requiring $b$ jet transverse momenta greater than 20 GeV is cutting significantly into the signal distribution. Additional loss of the signal is caused by the fact that the efficiency of tagging a $b$ jet with a transverse momentum of about 20 GeV is only about 40 % compared

**Table 6.3:** Numbers of simulated Monte Carlo events for the $A \to \mu^+\mu^-$ signal with $m_A = 150\,\text{GeV}$ and $\tan\beta = 40$ and the sum of all background events normalised to an integrated luminosity of $4.8\,\text{fb}^{-1}$ compared to the observed events in data after each step of the event selection. The selection criterion "MC weights" corresponds to the reweighting of events accounting for mismodelling of event generator and pileup predictions as well as the scaling factors which correct for mismodelling of the object reconstruction. The event selection criterion "DQ cuts" corresponds to the set of data taking quality cuts applied before the event selection (see text). The numbers in parentheses represent the statistical uncertainties in the last digit.

| Cut | $A \to \mu^+\mu^-$ | Total Background | Data |
|---|---|---|---|
| No Cut | $957[8]\cdot10^1$ | $18947[5]\cdot10^4$ | 18615384 |
| MC weights | $961[8]\cdot10^1$ | $19089[5]\cdot10^4$ | 18615384 |
| DQ cuts | $961[8]\cdot10^1$ | $18496[5]\cdot10^4$ | 17269696 |
| Vertex | $960[8]\cdot10^1$ | $18479[5]\cdot10^4$ | 16832708 |
| Trigger | $824[7]\cdot10^1$ | $2589[1]\cdot10^4$ | 4020924 |
| $\geq 2$ $\mu$ objects | $663[6]\cdot10^1$ | $2259[1]\cdot10^3$ | 2246244 |
| $\mu^+\mu^-$ pair | $663[6]\cdot10^1$ | $2257[1]\cdot10^3$ | 2244101 |
| $m_{\mu\mu} > 70$ GeV | $661[6]\cdot10^1$ | $2065[1]\cdot10^3$ | 2025858 |
| $E_{\text{T}}^{\text{miss}} < 40$ GeV | $634[6]\cdot10^1$ | $1993[1]\cdot10^3$ | 1956146 |

to the $b$–tagging efficiency of about 70 % for high–$p_{\text{T}}$ $b$ jets [167]. As can be seen in Table 6.4 the $b$–tag requirement reduces the signal acceptance by about a factor of 10.

In order not to reject the largest parts of the signal, the analysis is performed for two complementary event categories. The $b$–vetoed category contains events without tagged $b$ jets and is characterised by high signal selection efficiency but also a large contribution from the dominant $Z/\gamma^*$ boson background. The $b$–tagged category contains events with at least one tagged $b$ jet and is characterised by significantly reduced $Z/\gamma^*$ boson background contribution resulting in a better signal–to–background ratio. In addition to the remaining background contribution of $Z/\gamma^*$ boson production in association with $b$ quarks, the $t\bar{t}$ background has a significant contribution in this event category.

Figure 6.7 shows the distribution of the MV1 $b$–tagging weight for jets in $\mu^+\mu^-$ events passing the event selection and the multiplicity of tagged $b$ jets. It can be seen in Figure 6.7(b) that there is a statistically significant deficit of events without $b$ jets and a significant excess of events with at least one $b$ jet in the data compared to the simulation. Cross section measurements of the $Z/\gamma^*$ boson production in association with $b$ jets indicate an underestimation of the associated $b$ quark production rate by ALPGEN by about $20 - 30\,\%$ [168, 169]. This agrees very well with the observation of this analysis. Assuming that the $b$ jet rate in $t\bar{t}$ events is described correctly by the next–to–leading order Monte Carlo simulation, the observed deficit of simulated $b$–tagged events can be attributed exclusively to the $Z/\gamma^*$ production with $b$ jets. In this case the number of simulated $Z/\gamma^* \to \mu^+\mu^-$ events with at least one $b$ jet is underestimated by approximately

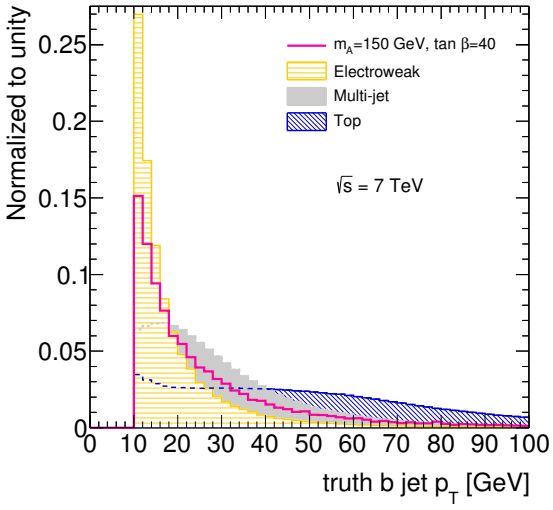


**Figure 6.6:** Distributions of the transverse momentum of truth $b$ jets in simulated events passing the selection for the relevant background processes and the sum of $pp \to b(b)A$ and $gg \to A$ signal processes $m_A = 150\,\text{GeV}$ and $\tan\beta = 40$. The electroweak $Z/\gamma^*$, $W$ and $W^+W^-$ background processes are combined for illustration purposes.

20 %, as can be seen in Table 6.4.

This mismodelling of the Monte Carlo prediction for $b$ jets in $Z/\gamma^*$ events is however not affecting the final results of this search since the background is estimated directly from data as discussed in Section 6.10.

The numbers of simulated background and observed data events passing the event selection and separated into the two event categories are shown in Table 6.4 for the $\mu^+\mu^-$ invariant mass range of 110 GeV to 300 GeV which is most relevant for the presented Higgs boson search.

The numbers of expected signal events in the two categories with neutral MSSM Higgs bosons in the $m_h^{\text{max}}$ scenario produced via both gluon fusion and in association with $b$ quarks is shown in Table 6.5. The contributions of the three Higgs bosons $h$, $A$ and $H$ are given separately according to the predictions of the signal model described in Section 6.9. The masses of the $h$ and $H$ bosons are predicted by the $m_h^{\text{max}}$ MSSM scenario for the given $m_A$–$\tan\beta$ point. The $A$ and $H$ bosons have very similar masses at the assumed benchmark point in the parameter space and thus cannot be observed separately. The lighter $h$ boson can be separated due to the high mass resolution in the $\mu^+\mu^-$ search channel. Two invariant mass peaks, one from the $h$ and one from the $A/H$ resonances, are therefore expected. The signal yields for simulated $A$ boson samples with different masses as well as more detailed tables with event selection efficiencies are shown in Appendix B.

The measured $\mu^+\mu^-$ invariant mass distributions for both the $b$–tagged and the $b$–vetoed

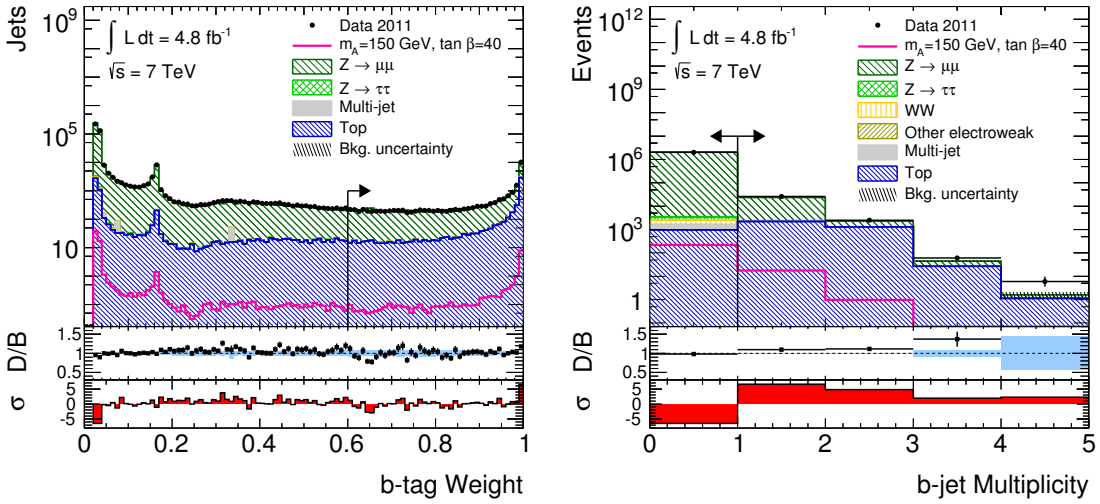


(a) (b)

**Figure 6.7:** Distributions of the MV1 $b$–tagging weight for reconstructed jets (a) and of the multiplicity of tagged $b$ jets (b) in events passing the selection shown for the data and Monte Carlo predictions for relevant background processes stacked and $pp \to b(b)A$ and $gg \to A$ signal processes for $m_A = 150\,\text{GeV}$ and $\tan\beta = 40$ summed. The ratio, $D/B$, of the data to the predicted background and the bin–by–bin significances, $\sigma$, of the deviation of the data from the background prediction are also shown. The cut on the $b$–tagging weight and the event categorisation according to the $b$ jet multiplicity are indicated.

event categories are shown in Figure 6.8 together with the simulated backgrounds and the full expected neutral MSSM Higgs boson ($h$, $A$ and $H$ contributions) signal with $m_A = 150\,\text{GeV}$ and $\tan\beta = 40$ assuming the $m_h^{\text{max}}$ benchmark scenario. The signal is expected to be present as a superposition of the narrow peaks of the three $h$, $A$ and $H$ resonances. The signal appears on top of the high–mass tail of the $Z$ boson resonance superimposed on a continuous contribution from non–resonant backgrounds. It can be seen that the signal–to-background ratio in the $b$–tagged event category is much better than in the $b$–vetoed category. On the other hand, the number of total events in the former category is much lower which leads to an increased statistical uncertainty.

As can be seen in Table 6.4, the total background contribution for events in the $\mu^+\mu^-$ invariant mass range of 110 GeV to 300 GeV consists to 99 % (54 %) of $Z/\gamma^*$ events in the $b$–vetoed ($b$–tagged) event category. The remaining non–resonant backgrounds from $t\bar{t}$, $W^+W^-$, and $b\bar{b}$ production contribute with 0.3 %, 0.5 % and 0.1 %, respectively, in the $b$–vetoed event category while in the $b$–tagged category the non–resonant background consists exclusively of $t\bar{t}$ events.

The expected signal shown in Figure 6.8 is the sum of the $h$, $A$ and $H$ invariant mass distributions from both production modes. The light $h$ boson resonance can be seen as a

**Table 6.4:** Total numbers of observed and expected background events in the $\mu^+\mu^-$ invariant mass range of 110 GeV to 300 GeV after the full event selection and in the two event categories, $b$-vetoed and $b$–tagged, for an integrated luminosity of 4.8 fb$^{-1}$. The numbers in parentheses represent the statistical uncertainties in the last digit.

| Process | event selection | $b$-vetoed sample | $b$-tagged sample |
|---|---|---|---|
| $Z/\gamma^* \to \mu^+\mu^-$ | $375[3]\cdot10^2$ | $370[3]\cdot10^2$ | $47[4]\cdot10^1$ |
| $Z/\gamma^* \to \tau^+\tau^-$ | $29[7]\cdot10^0$ | $28[7]\cdot10^0$ | $4[7]\cdot10^{-1}$ |
| Top | $58[2]\cdot10^1$ | $13[1]\cdot10^1$ | $45[2]\cdot10^1$ |
| $WW$ | $211[3]\cdot10^0$ | $209[3]\cdot10^0$ | $23[5]\cdot10^{-1}$ |
| Other electroweak | $3[3]\cdot10^0$ | $3[3]\cdot10^0$ | $0[5]\cdot10^0$ |
| Multi–jet | $0[1]\cdot10^2$ | $0[1]\cdot10^2$ | $0[4]\cdot10^1$ |
| Total | $384[4]\cdot10^2$ | $374[4]\cdot10^2$ | $92[5]\cdot10^1$ |
| Data | 39748 | 38710 | 1038 |

**Table 6.5:** Expected numbers of signal events for each of the neutral MSSM Higgs bosons, $\phi\,(= h/A/H)$, produced either via gluon fusion or in association with $b$ quarks for the $b$–tagged and $b$–vetoed event categories in the $\mu^+\mu^-$ invariant mass range of 110 GeV to 300 GeV. The masses for the $h$ and $H$ bosons are defined by the $m_h^{\text{max}}$ MSSM scenario for $m_A = 150$ GeV and $\tan\beta = 40$. The numbers in parentheses correspond to the uncertainty of the signal model prediction.

| $\phi$ | Mass [GeV] | gluon fusion | | $b$–quark associated production | |
|---|---|---|---|---|---|
| | | $b$–vetoed sample | $b$–tagged sample | $b$–vetoed sample | $b$–tagged sample |
| $h$ | 130.1 | $13[1]\cdot10^0$ | $23[2]\cdot10^{-2}$ | $45[4]\cdot10^{-1}$ | $46[5]\cdot10^{-2}$ |
| $A$ | 150.0 | $66[5]\cdot10^0$ | $12[1]\cdot10^{-1}$ | $14[1]\cdot10^1$ | $16[2]\cdot10^0$ |
| $H$ | 150.3 | $64[5]\cdot10^0$ | $12[1]\cdot10^{-1}$ | $13[1]\cdot10^1$ | $15[2]\cdot10^0$ |

shoulder on the low mass tail of the $A/H$ resonances given the rather coarse binning which is chosen for illustration purposes here. In fact, due to the high experimental resolution the $h$ boson resonance can be separated well for the shown point in the parameter space (see Figure 6.11). The masses, natural widths, cross sections and branching fractions of the three neutral MSSM Higgs bosons depend on $m_A$ and $\tan\beta$. To describe the rather complex signal superposition in dependence of these two parameters, a suitable signal model is required which is introduced in Section 6.9.

## 6.8 Statistical Methods

This section describes the statistical procedure based on Reference [170] for the interpretation of the selected data. The statistical combination of different search channels or event categories like the $b$–vetoed and $b$–tagged categories is introduced along with the procedures

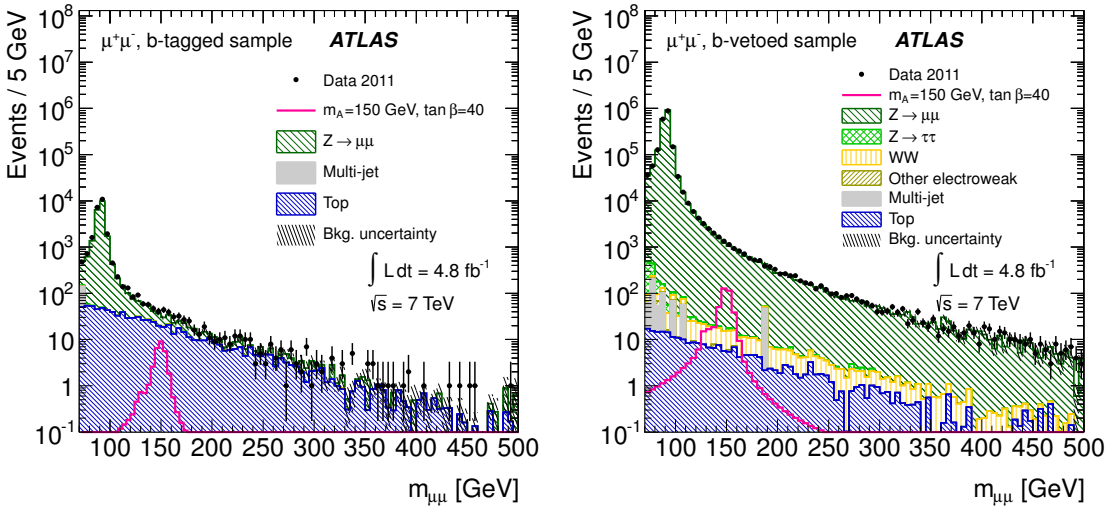


(a) (b)

**Figure 6.8:** Distribution of the $\mu^+\mu^-$ invariant mass in the $b$–tagged (a) and $b$–vetoed (b) event category shown for the data, stacked relevant background processes and the sum of $pp \to b(b)h/A/H$ and $gg \to h/A/H$ signal samples expected for $m_A = 150\,\text{GeV}$ and $\tan\beta = 40$ [132].

to compute observed and expected local $p_0$–values and exclusion limits. The statistical procedures described in the following are implemented in a software package [171–174] which is used for the computation of the results in Section 6.12 and Section 6.13.

**The Profile Likelihood Method** The selected data are interpreted by a statistical hypothesis test. Two hypotheses are compared in terms of their compatibility with the observed data. The null hypothesis is expected to be rejected against the alternative hypothesis. To quantify an excess of events above the expected background, the corresponding signal significance is evaluated by comparing the background–only hypothesis (in this case the null hypothesis) with the alternative signal–plus–background hypothesis. The presence of a signal can be excluded with a certain probability by interchanging the two hypotheses, i.e. the signal–plus–background hypothesis becomes the null hypothesis to be rejected.

In practice, a continuous set of hypotheses is defined by introducing the signal strength parameter, $\mu$, which scales the contribution of the signal. The combined model is described by

$$f\left(x, \boldsymbol{\theta}\right) = \mu \cdot f_{\text{S}}\left(x, \boldsymbol{\theta}_{\text{S}}\right) + f_{\text{B}}\left(x, \boldsymbol{\theta}_{\text{B}}\right), \tag{6.3}$$

with $f_{\text{S}}$ and $f_{\text{B}}$ describing the signal and background contributions as functions of the discriminating variable, $x$, and in general uncertain signal and background model parameters

(e.g. normalisation, resolution, ...). The variations in these model parameters due to the systematic uncertainties are constrained using either Gaussian or log–normal probability density functions of so–called nuisance parameters, $\boldsymbol{\theta}$. The explicit parametrisation of each nuisance parameter allows for a fully frequentist statistical treatment. The signal strength parameter is referred to as the parameter of interest of the search and is a free parameter of $f(x, \boldsymbol{\theta})$.

In the $h/A/H \to \mu^+\mu^-$ search, $x$ is the $\mu^+\mu^-$ invariant mass, $m_{\mu\mu}$. The $h/A/H \to \tau^+\tau^-$ searches combined with $h/A/H \to \mu^+\mu^-$ in Section 6.13 use the $\tau^+\tau^-$ invariant mass as discriminating variable.

The signal and background models used for this analysis will be discussed in detail in Sections 6.9 and 6.10. The signal strength parameter, $\mu$, is commonly expressed as the measured cross section times branching fraction normalised to the theoretical prediction for the signal. The case $\mu = 0$ corresponds to the background–only model while $\mu = 1$ corresponds to the signal–plus–background model with the signal contribution as predicted by the theory, for example the $m_h^{\text{max}}$ scenario of the MSSM.

The signal and background model functions in Equation 6.3 are probability density functions normalised to the numbers of expected signal and background events and can be factorised as

$$\begin{aligned} f_{\text{S}}\left(x, \boldsymbol{\theta}_{\text{S}}\right) &= N_{\text{S}}\left(\boldsymbol{\theta}_{\text{S}}^{\text{norm}}\right) \cdot f_s\left(x, \boldsymbol{\theta}_{\text{S}}^{\text{shape}}\right) \\ f_{\text{B}}\left(x, \boldsymbol{\theta}_{\text{B}}\right) &= N_{\text{B}}\left(\boldsymbol{\theta}_{\text{B}}^{\text{norm}}\right) \cdot f_b\left(x, \boldsymbol{\theta}_{\text{B}}^{\text{shape}}\right), \end{aligned} \tag{6.4}$$

in terms of normalisation parameters, $N_{\text{S}}\left(\boldsymbol{\theta}_{\text{S}}^{\text{norm}}\right)$ and $N_{\text{B}}\left(\boldsymbol{\theta}_{\text{B}}^{\text{norm}}\right)$ and probability density functions, $f_s\left(x, \boldsymbol{\theta}_{\text{S}}^{\text{shape}}\right)$ and $f_b\left(x, \boldsymbol{\theta}_{\text{B}}^{\text{shape}}\right)$, each depending on respective nuisance parameters.

The compatibility of $f\left(x, \boldsymbol{\theta}\right)$ with the data is determined in a frequentist hypothesis test with a test statistic based on a profile likelihood ratio. To this end, the binned likelihood function,

$$L\left(\mu, \boldsymbol{\theta}\right) = \prod_i \mathcal{F}_{\text{P}}\left(N_i \,|\, f\left(x, \boldsymbol{\theta}\right)\right) \prod_j \mathcal{F}_{\text{G}}\left(\theta_j \,|\, 0, 1\right). \tag{6.5}$$

is constructed from the expected number of signal and background events in each bin $i$ of the $\mu^+\mu^-$ invariant mass distribution using Equation 6.3. The Poisson distribution,

$$\mathcal{F}_{\text{P}}\left(N_i \,|\, f_i\left(x, \boldsymbol{\theta}\right)\right) = \frac{f_i\left(x, \boldsymbol{\theta}\right)^{N_i}}{N_i!} \exp\left[-f_i\left(x, \boldsymbol{\theta}\right)\right], \tag{6.6}$$

determines the probability density of observing $N_i$ events in bin $i$ given the expectation value $f_i\left(x, \boldsymbol{\theta}\right) = \mu \cdot f_{\text{S}\,i}\left(x, \boldsymbol{\theta}_{\text{S}}\right) + f_{\text{B}\,i}\left(x, \boldsymbol{\theta}_{\text{B}}\right)$ from Equation 6.3. The actual constraint terms for the nuisance parameters in the likelihood function are by convention Gaussian

distributions,

$$\mathcal{F}_{\mathrm{G}}\left(\theta_j|0,1\right) = \frac{1}{\sqrt{2\pi}} \exp\left[-\frac{\theta_j^2}{2}\right] \quad (j = 1, ..., n), \tag{6.7}$$

with mean 0 and variance 1, and $\theta_j$ is expressed in units of standard deviations. Therefore, each nuisance parameter needs to be connected to the size of the underlying systematic uncertainty.

To transfer the standard Gaussian of the constraint term to the log–normal ($LN$) or Gaussian ($G$) distribution of the uncertain model parameter, its nominal value in $f(x, \boldsymbol{\theta})$ is multiplied with the functions

$$\begin{aligned} K_{LN}\left(\delta, \theta_j\right) &= \exp\left[\sqrt{\log(1+\delta^2)}\theta_j\right], \quad \text{or} \\ K_{G}\left(\delta, \theta_j\right) &= 1 + \delta\theta, \end{aligned} \tag{6.8}$$

respectively, where the actual size of the systematic uncertainty, $\delta$, is determined by the relative uncertainty in the event yields and signal and background model parameters described in Section 6.11.

Systematic uncertainties may affect in general both the normalisation or the shape parameters of the signal or background models. Therefore, they are treated differently in the likelihood function in Equation 6.5. The explicit treatment of these two types of systematic uncertainties and associated nuisance parameters is shown in two examples:

For a signal–plus–background model with only one systematic uncertainty, $\delta N_{\mathrm{S}} = (\frac{\Delta N_{\mathrm{S}}}{N_{\mathrm{S}}})$, affecting for example the number of expected signal events, $N_{\mathrm{S}}$, the likelihood function is

$$\begin{aligned} L\left(\mu, \theta^{\mathrm{norm}}\right) = &\prod_i \mathcal{F}_{\mathrm{P}}\Big(N_i \,|\, \mu \cdot N_{\mathrm{S}} \cdot K_{LN}\left(\delta N_{\mathrm{S}}, \theta^{norm}\right)\, f_{\mathrm{s}\,i}\left(x\right) + f_{\mathrm{B}\,i}\left(x\right)\Big) \\ &\cdot \mathcal{F}_{\mathrm{G}}\left(\theta^{\mathrm{norm}} \,|\, 0, 1\right), \end{aligned} \tag{6.9}$$

using the first line in Equation 6.8 and the factorisation of $f_{\mathrm{S}}\left(x, \boldsymbol{\theta}_{\mathrm{S}}\right)$ in Equation 6.4.

For a signal–plus–background model with only one shape uncertainty, $\delta\sigma$, due to for example an uncertain resolution parameter, $\sigma$, the likelihood function is

$$\begin{aligned} L\left(\mu, \theta^{\mathrm{shape}}\right) = &\prod_i \mathcal{F}_{\mathrm{P}}\Big(N_i \,|\, \mu \cdot N_{\mathrm{S}} \cdot f_{\mathrm{s}\,i}\left(x, p \cdot K_G\left(\sigma, \theta\right)\right) + f_{\mathrm{B}\,i}\left(x\right)\Big) \\ &\cdot \mathcal{F}_{\mathrm{G}}\Big(\theta^{\mathrm{shape}} \,|\, 0, 1\Big), \end{aligned} \tag{6.10}$$

using the second line in Equation 6.8.

All systematic uncertainties in the presented analysis are treated accordingly. Uncertainties affecting the normalisation of signal or background yields are parametrised by log–normal distributions, uncertainties affecting the shape of the models with Gaussian distributions.

**Statistical Combination of Search Channels** Different search channels or complementary event categories in one search channel, like the $b$–tagged and $b$–vetoed categories in the $h/A/H \to \mu^+\mu^-$ search (see Section 6.7), can be combined in order to increase the sensitivity to the signal. In case that the channels have no overlap in selected events, the likelihood function for the statistical combination is simply the product of the likelihood functions for the individual channels or categories. Correlations of systematic uncertainties across the channels need to be taken into account. The following convention [175] is used for the combination of the search results presented in Sections 6.12 and 6.13: All sources of uncertainties are considered either as 100 %–correlated or uncorrelated. Partially correlated uncertainties are either broken down to 100 %–correlated or uncorrelated components or defined as either to be 100 %–correlated or to be uncorrelated. The decision is made according to which assumption is more conservative. To correlate two systematic uncertainties, one and the same associated nuisance parameter is used in the likelihood function for the combination.

**The Profile Likelihood Ratio** The compatibility of the data with a given hypothesised signal–plus–background model with signal strength parameter, $\mu$, is tested with the profile likelihood ratio,

$$\lambda(\mu) = \frac{L(\mu, \hat{\hat{\boldsymbol{\theta}}})}{L(\hat{\mu}, \hat{\boldsymbol{\theta}})}, \tag{6.11}$$

given by the ratio of the two maximised likelihood functions $L(\mu, \hat{\hat{\boldsymbol{\theta}}})$ and $L(\hat{\mu}, \hat{\boldsymbol{\theta}})$. The numerator, $L(\mu, \hat{\hat{\boldsymbol{\theta}}})$, is maximised over all nuisance parameters for a given value of $\mu$. The denominator, $L(\hat{\mu}, \hat{\boldsymbol{\theta}})$, is maximised over all parameters including the unconstrained $\mu$ parameter. Thus, the parameters $\hat{\mu}$ and $\hat{\boldsymbol{\theta}}$ are the maximum likelihood estimators of $\mu$ and $\boldsymbol{\theta}$ which maximise the likelihood function in the denominator and $\hat{\hat{\boldsymbol{\theta}}}$ is the conditional maximum likelihood estimator of $\boldsymbol{\theta}$ which maximises the likelihood function in the numerator under the condition of the given value of $\mu$, corresponding to the hypothesis test.

The null hypothesis can be either the background–only ($\mu = 0$) or the signal–plus–background hypothesis ($\mu > 0$) depending on whether a signal significance or an exclusion of the signal is to be determined. Different test statistics are defined for the two cases.

**Signal Significance** An excess of events observed in the data compared to the expected background contribution is interpreted as a signal with certain significance if the background–only hypothesis ($\mu = 0$) can be rejected with correspondingly high probability. The test statistic for this case is defined as

$$q_0 = \begin{cases} -2\ln(\lambda(0)) & \text{for } \hat{\mu} \geq 0, \\ 0 & \text{for } \hat{\mu} < 0, \end{cases} \tag{6.12}$$

with the profile likelihood ratio $\lambda(0)$ for $\mu = 0$ from Equation 6.11. High compatibility of the data with the background–only hypothesis corresponds to a small observed value, $q_0^{obs}$, of the test statistic. On the contrary, if a signal is present in the data, the observed value will be large. The level of agreement between data and background–only hypothesis is determined by the probability

$$p_0 = \int_{q_0^{\text{obs}}}^{\infty} f\left(q_0|0\right) dq_0, \tag{6.13}$$

the so–called "local" $p_0$–value, where $f\left(q_0|0\right)$ is the probability density function (pdf) of the test statistic $q_0$ (for $\mu = 0$). The local $p_0$–value is the probability of falsely rejecting the background–only hypothesis although it is true. It can be alternatively expressed in terms of the statistical significance given as the number of standard deviations, $Z$, for which the one–sided tail integral of a Gaussian distribution with a mean 0 and a variance 1 is equal to the local $p_0$–value as illustrated in Figure 6.9. Therefore, the local $p_0$–value and the statistical significance are related according to

$$Z = \Phi^{-1}(1 - p_0), \tag{6.14}$$

where $\Phi^{-1}$ is the inverse of the cumulative distribution function of the Gaussian function. A significance of $Z = 5$, corresponding to a local $p_0$–value of $2.87 \cdot 10^{-7}$, is usually required to claim a signal discovery.

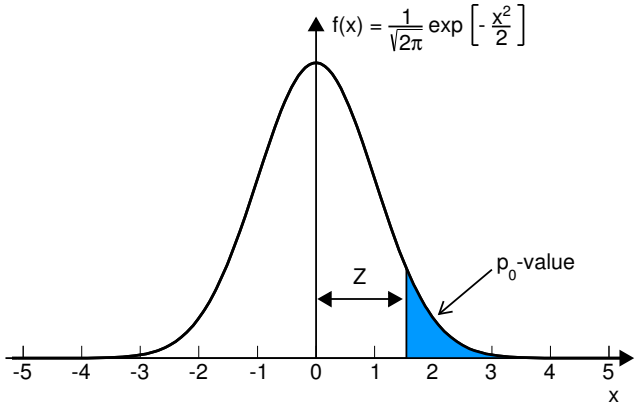


**Figure 6.9:** Illustration of the correspondence between the signal significance $Z$ and the local $p_0$–value for a standard Gaussian probability density function.

The probability density function, $f\left(q_0|0\right)$, of the test statistic in Equation 6.13 needs in principle be sampled from a large number of Monte Carlo pseudo–data. A less computational intensive method to approximate the pdf is discussed below.

The value of $\hat{\mu}$ for which local $p_0$ and $Z$ are determined and, therefore, local $p_0$ and $Z$ themselves depend on the exact model parameters in particular for the signal prediction. The neutral MSSM Higgs boson signal depends on the free parameters of $m_A$ and $\tan\beta$. In the search for neutral MSSM Higgs bosons, these parameters are scanned and the local $p_0$–value in Equation 6.13 is evaluated for each fixed point in the $m_A$–$\tan\beta$ plane.

**Exclusion Limits** If no signal is present in the data, an upper limit can be determined on the signal strength parameter $\mu$ and thus on the signal production rate. This means, that any signal–plus–background hypothesis with signal strength $\mu$ above the upper limit is excluded in favour of the background–only hypothesis. For the evaluation of exclusion limits in this thesis only hypotheses with $\mu \geq 0$ are considered. For that purpose, instead of the general test statistic $q_\mu = -2\ln\lambda(\mu)$ an alternative,

$$\tilde{q}_\mu = \begin{cases} -2\ln\left(\frac{L(\mu,\hat{\hat{\boldsymbol{\theta}}}(\mu))}{L(0,\hat{\hat{\boldsymbol{\theta}}}(0))}\right) & \text{for } \hat{\mu} < 0, \\ -2\ln\left(\frac{L(\mu,\hat{\hat{\boldsymbol{\theta}}}(\mu))}{L(\hat{\mu},\hat{\boldsymbol{\theta}})}\right) & \text{for } 0 \leq \hat{\mu} \leq \mu, \\ 0 & \text{for } \hat{\mu} > \mu, \end{cases} \tag{6.15}$$

is used. High compatibility of the data with the signal–plus–background model for a hypothesised value of $\mu$ results in a small observed value of the test statistic, $\tilde{q}_\mu$, and vice versa.

Note that the restriction to $\hat{\mu} \leq \mu$ is a special case used for setting upper limits and not a necessary consequence of Equation 6.11. The reason for this restriction is that an upward fluctuation in the data, $\hat{\mu} > \mu$, should not be considered as an incompatibility with tested the signal–plus–background hypothesis. In the general case, where both $\hat{\mu} \leq \mu$ and $\hat{\mu} < \mu$ are probed, a two–sided confidence interval for $\mu$ is obtained. In the case without nuisance parameters the latter is equivalent to the procedure introduced by Feldman and Cousins [176].

The limit setting procedure also relies on the $p_\mu$–value quantifying the agreement of the data with the signal–plus–background hypothesis for a given value of $\mu$. The $p_\mu$–value here is the probability of finding a $\tilde{q}_\mu$ value equal or greater than the observation $\tilde{q}_\mu^{\text{obs}}$,

$$p_\mu = \int_{\tilde{q}_\mu^{\text{obs}}}^{\infty} f\left(\tilde{q}_\mu|\mu\right) d\tilde{q}_\mu, \tag{6.16}$$

where $f\left(\tilde{q}_\mu|\mu\right)$ is the pdf of $\tilde{q}_\mu$ for a given value of $\mu$. Exclusion limits are usually set at the 95 % confidence level (CL). For that purpose, the upper limit on the signal strength is found by iteration as the largest value of $\mu$ for which $1 - p_\mu$ is still less than 95 %, i.e. $p_\mu$ is at least 0.05.

Since the expected number of signal events in the search presented in this thesis is much

smaller than the number of background events, there is the danger of wrongly excluding a hypothesis for which one has only little sensitivity. For example, this could mean exclusion of the signal–plus–background (null) hypothesis due to downward fluctuations of the background. To protect against excluding hypotheses for which the sensitivity of the hypothesis test is small, the modified frequentist method known as $\mathrm{CL_s}$ [177] is applied in which the $p_\mu$–value is determined relatively to the probability

$$p_b = 1 - \int_{\tilde{q}_\mu^{obs}}^{\infty} f\left(\tilde{q}_\mu|0\right) d\tilde{q}_\mu, \tag{6.17}$$

of the background–only (alternative) hypothesis for a given $\mu$, such that

$$p_\mu^{\mathrm{CL_s}} = \frac{p_\mu}{1 - p_b}. \tag{6.18}$$

The $\mathrm{CL_s}$ exclusion limit on the signal strength is then found as the largest value, $\mu_{up}$, of the tested signal strength parameters $\mu$ for which $1 - p_\mu^{\mathrm{CL_s}}$ is less than 95 %.

As for the local $p_0$–value discussed above, the limit $\mu_{up}$ in the search for the neutral MSSM Higgs bosons in the $m_h^{\mathrm{max}}$ scenario is determined for each scan point in the $m_A$–$\tan\beta$ plane. Regions in the $m_A$–$\tan\beta$ parameter plane with $\mu > \mu_{up}$ are excluded at 95 % CL. For exclusion limits on the production cross section of a Higgs boson produced in one particular production mode, the signal strength parameter is directly expressed as the measured production cross section times branching fraction not normalised to any prediction and $\mu_{up}$ is determined for each tested Higgs boson mass.

**Expected Limits and $p_0$–Values** Expected exclusion limits and local $p_0$–values provide important information of the sensitivity of the search and allow for the interpretation of the observed results.

In order to evaluate expected exclusion limits the procedure for the evaluation of observed exclusion limits described above needs to be applied to a large number of generated background–only Monte Carlo pseudo–data from the model in Equation 6.3 with $\mu = 0$ and the conditional maximum likelihood estimator $\hat{\hat{\boldsymbol{\theta}}}(0)$ obtained from the observed data. From the cumulative probability distribution function of the 95 % CL upper limits, $\mu_{up}$, obtained from the pseudo–data, the median as well as the $\pm 1\,\sigma(68\,\%)$ and $\pm 2\,\sigma(95\,\%)$ band is determined by the values of $\mu_{up}$, corresponding to a cumulative probability of 0.5 as well as $0.5 \cdot (1 \pm 0.68)$ and $0.5 \cdot (1 \pm 0.95)$, respectively [175].

Since the distributions of the test statistic $\tilde{q}_\mu$ are, however, independent of the generated pseudo–data, $f\left(\tilde{q}_\mu|\mu\right)$ and therefore the expected $p_\mu$–value are in practice only computed once for each hypothesised value of $\mu$.

The expected $p_0$–value and signal significance are obtained under the assumption that a signal is present. The $p_0$–value is computed for a representative signal–plus–background

pseudo–data distribution with $\mu = 1$ and the conditional maximum likelihood estimator obtained from the observed data.

**Asymptotic Approximation** The probability density functions $f(q_0|0)$ and $f(\tilde{q}_\mu|\mu)$ for the test statistics $q_0$ and $\tilde{q}_\mu$ required to evaluate the observed and expected local $p_0$ and $p_\mu$–values need to be obtained in principle from a large number of Monte Carlo pseudo–experiments generated from the null and the alternative hypotheses. For example, establishing a discovery with $5\,\sigma$ significance would require on the order of $10^7$ pseudo–experiments. However, Wilks [178] and Wald [179] showed that the pdf for the test statistic $q_\mu$ approaches a non–central $\chi^2$ distribution [170] with $n$ degrees of freedom (corresponding to the number of parameters of interest, $n$) for sufficiently large sample size. Based on these results, similar approximations are provided [170] for the test statistics in Equations 6.13 and 6.16 which can be used rather than sampling the pdfs. The validity of the asymptotic approximation for the evaluation of exclusion limits presented in Section 6.12 is validated with a large number of pseudo–experiments presented in Appendix B.

**The "Look–elsewhere Effect"** As discussed previously, when quantifying an excess of events, low compatibility of the data with the background–only (null) hypothesis results in a small local $p_0$–value corresponding to a high signal significance. However, when searching for a signal somewhere in a large parameter space one cannot construct a unique test statistic encompassing all possible signals and having asymptotic $\chi^2$ behaviour [175]. For example, if a signal appearing in one single bin somewhere in a spectrum with $\mathcal{O}(10^3)$ bins is searched for, it is rather natural to find a fluctuation incompatible with the background–only hypothesis and corresponding to a signal significance of $3\,\sigma$ ($p_0 = 1.35 \cdot 10^{-3}$) even though no signal is present. The possibility that a signal–like fluctuation can appear anywhere in the spectrum is called the look–elsewhere effect [180].

The look–elsewhere effect is particularly important for the $h/A/H \to \mu^+\mu^-$ search. Due to the excellent experimental mass resolution narrow signal resonances are expected somewhere in the $\mu^+\mu^-$ invariant mass distribution depending on the two MSSM parameters $m_A$ and $\tan\beta$. Therefore, many different signal hypothesis tests for each $m_A$–$\tan\beta$ point can be performed. Each possible hypothesis test, in this scope called a "trial", increases the probability of finding a fluctuation incompatible with the background–only hypothesis. If there are $N$ statistically independent trials, the probability of observing the null–hypothesis compatible with the data is not given by the local $p_0$–value introduced in Equation 6.13 but is given by

$$p_0^{global} = 1 - (1 - p_0)^N, \tag{6.19}$$

where $N$ is the so–called trials factor which increases the probability of rejecting the background–only (null) hypothesis. The look–elsewhere effect needs to be corrected for when an excess of events is found in the data.

In the asymptotic regime, methods are available to estimate the look–elsewhere effect for searches in one– [180] and multi–dimensional parameter scans [181] based on the number of observed upward fluctuations at certain levels of the signal significance, $Z$.

## 6.9 Signal Modelling

A possible $h/A/H \to \mu^+\mu^-$ signal is expected to appear in the form of three narrow resonances in the $\mu^+\mu^-$ invariant mass distribution corresponding to the contributions from the three Higgs bosons $h$, $A$ and $H$. In the largest part of the MSSM parameter space two of the three resonances are degenerate in mass (see for example Figure 2.6) such that only a combined resonance can be observed.

The $\mu^+\mu^-$ mass resolution in the mass range relevant for this search is about 2.5 %, increasing slightly with mass [182]. This, in most cases, allows for the separation of one resonance from the two degenerate ones. The signal model used for the statistical interpretation of the neutral MSSM Higgs boson search needs to account for this. Furthermore, to evaluate the sensitivity for the entire mass range of interest, the distance between investigated mass points should not be larger than the experimental mass resolution of about a few GeV. Because only seven mass points in the range of 110 GeV to 300 GeV were simulated, it is necessary to interpolate between them in order to obtain a continuous description of the signal invariant mass distribution as a function of $m_A$.

The dependence of the natural widths of the $h/A/H \to \mu^+\mu^-$ resonances on $\tan\beta$ needs to be taken into account as well. The natural widths of the neutral MSSM Higgs bosons increase with $\tan\beta$ as shown in Section 3.3. Due to the high $\mu^+\mu^-$ invariant mass resolution, the reconstructed width is sensitive to this variation of the natural width for large values of $\tan\beta$.

In order to obtain a signal model for all three resonances as a function of $m_A$ and $\tan\beta$, the simulated $A \to \mu^+\mu^-$ invariant mass distributions after event selection are parametrised by the function

$$f_{\mathrm{S}}\left(x|N_{\mathrm{S}}, m, \Gamma, \sigma, c, \varsigma\right) = N_{\mathrm{S}}\left[\mathcal{F}_{\mathrm{BW}}\left(x|m,\Gamma\right) \otimes \mathcal{F}_{\mathrm{G}}\left(x|0,\sigma\right) + c \cdot \mathcal{F}_{\mathrm{L}}\left(-x|m,\varsigma\right)\right], \tag{6.20}$$

with the running $\mu^+\mu^-$ invariant mass, $x$, and the convolution operator, $\otimes$. Function $f_{\mathrm{S}}$ is given by a Breit–Wigner function,

$$\mathcal{F}_{\mathrm{BW}}\left(x|m,\Gamma\right) = \frac{2\sqrt{2}m\Gamma\gamma}{\pi\sqrt{m^2+\gamma}} \cdot \frac{1}{\left[x^2-m^2\right]^2 + m^2\Gamma^2}, \tag{6.21}$$

with $\gamma = \sqrt{m^2(m^2+\Gamma^2)}$, mean $m$ and width $\Gamma$ describing the Higgs boson resonance which

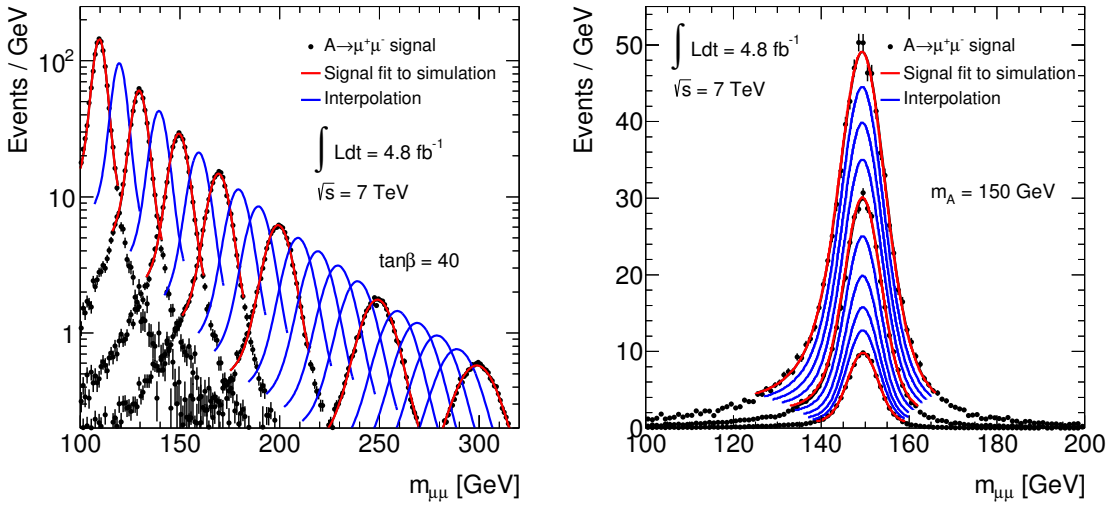


(a) (b)

**Figure 6.10:** Simulated $A \to \mu^+\mu^-$ invariant mass distributions for gluon fusion and $b$–quark associated production in the $b$–vetoed event category (black) with fits of the signal model (red) for different signal masses, $m_A$, together with the interpolated signal functions (blue) for $\tan\beta = 40$ (a). Invariant mass distributions (black) an fits of the signal model (red) for $m_A = 150\,\text{GeV}$ and $\tan\beta = 20$, 40 and 60, together with the interpolated signal functions (blue) (b).

is convolved with a Gaussian distribution,

$$\mathcal{F}_\text{G}\left(x|0,\sigma\right) = \frac{1}{\sigma\sqrt{2\pi}} \exp\left[-\frac{x^2}{2\sigma^2}\right], \tag{6.22}$$

with mean 0 and variance $\sigma^2$ describing the experimental mass resolution and complemented by a Landau distribution,

$$\mathcal{F}_\text{L}\left(-x|m,\varsigma\right) = \frac{1}{2\pi i}\int_{c-i\infty}^{c+i\infty} \exp\left[s\ln s + (-x)s\right] ds, \tag{6.23}$$

with left–hand side tail with $s = \frac{(-x)-m}{\varsigma}$, mean $m$ and scale parameter $\varsigma$ describing the low–mass tail due to photon radiation of the muons.

The width, $\Gamma$, of the Breit–Wigner function is fixed to the predicted value at a given $m_A$ and $\tan\beta$ in the $m_h^\text{max}$ scenario calculated with FeynHiggs [59, 62–64]. The function $f_\text{S}$ therefore has five free parameters, $N_\text{S}$, $m$, $\sigma$, $c$ and $\varsigma$. $N_\text{S}$ represents the normalisation of the signal curve and $c$ specifies the relative weight of the Landau function.

A binned likelihood fit of the function $f_\text{S}$ to the $\mu^+\mu^-$ invariant mass distributions of each simulated signal sample normalised to the integrated luminosity of the recorded

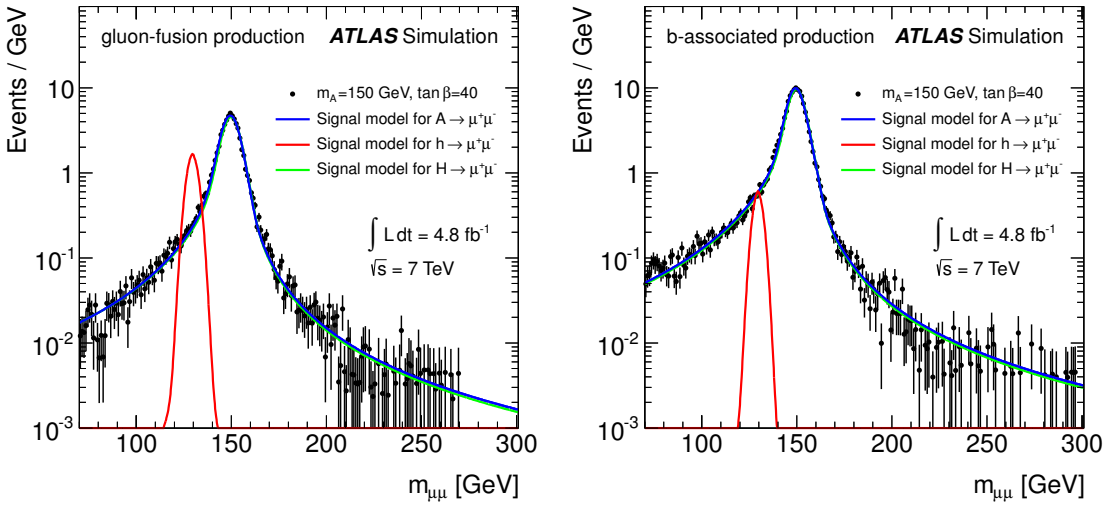


(a) (b)

**Figure 6.11:** Distributions of the $\mu^+\mu^-$ invariant mass for $m_A = 150\,\text{GeV}$ and $\tan\beta = 40$ (solid circles) for gluon fusion (a) and $b$–quark associated production (b) with signal model fit to the simulated $A$ boson sample (blue) and functions for the corresponding $h$ (red) and $H$ (green) bosons obtained from the signal modelling procedure [183]. For this point in the MSSM parameter space, the $A$ (blue) and $H$ (green) boson resonances are degenerate in mass and have almost equal cross section times branching fraction and are thus not distinguishable.

data set is performed. Each fit results in a set of parameters, $(N_\text{S}, m, \sigma, c, \varsigma)$, and their fit uncertainties, depending on $m_A$ and $\tan\beta$ of the simulated samples. The dependence on $m_A$ and $\tan\beta$ is interpolated with polynomials of orders 1 to 3. This set of parameters combined with the theoretical predictions for the natural width and production cross section times branching fraction of the signal fully defines the probability density function of the respective signal invariant mass normalised to the expected signal yield for an arbitrary point in the $m_A$–$\tan\beta$ plane. The propagated uncertainties in the model parameters are incorporated as contained nuisance parameters of the signal model as discussed in Section 6.8. For illustration, Figure 6.10 shows the $A \to \mu^+\mu^-$ invariant mass distributions from simulation in the $b$–vetoed event category, together with the fits of the signal model and the interpolated signal functions for different values of $m_A$ and $\tan\beta$.

Since the function $f_\text{S}$ is fitted to the reconstructed $\mu^+\mu^-$ invariant mass distribution of signal events passing the event selection criteria separately for the $b$–vetoed and $b$–tagged categories, the resulting fit parameters account for the dependence of the signal acceptance on the mass of the signal resonance in each event category. This dependence, especially important for the normalisation parameter, $N_\text{S}$, is also taken into account in the interpolation using higher order polynomials instead of just linear dependence.

Using the respective cross sections and natural widths, the signal parametrisation procedure is also used to model the $\mu^+\mu^-$ invariant mass distributions of the $h$ and $H$ bosons. The signal functions are modelled separately for the $b$–vetoed and $b$–tagged event categories and separately for the two Higgs boson production modes.

Figure 6.11 shows the full signal model with contributions from all three Higgs bosons for the MSSM $m_h^{\text{max}}$ scenario with $m_A = 150$ GeV and $\tan\beta = 40$ in the $b$–vetoed event category and for the two production modes. The normalised probability density functions of the $\mu^+\mu^-$ invariant mass for the $h$, $A$ and $H$ signal contributions are shown together with the $\mu^+\mu^-$ invariant mass distribution of the simulated $A \to \mu^+\mu^-$ events.

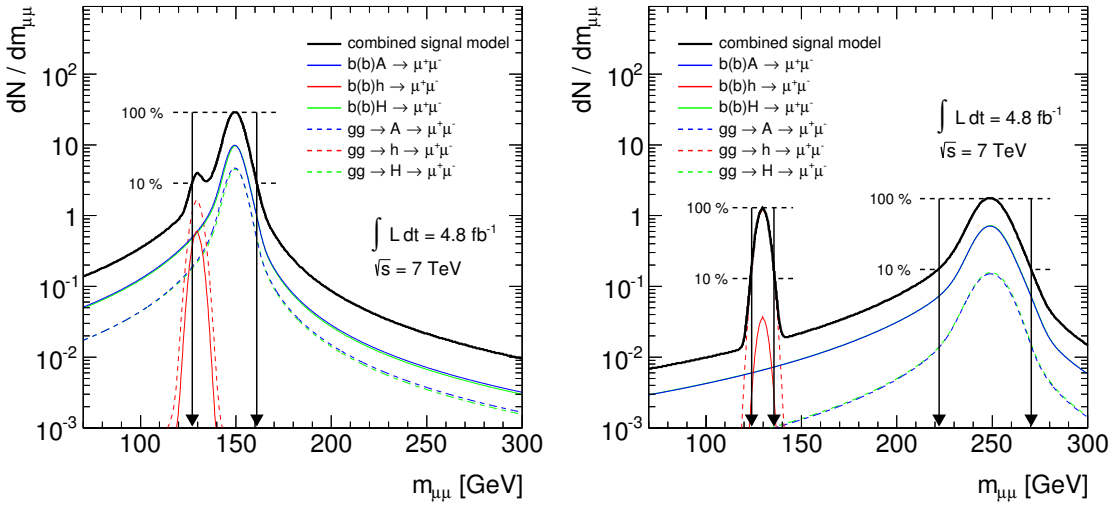


(a) (b)

**Figure 6.12:** Illustration of the signal mass window definition for the combined $h/A/H \to \mu^+\mu^-$ signal model for $\tan\beta = 40$ and $m_A = 150\,\text{GeV}$ (a) and $m_A = 250\,\text{GeV}$ (b). The signal contributions from MSSM Higgs boson production via gluon fusion (dashed colored lines) and in association with $b$ quarks (solid colored lines) are added up to the combined signal (solid black line). For $m_A = 150\,\text{GeV}$ all three resonances are enclosed by one mass window while for $m_A = 250\,\text{GeV}$ two mass windows, one for the $A/H$ boson signals and one for the $h$ boson signal, are used.

**Signal Mass Windows** Signal mass windows need to be defined for each of the three $(h/A/H)$ signal resonances at each point studied in the $m_A$–$\tan\beta$ plane in order to allow for a fit of the background model described in Section 6.10 to the signal–free data outside of the windows. To account for the asymmetries in the signal mass distributions, the upper and lower boundaries of the mass windows are defined by the mass values at which the resonance curves reach 10 % of their maximum values. If two or three of the signal mass windows overlap, they are combined to one or two larger windows. The definition of the

signal mass windows is illustrated in Figure 6.12 for two mass points $m_A = 150\,\text{GeV}$ and $m_A = 250\,\text{GeV}$, both for $\tan\beta = 40$. Outside of these windows the signal contribution to the total $\mu^+\mu^-$ invariant mass distribution is considered negligible (see next paragraph). The influence of the $\tan\beta$ value on the reconstructed widths of the $h/A/H \to \mu^+\mu^-$ resonances is automatically taken into account in the definition of the signal mass windows. Typically, the window size increases by 10 % when scanning over the $\tan\beta$ values from 5 to 70.

**Table 6.6:** Signal mass windows and numbers of signal events within the windows, $N^{\text{Window}}_{\text{Model}}$, as predicted by the signal model, and as found in the simulated signal samples, $N^{\text{Window}}_{\text{Simulation}}$, of $A$ production for different $m_A$ and $\tan\beta = 40$ in the $b$–vetoed event category. The agreement of both predictions is tested with $\chi^2$/Ndof and $\chi^2$ probability of the fit and by the probability, $P$(KS) of a Kolmogorov–Smirnov test. For comparison, the numbers of simulated background events in each mass window is also given. The numbers in parentheses correspond to the statistical uncertainties in the last digits.

| $m_A$ [GeV] | 110 | 130 | 150 | 170 | 200 | 250 | 300 |
|---|---|---|---|---|---|---|---|
| Window [GeV] | [99,118] | [117,139] | [134,161] | [152,183] | [178,215] | [221,270] | [266,326] |
| | | | | Gluon fusion production | | | |
| $N^{\text{Window}}_{\text{Model}}$ | 271[3] | 119[1] | 59.0[5] | 29.9[3] | 12.6[1] | 3.62[2] | 1.185[7] |
| $N^{\text{Window}}_{\text{Simulation}}$ | 272[3] | 120[1] | 59.2[5] | 30.0[3] | 12.7[1] | 3.63[2] | 1.188[7] |
| $\chi^2$/Ndof | 0.51 | 1.52 | 1.53 | 0.45 | 0.59 | 0.57 | 0.73 |
| $P(\chi^2)$ | 0.96 | 0.06 | 0.04 | 0.99 | 0.97 | 0.99 | 0.94 |
| $P$(KS) | 0.99 | 0.45 | 0.91 | 0.97 | 0.99 | 0.99 | 0.85 |
| $\frac{N^{\text{Window}}_{\text{Model}}}{N^{\text{Total}}_{\text{Model}}}$ | 0.82[2] | 0.89[1] | 0.88[1] | 0.83[2] | 0.82[2] | 0.84[1] | 0.83[1] |
| | | | | Associated production with $b$ quarks | | | |
| $N^{\text{Window}}_{\text{Model}}$ | 339[2] | 197[1] | 123[1] | 76.5[5] | 41.1[1] | 16.3[1] | 7.08[4] |
| $N^{\text{Window}}_{\text{Simulation}}$ | 340[2] | 197[1] | 122[1] | 76.6[5] | 41.2[3] | 16.4[1] | 7.11[4] |
| $\chi^2$/Ndof | 0.40 | 0.49 | 0.68 | 0.44 | 0.64 | 0.70 | 0.72 |
| $P(\chi^2)$ | 0.99 | 0.97 | 0.89 | 0.99 | 0.95 | 0.95 | 0.95 |
| $P$(KS) | 0.99 | 0.99 | 0.99 | 0.96 | 0.99 | 0.97 | 0.78 |
| $\frac{N^{\text{Window}}_{\text{Model}}}{N^{\text{Total}}_{\text{Model}}}$ | 0.83[1] | 0.83[1] | 0.84[1] | 0.85[1] | 0.84[1] | 0.89[1] | 0.88[1] |
| | | | | Total simulated background | | | |
| $N^{\text{Window}}_{\text{Bkg}}$ | $742[2]\cdot 10^2$ | $145[1]\cdot 10^2$ | $723[7]\cdot 10^1$ | $430[5]\cdot 10^1$ | $248[6]\cdot 10^1$ | $118[3]\cdot 10^1$ | $63[2]\cdot 10^1$ |

**Validation of the Signal Model** In order to validate the signal model, the predicted number of signal events in a given mass window is compared to the corresponding number of the simulated events (see Table 6.6 for the $b$–vetoed event category). Kolmogorov–Smirnov and $\chi^2$ tests show good agreement of the shape and normalisation. The test parameters are the global $\chi^2$ value divided by the number of degrees of freedom, $\chi^2$/Ndof, the corresponding $\chi^2$ probability, $P(\chi^2, \text{Ndof})$, and the Kolmogorov–Smirnov probability, $P$(KS). Both, $P(\chi^2, \text{Ndof})$ and $P$(KS) are at the level of 95 % or better. The small $\chi^2$

probability for the gluon fusion signal with $m_A = 130\,\text{GeV}$ and $150\,\text{GeV}$ was found to be due to large statistical fluctuations in the $\mu^+\mu^-$ invariant mass distribution of the respective simulated Monte Carlo event samples.

The fraction of signal events inside the mass windows is about 85 %. The influence of the signal contamination outside the mass windows on the estimated number of background events within the signal mass window is investigated using the background model described in Section 6.10. For the nominal signal mass window size the effect on the background normalisation from the sideband is about 5 ‰. The effect can be reduced to about 3 ‰ if the signal mass windows are increased such that they contain at least $\sim 90\,\%$ of the signal events. In this case, however, the statistical uncertainties in the background prediction increase by at least the amount of the signal bias up to the per cent level. In summary, the impact of the expected signal contamination outside the chosen mass windows on the estimated background contribution is negligible.

## 6.10 Background Modelling

The precise estimation of the large background contribution is crucial for the search for the neutral MSSM Higgs bosons in $\mu^+\mu^-$ decays. As shown in Table 6.6, the number of expected signal events in the search windows is of the same order of magnitude as the Monte Carlo statistical uncertainty of the simulated background estimate. Taking into account also the theoretical and detector–related systematic uncertainties (see Section 6.11), the total background uncertainty clearly exceeds the signal expectation, strongly reducing the expected signal significance. To reduce the sensitivity to the above uncertainties, the background is estimated directly from the data. The discriminating observable in the search for $h/A/H \to \mu^+\mu^-$ decays is the $\mu^+\mu^-$ invariant mass. Due to the high experimental mass resolution, the signal appears as narrow resonances above the continuously falling background composed of mainly $Z/\gamma^*$, $t\bar{t}$ and $W^+W^-$ decays.

The statistical and systematic uncertainty in the expected background rates in the signal mass windows can be reduced by means of additional information on the background shape and normalisation from the sideband data corresponding to the invariant mass distribution measured outside the signal mass window and within the fit range of 110 GeV to 350 GeV (250 GeV) for the $b$–vetoed ($b$–tagged) event category. The sensitivity can be further improved by describing the signal and background expectations by parametrised analytical functions avoiding uncertainties due to binning effects.

For this purpose, the background $\mu^+\mu^-$ invariant mass distribution is parametrised by the function

$$f_\text{B}\left(x|N_\text{B}, A, B, m_Z, \Gamma_Z, \sigma_Z\right) = N_\text{B} \cdot \left[f_Z\left(x|A, B, m_Z, \Gamma_Z\right) \otimes \mathcal{F}_\text{G}\left(x|0, \sigma_Z\right)\right], \tag{6.24}$$

with the running $\mu^+\mu^-$ invariant mass, $x$. Function $f_\text{B}$ is a convolution of the simplified

parton–level prediction of the $\mu^+\mu^-$ mass spectrum from $q\bar{q} \to Z/\gamma^* \to \mu^+\mu^-$ [182],

$$f_Z\left(x|A,B,m_Z,\Gamma_Z\right) = A\frac{1}{x^2} + B\frac{x^2-m_Z^2}{\left(x^2-m_Z^2\right)^2+m_Z^2\Gamma_Z^2} + \frac{x^2}{\left(x^2-m_Z^2\right)^2+m_Z^2\Gamma_Z^2}, \quad (6.25)$$

with the Gaussian resolution function, $\mathcal{F}_\mathrm{G}$ in Equation 6.22 with the $\mu^+\mu^-$ mass resolution, $\sigma_Z$ for $Z/\gamma^*$ events assumed to be constant over the whole fit range. The natural width, $\Gamma_Z$, of the $Z$ resonance is fixed to its world average of $\Gamma_Z = 2.4952\,\mathrm{GeV}$ [61] to avoid biases in the value of the fitted mass resolution parameter, $\sigma_Z$. The three terms in Equation 6.25 correspond to the pure $\gamma$, the pure $Z$ and the $Z$–$\gamma$ interference propagators. Strictly speaking, the function $f_Z$ only describes the $Z/\gamma^*$ background contribution. However, it is shown in the following that the parametrisation $f_\mathrm{B}$ is a good approximation for the description of the total background. This holds also for the $b$–tagged event category in which the contribution of the additional non–resonant background is significant.

The function $f_\mathrm{B}$ is described by five free parameters. The parameter $N_\mathrm{B}$ represents the overall background normalisation while the parameters $A$ and $B$ give the relative normalisations of the terms in Equation 6.24. The $Z$ boson mass parameter, $m_Z$, is taken as a free parameter to absorb uncertainties in the experimental mass scale.

Binned likelihood fits of the function $f_\mathrm{B}$ to the sidebands of the $\mu^+\mu^-$ invariant mass distribution determine the parameter set ($N_\mathrm{B}$, $A$, $B$, $m_Z$, $\sigma_Z$) and consequently the extrapolated background estimate in the mass windows. The final uncertainty in the background estimate originates only from the uncertainties of the fitted parameters as discussed in Section 6.11 and is incorporated as nuisance parameters of the background model as described in Section 6.8.

**Background Estimation in the *b*–vetoed and *b*–tagged Event Categories** The total background contribution is estimated for each scan point in the $m_A$–$\tan\beta$ plane, in both the $b$–vetoed and $b$–tagged event categories using the above background model. The measured $\mu^+\mu^-$ invariant mass distributions are shown in Figure 6.13 in comparison to the expected $h/A/H$ signal for both production modes and the background estimate from the sideband fits. The combined signal mass window for all three Higgs resonances is indicated. The binning is chosen such that there are at least 10 expected background events per bin in the fit range of 110 GeV to 200 GeV. The deviations of the data from the background estimate are well within the statistical uncertainties. The bin–by–bin significances, $\sigma$, of the deviations are at the level of 1 standard deviation. The ratio, $D/B$, of data events to predicted background measure the size of the data deviations in relation to the uncertainty in the background estimate which is obtained as described in Section 6.11. No systematic deviation between data and background estimate is observed. The other scan points in the $m_A$–$\tan\beta$ plane show similar behaviour.

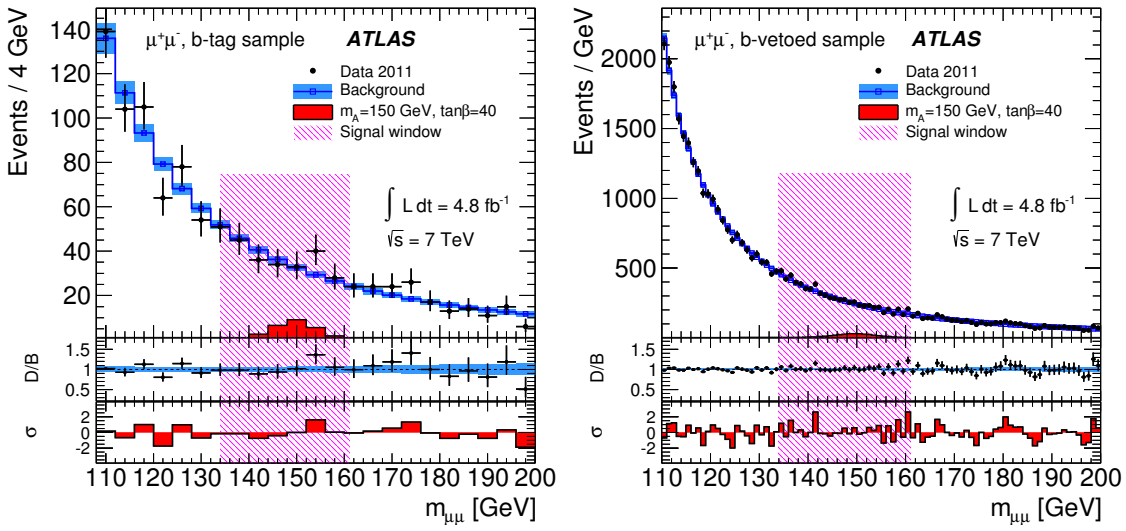


(a) (b)

**Figure 6.13:** Measured $\mu^+\mu^-$ invariant mass distribution together with the expected $h/A/H$ signal and background distribution from sideband fits for $m_A = 150\,\text{GeV}$ and $\tan\beta = 40$ for the $b$–tagged (a) and the $b$–vetoed event categories (b). The signal mass windows for the $m_A$–$\tan\beta$ point are indicated. The ratio, $D/B$, of the data to the predicted background and the bin–by–bin significances, $\sigma$, of the deviations of the data from the background prediction are also shown. The yellow bands indicate the 68 % CL uncertainty band of the background estimate [132].

## 6.11 Systematic Uncertainties

This section summarises the systematic uncertainties in the signal and background contributions which are considered in the presented analysis. In particular, systematic uncertainties related to the reconstruction of physics objects in the detector may affect both the event yield and the shape of the discriminating distributions such as the $\mu^+\mu^-$ invariant mass distribution. However, since the background contribution is fully estimated from observed data, such detector–related systematic uncertainties only affect the simulated signal contribution.

The expected number of signal events is small compared to the number of background events in the corresponding signal mass window. Thus, a variation of the shape of the signal invariant mass distribution due to detector–related systematic uncertainties can be neglected and only the variation of the signal event yields is considered.

In addition to the detector–related systematic uncertainties, the expected rates of the signal and background processes are affected by theoretical uncertainties on the prediction of the production cross sections and by uncertainties of the event modelling in the Monte Carlo simulation. Even though the background contribution is estimated from data and

therefore not affected by such sources of uncertainties, the impact of these is evaluated also for the background processes and compared with the corresponding background modelling uncertainty from the fit to the data.

**Cross Section Uncertainties** Uncertainties in the production cross section of the signal and background processes affect the normalisation of the expected event yields.

The cross section uncertainties for the neutral MSSM Higgs boson production contribute to the uncertainty in the normalisation parameters of the signal model and therefore reduce the sensitivity of the presented search. Uncertainties in the gluon fusion production and the production in association with $b$ quarks originating from PDF, $\alpha_s$ and renormalisation and factorisation scale uncertainties are evaluated separately for the $h$, $A$ and $H$ bosons for each scan point in the $m_A$–$\tan\beta$ parameter plane [184]. The corresponding uncertainties amount to about 10 % to 15 %. The cross section uncertainties for the gluon fusion production are dominated by the scale uncertainties while the remaining contributions of PDF and $\alpha_s$ uncertainties are of similar size. For the Higgs boson production in association with $b$ quarks all three contributions from the PDF, $\alpha_s$ and scale uncertainties contribute by a similar amount to the total cross section uncertainty.

According to Reference [185], an uncertainty of $\pm 5$ % is assigned for the $W$ and $Z/\gamma^*$ boson production. An uncertainties of $\pm 10$ % is assumed for $t\bar{t}$ and $\pm 7$ % for $W^+W^-$ production. As these backgrounds are by far the dominant ones, the cross section uncertainties of remaining background processes in the presented search can be neglected. These uncertainties are large compared to the uncertainties of the background modelling from data described below.

**Monte Carlo Simulation Uncertainties** Systematic uncertainties originating from the mis–modelling of the event topology with the Monte Carlo simulation are evaluated for the dominant background process $Z \to \mu^+\mu^-$. To estimate the change in acceptance introduced by the PDF uncertainties, the predictions from two PDF sets (CTEQ [186–188] and MSTW [189]) are compared, using the reweighting procedure described in Appendix B. Comparing the nominal and the reweighted $Z/\gamma^*$ boson background samples, a deviation of 3.5 % (2.9 %) in the event yield is evaluated for the $Z/\gamma^*$ boson production in association with light ($b$) jets.

In addition, the underestimation of $b$ jets in the simulation of $Z/\gamma^*$ boson production in association with $b$ quarks mentioned in Section 6.7 needs to be assigned to the event yields after the separation of the events into the two categories. An uncertainty of about 20 % in the prediction of $Z/\gamma^*$ boson events with $b$ jets is associated to the ALPGEN event generator [168, 169]. Other event generators such as Sherpa or MCFM show a better agreement with the data [168].

**Signal and Background Modelling Uncertainties** As discussed in Sections 6.9 and 6.10, the $\mu^+\mu^-$ invariant mass distributions for both the signal and total background contributions are modelled with analytic functions fitted to the simulated signal samples and the data, respectively.

The fit uncertainties of the model parameters in Equations 6.20 and 6.24 are taken into account as systematic uncertainties. For the signal modelling procedure, the uncertainties of the model parameters from the fits to the simulated Monte Carlo samples are propagated to the parameters of the interpolated signal models for the $h$, $A$ and $H$ bosons depending on $m_A$ and $\tan\beta$ using the general Gaussian error propagation. The uncertainties of the background model parameters are obtained from each fit to the sidebands of the scanned signal regions.

Total uncertainties are evaluated by variation of the fitted functions, $f_{\mathrm{S}}$ and $f_{\mathrm{B}}$, within their 68 % confidence level (CL) uncertainty bands which are obtained from the general Gaussian error propagation of the uncertainties of the respective fit parameters taking into account also their correlations. Resulting uncertainties for the expected background yield within the mass window for the benchmark signal point of $m_A = 150\,\mathrm{GeV}$ and $\tan\beta = 40$ amount to 5 % (2 %) for the $b$–tagged ($b$–vetoed) event category and are clearly smaller than the total uncertainty in the Monte Carlo simulated background.

The uncertainties for the expected signal yield are estimated to be of the order of 10 % for the $A$ and $H$ boson contributions and of the order of 10 % to 20 % for the $h$ boson contributions. The $h$ boson signal yield uncertainty is typically higher compared to $A$ and $H$ boson signals because of the following reason: the signal model parameters are evaluated from $A$ boson samples in which the reconstructed width of the $\mu^+\mu^-$ invariant mass distribution is to a large extent affected by the natural width of the $A$ boson. In the $m_A$ and $\tan\beta$ range relevant for the presented search, this applies also for the $H$ boson signal. However, since the natural width of the $h$ boson is very small (see Figure 3.9), the corresponding reconstructed width of the $\mu^+\mu^-$ system is almost exclusively defined by the detector resolution which is a free model parameter. Therefore, the uncertainty of this model parameter has a much greater impact on the modelled $h$ boson signal compared to the modelled $A$ and $H$ boson signals, resulting in the increased signal modelling uncertainty for the $h$ boson. The uncertainties for both, the signal and background modelling are comparable for all scan points in the $m_A$–$\tan\beta$ plane.

**Detector–Related Uncertainties** Detector–related systematic uncertainties which contribute to the analysis concern the trigger and the reconstruction of muons, jets and the tagging of $b$ jets.

To account for the differences between the simulation and the actual single muon trigger efficiency measured with $Z \to \mu^+\mu^-$ data [131] in dependence of the muon $p_{\mathrm{T}}$ and the $\eta$–$\phi$ detector region, scale factors are applied to the simulated events according to the number

of reconstructed muons. At least one reconstructed muon is required to match in its $\eta$–$\phi$ coordinates to the region of interest of the active trigger as mentioned in Section 6.6. On average these scale factors amount to 0.995 with a typical variation of approximately 0.03. The uncertainty of the measured trigger scale factors is at the level of about 1 %. To evaluate the effect of the systematic uncertainty of the trigger efficiency on the analysis, the measured trigger scale factors are varied coherently in both directions, i.e. subsequently increased and decreased, by the measured uncertainty of the trigger scale factors. These variations change the number of selected signal events independently of the event category and the signal mass by $\pm 0.7$ %.

The description of the transverse momentum scale, transverse momentum resolution and identification efficiency of reconstructed muons is slightly different in the simulation compared to the observations in data [182, 190]. Therefore these quantities are corrected at the level of the muon selection described in Section 6.5.2.

The transverse momentum scale of selected muons is corrected depending on the muon four–momentum by on average 0.998 of the original momentum.

In addition, the transverse momenta measured in the inner detector (ID) and the muon spectrometer (MS) are smeared separately to account for the somewhat lower observed detector resolution compared to the simulation. The inverse transverse momenta in the simulation are smeared randomly based on a Gaussian probability density function with the respective inverse transverse momentum as mean value and a smearing constant as variance. The smearing constant depends on the detector region as well as on the combined (ID+MS) transverse momentum an amounts to typically 2 % with an RMS of about 3 %.

To account for the measured muon identification efficiency in data, scale factors of on average 0.992 are applied to the simulated muons.

To evaluate the impact of the related muon systematic uncertainties discussed above, the introduced corrections are varied independently. The muon transverse momentum scale is varied by one standard deviation which typically amounts to $\pm 3 \cdot 10^{-4}$. The uncertainty in the transverse momentum resolution is evaluated by smearing separately, either the transverse momentum measured in the inner detector or the muon spectrometer by one standard deviation. Typical variations of the corresponding combined transverse momentum are at the level of $< 10^{-3}$ compared to the original value. To account for both the statistical and systematic uncertainty of the muon identification efficiency measurement, the analysis results after a systematic shift of about 0.4 % in the muon identification efficiency are compared to the nominal results without such a shift.

The resulting relative changes in acceptance of the signal events produced in gluon fusion and in association with $b$ quarks are evaluated separately for all simulated signal points, separately for the $b$–vetoed and $b$–tagged event categories. A relevant impact on the event yield is observed only from the uncertainty in the muon identification efficiency. It results in a relative change in the number of selected events at the level of 0.6 % to 0.7 %, slightly

depending on the signal mass. Relative changes in the signal yield due to the uncertainty of the muon transverse momentum scale and resolution are at the level of $10^{-5}$ or smaller.

**Table 6.7:** Relative change (%) in the signal yield for different $m_A$ and $\tan\beta = 40$ due to detector–related systematic uncertainties for the $b$–vetoed event category separately for the signal produced in association with $b$ quarks ($pp \to b(b)A$) and through gluon fusion ($gg \to A$).

| Process | $pp \to b(b)A$ | | | | | | |
|---|---|---|---|---|---|---|---|
| $m_A$ | 110 GeV | 130 GeV | 150 GeV | 170 GeV | 200 GeV | 250 GeV | 300 GeV |
| Muons | $^{+0.95}_{-0.96}$ | $^{+0.96}_{-0.96}$ | $^{+0.96}_{-0.96}$ | $^{+0.96}_{-0.96}$ | $^{+0.97}_{-0.97}$ | $^{+0.99}_{-0.99}$ | $^{+1.01}_{-1.01}$ |
| Jets | $^{+0.96}_{-0.03}$ | $^{+0.96}_{-0.03}$ | $^{+0.96}_{-0.01}$ | $^{+0.97}_{-0.01}$ | $^{+0.97}_{-0.01}$ | $^{+1.00}_{-0.02}$ | $^{+1.02}_{-0.02}$ |
| $b$-tagging | $^{+0.96}_{-0.10}$ | $^{+0.97}_{-0.11}$ | $^{+0.97}_{-0.14}$ | $^{+0.98}_{-0.14}$ | $^{+0.98}_{-0.15}$ | $^{+1.01}_{-0.17}$ | $^{+1.04}_{-0.20}$ |
| $E_{\mathrm{T}}^{\mathrm{miss}}$(soft) | $^{+1.18}_{-1.75}$ | $^{+1.20}_{-1.71}$ | $^{+1.17}_{-1.90}$ | $^{+1.09}_{-1.79}$ | $^{+1.08}_{-1.84}$ | $^{+1.16}_{-1.66}$ | $^{+1.30}_{-1.96}$ |
| Process | $gg \to A$ | | | | | | |
| $m_A$ | 110 GeV | 130 GeV | 150 GeV | 170 GeV | 200 GeV | 250 GeV | 300 GeV |
| Muons | $^{+0.95}_{-0.96}$ | $^{+0.95}_{-0.95}$ | $^{+0.95}_{-0.95}$ | $^{+0.96}_{-0.96}$ | $^{+0.97}_{-0.97}$ | $^{+0.99}_{-0.99}$ | $^{+1.01}_{-1.01}$ |
| Jets | $^{+1.06}_{-0.07}$ | $^{+1.05}_{-0.07}$ | $^{+1.05}_{-0.05}$ | $^{+1.09}_{-0.05}$ | $^{+1.12}_{-0.08}$ | $^{+1.19}_{-0.09}$ | $^{+1.14}_{-0.06}$ |
| $b$-tagging | $^{+1.12}_{-0.38}$ | $^{+1.12}_{-0.39}$ | $^{+1.15}_{-0.47}$ | $^{+1.21}_{-0.52}$ | $^{+1.28}_{-0.61}$ | $^{+1.38}_{-0.70}$ | $^{+1.42}_{-0.83}$ |
| $E_{\mathrm{T}}^{\mathrm{miss}}$(soft) | $^{+1.14}_{-1.66}$ | $^{+0.92}_{-1.49}$ | $^{+0.93}_{-1.51}$ | $^{+1.14}_{-1.57}$ | $^{+1.02}_{-1.69}$ | $^{+1.26}_{-1.64}$ | $^{+0.96}_{-2.09}$ |

The separation of events into the $b$–vetoed and $b$–tagged event categories is performed based on the number of reconstructed $b$ jets in the $\mu^+\mu^-$ final state. This measured number can be affected by the energy scale and resolution of the reconstructed jets, the efficiency of the $b$–jet tagging and the corresponding mistagging efficiency for the jets from $c$– or light flavour ($u$, $d$, $s$) quarks and gluons.

The systematic uncertainty in the jet energy scale is accounted by scaling the jet energies by on average $\pm 2.5\,\%$ depending on the jet four–momentum and maximally by $\pm 8\,\%$. The systematic uncertainty in the jet energy resolution is taken into account by smearing the energy and $p_{\mathrm{T}}$ of the selected jets by on average $20\,\%$. The relative change in the number of selected signal events due to the jet energy scale and resolution uncertainties is typically $10^{-3}$ in the $b$–vetoed and $10^{-2}$ in the $b$–tagged event category.

The number of jets tagged as $b$ jets are scaled according to their true flavour by on average 0.986 with typical variations of $\pm 5\,\%$ in dependence of the jet $p_{\mathrm{T}}$ and $\eta$ to account for the actual performance of the $b$–tagging algorithm [191]. The jets identified as light flavour jets are scaled by on average 1.008 with typical variations of $\pm 5\,\%$. To account for the systematic uncertainties of the measured $b$–tagging and mistagging efficiencies, the mentioned scale factors are varied depending on the true jet flavour by typically $\pm 3\,\%$ to $\pm 7\,\%$ separately for $b$–, $c$– and light flavour jets. In the $b$–vetoed event category, the uncertainty in the $b$–jet tagging efficiency results in the relative changes in the event yield at the level of $10^{-3}$ for the signal produced in association with $b$ quarks and $10^{-2}$ for the signal produced in gluon fusion. In the $b$–tagged event category the corresponding event yield changes are at the level of $2 - 4\,\%$ in each production mode. The uncertainty of the mistagging efficiency for $c$– and light flavour jets affect the event yield by a factor of $10^{-3}$ for gluon fusion and $10^{-4}$ for the associated production with $b$ quarks in the $b$–vetoed event category. In the $b$–tagged event category the corresponding relative changes in the event yields are $10^{-2}$ and $10^{-3}$, respectively.

An imperfect knowledge of the transverse momentum scale and resolution of each physics objects in the event translates into a systematic uncertainty of the missing transverse momentum measurement. To evaluate these uncertainties, $E_{\mathrm{T}}^{\mathrm{miss}}$ is recalculated after the subsequent variation of the following quantities: transverse momentum or energy scale and resolution of muons and jets, energy scale of the calorimeter clusters and soft jets not associated to the above reconstructed objects, as well as the contribution of pileup events. The biggest relative changes in the signal yield are at the level of $10^{-2}$ and caused by variations of energy deposits in the calorimeter clusters outside the high–$p_{\mathrm{T}}$ physics objects and by the pileup contribution. The uncertainty of the measured photon, electron and $\tau$ reconstruction performance does not contribute to the missing transverse momentum in the selected event topologies and are thus not taken into account.

The different systematic uncertainties for each physics object introduced above are considered as uncorrelated and therefore summed quadratically. Table 6.7 shows the resulting relative changes in the event yield of simulated signal samples due to the discussed sources of systematic uncertainties for the $b$–vetoed event category. Equivalent numbers for the $b$–tagged event category are shown in Table 6.8. The muon– and jet–related uncertainties include the corresponding systematic uncertainty in the missing transverse momentum measurement. Remaining $E_{\mathrm{T}}^{\mathrm{miss}}$ uncertainties such as the impact of pileup events and the energy measured in the calorimeter clusters outside of the high–$p_{\mathrm{T}}$ physics objects are combined and presented in the last row of the tables denoted as $E_{\mathrm{T}}^{\mathrm{miss}}$(soft).

In summary, it can be seen that the different detector–related systematic uncertainties in the $b$–vetoed event category which are at the order of $1\,\%$ each contribute much less to the total uncertainty of the expected signal yield compared to the cross section and signal modelling uncertainties. In the $b$–tagged event category the detector–related uncertainties concerning the muon, jet and $E_{\mathrm{T}}^{\mathrm{miss}}$ reconstruction affect the expected signal yield also at

**Table 6.8:** Relative change (%) in the signal yield for different $m_A$ and $\tan\beta = 40$ due to detector–related systematic uncertainties for the $b$–tagged event category separately for the signal produced in association with $b$ quarks ($pp \to b(b)A$) and through gluon fusion ($gg \to A$).

| Process | $pp \to b(b)A$ | | | | | | |
|---|---|---|---|---|---|---|---|
| $m_A$ | 110 GeV | 130 GeV | 150 GeV | 170 GeV | 200 GeV | 250 GeV | 300 GeV |
| Muons | +0.97<br>−0.99 | +0.97<br>−1.01 | +0.97<br>−0.97 | +0.98<br>−0.98 | +0.98<br>−0.98 | +1.00<br>−0.99 | +1.02<br>−1.02 |
| Jets | +0.80<br>−5.33 | +0.68<br>−4.56 | +0.48<br>−3.86 | +0.46<br>−4.22 | +0.62<br>−4.17 | +0.65<br>−4.45 | +0.38<br>−3.22 |
| $b$-tagging | +3.06<br>−6.16 | +3.54<br>−5.78 | +3.75<br>−5.39 | +3.78<br>−5.69 | +3.81<br>−5.67 | +4.01<br>−6.01 | +4.31<br>−5.41 |
| $E_{\mathrm{T}}^{\mathrm{miss}}$(soft) | +1.18<br>−1.75 | +1.20<br>−1.71 | +1.17<br>−1.90 | +1.09<br>−1.79 | +1.08<br>−1.84 | +1.16<br>−1.66 | +1.30<br>−1.96 |
| Process | $gg \to A$ | | | | | | |
| $m_A$ | 110 GeV | 130 GeV | 150 GeV | 170 GeV | 200 GeV | 250 GeV | 300 GeV |
| Muons | +0.96<br>−0.96 | +0.98<br>−0.98 | +0.95<br>−0.95 | +1.00<br>−1.00 | +0.97<br>−0.97 | +1.00<br>−1.00 | +1.01<br>−1.01 |
| Jets | +1.88<br>−4.67 | +0.06<br>−5.46 | +0.37<br>−2.21 | +0.68<br>−4.49 | +0.31<br>−2.54 | +1.18<br>−4.13 | +0.62<br>−3.84 |
| $b$-tagging | +5.65<br>−7.36 | +5.65<br>−7.85 | +6.17<br>−6.58 | +5.49<br>−7.10 | +6.36<br>−6.85 | +5.95<br>−7.27 | +6.01<br>−7.13 |
| $E_{\mathrm{T}}^{\mathrm{miss}}$(soft) | +1.14<br>−1.66 | +0.92<br>−1.49 | +0.93<br>−1.51 | +1.14<br>−1.57 | +1.02<br>−1.69 | +1.26<br>−1.64 | +0.96<br>−2.09 |

the order of only 1 % each. Only the systematic uncertainty related to the $b$–tagging has a larger impact on the expected signal yield of at the order of 5 %.

The differences in the number of observed and simulated background events as reported in Section 6.6 can be compared to the detector–related systematic uncertainties on the expected background yield from simulation. The impact of the above systematic sources is evaluated for the dominant background processes, the $Z/\gamma^*$ production in association with jets and $b$ jets and the $t\bar{t}$ production. The corresponding relative changes in the numbers of selected events are summarised in Table 6.9, separately for the $b$–vetoed and $b$–tagged event categories. The numbers of observed and expected background events given in Table 6.4 agree well within the relevant detector–related, cross section and Monte Carlo modelling uncertainties.

**Table 6.9:** Relative change (%) in the number of selected background events in the $b$–vetoed and $b$–tagged event categories due to detector–related systematic uncertainties.

| Event Category | $b$–vetoed | | | $b$–tagged | | |
|---|---|---|---|---|---|---|
| Process | $Z$+jets | $Z$+$b$-jets | $t\bar{t}$ | $Z$+jets | $Z$+$b$-jets | $t\bar{t}$ |
| Muons | +0.95<br>−0.97 | +0.97<br>−2.36 | +0.98<br>−1.11 | +0.99<br>−1.01 | +0.99<br>−1.03 | +0.99<br>−1.08 |
| Jets | +0.95<br>−0.02 | +1.48<br>−0.12 | +2.40<br>−0.25 | +1.39<br>−5.20 | +1.04<br>−4.83 | +0.26<br>−1.26 |
| $b$-tagging | +0.95<br>−0.06 | +1.83<br>−1.06 | +15.5<br>−13.9 | +7.58<br>−9.21 | +3.71<br>−6.12 | +4.43<br>−4.87 |
| $E_{\mathrm{T}}^{\mathrm{miss}}$(soft) | +1.15<br>−1.65 | +1.16<br>−1.75 | +5.37<br>−6.55 | +1.15<br>−1.65 | +1.16<br>−1.75 | +5.37<br>−6.55 |

**Luminosity Uncertainty** In addition to the above uncertainties, the imperfect knowledge of the luminosity is taken into account as mentioned in Section 4.3. The corresponding uncertainty in the total integrated luminosity is 3.9 % [113, 114]. Signal and background distributions from Monte Carlo simulations which are scaled to the integrated luminosity of the recorded data set are affected by this uncertainty. For the final results only the expected signal event yield is affected, the normlisation of the background estimate is not sensitive to this systematic uncertainty as the background contribution is estimated from data.

## 6.12 Results

This section presents the results of the statistical interpretation of the data based on a statistical hypothesis test using the profile likelihood ratio as test statistic as described in Reference [170] and summarised in Section 6.8.

The background model used for the hypothesis test is extracted from the data as described in Section 6.10. The signal model is obtained from the interpolation procedure of the simulated event samples as described in Section 6.9. Uncertainties in the signal production cross sections and systematic uncertainties in the integrated luminosity and the muon, jet and $E_{\mathrm{T}}^{\mathrm{miss}}$ reconstruction and the $b$–tagging (see Section 6.11) are assigned to the expected signal yield. Uncertainties in the signal and background model parameters are taken into account in terms of contributions affecting the normalisation and the shape of the signal and background expectations. The uncertainties are incorporated in the likelihood function in terms of nuisance parameters as discussed in Section 6.8.

The probability density functions of the test statistics used to evaluate local $p_0$–values

and exclusion limits are approximated using the asymptotic formulae (see Section 6.8). The validation of the method with Monte Carlo pseudo–experiments is described in Appendix B.

The results of the statistical interpretation presented in the following are obtained separately for the $b$–vetoed and the $b$–tagged event categories and for their statistical combination (see Section 6.8).

The mass ranges explored in the two event categories are different. For the $b$–vetoed event category, the $m_A$ is restricted to the range of 120 GeV to 300 GeV. For masses $m_A$ below 120 GeV the background cannot be modelled with sufficient precision using the present method due to the steep rise of the $Z/\gamma^*$ background contribution close to the $Z$ resonance. For $m_A$ above 300 GeV the sensitivity of the search becomes small given the integrated luminosity of the considered data sample. One the one hand, the expected signal yield becomes very small in the high mass range due to the production cross section decreasing with mass (see Figure 3.7). Furthermore, the small number of events observed at high invariant masses complicates the precise shape analysis of the $\mu^+\mu^-$ invariant mass distribution in this region due to the increasing impact of statistical fluctuations in each bin.

For the same reasons the maximum mass considered in the $b$–tagged event category, $m_A = 200$ GeV, is even lower since the event selection efficiency is substantially reduced compared to the $b$–vetoed event category.

The statistical combination of both event categories is consequently performed in the $m_A$ range of 120 GeV to 200 GeV. For higher $m_A$ values, results are only obtained in the $b$–vetoed event category.

The explored $\tan\beta$ values range from 5 to 70 in both event categories. For low values of $\tan\beta$, the production cross section of neutral MSSM Higgs bosons is small (see Figure 3.7) and, therefore, the sensitivity of the search to low $\tan\beta$ values is limited. The upper value of $\tan\beta$ is due to theoretical constraints. As discussed in Section 2.2.6, the theoretical predictions of the MSSM loose their validity for very high values of $\tan\beta$ since the couplings increase such that perturbation theory breaks down. The theoretical bound on $\tan\beta$ depends on the choice of the model parameters. For the $m_h^{\text{max}}$ scenario, no theoretical predictions are made for $\tan\beta > 70$.

**Signal Significance in the $m_A$–$\tan\beta$ Plane** In order to quantify a possible excess in the data compatible to the signal shape expected in the MSSM $m_h^{\text{max}}$ scenario, the observed and expected local $p_0$–values are determined in dependence on $m_A$ and $\tan\beta$. The local $p_0$–value defined in Equation 6.13 is the probability of observing a statistical fluctuation of the background with at least the size of the observed excess. It is related to the signal significance through Equation 6.14 such that smaller local $p_0$–values correspond to higher signal significance of the observed excess of events.

The expected $3\,\sigma$ evidence and $5\,\sigma$ discovery contours are evaluated in the $m_A$–$\tan\beta$ plane for the statistical combination of the two event categories and are shown in Figure 6.14(a). The sensitivity of the $h/A/H \to \mu^+\mu^-$ search in the $m_h^{\text{max}}$ scenario with positive Higgs mixing parameter is at the maximum for the lowest value of $m_A$ and decreases with mass. For $m_A = 120\,\text{GeV}$, the signal can be discovered with a significance of $5\,\sigma$ for $\tan\beta \gtrsim 40$, a $3\,\sigma$ evidence is expected for $\tan\beta \gtrsim 26$. For increasing masses, the signal can only be discovered for higher $\tan\beta$ values. Even for the highest $\tan\beta$ value of 70 a discovery is only possible for $m_A \lesssim 200\,\text{GeV}$ and an evidence only for $m_A$ values up to about 260 GeV. The step in the $3\,\sigma$ contour at $m_A = 200\,\text{GeV}$ comes from the increase in sensitivity due to the combination of the $b$–vetoed and $b$–tagged event categories for $m_A < 200\,\text{GeV}$ while for $m_A > 200\,\text{GeV}$ only the $b$–vetoed category is used.

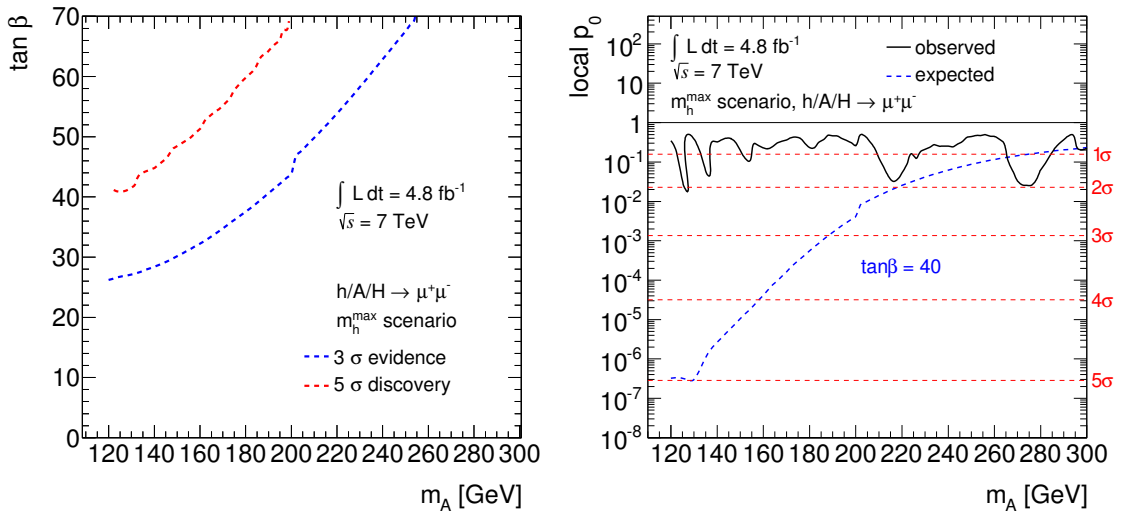


(a) (b)

**Figure 6.14:** Expected $3\,\sigma$ and $5\,\sigma$ signal significance contours in the $m_A$–$\tan\beta$ plane (a) and expected (dashed line) and observed (solid line) local $p_0$–values as a function of $m_A$ and $\tan\beta = 40$ (b) for neutral MSSM Higgs boson decays to $\mu^+\mu^-$ in the $m_h^{\text{max}}$ scenario with positive Higgs mixing parameter.

For the example of $\tan\beta = 40$, Figure 6.14(b) shows the expected and observed local $p_0$–values as a function of $m_A$. The fluctuations in the $\mu^+\mu^-$ invariant mass distribution result signal significances of typically less than $2\,\sigma$. The lowest expected local $p_0$–value is at $m_A = 130\,\text{GeV}$ where all three neutral MSSM Higgs bosons have almost equal masses and cannot be resolved experimentally for $\tan\beta = 40$. The step in the expected local $p_0$–value indicates the increase of sensitivity due to the combination of the two event categories. The expected and observed local $p_0$–values evaluated separately for the two event categories are shown in Figure 6.15.

It can be seen that the sensitivity to a $h/A/H \to \mu^+\mu^-$ signal is much higher in the $b$–vetoed than in the $b$–tagged event category. This is due to the fact that, although the signal–to–background ratio is much better in the $b$–tagged category, the uncertainty in the expected background is substantially higher compared to the $b$–vetoed event category. This is caused by the strongly reduced number of selected events in the $b$–tagged category resulting in rather large statistical fluctuations in the $\mu^+\mu^-$ invariant mass distribution which affect the precision of the background estimate from the fit to the data. Once a larger data set is available, the sensitivity in the $b$–tagged event category is expected to improve significantly and to exceed the sensitivity in the $b$–vetoed category.

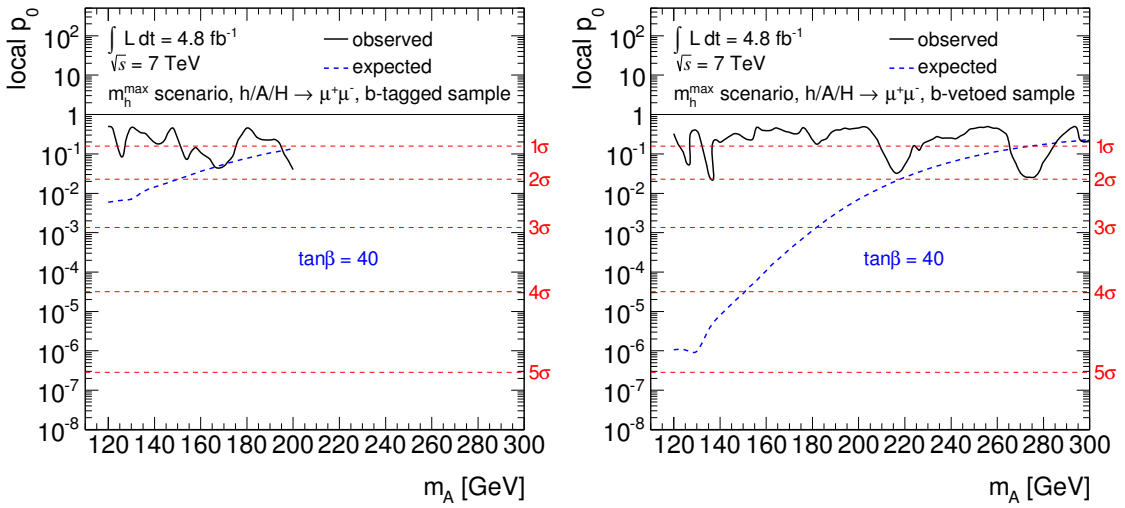


(a) (b)

**Figure 6.15:** Expected (dashed line) and observed (solid line) local $p_0$–values for the neutral MSSM Higgs boson search in the $m_h^{\text{max}}$ scenario for $\tan\beta = 40$ as a function of $m_A$ for the $b$-tagged (a) and $b$–vetoed (b) event categories.

The lowest observed local $p_0$–value is found for the combination of the two event categories at $m_A = 126\,\text{GeV}$ and $\tan\beta = 13$ and corresponds to a signal significance of $2.2\,\sigma$. After taking into account the look–elsewhere effect [181] in the whole scanned two–dimensional $m_A$–$\tan\beta$ parameter region with $120\,\text{GeV} \leq m_A \leq 300\,\text{GeV}$ and the $5 \leq \tan\beta \leq 70$, the fluctuation corresponds to a global signal significance of only $1.1\,\sigma$.

In summary, no significant excess of events compared to the Standard Model background expectation is found in either the $b$–tagged or the $b$–vetoed event category and in their combination. This is supported by the results of the model–independent BumpHunter [192] analysis described in Appendix B. Exclusion limits on the signal production cross section are evaluated at the 95 % confidence level (CL) using the $\text{CL}_\text{s}$ method described in Section 6.8.

The limits are evaluated in the $m_A$–$\tan\beta$ plane under the assumption of a neutral MSSM Higgs boson signal in the $m_h^{\text{max}}$ benchmark scenario with positive Higgs mixing parameter. In addition, less model–dependent exclusion limits are evaluated on the production cross section times branching fraction to $\mu^+\mu^-$ of a generic scalar or pseudo–scalar boson, $\phi$, produced either in gluon fusion or in association with $b$ quarks. No distinction between a scalar and a pseudo–scalar boson can be made in this analysis. This interpretation serves as test of models beyond the MSSM $m_h^{\text{max}}$ scenario.

**Exclusion Limits in the $m_A$–$\tan\beta$ Plane** The exclusion limits for neutral MSSM Higgs bosons produced in gluon fusion and in association with $b$ quarks are evaluated for both the $b$–tagged and $b$–vetoed event categories assuming the MSSM signal model in the $m_h^{\text{max}}$ scenario as described in Section 6.9. The resulting exclusion limits at 95 % CL are shown as functions of $m_A$ and $\tan\beta$ in Figure 6.16 for the two event categories separately and in Figure 6.17 for their statistical combination.

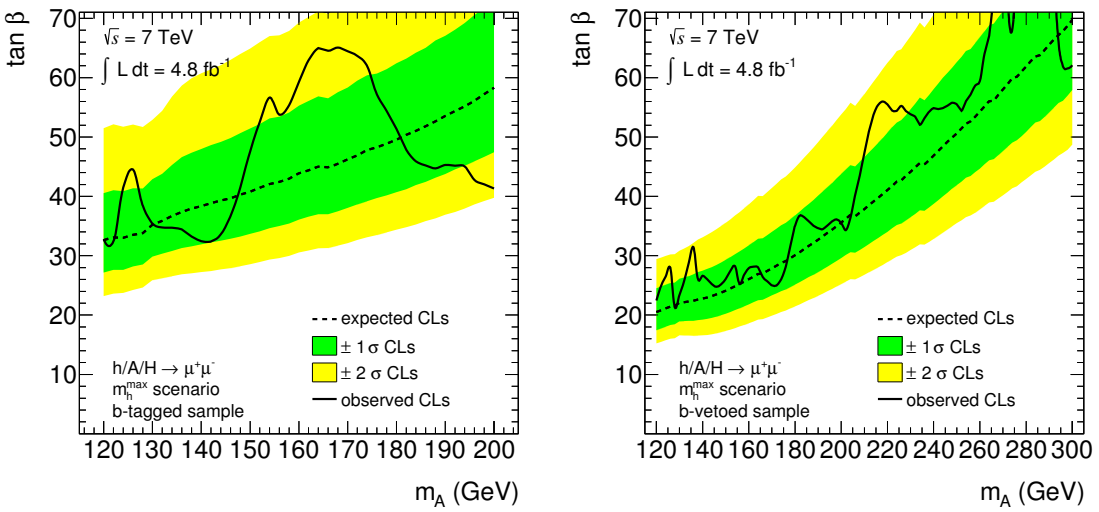


(a) (b)

**Figure 6.16:** Expected (dashed line) and observed (solid line) exclusion limits at the 95 % CL as a function of $m_A$ and $\tan\beta$ for neutral MSSM Higgs boson decays to $\mu^+\mu^-$ in the $m_h^{\text{max}}$ scenario with positive Higgs mixing parameter for the $b$–tagged (a) and $b$–vetoed (b) event categories. The green and yellow bands represent the $\pm 1\,\sigma$ and $\pm 2\,\sigma$ uncertainty bands on the expected exclusion limit. The area of the $m_A$–$\tan\beta$ plane above the solid lines is excluded at the 95 % CL.

Also in the exclusion limits one can see that the sensitivity for a MSSM Higgs boson signal is higher in the $b$–vetoed event category than in the $b$–tagged event category for the analyzed data set. The allowed parameter space by the $b$–vetoed event category is

therefore more restricted with a maximum $\tan\beta$ value of about 21 for $m_A = 120\,\text{GeV}$.

The combination of the two event categories shown in Figure 6.17 improves the expected limit from the $b$–vetoed event category by about 10 % with respect to the limit for the $b$–vetoed category below $m_A = 200\,\text{GeV}$. The expected excludable parameter space reaches from $\tan\beta \gtrsim 70$ at $m_A = 300\,\text{GeV}$ to $\tan\beta \gtrsim 20$ for $m_A = 120\,\text{GeV}$. The observed limit shows statistical fluctuations, especially for low $m_A$ values, contained within the $\pm 2\,\sigma$ uncertainty band of the expected limit. The fluctuations are caused by the fact that the signal is expected to appear as narrow resonances with a structure similar to the statistical fluctuations of the background. This is in particular the case for low values of $m_A$ and $\tan\beta$, where the expected signal resonances are very narrow.

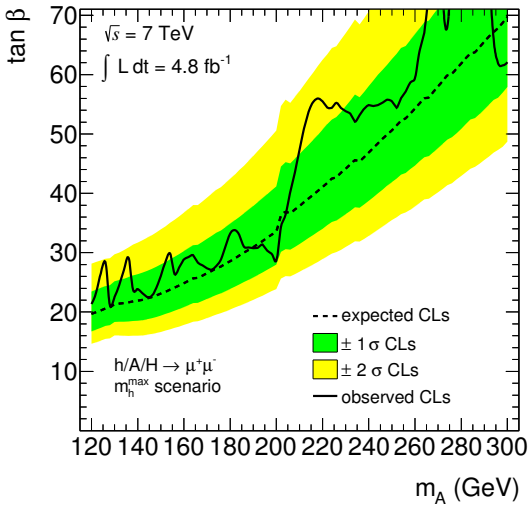


**Figure 6.17:** Expected (dashed line) and observed (solid line) exclusion limits at the 95 % CL as a function of $m_A$ and $\tan\beta$ for neutral MSSM Higgs boson decays to $\mu^+\mu^-$ in the $m_h^{\text{max}}$ scenario for the statistical combination of $b$–tagged and $b$–vetoed event categories below $m_A = 200\,\text{GeV}$ and the $b$–vetoed category alone above $m_A = 200\,\text{GeV}$.

**Exclusion Limits on the Production Cross Section** Exclusion limits on the production cross section of a generic scalar or pseudo–scalar boson, $\phi$, multiplied by the branching fraction to a muon pair, $\mathcal{B}(\phi \to \mu^+\mu^-)$, are useful for a less model–dependent interpretation of the search results beyond the $m_h^{\text{max}}$ MSSM benchmark scenario. The limit calculation is performed as for the above model–dependent interpretation with the two differences that no uncertainty in the signal production cross section is assigned (since the limit is set on this parameter) and only the $A$ boson resonance at $\tan\beta = 20$ is considered as the signal model. Even though the results are interpreted as exclusion limits on the production of a generic (pseudo–)scalar boson, the obtained exclusion limits are not entirely model–independent as are the results presented in Appendix B. Firstly, the signal model

has a predefined width of the resonance. In addition, the result is only valid for $\phi \to \mu^+\mu^-$ decays with event selection efficiency comparable to the one for the $A$ boson at $\tan\beta = 20$.

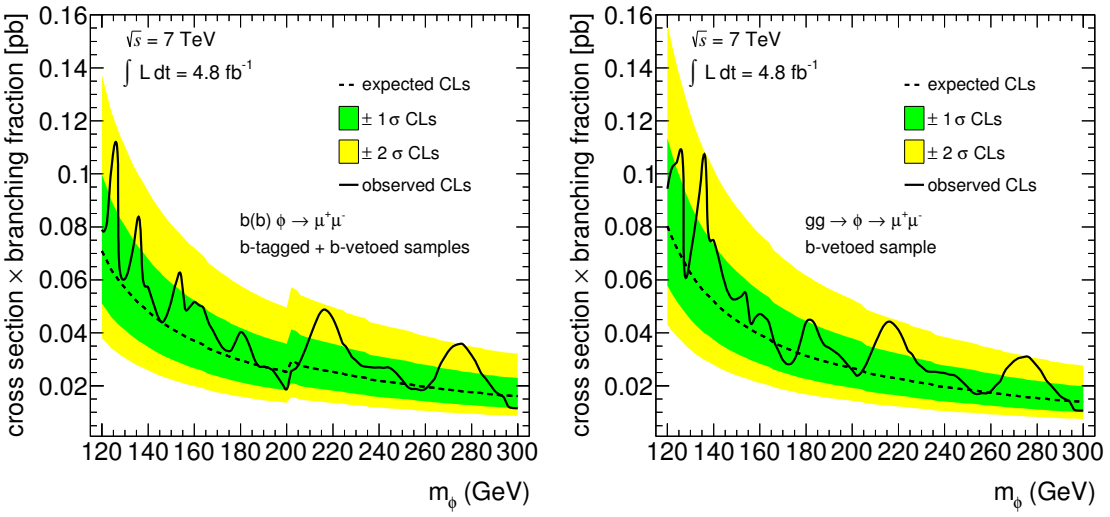


(a) (b)

**Figure 6.18:** Expected (dashed line) and observed (solid line) exclusion limits at the 95 % CL on the production cross section times the branching fraction of a generic (pseudo–)scalar boson, $\phi$, produced in association with $b$–quarks for the combination of the $b$–tagged and $b$–vetoed event categories (a) and in gluon fusion for the $b$–vetoed event category only (b). The green and yellow bands represent the $\pm 1\,\sigma$ and $\pm 2\,\sigma$ uncertainty bands on the expected exclusion limit, respectively. Cross sections times branching fractions above the solid lines are excluded at the 95 % CL.

The 95 % CL exclusion limits on the cross section times the branching ratio for a (pseudo–)scalar boson produced in association with $b$ quarks and decaying to $\mu^+\mu^-$ are evaluated for the combination of the $b$–tagged and $b$–vetoed event categories in the $m_\phi$ range of 120 GeV to 200 GeV. For masses $m_\phi$ greater than 200 GeV the results are obtained for the $b$–vetoed event category alone. The results are shown in Figure 6.18(a). The expected limit decreases from approximately 0.07 pb for $m_\phi = 120$ GeV to approximately 0.015 pb for $m_\phi = 300$ GeV since the amount of background decreases with $m_\phi$. The benefit of the combination of the $b$–tagged and $b$–vetoed event categories can be seen in the step in the expected limit around $m_\phi = 200$ GeV and amounts to about 20 %. The observed limit is fluctuating within the expected $\pm 2\,\sigma$ uncertainty band due to reasons discussed above.

The exclusion limits for gluon fusion production of a (pseudo–)scalar boson with subsequent decay to muon pairs are evaluated in the $b$–vetoed event category alone since the acceptance of a gluon fusion signal in the $b$–tagged event category is very low. The result is shown in Figure 6.18(b). The expected exclusion limit decreases from approximately 0.08 pb for $m_\phi = 120$ GeV to approximately 0.015 pb for $m_\phi = 300$ GeV. The fluctuations

in the observed limit are contained in the $\pm 2\,\sigma$ uncertainty band of the expected limit.

The exclusion limits for the two production modes in the $b$–vetoed event category are very similar because the signal topology and consequently the event acceptance are very similar for the signal events from both production modes (see Appendix B).

## 6.13 Combination with $h/A/H \to \tau^+\tau^-$ Decay Channels

The presented search for $h/A/H \to \mu^+\mu^-$ decays contributes to the combined search results for neutral MSSM Higgs bosons with the ATLAS detector [132] which include the $h/A/H \to \mu^+\mu^-$ and $h/A/H \to \tau^+\tau^-$ decay channels. The $h/A/H \to \tau^+\tau^-$ searches are performed in three final states according to the decay products of the two $\tau$ leptons: the fully leptonic, the semi–leptonic and the fully hadronic search channels which are briefly outlined below. Details of the event selection, background estimation techniques and systematic uncertainties can be found in the original publication [132]. The $\tau^+\tau^-$ invariant mass cannot be reconstructed directly due to the neutrinos in the $\tau$ decays. An algorithm known as the Missing Mass Calculator (MMC) [193] is applied which performs a scan over the possible angles between the neutrinos and the visible $\tau$ decay products and determines the most likely value of the $\tau^+\tau^-$ invariant mass relying on simulation. The MMC $\tau^+\tau^-$ invariant mass is used as discriminating variable for the three $h/A/H \to \tau^+\tau^-$ channels below.

**The Fully Leptonic $\boldsymbol{\tau^+\tau^-}$ Channel** In the fully leptonic $\tau^+\tau^-$ channel each $\tau$ lepton decays to an electron or muon and two neutrinos resulting in the final states $e^+e^- + 4\nu$, $\mu^+\mu^- + 4\nu$ or $e^\pm\mu^\mp + 4\nu$. Only the $e^\pm\mu^\mp + 4\nu$ final state is considered in this analysis. The corresponding branching fraction amounts to 6 %. Final states with both $\tau$ leptons decaying either to electrons or to muons are not considered because of the large background contribution from $Z/\gamma^* \to e^+e^-$ and $Z/\gamma^* \to \mu^+\mu^-$. In addition, the $h/A/H \to \tau^+\tau^- \to \mu^+\mu^-$ and $h/A/H \to \mu^+\mu^-$ decay channels have a certain overlap which would complicate their combination. The dominant background for the studied final state is the $Z/\gamma^* \to \tau^+\tau^-$ process. Remaining non–resonant backgrounds such as $t\bar{t}$ and multi–jet production play a minor role.

**The Semi–Leptonic $\boldsymbol{\tau^+\tau^-}$ Channel** For the semi–leptonic $\tau^+\tau^-$ final state, one $\tau$ lepton decays to either an electron or a muon and two neutrinos while the other $\tau$ lepton decays hadronically accompanied by one neutrino. This final state has the largest branching fraction of 46 %. A hadronic $\tau$ decay is characterised by one, three or five charged hadrons with a total electric charge of $\pm 1$ and possibly several neutral hadrons. The $\tau$ decay products are boosted and therefore collimated such that the visible decay products form a structure similar to a jet, a so–called $\tau$ jet. The energy of the reconstructed $\tau$ jets is

calibrated separately from quark and gluon jets. A multivariate discriminant is used to separate $\tau$ jets from quark and gluon jets [194]. The dominant background also in this final state is the $Z/\gamma^* \to \tau^+\tau^-$ process while also contributions from multi–jet production and $W$ production in association with jets are significantly increased compared to the fully leptonic final state.

**Fully Hadronic $\boldsymbol{\tau^+\tau^-}$ Channel** In the fully hadronic $\tau^+\tau^-$ final state, both $\tau$ leptons decay hadronically accompanied by two neutrinos with a branching fraction of 42 %. In this channel the multi–jet background contributes by a similar amount as the $Z/\gamma^* \to \tau^+\tau^-$ process while remaining backgrounds such as $t\bar{t}$ are a minor contribution.

**Combination of All Search Channels** The statistical combination of all three $\tau^+\tau^-$ channels and of the $\mu^+\mu^-$ channel employs the product of the corresponding binned likelihood functions shown in Equation 6.5 for both event categories. As described in Section 6.8, the likelihood functions for each category are a product of Poisson probabilities for the bins of the distributions of the discriminating variables in the signal regions and in signal–free control regions for the $\tau^+\tau^-$ channels and of nuisance parameter probabilities which take into account the systematic uncertainties. The correlations of the systematic uncertainties across the different channels are taken into account (see Section 6.8).

The combination of the $\mu^+\mu^-$ channel with the $\tau^+\tau^-$ channels is performed in the mass range of 120 GeV to 300 GeV defined by the $h/A/H \to \mu^+\mu^-$ search. Even though in this range there are more $m_A$ points scanned in the $h/A/H \to \mu^+\mu^-$ search due to the better mass resolution compared to the search in the $h/A/H \to \tau^+\tau^-$ channels, the combination is performed only for those $m_A$ points which are scanned by the $h/A/H \to \tau^+\tau^-$ searches. The data set used for the $h/A/H \to \tau^+\tau^-$ searches corresponds to an integrated luminosity of $4.7\,\text{fb}^{-1}$ which is slightly smaller than the data set used for the $h/A/H \to \mu^+\mu^-$ search since the $\tau_{\text{had}}$ reconstruction imposes further data quality requirements which do not have to be applied to the events in the data set used for the $h/A/H \to \mu^+\mu^-$ search.

Combining the four search channels, no significant excess of events above the expected background is observed. Exclusion limits at 95 % CL are evaluated for the neutral MSSM Higgs boson signal expected in the $m_h^{\text{max}}$ scenario with positive Higgs mixing parameter as well as for the production cross section of a generic scalar boson, $\phi$, times branching fractions to $\mu^+\mu^-$ or $\tau^+\tau^-$ as discussed in Section 6.12. The results are shown in Figure 6.19 and Figure 6.20.

The combined exclusion limit in the $m_h^{\text{max}}$ MSSM scenario is evaluated in the mass range of 90 GeV to 500 GeV. The highest sensitivity is expected for $m_A \approx 140\,\text{GeV}$. The excluded parameter space reaches from $\tan\beta \gtrsim 56$ for $m_A = 500\,\text{GeV}$ down to the tightest constraint of $\tan\beta > 9.3$ for $m_A = 130\,\text{GeV}$. These results significantly reduce the allowed $m_A$–$\tan\beta$ parameter space of the MSSM $m_h^{\text{max}}$ scenario compared to previous results by

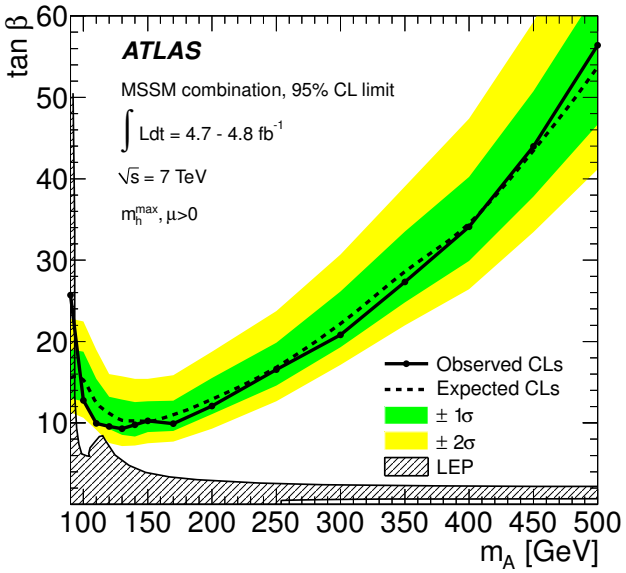


(a)

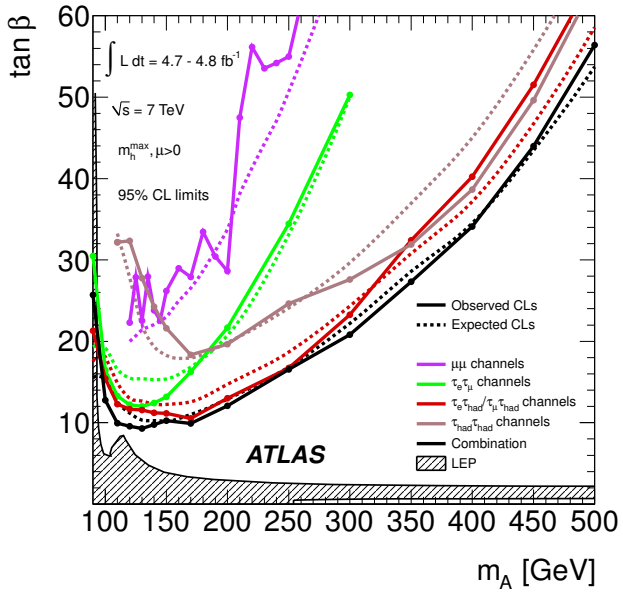


(b)

**Figure 6.19:** Expected (dashed line) and observed (solid line) exclusion limits at 95 % CL on $\tan\beta$ as a function of $m_A$ for the combined search in the $\mu^+\mu^-$ and $\tau^+\tau^-$ decay channels with the $\pm 1\,\sigma$ and $\pm 2\,\sigma$ uncertainty bands on the expected limit (a) and with the contributions of the different final states, $\mu^+\mu^-$, fully leptonic ($\tau_{\mathrm{lep}}\tau_{\mathrm{lep}}$), semi–leptonic ($\tau_{\mathrm{lep}}\tau_{\mathrm{had}}$) and fully hadronic ($\tau_{\mathrm{had}}\tau_{\mathrm{had}}$) $\tau^+\tau^-$ decays (b). Values of $\tan\beta$ above the shown solid lines are excluded. The parameter space region excluded by the LEP experiments is shown as hatched area [132].

the ATLAS collaboration [195]. Results from the searches at the LEP experiments [96] exclude a complementary region in the parameter space at low values of $\tan\beta$ as shown in Figure 6.19. A large fraction of the allowed parameter space also remains unconstrained if one assumes that the new Higgs–like particle discovered at the LHC is one of the neutral CP–even MSSM Higgs bosons as discussed in Section 3.4 [90, 98].

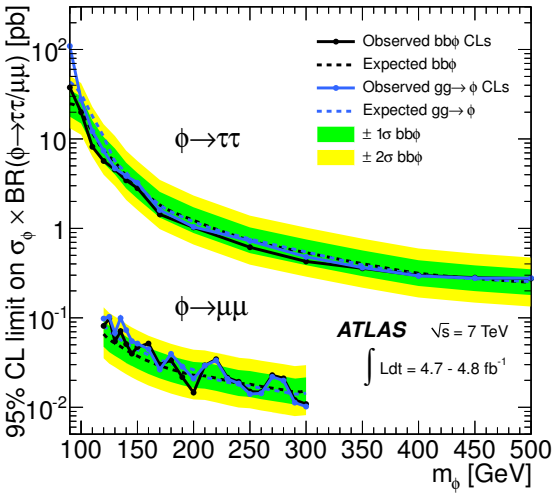


(a)

**Figure 6.20:** Expected (dashed line) and observed (solid line) exclusion limits at 95 % CL on the production cross section times the branching fractions of a generic (pseudo–)scalar boson, $\phi$, decaying to $\tau^+\tau^-$ and $\mu^+\mu^-$ pairs for gluon–fusion (blue) and associated production with $b$ quarks (black). The green and yellow bands represent the $\pm 1\,\sigma$ and $\pm 2\,\sigma$ uncertainty bands on the expected limit for the $b$–quark associated production [132].

The $h/A/H \to \mu^+\mu^-$ decay channel clearly provides lower sensitivity compared to the $h/A/H \to \tau^+\tau^-$ search channels due to the about 300 times lower branching fraction. The difference in sensitivity, however, is much smaller than the difference in the branching fraction. The $\mu^+\mu^-$ channel is competitive with the fully hadronic $\tau^+\tau^-$ final state in the intermediate $m_A$ range and even more sensitive for $m_A \leq 130\,\text{GeV}$.

In addition to the exclusion limits, the signal significances of the largest excesses of events have been evaluated. The smallest local $p_0$–values per channel are 0.014 ($2.2\sigma$) at $m_A = 125\,\text{GeV}$ in the $\mu^+\mu^-$ channel, 0.014 ($2.2\sigma$) at $m_A = 90\,\text{GeV}$ in the fully leptonic $\tau^+\tau^-$ channel, 0.067 ($1.5\sigma$) at $m_A = 90\,\text{GeV}$ in the semi–leptonic $\tau^+\tau^-$ channel and 0.097 ($1.3\sigma$) at $m_A = 140\,\text{GeV}$ in the fully hadronic $\tau^+\tau^-$ channel. The smallest local $p_0$–value for the statistical combination of all channels is 0.004 ($2.7\sigma$) at $m_A = 90\,\text{GeV}$. The significance of this excess is below $2\,\sigma$ after taking into account the look–elsewhere effect in the range $90\,\text{GeV} \leq m_A \leq 500\,\text{GeV}$ and $5 \leq \tan\beta \leq 60$ [181].

**Comparison with Neutral MSSM Higgs Boson Searches with CMS** Similar searches for neutral MSSM Higgs bosons have been performed by the CMS collaboration [134, 135].

Searches for $h/A/H \to \tau^+\tau^-$ decays used the semi–leptonic channel with one $\tau$ lepton decaying either to an electron or a muon and the fully leptonic final states $\mu^+\mu^- + 4\nu$ and $e^\pm\mu^\mp + 4\nu$. The searches have been performed on a substantially larger data set compared to the ATLAS search corresponding to a total integrated luminosity of $17\,\text{fb}^{-1}$ recorded at $\sqrt{s} = 7\,\text{TeV}$ and $8\,\text{TeV}$. No significant excess was found in the data and 95 % CL exclusion limits have been evaluated shown in Figure 6.21(a). The results further reduce the allowed $m_A$–$\tan\beta$ parameter space of the MSSM $m_h^{\text{max}}$ scenario to $\tan\beta \leq 5$ for $90\,\text{GeV} \lesssim m_A \lesssim 150\,\text{GeV}$ and $\tan\beta \leq 50$ for $m_A \leq 800\,\text{GeV}$.

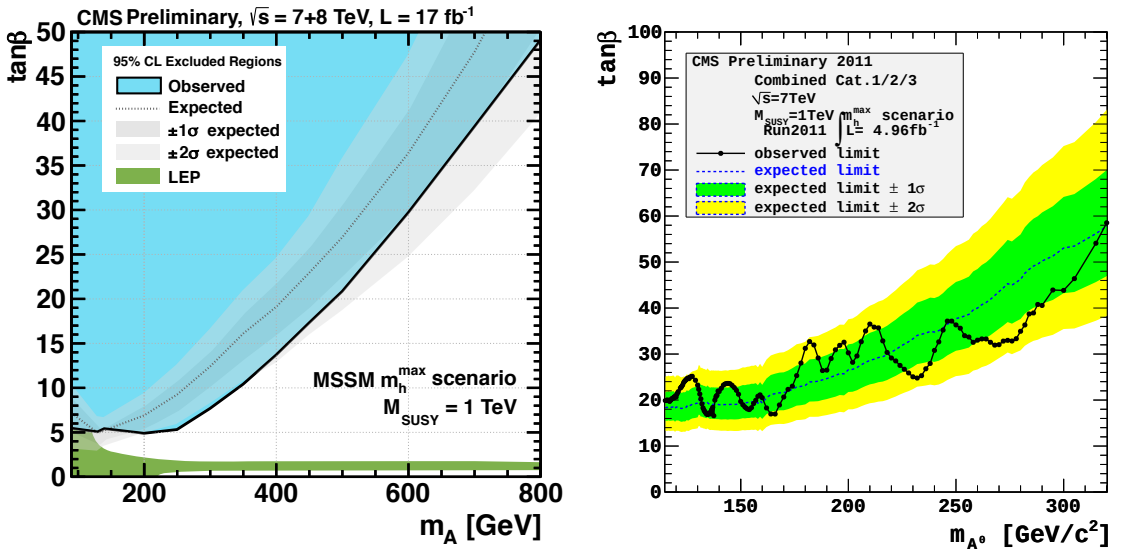


(a) (b)

**Figure 6.21:** Expected (dashed line) and observed (solid line) 95 % CL exclusion limits as a function of $m_A$ and $\tan\beta$ for the MSSM $m_h^{\text{max}}$ scenario obtained in the $h/A/H \to \tau^+\tau^-$ decay channel for a total integrated luminosity of $17\,\text{fb}^{-1}$ at $\sqrt{s} = 7\,\text{TeV}$ and $8\,\text{TeV}$ data [134] (a) and in the $h/A/H \to \mu^+\mu^-$ decay channel for a total integrated luminosity of $4.9\,\text{fb}^{-1}$ at $\sqrt{s} = 7\,\text{TeV}$ [135] (b).

In addition, the CMS collaboration has performed a search in the $h/A/H \to \mu^+\mu^-$ decay channel using a proton–proton collision data sample with integrated luminosity of $4.96\,\text{fb}^{-1}$ at $\sqrt{s} = 7\,\text{TeV}$. The results shown in Figure 6.21(b) are similar to the results presented in this thesis.

Similar to the results from the ATLAS collaboration discussed above, a significant fraction of the allowed parameter space remains unconstrained assuming the Higgs boson candidate discovered at the LHC is the light CP–even Higgs boson in the MSSM $m_h^{\text{max}}$

scenario (see Section 3.4). The allowed $m_A$–$\tan\beta$ region for the heavy CP–even MSSM Higgs boson being the discovered particle shown in Figure 3.13(b) is excluded by the $h/A/H \to \tau^+\tau^-$ results of CMS (see Figure 6.21(a)).

# Chapter 7

# Prospects for the Standard Model Higgs Boson Search in $\mu^+\mu^-$ Decays

This chapter presents a study of the prospects for the search for the Standard Model Higgs boson with a mass of $m_H = 125\,\text{GeV}$ in the rare decay to two muons with the ATLAS detector. The study is performed with simulated proton–proton collision data at the design LHC centre–of–mass energy of $\sqrt{s} = 14\,\text{TeV}$ for two benchmark scenarios with integrated luminosities of $300\,\text{fb}^{-1}$ and $3000\,\text{fb}^{-1}$ which are expected to be reached after several stages of LHC upgrades. The search in the $H \to \mu^+\mu^-$ channel is motivated in Section 7.1 and the analysis strategy is outlined in Section 7.2. The signal and background processes considered and the corresponding simulated data samples are summarised in Section 7.3. Parametrisations of the muon trigger and reconstruction efficiencies and of the transverse momentum resolution assumed for the ATLAS detector performance at the HL–LHC are discussed in Section 7.4. Section 7.5 explains the event selection criteria adopted from the $h/A/H \to \mu^+\mu^-$ search with only minor modifications. The signal and background models employed to extract the expected numbers of signal and background events are discussed in Section 7.6. Systematic uncertainties are summarised in Section 7.7. The expected sensitivity to the $H \to \mu^+\mu^-$ decay is evaluated in Section 7.8 for the considered future LHC upgrade scenarios. The results also contribute to the evaluation of the prospects for the measurement of the Higgs boson properties.

## 7.1 Motivation

After the discovery of a Higgs boson candidate with a mass of about 125.5 GeV in the bosonic decay modes $\gamma\gamma$, $ZZ^*$ and $W^+W^-$ (see Section 3.4), the emphasis of the LHC experiments is now to characterise the new boson and probe the compatibility of its properties with the predictions for the Standard Model Higgs boson. In case it is indeed the Standard Model Higgs boson, it must also decay to fermions. In addition, the spin, charge conjugation and parity (CP) quantum number as well as the couplings to Standard Model particles need to be evaluated precisely in order to pin down the exact nature of the new boson.

As for the neutral MSSM Higgs bosons the decay of the Standard Model Higgs boson to a muon pair allows for precision mass measurement because of the excellent experimental mass resolution as discussed in Section 6.1. In addition, this channel provides information on the fermionic couplings of the Higgs boson. On the other hand, the branching fraction of decays to $\mu^+\mu^-$ is very small, about $2 \cdot 10^{-4}$ for $m_H = 125\,\text{GeV}$ [69]. A search for the Standard Model $H \to \mu^+\mu^-$ decays has been performed by the ATLAS collaboration using proton–proton collision data recorded in 2012 with an integrated luminosity of $20.7\,\text{fb}^{-1}$ at a centre–of–mass energy of $\sqrt{s} = 8\,\text{TeV}$ [196] showing that a much larger data sample is needed in order to be sensitive to this rare process.

Several upgrades of the LHC are planned for the next 10 years in oder to achieve and exceed the design parameters of the machine as discussed in Section 4.3.1. Two benchmarks are set for the operation at design centre–of–mass energy of $\sqrt{s} = 14\,\text{TeV}$. An integrated luminosity of $300\,\text{fb}^{-1}$ is expected by the end of the approved LHC physics programme. After a possible upgrade to the high–luminosity LHC (HL–LHC), an ultimate total integrated luminosity of $3000\,\text{fb}^{-1}$ can be reached at the end of the accelerator's lifetime.

Various studies are carried out to evaluate the expected physics potential of the ATLAS experiment in the scope of the upgraded LHC machine. Also in the frame of the precision Higgs boson physics programme, new search channels are probed and prospects for the measurements of the spin, CP and coupling properties are determined assuming a Standard Model Higgs boson with a mass of $m_H = 125\,\text{GeV}$ [197, 198].

In view of the possible high–luminosity upgrade of the LHC, the expected ATLAS sensitivity to the decay of the Standard Model Higgs boson with $m_H = 125\,\text{GeV}$ to $\mu^+\mu^-$ is evaluated for a proton–proton collision energy of $\sqrt{s} = 14\,\text{TeV}$ and the two benchmark integrated luminosities of $300\,\text{fb}^{-1}$ and $3000\,\text{fb}^{-1}$. The results have been published in References [197, 198] and used for the Physics Briefing Book for the European Strategy for Particle Physics [199].

## 7.2 Analysis Strategy

Prospects for the sensitivity of the ATLAS experiment to the Standard Model Higgs boson with $m_H = 125\,\text{GeV}$ in decays to muon pairs are evaluated in an inclusive search in the HL–LHC regime. The analysis follows to a large degree the analysis developed for the neutral MSSM Higgs boson search presented in Chapter 6.

For the inclusive $H \to \mu^+\mu^-$ search only the presence of two oppositely charged muons with high transverse momenta is required. The inclusive signal signature and the dominant backgrounds are equal to the MSSM Higgs boson search. Differences are that the signal appears as only one resonance and that the production cross section times branching fraction is significantly smaller for the Standard Model Higgs boson than for the neutral MSSM Higgs bosons in largest parts of the allowed MSSM parameter space.

To evaluate the sensitivity with a future ATLAS detector at the HL–LHC, the presented study uses simulated events accounting for the expected detector response by simplified parametrisations of the muon trigger and reconstruction efficiencies and the muon transverse momentum resolution. Detailed Monte Carlo simulation of the detector response is not yet available for the high–pileup environment of the HL–LHC.

Additional correction factors for the event selection efficiencies for the signal and different background processes are derived from comparisons of the parametrised by the detailed detector simulation at $\sqrt{s} = 7\,\text{TeV}$ and applied to the event yields of the $\sqrt{s} = 14\,\text{TeV}$ selection.

The total expected background in the signal region is determined from a sideband fit to the $\mu^+\mu^-$ invariant mass distribution in the mass range of 100 GeV to 160 GeV.

Systematic uncertainties affecting the signal and background expectations arise from the background modelling uncertainty and the theoretical uncertainties in the signal production cross sections and branching fraction. No systematic uncertainties in the expected performance parametrisations are considered.

The sensitivity prospects are evaluated in terms of expected exclusion limits and signal significances. In addition, the results also contribute to the determination of the Higgs boson couplings to Standard Model particles combining several complementary search channels.

## 7.3 Signal and Background Processes

In the inclusive search for Standard Model $H \to \mu^+\mu^-$ decays, the signal signature is only a pair of oppositely charged isolated muons with high transverse momenta. The contributing Higgs boson production processes are the gluon fusion, vector boson fusion, vector–boson–associated and top–quark–pair–associated production modes discussed in

Section 3.2. The tree–level Feynman diagrams for the different processes are shown in Figure 3.3.

The dominant Standard Model background processes are the $Z/\gamma^*$ boson, $t\bar{t}$ pair and $W^+W^-$ production. Their tree–level Feynman diagrams are shown in Figure 6.2.

The production cross sections times branching fractions for the signal and background processes in proton–proton collisions at a centre–of–mass energy of $\sqrt{s} = 14\,\text{TeV}$ are listed in Table 7.1. The cross section for gluon fusion production is calculated in NNLO with NNLL QCD and NLO electroweak (EW) corrections [200] using the complex–pole–scheme [70]. The cross sections for Higgs boson production via vector boson fusion and in association with vector bosons are calculated in NNLO QCD with NLO EW corrections using the zero–width approximation [69] treating separately the production in association with $W$ (WH) and $Z$ (ZH) bosons. For the production in association with top quark pairs, the cross section is calculated with NLO QCD corrections using the zero–width approximation as well. The branching fraction of the $H \to \mu^+\mu^-$ decay for $m_H = 125\,\text{GeV}$ is evaluated to be $2.2 \cdot 10^{-4}$ [69].

The production cross sections of $Z/\gamma^*$ and $W^+W^-$ processes are calculated in NNLO and NLO, respectively, using the MCFM programme [201]. The $t\bar{t}$ production cross section is calculated at NNLO with HATHOR [202]. The Standard Model input parameters used for the cross section calculations are given in Reference [203].

**Table 7.1:** Cross sections times branching fractions for the signal and background processes at $\sqrt{s} = 14\,\text{TeV}$. The cross sections for the signal processes for a Higgs boson mass of 125 GeV are given in fb, the cross sections for the background processes in pb.

| Process | Cross section |
|---|---|
| ggF $H \to \mu^+\mu^-$ | 11.08 |
| VBF $H \to \mu^+\mu^-$ | 0.9178 |
| VH $H \to \mu^+\mu^-$ | 0.5251 |
| ttH $H \to \mu^+\mu^-$ | 0.1345 |
| $Z \to \mu^+\mu^-$ $(60 < m_{\mu\mu} < 2000\,\text{GeV})$ | 2114 |
| $t\bar{t}$ $(m_t = 172.5\,\text{GeV})$ | 977.7 |
| $W^+W^- \to \mu^+\nu\mu^-\nu$ | 1.419 |

For the signal only the dominant gluon fusion production mode has been simulated. The signal events for a Standard Model Higgs boson with $m_H = 125\,\text{GeV}$ are generated with POWHEG [139–141] interfaced with PYTHIA [142] for the description of the underlying event. To obtain the signal expectation for each Higgs boson production mode, the signal events passing all selection criteria introduced in Section 7.5 are scaled according to the respective cross sections. This is justified, since for the presented inclusive search the signal selection efficiency is expected to be very similar for the different production modes.

The $Z/\gamma^*$ bosons are generated with the ALPGEN event generator [144] and the $t\bar{t}$ and $W^+W^-$ pairs are generated with the MC@NLO generator [145]. For the background samples the hadronisation is simulated using HERWIG [152] and the underlying event is simulated using the JIMMY package [153].

To account for the expected performance of the ATLAS detector in the HL–LHC environment several assumptions are taken into account and applied on the generated physics objects as discussed in Section 7.4.

## 7.4 Muon Performance Assumptions

Simplified parametrisations of the detector response are applied to the generated muons in order to account for the trigger, the reconstruction and identification efficiencies as well as the momentum resolution, based on expectations for an upgraded ATLAS detector at the HL–LHC [204]. The performance assumptions rely on measurements and simulations of the current performance under pileup conditions with up to 70 proton–proton interactions on average in one bunch crossing. These are extrapolated to the nominal and peak HL–LHC luminosities of $5 \cdot 10^{34}\text{cm}^{-2}\text{s}^{-1}$ and $7 \cdot 10^{34}\text{cm}^{-2}\text{s}^{-1}$ corresponding to 140 and 200 pileup interactions on average per bunch crossing, respectively.

Conservative performance assumptions for the muon trigger and reconstruction at a future ATLAS detector are made. Even though, the muon performance under the HL–LHC pileup conditions is expected to be similar to the present [204].

**Single Muon Trigger** For an upgraded ATLAS detector a new trigger system is planned where the current Level–1 trigger (see Section 4.2.6) is replaced by a two stage Level–0/Level–1 trigger design [205, 206]. With new trigger and precision tracking chambers in the inner end–cap region of the muon spectrometer, this configuration is expected to preserve the current high single muon trigger efficiency. The baseline single muon trigger for the HL–LHC running is a combination of the `MU20` Level–0/Level–1 single muon trigger with 20 GeV momentum threshold and the Level–1 inner detector track trigger. The combination reduces the number of fake triggers due to a better $p_{\text{T}}$ resolution compared to the `MU20` trigger alone. The corresponding single muon trigger efficiency at HL–LHC is expected to be about the same as for the current Level–1 `MU20` trigger. For muons with transverse momenta greater than 25 GeV the efficiency amounts to typically 67 % (91 %) for pseudorapidities $|\eta| < 1.0$ ($|\eta| > 1.0$) multiplied by the expected Level–1 track trigger efficiency which amounts to about 95 % [204].

**Muon Reconstruction** To account for the performance of the muon reconstruction and identification expected for HL–LHC conditions, two corrections are applied to the generated muons based on the current muon performance measurements. The muon identification

efficiency is assumed to be 97 %, independently of $p_{\mathrm{T}}$, $\eta$ and $\phi$ for $p_{\mathrm{T}} > 7\,\mathrm{GeV}$ and $|\eta| < 2.5$ [204]. Each event generated in the samples introduced in Section 7.3 is weighted with the efficiency corresponding to the number of reconstructed muons in the event fulfilling the above $p_{\mathrm{T}}$ and $\eta$ criteria. The momentum resolution of the muons reconstructed with the combined algorithm is parametrised using separate transverse momentum smearing functions for the inner detector and the muon spectrometer tracks [204]. The combined inner detector and muon spectrometer momentum resolution is approximately 1.7 % in the barrel and 2.7 % in the end–caps for muons with a transverse momentum of 50 GeV. The transverse momentum of each generated muon is smeared using a Gaussian probability density function with the mean set to the generated muon transverse momentum and its width set to the respective resolution.

## 7.5 Event Selection

This section describes the selection criteria applied to the generated events corrected for the expected detector response as described in Section 7.4. The event selection follows closely the $\mu^+\mu^-$ selection for the neutral MSSM Higgs boson search (see Section 6.6) for which the acceptance of simulated background events is validated against the $\sqrt{s} = 7\,\mathrm{TeV}$ proton–proton collision data. Modifications are applied in order to maximise the sensitivity of the search for the Standard Model Higgs decays, to account for higher trigger thresholds in the HL–LHC conditions and to minimise the impact of systematic uncertainties on the sensitivity for the search.

The selection requires that the event is triggered by the `MU20` Level–0/Level–1 single muon trigger described in Section 7.4 and that at least one reconstructed muon with $p_{\mathrm{T}} > 25\,\mathrm{GeV}$ matches the $\eta$–$\phi$ region of interest of the triggered object. Since the trigger decision is not simulated in the generated events, this requirement is emulated by requiring at least one muon with a transverse momentum greater 25 GeV in the fiducial acceptance of the trigger, $|\eta| < 2.4$. These events are weighted with the trigger efficiencies discussed in Section 7.4 taking into account the $\eta$ coordinates of both muons.

At least one additional muon with $p_{\mathrm{T}} > 20\,\mathrm{GeV}$ and $|\eta| < 2.5$ is required. The two muons with the highest transverse momenta and opposite electric charges are used to form a $\mu^+\mu^-$ pair. Since the $Z/\gamma^*$ and $t\bar{t}$ background events are generated only for invariant masses of greater than 40 GeV and 60 GeV, respectively, the event selection is completed by requiring that the $\mu^+\mu^-$ pairs have an invariant mass of $m_{\mu\mu} > 70\,\mathrm{GeV}$.

With respect to the event selection for the neutral MSSM Higgs boson search, no cut on the missing transverse momentum is applied because of the large uncertainties of the expected performance of the $E_{\mathrm{T}}^{\mathrm{miss}}$ reconstruction under the HL–LHC pileup conditions. As a consequence, the expected $t\bar{t}$ background contribution is higher than for the MSSM Higgs boson selection. Furthermore, no cuts on the track–based isolation and impact parameters

can be applied since these quantities are not simulated for the generated muons. However, these cuts are important to reduce the contribution of pileup and background events with non–isolated muons.

In order to correct for the selection efficiencies of these missing cuts and for selection efficiencies of cuts not correctly modelled by the simplified parametrisations of the detector response, correction factors are evaluated.

**Table 7.2:** Ratios of selection efficiencies, $\epsilon$, for signal and background events determined with the full detector simulation and with the simplified response parametrisation at $\sqrt{s} = 7\,\text{TeV}$, used as efficiency correction factors for $\sqrt{s} = 14\,\text{TeV}$.

| Process | $\epsilon$(full simulation)/$\epsilon$(parametrised simulation) |
|---|---|
| Signal | |
| $gg \to A \to \mu^+\mu^-$, $m_A = 130$ GeV, $\tan\beta = 40$ | 0.894 |
| Background | |
| $Z \to \mu^+\mu^-$ | 0.894 |
| $t\bar{t}$ | 0.519 |
| $W^+W^- \to \mu^+\nu\mu^-\nu$ | 0.647 |

For that purpose, a validation analysis is performed on signal and background Monte Carlo samples for $\sqrt{s} = 7\,\text{TeV}$ with the detailed detector response simulation. The validation analysis is performed subsequently applying once the above "nominal" event selection and using only the introduced simplified parametrisations of the detector response and once the full set of $\mu^+\mu^-$ event selection criteria of the MSSM $h/A/H \to \mu^+\mu^-$ search (see Section 6.6) taking advantage of the full detector simulation. In the latter case, the transverse momentum thresholds for the muon trigger and the reconstructed muons are adjusted to the respective values of the nominal event selection. The full set of $\mu^+\mu^-$ event selection criteria in particular contains also cuts on the track–based muon isolation and impact parameter variables, representing a more realistic selection. The resulting selection efficiencies for both event selections are compared for each signal and background process and their ratios are used as correction factors for the nominal event selection. These correction factors are summarised in Table 7.2. The efficiencies of the $Z/\gamma^*$ background and of the signal selection agree at the 10 % level. For the $t\bar{t}$ and $W^+W^-$ backgrounds having more activity in the detector and less muons passing the isolation cut, the correction factors are at the order of 50 % and 65 %, respectively. In Figure 7.1(a), the $\mu^+\mu^-$ invariant mass distributions for the background contributions simulated with full and simplified detector response are compared after applying the efficiency correction factors and found to be in good agreement, also in terms of their shapes.

The fully simulated background samples used for the validation analysis are the same as for the neutral MSSM $h/A/H \to \mu^+\mu^-$ search. As no full simulation sample for

the Standard Model Higgs boson production in gluon fusion with decays to $\mu^+\mu^-$ was generated for $\sqrt{s} = 7\,\text{TeV}$, the MSSM $gg \to A \to \mu^+\mu^-$ sample for $m_A = 130\,\text{GeV}$ and $\tan\beta = 40$ at $\sqrt{s} = 7\,\text{TeV}$ was used. This is justified by the fact that the kinematic properties of the muons from MSSM $A$ boson decays are the same as for the Standard Model Higgs boson decays. Therefore, the signal selection efficiencies for an $A \to \mu^+\mu^-$ signal (with $m_A = 130\,\text{GeV}$) are expected to be very similar to an $H \to \mu^+\mu^-$ signal with $m_H = 125\,\text{GeV}$ having almost the same mass.

**Table 7.3:** Numbers of expected signal and background events after each selection cut in the $H \to \mu^+\mu^-$ search for an integrated luminosity of $3000\,\text{fb}^{-1}$ at $\sqrt{s} = 14\,\text{TeV}$. The numbers in parentheses represent the statistical uncertainties in the last digit.

| Cut | $H \to \mu^+\mu^-$ | $Z/\gamma^*$ ($m_{\mu\mu} > 40\,\text{GeV}$) | $t\bar{t}$ ($m_{\mu\mu} > 60\,\text{GeV}$) | $W^+W^-$ |
|---|---|---|---|---|
| No cut | $339[1]\cdot10^2$ | $566[8]\cdot10^7$ | $1433[4]\cdot10^6$ | $2754[1]\cdot10^3$ |
| Trigger | $323[1]\cdot10^2$ | $459[8]\cdot10^7$ | $897[3]\cdot10^6$ | $14233[7]\cdot10^2$ |
| 2+ muons | $2383[9]\cdot10^1$ | $253[6]\cdot10^7$ | $293[2]\cdot10^6$ | $3043[3]\cdot10^2$ |
| $\mu^+\mu^-$ pair | $2357[9]\cdot10^1$ | $249[6]\cdot10^7$ | $192[1]\cdot10^6$ | $2775[3]\cdot10^2$ |
| $m_{\mu\mu} > 70\,\text{GeV}$ | $2299[9]\cdot10^1$ | $233[5]\cdot10^7$ | $240[5]\cdot10^5$ | $1200[2]\cdot10^2$ |
| $m_{\mu\mu} = m_H \pm 4\,\text{GeV}$ | $1930[8]\cdot10^1$ | $6[3]\cdot10^6$ | $11[1]\cdot10^5$ | $600[5]\cdot10^1$ |

The correction factors obtained for $\sqrt{s} = 7\,\text{TeV}$ are applied to the event selection efficiencies for the signal and background events at $\sqrt{s} = 14\,\text{TeV}$ which are parametrised by the simplified detector response. Thereby, the correction factors are considered to be independent of the increase in centre–of–mass energy from 7 TeV to 14 TeV. Also, the increase in the pileup condition of the HL–LHC is expected not to affect the selection efficiencies for muons [204]. Measurements using $\sqrt{s} = 7\,\text{TeV}$ data show that the track–based isolation efficiency for muons (which is addressed by the correction factors) is independent of the pileup condition and well described by the simulation [207].

Table 7.3 shows the numbers of expected signal and background events after each selection cut and in the signal mass window of $m_H = 125\,\text{GeV} \pm 4\,\text{GeV}$ for an integrated luminosity of $3000\,\text{fb}^{-1}$ at $\sqrt{s} = 14\,\text{TeV}$ taking into account all parametrisations and correction factors.

The corresponding $\mu^+\mu^-$ invariant mass distributions for signal and background events after all selection cuts are shown in Figure 7.1(b). The $Z/\gamma^*$ boson production is the dominant background contribution even for invariant masses well beyond the $Z$ boson mass. In the signal mass window of $125\,\text{GeV} \pm 4\,\text{GeV}$, it amounts to 84.4 % while the $t\bar{t}$ and $W^+W^-$ processes contribute 15.5 % and 0.1 %, respectively.

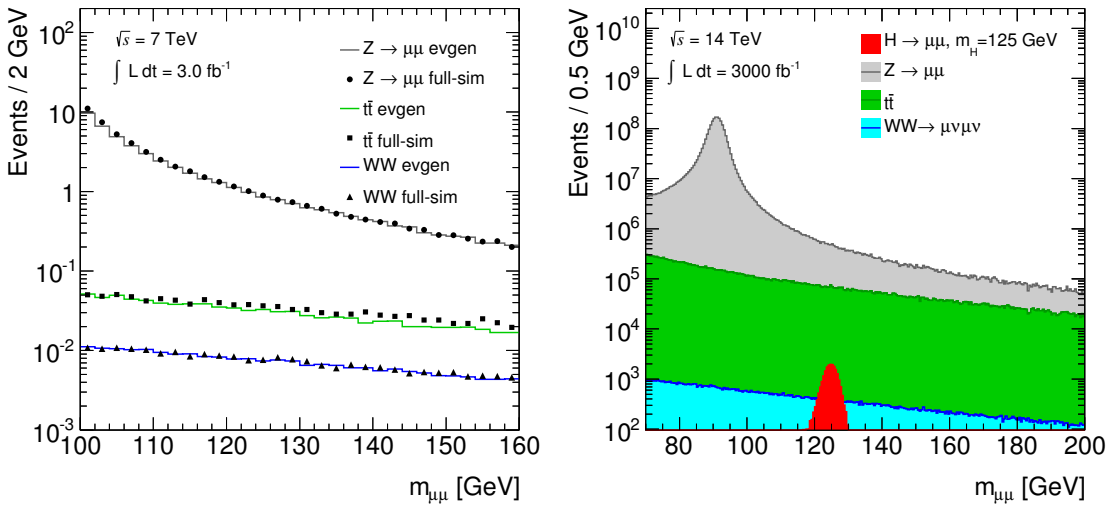


(a) (b)

**Figure 7.1:** Distributions of the $\mu^+\mu^-$ invariant mass of the background contributions simulated with simplified parametrisations of the detector response compared to the background contributions expected with the detailed detector simulation for an integrated luminosity of $3\,\text{fb}^{-1}$ at $\sqrt{s} = 7\,\text{TeV}$ (a) and $\mu^+\mu^-$ invariant mass distributions for the $H \to \mu^+\mu^-$ signal and background contributions with simplified response parametrisation and efficiency correction for an integrated luminosity of $3000\,\text{fb}^{-1}$ at $\sqrt{s} = 14\,\text{TeV}$ (b).

## 7.6 Signal and Background Modelling

The final discriminating variable for the inclusive $H \to \mu^+\mu^-$ search is the $\mu^+\mu^-$ invariant mass. As in the search for the neutral MSSM $h/A/H \to \mu^+\mu^-$ decays, the total background can be estimated from data by fitting the parametrised background model to the sidebands of the measured $\mu^+\mu^-$ invariant mass distribution. The sensitivity is improved by modelling the complete shape of both, the signal and background invariant mass distributions in a wide range of the mass spectrum.

The modelling of the signal is much simplified compared to Section 6.9 since there is only one signal resonance and one fixed signal mass. Therefore, the binned $\mu^+\mu^-$ invariant mass distribution of the simulated signal events with parametrised detector response after the full event selection is used as signal model.

The total $\mu^+\mu^-$ background is modelled following the procedure discussed in Section 6.10. A binned likelihood fit of the function $f_B$ defined in Equation 6.24 is performed to the background $\mu^+\mu^-$ invariant mass distribution in the mass range of 100 GeV to 160 GeV to estimate the model parameters.

The background model is validated using the methods discussed in Appendix B. The result of the binned likelihood fit to the invariant mass distribution of the total background

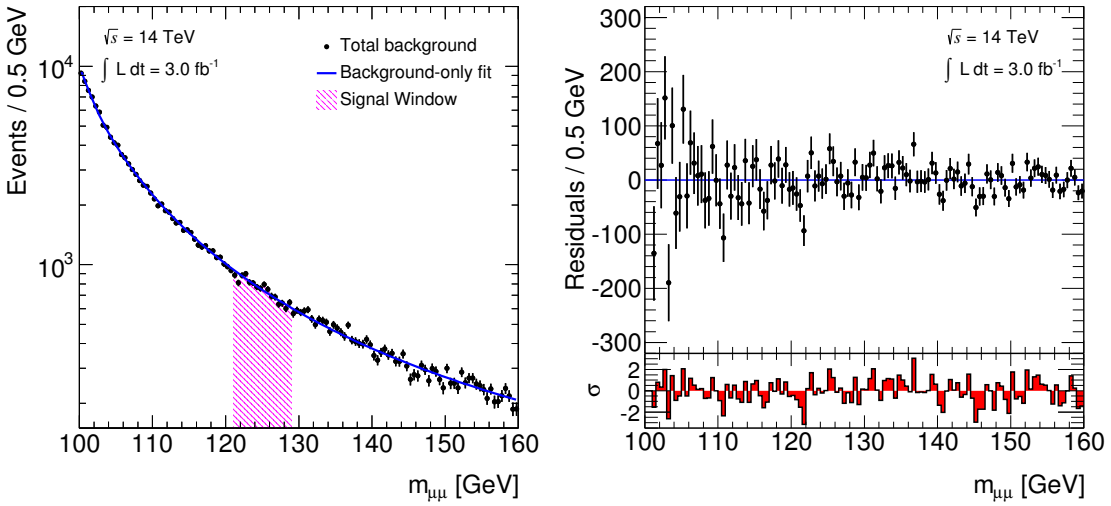


(a) (b)

**Figure 7.2:** Distribution of the $\mu^+\mu^-$ invariant mass for the total background together with the analytical background parametrisation, labelled "Background–only fit" (a) and corresponding residuals and their bin–by–bin significances, $\sigma$, for an integrated luminosity of $3\,\text{fb}^{-1}$ at $\sqrt{s} = 14\,\text{TeV}$ corresponding to the available Monte Carlo statistics (b).

is shown in Figure 7.2(a) for the background expectation for $\sqrt{s} = 14\,\text{TeV}$ and an integrated luminosity of $3\,\text{fb}^{-1}$. The fit result has a $\chi^2$ probability of 0.76 and a Kolmogorov–Smirnov test probability of 0.97 demonstrating very good description of the background by the model. Residuals of the simulated background with respect to the background estimate are shown in Figure 7.2(b). The $\mu^+\mu^-$ invariant mass distribution is normalised to $3\,\text{fb}^{-1}$ since this integrated luminosity corresponds to the available Monte Carlo statistics. The bin–by–bin significances, $\sigma$, of the deviations are typically below $2\,\sigma$.

The background model obtained from the fit to the simulated background distribution for $3\,\text{fb}^{-1}$ is used together with the signal model to generate signal–plus–background pseudo–data samples corresponding to integrated luminosities of $300\,\text{fb}^{-1}$ and $3000\,\text{fb}^{-1}$ using the expected signal and background yields after the event selection given in Table 7.3. These pseudo–data distributions have the correct statistical fluctuations expected for the respective integrated luminosities and are used for the statistical interpretation of the search results. A binned likelihood fit to the sidebands in the $\mu^+\mu^-$ invariant mass is performed to the signal–plus–background pseudo–data distributions to evaluate the background estimate for the statistical interpretation. The sidebands are defined by the fit range of 100 GeV to 160 GeV excluding the signal window at $125\,\text{GeV} \pm 4\,\text{GeV}$. The residuals of the fit are shown in Figure 7.3 compared to the background–subtracted signal–plus–background and background–only hypotheses indicating that for $3000\,\text{fb}^{-1}$ a significant excess of events can

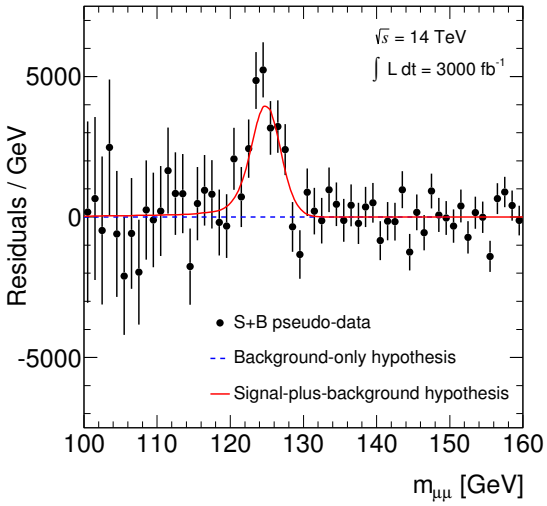


**Figure 7.3:** Distribution of the $\mu^+\mu^-$ invariant mass of a pseudo–experiment corresponding to $3000\,\text{fb}^{-1}$ at $\sqrt{s} = 14\,\text{TeV}$ generated from the signal–plus–background model after subtracting the background contribution obtained from the sideband fit in the mass range of 100 GeV to 160 GeV excluding the signal window $125\,\text{GeV} \pm 4\,\text{GeV}$. The signal–plus–background and background–only models are shown as well.

be observed in the presence of the Higgs boson signal.

## 7.7 Systematic Uncertainties

This section summarises the systematic uncertainties which are considered in the analysis and taken into account for the evaluation of the final results presented in Section 7.8.

**Theoretical Uncertainties** Uncertainties in the expected signal yield arise from theoretical uncertainties of the cross sections for the different Higgs boson production modes as well as from the uncertainty of the branching fraction for the $H \to \mu^+\mu^-$ decay [208]. Uncertainties in the production cross sections originate from PDF and $\alpha_s$ as well as renormalisation and factorisation scale uncertainties. For a Standard Model Higgs boson with $m_H = 125\,\text{GeV}$ produced in proton–proton collisions at $\sqrt{s} = 14\,\text{TeV}$ the production cross section uncertainty in the gluon fusion process amounts to $^{+7.5\,\%}_{-8.0\,\%}$ due to the scale uncertainty and $^{+7.2\,\%}_{-6.0\,\%}$ due to PDF and $\alpha_s$ uncertainties. For the vector boson fusion process the scale uncertainty amounts to $^{+0.4\,\%}_{-0.3\,\%}$ and PDF and $\alpha_s$ uncertainties add up to $^{+1.9\,\%}_{-1.5\,\%}$. For the Higgs boson production in association with vector bosons the cross section uncertainties are treated separately for the associated $W$ and $Z$ bosons. The uncertainties for WH (ZH) production amount to $^{+0.3\,\%}_{-0.6\,\%}$ ($^{+2.7\,\%}_{-1.8\,\%}$) due to scale uncertainties and to $\pm 3.8\,\%$

($\pm 3.7\,\%$) due to PDF and $\alpha_s$ uncertainties. Corresponding cross section uncertainties for the ttH production mode amount to $^{+5.9\,\%}_{-9.3\,\%}$ from scale uncertainties and $\pm 8.9\,\%$ from PDF and $\alpha_s$ uncertainties. The uncertainty in the $H \to \mu^+\mu^-$ branching fraction amounts to $^{+6.0\,\%}_{-5.9\,\%}$.

**Background Modelling Uncertainties** Uncertainties from the modelling of the background are defined by the variation of the fitted background function within its $68\,\%$ confidence level uncertainty band as discussed in Section 6.11. For the evaluation of the final results the uncertainties are factorised in terms of the normalisation and the shape of the background mass spectrum prediction. The background uncertainties evaluated for a mass range of $(125 \pm 4)\,\text{GeV}$ for the two HL–LHC scenarios with integrated luminosities of $300\,\text{fb}^{-1}$ and $3000\,\text{fb}^{-1}$ are shown in Table 7.4. The relative uncertainties for both, the shape and the normalisation of the background prediction for $300\,\text{fb}^{-1}$ are at the same order of magnitude of about $\mathcal{O}(10^{-4})$. For $3000\,\text{fb}^{-1}$ the normalisation uncertainty is also at the level of $\mathcal{O}(10^{-4})$ while the shape systematic reduces to $\mathcal{O}(10^{-5})$ due to the increased statistics in the expected data sample.

## 7.8 Results

This section presents the prospects for the inclusive search for decays of the Standard Model Higgs boson with $m_H = 125\,\text{GeV}$ to $\mu^+\mu^-$ pairs and for the measurement of the Higgs boson couplings to the Standard Model particles in proton–proton collisions at $\sqrt{s} = 14\,\text{TeV}$ for integrated luminosities of $300\,\text{fb}^{-1}$ and $3000\,\text{fb}^{-1}$ at the HL–LHC. Exclusion limits on the Higgs boson production cross section times the branching fraction to $\mu^+\mu^-$ and $p_0$–values under the background–only hypothesis (see Section 6.8) are derived. The results for the $\mu^+\mu^-$ channel contribute to the combined fit of the Standard Model Higgs boson couplings to gauge bosons and fermions.

### 7.8.1 Sensitivity of the $H \to \mu^+\mu^-$ Search

The numbers of signal ($N_\text{S}$) and background ($N_\text{B}$) events after the full event selection and in the signal mass window of $125\,\text{GeV} \pm 4\,\text{GeV}$ are shown in Table 7.4. The mass window around $m_H = 125\,\text{GeV}$ is chosen to maximise $\frac{N_\text{S}}{\sqrt{N_\text{B}}}$. The expected exclusion limits on the signal production cross section times branching fraction with respect to the Standard Model prediction and the $p_0$–values are obtained from a fit of the signal and background shapes defined in Section 7.6 to the $\mu^+\mu^-$ invariant mass distribution in the range of $100\,\text{GeV}$ to $160\,\text{GeV}$ using the statistics framework described in Section 6.8.

Systematic uncertainties in the production cross sections for the different Higgs boson production modes and on the branching fraction for $H \to \mu^+\mu^-$ decays affecting the

expected signal yield as well as uncertainties in the background modelling as described in Section 7.7 are taken into account as nuisance parameters in the likelihood function (see Section 6.8). Standard Model Higgs boson decays to $\mu^+\mu^-$ can be excluded already at an integrated luminosity of about $300\,\text{fb}^{-1}$. A discovery is possible with an integrated luminosity of slightly less than $3000\,\text{fb}^{-1}$.

At $300\,\text{fb}^{-1}$, the sensitivity of the $H \to \mu^+\mu^-$ search is dominated by the statistical uncertainty. The expected $p_0$–values under the background–only hypothesis correspond to a signal significance of $2.2\,\sigma$ and $2.5\,\sigma$ with and without theoretical uncertainties in the predicted signal yield. The significance without theoretical uncertainties scales approximately with the square root of the integrated luminosity. At $3000\,\text{fb}^{-1}$, the expected signal significance without theoretical uncertainties is $7.1\,\sigma$. For this integrated luminosity, however, the theoretical systematic uncertainties become important leading to an expected signal significance of $6.2\,\sigma$.

**Table 7.4:** Numbers of expected signal, $N_\text{S}$, and background events, $N_\text{B}$, in the mass window of $\pm 4\,\text{GeV}$ around $m_H = 125\,\text{GeV}$ for integrated luminosities of $300\,\text{fb}^{-1}$ and $3000\,\text{fb}^{-1}$. The uncertainty in the number of background events has contributions from the normalisation, $\Delta N_\text{B}^\text{norm}$, and from the shape, $\Delta N_\text{B}^\text{shape}$. Expected 95 % confidence level upper limits on the signal strength with respect to the Standard Model prediction and $p_0$–values under the background–only hypothesis and corresponding signal significances are also given.

| $\mathcal{L}$ [$\text{fb}^{-1}$] | 300 | 3000 |
|---|---|---|
| $N_\text{S}$ | $1.7319 \cdot 10^3$ | $1.7319 \cdot 10^4$ |
| $N_\text{B}$ | $5.65089 \cdot 10^5$ | $5.65279 \cdot 10^6$ |
| $\Delta N_\text{B}^\text{norm}$ | $3.39083 \cdot 10^2$ | $1.08003 \cdot 10^3$ |
| $\Delta N_\text{B}^\text{shape}$ | $1.93984 \cdot 10^2$ | $1.37406 \cdot 10^2$ |
| CLs limit | 0.92 | 0.23 |
| $p_0$–value | $1.25 \cdot 10^{-2}$ | $2.65 \cdot 10^{-10}$ |
| Significance | $2.2\,\sigma$ | $6.2\,\sigma$ |

### 7.8.2 Higgs Boson Couplings to Standard Model Particles

Similar studies as for the $\mu^+\mu^-$ channel have been performed for the other decay channels of the Standard Model Higgs boson to $\gamma\gamma$, $ZZ^*$, $W^+W^{-*}$ and $\tau^+\tau^-$ for inclusive or exclusive Higgs boson production via vector boson fusion (VBF) or in association with vector bosons (VH) or top quark pairs (ttH) [198]. A summary of the prospects for the combined measurement of the Higgs boson couplings from these studies is given in this section. Details on the searches performed in the individual channels can be found in the original documentation.

The expected precision, $\frac{\Delta\mu}{\mu}$, in the signal strength parameter, $\mu$, for each channel is shown in Figure 7.4(a) for $300\,\text{fb}^{-1}$ and $3000\,\text{fb}^{-1}$. The highest sensitivity is obtained

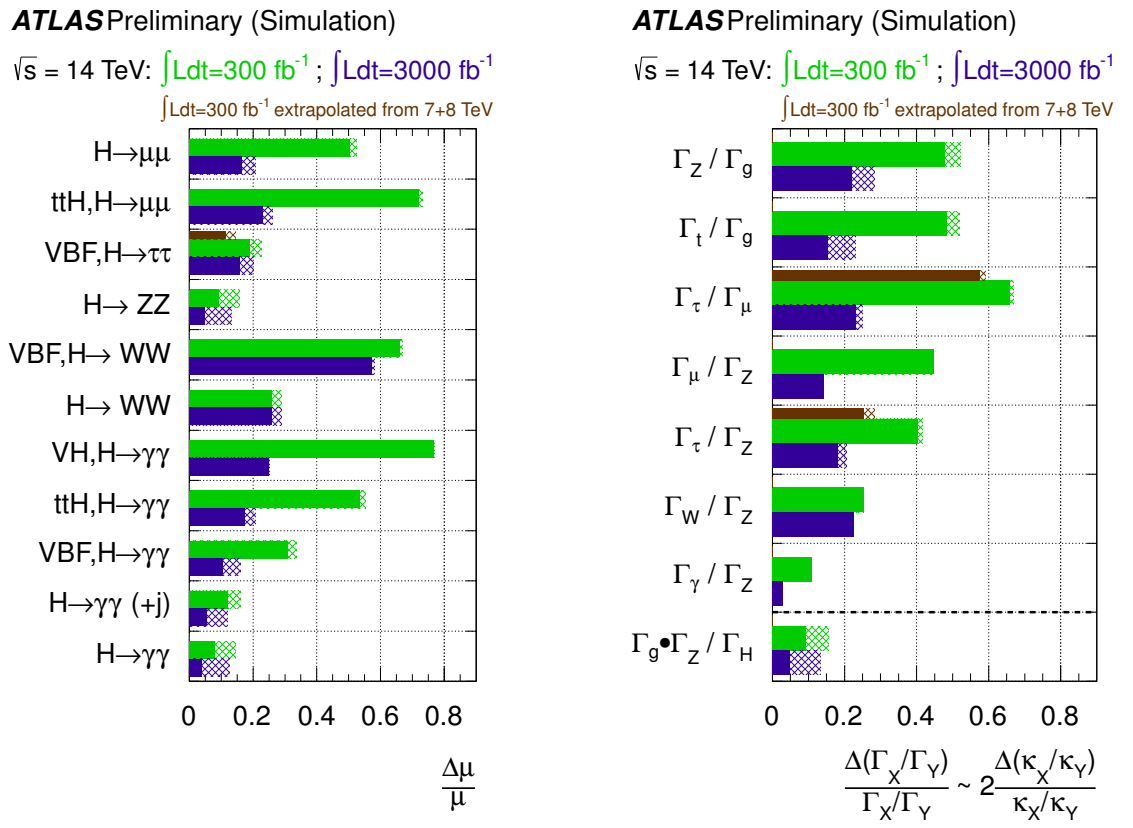


**Figure 7.4:** Expected precision in the signal strength $\mu = (\sigma \cdot \mathrm{BR})/(\sigma \cdot \mathrm{BR})_{\mathrm{SM}}$ for different production and decay channels of the Standard Model Higgs boson with $m_H = 125\,\mathrm{GeV}$ (a) and on the ratio of the Higgs boson partial decay widths (b) [198]. The hatched areas indicate current signal uncertainties from QCD scale and PDF variations. For the $\tau^+\tau^-$ final state, the brown bars show the precision expected from extrapolating the results of the combined $\tau^+\tau^-$ search of $\sqrt{s} = 7\,\mathrm{TeV}$ and $8\,\mathrm{TeV}$ data to $\sqrt{s} = 14\,\mathrm{TeV}$ and $300\,\mathrm{fb}^{-1}$. Channels where no production mode is specified correspond to inclusive searches.

in the inclusive searches for the decays to gauge bosons, $H \to \gamma\gamma$ and $H \to ZZ^* \to 4\ell$, providing similar precision on the signal strength parameter of approximately 10 % (5 %) at $\sqrt{s} = 14\,\mathrm{TeV}$ for $300\,\mathrm{fb}^{-1}$ ($3000\,\mathrm{fb}^{-1}$). The fermionic decay channels studied are $H \to \tau^+\tau^-$ and $H \to \mu^+\mu^-$. For the latter, in addition to the inclusive results of this thesis the exclusive search for the Higgs boson produced in association with top quark pairs have been studied. For the $\tau^+\tau^-$ final state only the VBF production mode has been considered resulting in a precision of the signal strength parameter of about 20 % (15 %) for $300\,\mathrm{fb}^{-1}$ ($3000\,\mathrm{fb}^{-1}$). However, as indicated by the brown bar in Figure 7.4(a), the combination of all Higgs boson production modes for the $\tau^+\tau^-$ decay in the analyses of

the 7 TeV and 8 TeV data [209] extrapolated to $\sqrt{s} = 14\,\text{TeV}$ and $300\,\text{fb}^{-1}$ shows significant improvement of the measurement precision. The $H \to \mu^+\mu^-$ channel is competitive with the $H \to \tau^+\tau^-$ channel for $3000\,\text{fb}^{-1}$ reaching a precision of about 15 %. In particular the $H \to \gamma\gamma$, $H \to ZZ^*$ and $H \to \mu^+\mu^-$ decay channels profit from the increase of integrated luminosity since both the statistical and also parts of the systematic uncertainties can be significantly reduced with an increased data set. For the $H \to W^+W^-$ decay channel the integrated luminosity is not the limiting factor due to the dominant contribution of systematic uncertainties in the background estimate.

The individual channels are combined to determine the sensitivity to possible deviations from the Standard Model Higgs boson couplings to fermions and gauge bosons. The combined fit is performed under several assumptions [210]. It is assumed that the signal found in each channel originates from the same single narrow resonance corresponding to a generic Higgs boson with mass of 125 GeV. Furthermore, the total width, $\Gamma_H$, of this Higgs boson is assumed to be negligible compared to the Higgs boson mass. This zero–width approximation allows for factorisation of the Higgs boson production cross section and decay rates,

$$(\sigma \cdot \text{BR})_{ii \to H \to ff} = \sigma_{ii} \cdot \frac{\Gamma_f}{\Gamma_H} \tag{7.1}$$

where $\sigma_{ii}$ is the $ii \to H$ production cross section, $\Gamma_f$ the partial decay width for the $H \to ff$ decay process and $\Gamma_H$ is the total decay width of the Higgs boson. Finally, only modifications of the probed coupling strengths are assumed, changes in the structure of the coupling tensor are not considered and only a CP–even boson state is probed. No explicit assumptions are made on the existence of particles in addition to the Standard Model particles and on their contributions to the effective couplings.

The Higgs boson couplings are in principle not directly measurable but within a certain model, they enter as free parameters in the predictions of $\sigma \cdot \text{BR}$ for the signal processes. In the Standard Model, the couplings of the Higgs boson are fully determined once its mass is known. In order to measure deviations from these couplings in the framework of the Standard Model, the couplings of the Higgs boson to a particle $j$ are multiplied by scale factors, $\kappa_j$, such that the quantities $\sigma_{jj}$ and $\Gamma_j$ scale with $\kappa_j^2$. The scale factors for the loop–induced effective coupling strengths to gluons and photons are denoted as $\kappa_g$ and $\kappa_\gamma$, respectively. The former is a function of $\kappa_t$, $\kappa_b$ and the Higgs boson mass, $m_H$, the latter of $\kappa_t$, $\kappa_b$, $\kappa_\tau$, $\kappa_W$, and $m_H$. The scale factor $\kappa_H$ is a function of all $\kappa_j$ and $m_H$ and accounts for non–trivial relationships between the individual scale factors and the cross sections or partial decay widths. In the example of the $gg \to H \to \mu^+\mu^-$ channel, the cross section times branching fraction factorises as

$$(\sigma \cdot \text{BR})(gg \to H \to \mu^+\mu^-) = \sigma_{\text{SM}}(gg \to H) \cdot \text{BR}_{\text{SM}}(H \to \mu^+\mu^-) \cdot \frac{\kappa_g^2 \cdot \kappa_\mu^2}{\kappa_H^2}, \tag{7.2}$$

where for the Standard Model Higgs boson cross section, $\sigma_{\mathrm{SM}}$, and branching fraction, $\mathrm{BR}_{\mathrm{SM}}$, the current most precise theoretical predictions including higher–order QCD and electroweak corrections are used [208].

Two benchmark scenarios have been probed following Reference [211]. In the most general scenario, no restrictions are made on the total decay width of the Higgs boson allowing for Higgs boson decays to potential new particles, beyond the Standard Model. In this case, only ratios of coupling parameters or partial decay widths can be determined in the combined fit. The following free parameters have been chosen:

$$\frac{\Gamma_W}{\Gamma_Z}, \frac{\Gamma_\gamma}{\Gamma_Z}, \frac{\Gamma_\tau}{\Gamma_Z}, \frac{\Gamma_\mu}{\Gamma_Z}, \frac{\Gamma_t}{\Gamma_g}, \frac{\Gamma_Z}{\Gamma_g} \text{ and } \frac{\Gamma_g \cdot \Gamma_Z}{\Gamma_H} \ , \tag{7.3}$$

wherein the nomenclature [210] $\Gamma_X/\Gamma_Y = \kappa_X^2/\kappa_Y^2 = \lambda_{XY}^2$ with the relative uncertainty $\frac{\Delta(\Gamma_X/\Gamma_Y)}{\Gamma_X/\Gamma_Y} \approx 2 \cdot \frac{\Delta\lambda_{XY}}{\lambda_{XY}}$ is used. In the second scenario, the combined fit of the couplings is more constrained assuming that no processes beyond the Standard Model contribute to the $gg \to H$ and $H \to \gamma\gamma$ loops and to the decay widths of the Higgs boson. Furthermore, the couplings to all fermions and vector bosons are assumed to scale with common scale factors, $\kappa_{\mathrm{F}}$ and $\kappa_{\mathrm{V}}$, respectively, which are the only free parameters in this scenario.

**Table 7.5:** Results for $\kappa_V$ and $\kappa_F$ in a minimal coupling fit at 14 TeV for integrated luminosities of 300 $\mathrm{fb}^{-1}$ and 3000 $\mathrm{fb}^{-1}$ [198].

| Coupling scale factor | no theory uncertainties | all systematic uncertainties |
|---|---|---|
| | 300 $\mathrm{fb}^{-1}$ | |
| $\kappa_{\mathrm{V}}$ | $\pm 3.0\%$ | $^{+5.9\%}_{-5.4\%}$ |
| $\kappa_{\mathrm{F}}$ | $^{+9.1\%}_{-8.6\%}$ | $^{+10.6\%}_{-\ 9.9\%}$ |
| | 3000 $\mathrm{fb}^{-1}$ | |
| $\kappa_{\mathrm{V}}$ | $\pm 1.9\%$ | $^{+4.6\%}_{-4.3\%}$ |
| $\kappa_{\mathrm{F}}$ | $\pm 3.6\%$ | $^{+6.1\%}_{-5.7\%}$ |

The expected precision in the ratio of decay widths and in the common scale factors $\kappa_{\mathrm{F}}$ and $\kappa_{\mathrm{V}}$ from the combined fit in the two scenarios are shown in Figure 7.4(b) and Table 7.5, respectively, for integrated luminosities of 300 $\mathrm{fb}^{-1}$ and 3000 $\mathrm{fb}^{-1}$. For the latter, the results are given with and without theoretical uncertainties in the signal production rates. Only the expected precisions are shown, the fitted parameter values are compatible with the Standard Model predictions which are the input to the fit.

The uncertainties in all coupling parameter ratios decrease by at least a factor of two when increasing the integrated luminosity from $300\,\mathrm{fb}^{-1}$ to $3000\,\mathrm{fb}^{-1}$ except for the ratio $\frac{\Gamma_W}{\Gamma_Z}$ due to the fact that the $H \to W^+W^-$ channel is systematically limited already for $300\,\mathrm{fb}^{-1}$ as discussed above. The ratio $\Gamma_\tau/\Gamma_\mu$, related to the study presented in this thesis, probing the relation between couplings to the second and third fermion generations can be determined with a precision of about 25 % at the highest integrated luminosity.

The precision in the determination of the common scale factors improves considerably for an integrated luminosity of $3000\,\mathrm{fb}^{-1}$ in particular for the fermionic coupling parameter, and amounts to about 4 % for $\kappa_\mathrm{V}$ and about 6 % for $\kappa_\mathrm{F}$ after accounting for the theoretical uncertainties.

# Chapter 8

# Summary

The Standard Model of particle physics describes with high precision the fundamental interactions between the elementary constituents of matter — with the exception of gravitation. A candidate for the last missing constituent of the Standard Model, the Higgs boson, has been discovered by the ATLAS and CMS collaborations in July 2012. The properties of the new boson with a mass of $125.5 \pm 0.2(\text{stat})^{+0.5}_{-0.6}(\text{syst})$ GeV are consistent with the predictions of the Standard Model Higgs boson. However, more data is needed to fully determine the properties of the new particle and probe for possible deviations from the Standard Model Higgs boson predictions.

If the new state is indeed the Standard Model Higgs boson, the question arises how its mass can be so much smaller than the GUT scale under radiative corrections. Furthermore, without new phenomena beyond the Standard Model at energies well below the GUT scale such a low Higgs boson mass violates the vacuum stability bound and, including the above hierarchy problem, the electroweak vacuum would be of best metastable.

Supersymmetry provides elegant solutions to several open questions in the Standard Model. The Minimal Supersymmetric extension of the Standard Model (MSSM) is the most studied supersymmetric theory. The Higgs sector of the MSSM contains five physical Higgs bosons, three are electrically neutral and two with opposite electric charges. Two of the three neutral MSSM Higgs bosons have even CP quantum number while the remaining one is CP–odd. The new boson discovered at the LHC can also be interpreted as one of the CP–even MSSM Higgs bosons. The direct search for MSSM Higgs bosons is therefore important to determine the nature of the discovered particle.

Two studies with the ATLAS detector at the LHC have been performed in this thesis: the search for the neutral MSSM Higgs bosons and the investigation of the sensitivity for the search for the Standard Model Higgs boson in decays to two oppositely charged muon pairs.

The ATLAS detector is designed to reconstruct muons with high efficiency and to provide precise measurements of their momenta. Monitoring of the muon reconstruction

performance of the ATLAS detector during data taking and the development of methods for the data quality assessment were important tasks for the analyses presented in this thesis.

The excellent performance of the ATLAS muon reconstruction makes the searches for Higgs boson decays to $\mu^+\mu^-$ pairs feasible. The $\mu^+\mu^-$ final state allows for a precise measurement of the Higgs boson mass.

The search for the neutral MSSM Higgs bosons has been performed using LHC proton–proton collision data at a centre–of–mass energy of 7 TeV recorded in 2011 corresponding to an integrated luminosity of $4.8\,\text{fb}^{-1}$. Narrow signal resonances corresponding to the three neutral MSSM Higgs bosons are searched for in the $\mu^+\mu^-$ invariant mass distribution on top of a large continuous background. In order to reduce the sensitivity to systematic uncertainties the background is estimated from the side–bands of the signal region in the measured $\mu^+\mu^-$ invariant mass distribution. The shapes of the mass distributions of the background and the expected signals are parametrised with analytic functions. No significant excess of events above the estimated Standard Model background contribution has been found. Exclusion limits at the 95 % confidence level have been determined for the MSSM $m_h^{\text{max}}$ benchmark scenario with positive Higgs mixing parameter as a function of the free parameters $m_A$ and $\tan\beta$, as well as less model–dependent on the cross section times branching fraction to $\mu^+\mu^-$ for the production of a generic (pseudo–)scalar Higgs boson via gluon fusion or in association with $b$ quarks. The results of the search in the $\mu^+\mu^-$ final state are combined with the results of the more sensitive search in the $\tau^+\tau^-$ decay channel. The combined exclusion limits considerably constrain the allowed parameter space of the MSSM Higgs sector beyond previous results from hadron collider experiments.

Due to the clear experimental signature, the $\mu^+\mu^-$ decay channel can also be used for future tests of the Standard Model Higgs boson properties at a prospected high–luminosity phase of the LHC. The $H \to \mu^+\mu^-$ decay channel can contribute significantly to the combined Higgs boson coupling measurement to fermions and in particular to the Higgs boson mass measurement, helping to discriminate between Higgs bosons of the Standard Model and of its extensions. The sensitivity of the search for the Standard Model Higgs boson with a mass of 125 GeV decaying to $\mu^+\mu^-$ is evaluated using Monte Carlo simulations of signal and background processes at $\sqrt{s} = 14\,\text{TeV}$ and corresponding to integrated luminosities of $300\,\text{fb}^{-1}$ and $3000\,\text{fb}^{-1}$ expected after luminosity upgrades of the LHC. Using the $\mu^+\mu^-$ decay channel alone, the Standard Model Higgs boson with $m_H = 125\,\text{GeV}$ can be excluded with a data set of less than $300\,\text{fb}^{-1}$ or discovered with a significance of more than $6\,\sigma$ with a data set of $3000\,\text{fb}^{-1}$. The Higgs boson couplings to second–generation fermions relative to the third lepton generation can be determined with an accuracy of about 25 % in this channel.

# Appendix A

# Additional Information for the Muon Data Quality Monitoring

This appendix summarises technical details concerning the muon performance data quality monitoring presented in Section 5.2. Descriptions of the individual data taking periods in the ATLAS proton–proton data taking in 2011 are given in Section A.1. The ATLAS detector operation and data reconstruction aspects relevant for the data quality assurance are described in Section A.2 together with an overview of the online and offline data quality monitoring tools and the data quality assessment based on References [212–215]. The muon performance data quality assessments in the 2011 ATLAS data taking are summarised. Section A.3 introduces the definitions of the logical detector regions in the $\eta$ and $\phi$ coordinates used for the monitoring of the muon trigger and identification efficiencies presented in Section 5.2.2.

## A.1 Data Taking Periods in the 2011 Proton–Proton Run

The ATLAS data taking for the 2011 proton–proton physics run is divided into individual data taking periods which contain runs with a common configuration of the LHC beam, the ATLAS detector and the trigger menu. Each period may be divided into several sub–periods due to smaller changes in the detector configuration, for example. Any significant changes to either the detector configuration, calibration or to the trigger menu causes the definition of a new period.

A list of all data taking periods and sub–periods of the 2011 proton–proton run is shown in Table A.1, together with the number of single runs in each sub–period. The integrated luminosity of each sub–period is also given for ATLAS ready conditions (see Section A.2.1).

A short description of the LHC beam and ATLAS detector conditions, as well as significant data quality and trigger menu issues are listed.

## A.2 Data Quality

The ATLAS detector introduced in Section 4.2 is a highly complex particle detector with approximately 100 million read–out channels, various different sub–systems and technologies and sophisticated data aquisition, trigger system and event reconstruction. During operation problems of numerous sources can appear in single parts of the system, such that the data from certain sub–detectors or particular reconstructed higher level physics objects may not be usable for some physics analyses. As not all analyses exploit all detector components and due to the fact that many problems occurring during detector operation are recoverable offline, the data taking is not aborted in such cases. Instead, the quality of the recorded data is continuously being assessed.

The detector problems are tracked and documented such that particular bad–quality data which might affect the physics measurement can be excluded from a given analysis. The recorded detector condition allows for the evaluation and recording of the data quality properties involving online and offline data quality monitoring with both fully automated and manual tasks. These are summarised in the following based on the References [212–214].

### A.2.1 ATLAS Run Conditions

One complete data taking cycle of the ATLAS detector, an ATLAS run, consists of a sequence of different detector configurations. A typical ATLAS run [212] starts before the beam injection to the LHC ring and ends after the beam dump. For the period of the injection and the ramp–up of the beam to the operation energy, as well as the beam squeeze to the nominal size, the ATLAS detector is held in a standby mode. In this mode sensitive detector elements such as tracking devices are operated at lower voltages and specific read–out conditions as well as a special trigger menu are used to allow for the monitoring of the general detector and beam conditions. After the LHC beams are declared stable, the ATLAS sub–detectors are brought to their nominal operating state and the physics trigger menu is configured. This procedure is called the warm start after which the detector status is transferred to the “ready” mode and data taking starts. During a run the trigger menu may need to be changed or the read–out of single detector components can be brought to a halt if causing dead–time and can be re–started once problems are fixed in so–called stopless removal and recovery procedures. All such changes cause modified detector conditions during the run which need to be monitored and documented. The time granularity in which the system status is documented is a luminosity block introduced in Section 4.2.7 which typically takes one minute. Any change in the detector condition starts a new luminosity block such that the system is stable within each luminosity measurement

**Table A.1:** Data taking periods for the $\sqrt{s} = 7\,\text{TeV}$ proton–proton run in 2011. The numbers of runs and the integrated luminosity for ATLAS ready condition are shown for each sub–period. Changes in the LHC beam conditions or ATLAS setup and ATLAS data taking problems are also listed [216].

| Period | Sub-Periods | Runs | $\mathcal{L}$ [pb$^{-1}$] | Description |
|---|---|---|---|---|
| A | A1 | 5 | $1.0 \cdot 10{-}1$ | trigger commissioning |
| | A2 | 7 | 8.6 | 75 ns bunch spacing, magnets off |
| B | B1 | 4 | 4.5 | solenoid on, toroid off |
| | B2 | 3 | 13 | magnets on, ATLAS standard physics setup |
| D | D1 | 3 | 12 | 50 ns bunch spacing, 214 colliding bunches, changed L1Calo timing |
| | D2 | 2 | 11 | 322 colliding bunches |
| | D3 | 7 | 36 | $322 - 424$ colliding bunches |
| | D4 | 4 | 37 | no changes w.r.t. previous |
| | D5 | 3 | 31 | no changes w.r.t. previous |
| | D6 | 3 | 31 | no changes w.r.t. previous |
| | D7 | 1 | 24 | L1Calo update |
| E | E1 | 5 | 52 | LAr problem in EMBA: 6 FEBs not operational |
| F | F1 | 3 | $1.5 \cdot 10^{-1}$ | special runs, van der Meer scans for luminosity calibration |
| | F2 | 11 | 136 | 50 ns physics data taking |
| | F3 | 3 | 19 | no changes w.r.t. previous |
| G | G1 | 1 | 6.2 | new trigger cache with pileup noise suppression EMEC sagging correction |
| | G2 | 6 | 115 | no changes w.r.t. previous |
| | G3 | 3 | 78 | no changes w.r.t. previous |
| | G4 | 9 | 119 | no changes w.r.t. previous |
| | G5 | 4 | 106 | no changes w.r.t. previous |
| | G6 | 5 | 142 | no changes w.r.t. previous |
| H | H1 | 4 | 53 | L1 muon firmware update: fix misconfiguration affecting A-side (improving efficiency in $\eta = 0.8 - 1.0$) |
| | H2 | 1 | 48 | no changes w.r.t. previous |
| | H3 | 4 | 67 | fix to trigger chain EF_b10_medium_4j30_a4tc_EFFS |
| | H4 | 4 | 115 | no changes w.r.t. previous |
| I | I1 | 5 | 22 | 4 LAr FEBs recovered |
| | I2 | 6 | 36 | ramp-up after technical stop; increasing number of 1000 bunches |
| | I3 | 8 | 149 | TRT ROD problems |
| | I4 | 8 | 198 | no changes w.r.t. previous |
| J | J1 | 5 | 76 | LHC beam current increasing adiabatically. Unprescaled L1 muon triggers changed. |
| | J2 | 4 | 161 | no changes w.r.t. previous |
| K | K1 | 6 | 257 | new trigger menu |
| | K2 | 4 | 208 | no changes w.r.t. previous |
| | K3 | 5 | 90 | no changes w.r.t. previous |
| | K4 | 1 | 42 | no changes w.r.t. previous |
| | K5 | 2 | 51 | L1_MU4 used instead of L1_M0 for low pt muon triggers for runs 187811 and 187812 |
| | K6 | 1 | 27 | no changes w.r.t. previous |
| L | L1 | 6 | 5.3 | new trigger menu, new L1_MU11 road, L1_MU0 -> L1_MU4, toroid off |
| | L2 | 9 | 140 | toroid on after technical stop, physics data taking |
| | L3 | 10 | 362 | wrong L1_RPC timing configuration for all runs from 189205 |
| | L4 | 8 | 256 | wrong L1_RPC timing configuration |
| | L5 | 10 | 160 | L1_RPC timing fixed |
| | L6 | 10 | 324 | no changes w.r.t. previous |
| | L7 | 6 | 352 | no changes w.r.t. previous |
| M | M1 | 3 | $5.4 \cdot 10^{-1}$ | 25 ns bunch spacing |
| | M2 | 8 | 222 | 50 ns physics data taking |
| | M3 | 1 | $5.3 \cdot 10^{-2}$ | high pileup run |
| | M4 | 7 | 347 | nominal physics data taking |
| | M5 | 3 | 160 | change in LHC filling pattern, 1331 colliding bunches |
| | M6 | 4 | 40 | change in RPC trigger timing improves muon efficiency |
| | M7 | 10 | $6.0 \cdot 10^{-4}$ | $\beta^* = 90\,\text{m}$ runs for ALFA |
| | M8 | 6 | 229 | nominal physics data taking |
| | M9 | 1 | $3.6 \cdot 10^{-1}$ | high pileup run |
| | M10 | 5 | 160 | nominal physics data taking |
| AllYear | | 267 | 5341 | all 2011 7 TeV data |

period. Before the beams are dumped, the ATLAS detector stops the data taking and is transferred back to the standby mode. This procedure is called a warm stop and marks the end of an ATLAS run.

### A.2.2 Online Detector Monitoring

The monitoring of the detector conditions and configuration during each ATLAS run outlined above is an essential requirement for a safe detector operation and efficient data taking. During the data taking the operation of detector sub–systems, the detector control system (DCS), LHC interfaces and trigger rates are monitored in real–time in the ATLAS control room. Fragments of the raw data output can also be inspected by reconstructing a few full events with an offline reconstruction code adapted for the online environment. The ATLAS Data Quality Monitoring Framework (DQMF) [213] is designed to monitor the huge amount of detector information and performs automatic data quality assessments. The automated tools compare thousands of measured distributions to their expectations, note anomalies and alert data quality responsibles in case of problems. The detector conditions in each luminosity block as well as automated or manual data quality assessments are stored in the ATLAS conditions database [217, 218] to be traceable at any later point in time.

### A.2.3 Offline Data Reconstruction

After the data is recorded, the events are processes by the offline reconstruction packages at CERN's Tier–0 farm [215]. The reconstruction is performed in three main stages [159] as sketched in Figure A.1.

A prompt reconstruction is started immediately as the data files are copied to the mass storage and runs within less than 8 hours. The prompt reconstruction runs on the so–called "express stream", a subset of approximately 5 % of the data from a specific set of triggers with a rate of 10 Hz. In addition to the reconstruction, data quality monitoring histograms are generated and stored at Tier–0 and automated checks are performed by the offline DQMF (see below).

The second stage is the so–called calibration loop. Special "calibration streams" containing partial event information needed for inner detector, calorimeter and muon spectrometer calibration and alignment are processed at dedicated calibration centres within the worldwide LHC computing grid [219, 220]. Also at this stage a separate data quality monitoring ensures the validity of the calibrations. The calibration loop finishes within 24 hours and the resulting new calibration measurements are uploaded to the conditions data base.

The third stage is the so–called bulk reconstruction starting 36 hours after the end of the run. In the bulk reconstruction all data streams involving various triggers including the express stream are processed using the updated calibrations. The calibrations used for

the prompt and the bulk reconstruction are kept separately in the conditions data base for reproducibility. After the bulk reconstruction the output data is distributed worldwide to the Tier–1 grid sites for permanent storage where the data can also be reprocessed later in time if needed. With this three–stage reconstruction procedure the data is available for physics analyses 96 hours after it has been taken.

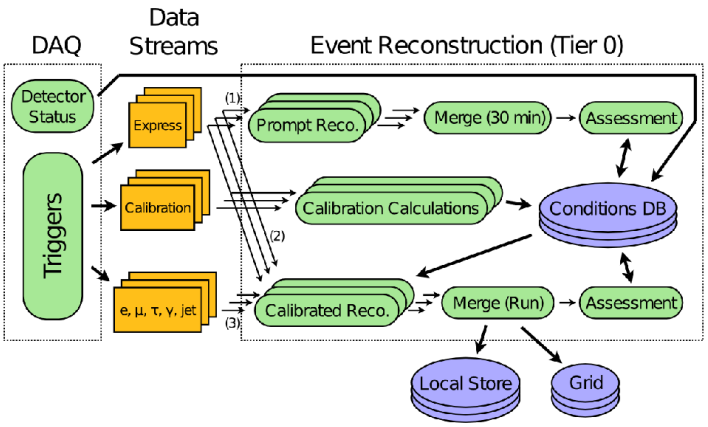


**Figure A.1:** Schematic overview of the ATLAS offline event reconstruction [212].

### A.2.4 Offline Data Quality Assessment

Besides of the online monitoring the DQMF also performs offline checks of the reconstructed data [214]. Requirements on latency and processing speed are relaxed for the offline data quality monitoring (DQM) so that higher complexity checks can be performed. In the automated offline data quality assessment (DQA) histograms produced during reconstruction are checked against reference histograms to monitor read–out thresholds, detector occupancies and the performance of various algorithms. The automated assessment ranges in complexity from simple checks for histogram entries to more sophisticated $\chi^2$–tests and shape comparisons.

Results of the offline DQA are visualised in a set of static HTML pages on the ATLAS web display and need to be cross–checked by data quality shifters. The data quality assessments of detector sub–systems and physics objects are grouped and stored in the ATLAS conditions database. The offline data quality shifters need to validate the results of the automated assessment on a run–by–run basis and possibly resolve certain decisions in the conditions database.

Offline DQA also runs on Tier–1 centres during reprocessing campaigns [159] which are foreseen to take advantage of improved calibrations, alignment and reconstruction algorithms.

Deviations from nominal detector conditions assigned by the automated DQA or the shifters are treated internally as so–called "defects" [221]. A defect is associated to a luminosity block and is either present or absent. So–called "primary defects" are stored in the conditions data base while higher level defects, so–called "virtual defects", can be defined from arbitrary logical combinations of primary or other virtual defects and are computed on access. An example of the virtual defect logic is shown in Figure A.2. The number of primary defects is not limited and each problem occurring in the DQA causing data not to be used in analyses can be assigned to a defect. To facilitate tracking or studies of systematic effects certain defects can also be considered as tolerable so that their presence does not affect the higher level virtual defects.

The final product of the online and offline data quality assessments is a list of luminosity blocks per run which are usable in analyses, the so–called good runs list (GRL). Several GRLs are produced with the requirement of no virtual defects for different sub–systems or physics objects and the requirement that the specific detector components are operational according to the needs of various analysis groups.

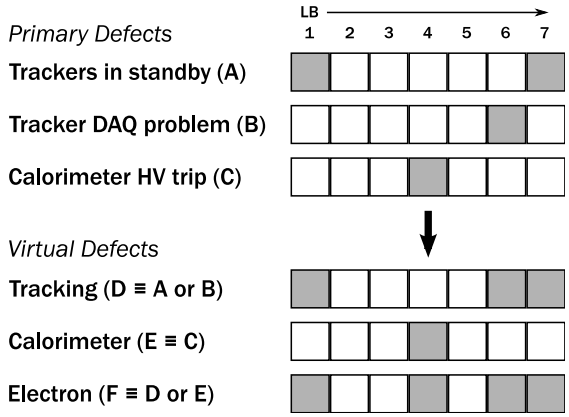


**Figure A.2:** Schematic demonstration how primary defects are propagated to virtual defects. A simplified set of defects is illustrated, along with their states for various luminosity blocks during a run. Grey shaded blocks mark present defects. In this example an analysis would depend only on the electron virtual defect, representing the quality of the electron reconstruction, without the need to consider all possible underlying problems [221].

### A.2.5 Muon Performance Data Quality Defects

Since the monitored muon reconstruction algorithms depend on each detector sub–system and various service tools, muon performance data quality monitoring may to some extent be also sensitive to problems upstream the actual muon reconstruction. This generates a certain overlap of the muon performance DQM with the DQM of the single sub–systems, in particular for the muon spectrometer, the inner detector and the magnet system. To

avoid double assessments of defects which are anyways combined to virtual defects later on the strategy of muon performance DQM is to separate between DQ problems with origin in the sub–systems and in the muon reconstruction itself. If possible, problems are first traced back to the sub–systems. Such problems are in general defined as tolerable muon performance defects, mainly for bookkeeping reasons. Intolerable muon performance defects on the other hand are only assigned if the problem is found to occur during the muon reconstruction or in common service tools.

**Table A.2:** List of the muon performance data quality defects for the data taking in 2011 relevant for proton–proton physics analyses and the corresponding number of runs in which these defects were present.

| Defect Name | Description | # Runs |
|---|---|---|
| | intolerable defects | |
| MCP_ALIGN_GEO | bad alignment / geometry | 0 |
| MCP_B_FIELD | no B field / wrong B field map | 4 |
| MCP_MAT_DESCR | bad / wrong material description | 0 |
| MCP_SERV_TOOL | bug in service tool | 0 |
| MCP_UNCHECKED | not checked by shifter | 0 |
| | tolerable defects | |
| MCP_BAD_TRT | MCP affected by TRT problem. | 1 |
| MCP_DETECTOR_PROBLEM | MCP affected by detector issue. | 0 |
| MCP_MUCALOLR_UNKNOWN | DQ of algorithm affected by unknown cause or cannot be mapped to current set of defects. | 4 |
| MCP_MUCALOTAG_UNKNOWN | | 4 |
| MCP_MUGIRL_UNKNOWN | | 4 |
| MCP_MUIDCB_UNKNOWN | | 4 |
| MCP_MUIDSA_UNKNOWN | | 4 |
| MCP_MUONBOY_UNKNOWN | | 4 |
| MCP_MUTAGIMO_UNKNOWN | | 4 |
| MCP_MUTAG_UNKNOWN | | 4 |
| MCP_STACO_UNKNOWN | | 4 |
| MCP_UNKNOWN | DQ affected by unknown cause or cannot be mapped to current set of defects. No DQ information available. | 4 |

The list of tolerable and intolerable defects is dynamic and a new defect is added once a certain new type of problem is identified. The list of muon performance defects identified by the end of 2011 is shown in Table A.2. For each type of a defect the number of runs is given in which this defect was present. There are four intolerable defects corresponding to alignment and detector geometry, magnetic field setup, material description and common service tools. An additional intolerable defect is present by default once the run is available for DQA and needs to be set absent by the shifter when signing off the run. The defect corresponding to the magnet field setup was present in four runs all belonging to the short data taking period beginning of 2011 in which the toroid magnets were off to collect data with straight muon tracks for the muon spectrometer alignment. Defects are created upon

request as mentioned above. Therefore, no explicit intolerable defect corresponding to the muon reconstruction is listed in Table A.2 as no problem in the muon reconstruction itself occurred since the beginning of the physics data taking with ATLAS in 2010. Listed defects which did not occur in the 2011 data taking period have been created earlier due to corresponding problems occurring in 2010.

**Table A.3:** Muon performance data quality assessments and underlying problems during the 2011 data taking.

| Period | Run Nr. | Defect | Problem |
|---|---|---|---|
| A | 177531 | MCP_B_FIELD | Magnets off. |
| | 177539 | MCP_B_FIELD | Magnets off. |
| | 177540 | MCP_B_FIELD | Magnets off. |
| | 177593 | MCP_B_FIELD | Magnets off. |
| | 177682 | MCP_B_FIELD | Magnets off. |
| | 177904 | MCP_B_FIELD | Magnets off. |
| | 177911 | MCP_B_FIELD | Magnets off. |
| | 177912 | MCP_B_FIELD | Magnets off. |
| | 177924 | MCP_B_FIELD | Magnets off. |
| | 177929 | MCP_B_FIELD | Magnets off. |
| | 177960 | MCP_B_FIELD | Magnets off. |
| | 177965 | MCP_B_FIELD | Magnets off. |
| B | 177986 | MCP_B_FIELD | Toroid magnets off. |
| | 178020 | MCP_B_FIELD | Toroid magnets off. |
| | 178021 | MCP_B_FIELD | Toroid magnets off. |
| | 178026 | MCP_B_FIELD | Toroid magnets off. |
| D | | | |
| E | | | |
| F | | | |
| G | | | |
| H | | | |
| I | 186049 | MCP_BAD_TRT | 4 TRT ROD missing. |
| J | | | |
| K | | | |
| L | 189692 | MCP_UNKNOWN | Low statistics. |
| M | 190503 | MCP_UNKNOWN | Low statistics. |
| | 190504 | MCP_UNKNOWN | Low statistics. |
| | 190505 | MCP_UNKNOWN | Low statistics. |

In addition to the intolerable defects, 12 tolerable defects are listed in Table A.2. Apart from two defects corresponding to problems in the TRT or the detector sub–systems in general, the tolerable defects are dummy–defects which can be set for one particular muon reconstruction algorithm or the complete muon reconstruction due to an unknown type of data quality problem which requires further investigation. Once the corresponding origin

of the problem is identified these dummy–defects are marked absent and a new dedicated defect is created and marked present. The dummy–defects are tolerable because of the muon performance DQM strategy to only exclude muons from physics analyses if a specific problem associated to the muon performance is identified. An example for this procedure is the defect corresponding to problems in the TRT where four read–out drivers were not operational in one run in 2011. After the issue was traced back a dedicated defect was created. Since the problem is associated to a sub–detector system, the muon performance DQM defect is tolerable.

The remaining four runs with present dummy–defects all have too few events for a proper data quality assessment using the muon performance monitoring plots introduced in Section 5.2.1. For the data taking period in 2012 a dedicated tolerable defect for such runs with low statistics was created which is not listed for the 2011 data taking period.

A detailed list of ATLAS runs with present muon performance data quality defects is given in Table A.3, together with a short description of the underlying data quality problem. The data taking period A does not count to the nominal 2011 proton–proton data for used for physics analyses since the full magnet system was switched of in this period to record straight charged particle tracks for the alignment of the inner detector and the muon spectrometer.

## A.3 Detector Regions for Muon Efficiency Monitoring

This section introduces the definitions of the logical detector regions used for the monitoring of the muon trigger and identification efficiencies presented in Section 5.2.2.

Table A.4 lists the definitions of the logical detector regions in the $\eta$ coordinate of the ATLAS coordinate system. The $\eta$ acceptance of the muon spectrometer ($|\eta| < 2.7$) is divided in 9 bins corresponding to the barrel, end–cap, CSC and magnetic field transition regions for each detector side (A and C) and one narrow central region corresponding to the detector region with limited coverage of the muon spectrometer.

Table A.5 lists the definitions of the logical detector regions in the $\phi$ plane of the ATLAS coordinate system. The acceptance in $\phi$ is divided into three bins corresponding to sectors which are equipped with large or small muon stations in the muon spectrometer and a feet region dedicated to the two sectors where the muon spectrometer has limited coverage due to the detector feet.

**Table A.4:** Logical ATLAS detector regions in $\eta$ used for the monitoring of the muon trigger and identification efficiencies within the offline data quality monitoring.

| Name | Range | Detector region |
|---|---|---|
| CSCA | $2.0 \leq \eta < 2.7$ | CSC region (small wheel) side A |
| ECA | $1.3 \leq \eta < 2.0$ | End–cap region side A |
| TRA | $1.1 \leq \eta < 1.3$ | Transition region side A |
| BA | $0.05 \leq \eta < 1.1$ | Barrel region side A |
| CR | $-0.05 < \eta < 0.05$ | Central region |
| BC | $-1.1 < \eta \leq -0.05$ | Barrel region side C |
| TRC | $-1.3 < \eta \leq -1.0$ | Transition region side C |
| ECC | $-2.0 < \eta \leq -1.3$ | End–cap region side C |
| CSCC | $-2.7 < \eta \leq -2.0$ | CSC region (small wheel) side C |

**Table A.5:** Logical ATLAS detector regions in $\phi$ used for the monitoring of the muon trigger and identification efficiencies within the offline data quality monitoring.

| Name | Range | Sector |
|---|---|---|
| Large chamber sectors | $-0.235 < \phi \leq 0.235$ | 1 |
| | $0.55 < \phi \leq 1.02$ | 3 |
| | $1.335 < \phi \leq 1.805$ | 5 |
| | $2.12 < \phi \leq 2.59$ | 7 |
| | $2.905 < \phi \geq -2.905$ | 9 |
| | $-2.59 < \phi \leq -2.12$ | 11 |
| | $-1.805 < \phi \leq -1.335$ | 13 |
| | $-1.02 < \phi \leq -0.55$ | 15 |
| Small chamber sectors | $0.235 < \phi \leq 0.55$ | 2 |
| | $1.02 < \phi \leq 1.335$ | 4 |
| | $1.805 < \phi \leq 2.12$ | 6 |
| | $2.59 < \phi \leq 2.905$ | 8 |
| | $-2.905 < \phi \leq -2.59$ | 10 |
| | $-0.55 < \phi \leq -0.235$ | 16 |
| Detector feet region | $-2.12 < \phi \leq -1.805$ | 12 |
| | $-1.335 < \phi \leq -1.02$ | 14 |

# Appendix B

# Additional Studies for the MSSM Higgs Boson Search

This appendix provides additional information and several technical details concerning the search for the neutral MSSM Higgs bosons in the decay channel $h/A/H \to \mu^+\mu^-$ presented in Chapter 6. A detailed list of all simulated data sets used in the analysis is given in Section B.1. Details to the event selection efficiency of simulated the signal given in Section B.2 together with a discussion of the effect of the parton distribution functions on the description of the dominant $Z/\gamma^*$ background. The validation fo the background modelling is presented in Section B.3. A model–independent search for local excess in the data compared to the background expectation is discussed in Section B.4. The validation of the asymptotic approximation used for the evaluation of the exclusion limits is presented in Section B.5.

## B.1 Monte Carlo Samples

A detailed list of Monte Carlo samples used for the neutral MSSM $h/A/H \to \mu^+\mu^-$ search presented in Chapter 6 is given in this section.

Table B.1 shows the samples for the $A$ boson signal production via gluon fusion and in association with $b$ quarks. For $\tan\beta = 40$, 7 samples for different $A$ boson masses, $m_A$, are generated for both production modes using the full ATLAS detector simulation. Additional samples are generated to study the dependence of the reconstructed width of the $\mu^+\mu^-$ resonance on $\tan\beta$. For the two mass points $m_A = 150$ and 250 GeV signal samples for the $\tan\beta$ values 20, 40 and 60 are produced for both production modes using the fast ATLAS detector simulation, ATLFAST–II [157], as described in Section 6.4.

**Table B.1:** List of $A$ boson signal Monte Carlo samples simulated with the detailed or the fast detector simulation and event generators used in the sample production. The cross sections times $A \to \mu^+\mu^-$ branching fractions, $\sigma_A \times \mathrm{BR}$, for the given processes correspond to NNLO calculations as described in Section 3.3. The numbers of events in the simulated samples are labelled $N_{\mathrm{evt}}$ and the corresponding integrated luminosity of the samples is labelled $\mathcal{L}$.

| Process | Generator | $m_A$ [GeV] | $\tan\beta$ | $\sigma_A \times \mathrm{BR}$ [fb] | $N_{\mathrm{evt}}$ | $\mathcal{L}$ [fb$^{-1}$] |
|---|---|---|---|---|---|---|
| full simulation samples | | | | | | |
| $gg \to A \to \mu^+\mu^-$ | PowHeg | 110 | 40 | 109.6 | 20000 | 182 |
| $gg \to A \to \mu^+\mu^-$ | PowHeg | 130 | 40 | 47.2 | 20000 | 424 |
| $gg \to A \to \mu^+\mu^-$ | PowHeg | 150 | 40 | 22.5 | 25000 | 1111 |
| $gg \to A \to \mu^+\mu^-$ | PowHeg | 170 | 40 | 11.6 | 20000 | 1724 |
| $gg \to A \to \mu^+\mu^-$ | PowHeg | 200 | 40 | 4.8 | 20000 | 4167 |
| $gg \to A \to \mu^+\mu^-$ | PowHeg | 250 | 40 | 1.3 | 50000 | 38462 |
| $gg \to A \to \mu^+\mu^-$ | PowHeg | 300 | 40 | 0.4 | 50000 | 125000 |
| $pp \to b(b)A,\ A \to \mu^+\mu^-$ | SHERPA | 110 | 40 | 142.5 | 50000 | 351 |
| $pp \to b(b)A,\ A \to \mu^+\mu^-$ | SHERPA | 130 | 40 | 81.3 | 50000 | 615 |
| $pp \to b(b)A,\ A \to \mu^+\mu^-$ | SHERPA | 150 | 40 | 49.1 | 50000 | 1018 |
| $pp \to b(b)A,\ A \to \mu^+\mu^-$ | SHERPA | 170 | 40 | 31.1 | 50000 | 1608 |
| $pp \to b(b)A,\ A \to \mu^+\mu^-$ | SHERPA | 200 | 40 | 16.6 | 49900 | 3006 |
| $pp \to b(b)A,\ A \to \mu^+\mu^-$ | SHERPA | 250 | 40 | 6.7 | 30000 | 4478 |
| $pp \to b(b)A,\ A \to \mu^+\mu^-$ | SHERPA | 300 | 40 | 3.0 | 49999 | 16666 |
| fast simulation samples | | | | | | |
| $gg \to A \to \mu^+\mu^-$ | PowHeg | 150 | 20 | 5.4 | 29000 | 5370 |
| $gg \to A \to \mu^+\mu^-$ | PowHeg | 150 | 40 | 22.5 | 30000 | 1333 |
| $gg \to A \to \mu^+\mu^-$ | PowHeg | 150 | 60 | 51.9 | 30000 | 578 |
| $gg \to A \to \mu^+\mu^-$ | PowHeg | 250 | 20 | 0.3 | 30000 | 100000 |
| $gg \to A \to \mu^+\mu^-$ | PowHeg | 250 | 40 | 1.3 | 30000 | 23077 |
| $gg \to A \to \mu^+\mu^-$ | PowHeg | 250 | 60 | 3.1 | 30000 | 9677 |
| $pp \to b(b)A,\ A \to \mu^+\mu^-$ | SHERPA | 150 | 20 | 12.2 | 30000 | 2459 |
| $pp \to b(b)A,\ A \to \mu^+\mu^-$ | SHERPA | 150 | 40 | 49.1 | 30000 | 611 |
| $pp \to b(b)A,\ A \to \mu^+\mu^-$ | SHERPA | 150 | 60 | 112.3 | 30000 | 267 |
| $pp \to b(b)A,\ A \to \mu^+\mu^-$ | SHERPA | 250 | 20 | 1.6 | 29999 | 18749 |
| $pp \to b(b)A,\ A \to \mu^+\mu^-$ | SHERPA | 250 | 40 | 6.7 | 30000 | 4478 |
| $pp \to b(b)A,\ A \to \mu^+\mu^-$ | SHERPA | 250 | 60 | 15.3 | 30000 | 1961 |

For each simulated process Table B.1 lists the $m_A$–$\tan\beta$ point, the used Monte Carlo event generator and the cross section times branching fraction corresponding to NNLO calculations as described in Section 3.3. These cross sections are used to scale the number of generated events to the integrated luminosity of the recorded data set. The number of generated events and the corresponding integrated luminosity of the signal data samples are also given.

The considered Standard Model background processes are listed in Table B.2 for the $Z/\gamma^*$ boson production processes and in Table B.3 for $W$, $W^+W^-$ and heavy quark production processes. The processes are listed with the used generators, the applied cross sections as well as the number of generated events and the integrated luminosities corresponding

to the sample sizes. For the production cross sections for the ALPGEN samples for $Z/\gamma^*$ boson production in association with light and $b$ jets, the generator cross sections for the separate samples have been scaled with $k$–factors such that the sum of the cross sections is equal to the NNLO calculation for the inclusive cross section.

**Table B.2:** List of background Monte Carlo samples for $Z/\gamma^*$ boson production with the applied event generators. The cross sections, $\sigma$, correspond to the generator cross section times the generator filter efficiency and a $k$–factor to match to the NNLO calculations given in Table 6.1. The number of events in the simulated samples are labelled $N_{\text{evt}}$ and the corresponding integrated luminosity of the samples is labelled $\mathcal{L}$.

| Process | Generator | $\sigma$ [pb] | $N_{\text{evt}}$ | $\mathcal{L}$ [fb$^{-1}$] |
|---|---|---|---|---|
| $Z \to \mu^+\mu^-$ (40 GeV $< m_{\mu\mu} <$ 2 TeV) + Np0 | Alpgen | 836.95 | 6615230 | 8 |
| $Z \to \mu^+\mu^-$ (40 GeV $< m_{\mu\mu} <$ 2 TeV) + Np1 | Alpgen | 168.19 | 1334296 | 8 |
| $Z \to \mu^+\mu^-$ (40 GeV $< m_{\mu\mu} <$ 2 TeV) + Np2 | Alpgen | 50.80 | 404947 | 8 |
| $Z \to \mu^+\mu^-$ (40 GeV $< m_{\mu\mu} <$ 2 TeV) + Np3 | Alpgen | 14.10 | 110000 | 8 |
| $Z \to \mu^+\mu^-$ (40 GeV $< m_{\mu\mu} <$ 2 TeV) + Np4 | Alpgen | 3.55 | 30000 | 8 |
| $Z \to \mu^+\mu^-$ (40 GeV $< m_{\mu\mu} <$ 2 TeV) + Np5 | Alpgen | 0.95 | 10000 | 11 |
| $Z \to \tau^+\tau^-$ (40 GeV $< m_{\tau\tau} <$ 2 TeV) + Np0 | Alpgen | 836.94 | 10613179 | 13 |
| $Z \to \tau^+\tau^-$ (40 GeV $< m_{\tau\tau} <$ 2 TeV) + Np1 | Alpgen | 168.32 | 3334137 | 20 |
| $Z \to \tau^+\tau^-$ (40 GeV $< m_{\tau\tau} <$ 2 TeV) + Np2 | Alpgen | 50.81 | 1004847 | 20 |
| $Z \to \tau^+\tau^-$ (40 GeV $< m_{\tau\tau} <$ 2 TeV) + Np3 | Alpgen | 14.07 | 509847 | 36 |
| $Z \to \tau^+\tau^-$ (40 GeV $< m_{\tau\tau} <$ 2 TeV) + Np4 | Alpgen | 3.55 | 144999 | 41 |
| $Z \to \tau^+\tau^-$ (40 GeV $< m_{\tau\tau} <$ 2 TeV) + Np5 | Alpgen | 0.95 | 45000 | 47 |
| $Z \to \mu^+\mu^-$ (10 GeV $< m_{\mu\mu} <$ 40 GeV) + Np0 | Alpgen | 3054.90 | 999849 | 0.3 |
| $Z \to \mu^+\mu^-$ (10 GeV $< m_{\mu\mu} <$ 40 GeV) + Np1 | Alpgen | 84.87 | 300000 | 4 |
| $Z \to \mu^+\mu^-$ (10 GeV $< m_{\mu\mu} <$ 40 GeV) + Np2 | Alpgen | 41.45 | 999995 | 24 |
| $Z \to \mu^+\mu^-$ (10 GeV $< m_{\mu\mu} <$ 40 GeV) + Np3 | Alpgen | 8.38 | 150000 | 18 |
| $Z \to \mu^+\mu^-$ (10 GeV $< m_{\mu\mu} <$ 40 GeV) + Np4 | Alpgen | 1.85 | 39999 | 22 |
| $Z \to \mu^+\mu^-$ (10 GeV $< m_{\mu\mu} <$ 40 GeV) + Np5 | Alpgen | 0.46 | 10000 | 22 |
| $Z \to \tau^+\tau^-$ (10 GeV $< m_{\tau\tau} <$ 40 GeV) + Np0 | Alpgen | 3055.10 | 999649 | 0.3 |
| $Z \to \tau^+\tau^-$ (10 GeV $< m_{\tau\tau} <$ 40 GeV) + Np1 | Alpgen | 84.93 | 299999 | 4 |
| $Z \to \tau^+\tau^-$ (10 GeV $< m_{\tau\tau} <$ 40 GeV) + Np2 | Alpgen | 41.47 | 498899 | 12 |
| $Z \to \tau^+\tau^-$ (10 GeV $< m_{\tau\tau} <$ 40 GeV) + Np3 | Alpgen | 8.36 | 150000 | 18 |
| $Z \to \tau^+\tau^-$ (10 GeV $< m_{\tau\tau} <$ 40 GeV) + Np4 | Alpgen | 1.85 | 39999 | 22 |
| $Z \to \tau^+\tau^-$ (10 GeV $< m_{\tau\tau} <$ 40 GeV) + Np5 | Alpgen | 0.46 | 10000 | 22 |
| $b\bar{b}Z$, $Z \to \mu^+\mu^-$ (30 GeV $< m_{\mu\mu} <$ 10 TeV) + Np0 | Alpgen | 8.21 | 149950 | 18 |
| $b\bar{b}Z$, $Z \to \mu^+\mu^-$ (30 GeV $< m_{\mu\mu} <$ 10 TeV) + Np1 | Alpgen | 3.09 | 100000 | 32 |
| $b\bar{b}Z$, $Z \to \mu^+\mu^-$ (30 GeV $< m_{\mu\mu} <$ 10 TeV) + Np2 | Alpgen | 1.11 | 40000 | 36 |
| $b\bar{b}Z$, $Z \to \mu^+\mu^-$ (30 GeV $< m_{\mu\mu} <$ 10 TeV) + Np3 | Alpgen | 0.49 | 9999 | 20 |
| $b\bar{b}Z$, $Z \to \tau^+\tau^-$ (30 GeV $< m_{\tau\tau} <$ 10 TeV) + Np0 | Alpgen | 8.20 | 150000 | 18 |
| $b\bar{b}Z$, $Z \to \tau^+\tau^-$ (30 GeV $< m_{\tau\tau} <$ 10 TeV) + Np1 | Alpgen | 3.10 | 99999 | 32 |
| $b\bar{b}Z$, $Z \to \tau^+\tau^-$ (30 GeV $< m_{\tau\tau} <$ 10 TeV) + Np2 | Alpgen | 1.11 | 40000 | 36 |
| $b\bar{b}Z$, $Z \to \tau^+\tau^-$ (30 GeV $< m_{\tau\tau} <$ 10 TeV) + Np3 | Alpgen | 0.47 | 9000 | 19 |
| $Z \to \mu^+\mu^-$ inclusive (60 GeV $< m_{\mu\mu} <$ 2 TeV) | Pythia | 989.66 | 5896736 | 6 |

**Table B.3:** List of background Monte Carlo samples for $W$ and heavy quark production with the applied event generators. The cross sections , $\sigma$, correspond to the generator cross section times the generator filter efficiency and a $k$–factor to match to the NNLO calculations for $W$, NLO+NNLL for $t\bar{t}$ and LO for $b\bar{b}$ production given in Table 6.1. The number of events in the simulated samples are labelled $N_{\text{evt}}$ and the corresponding integrated luminosity of the samples is labelled $\mathcal{L}$.

| Process | Generator | $\sigma$ [pb] | $N_{\text{evt}}$ | $\mathcal{L}$ [fb$^{-1}$] |
|---|---|---|---|---|
| $t\bar{t} \to \ell\ell X$ ($M_{\ell\ell} > 60$ GeV) | MC@NLO | 12.71 | 499948 | 39 |
| singletop $Wt$ channel | Acer | 15.74 | 994897 | 63 |
| singletop $t$ channel $\to e\nu$ | Acer | 6.97 | 999295 | 143 |
| singletop $t$ channel $\to \mu\nu$ | Acer | 6.97 | 999948 | 143 |
| singletop $t$ channel $\to \tau\nu$ | Acer | 6.97 | 998995 | 143 |
| singletop $s$ channel $\to e\nu$ | Acer | 0.50 | 199899 | 400 |
| singletop $s$ channel $\to \mu\nu$ | Acer | 0.50 | 199850 | 400 |
| singletop $s$ channel $\to \tau\nu$ | Acer | 0.50 | 195000 | 390 |
| $b\bar{b} \to \mu\mu X$ ($p_{\text{T}}^{\ell} > 10$ GeV) | PythiaB | 2830.00 | 296599 | 0.1 |
| $b\bar{b} \to e\mu X$ ($p_{\text{T}}^{\ell} > 10$ GeV) | PythiaB | 4017.00 | 795695 | 0.2 |
| $b\bar{b} \to eeX$ ($p_{\text{T}}^{\ell} > 10$ GeV) | PythiaB | 1693.00 | 2920985 | 1.7 |
| $W \to \mu\nu$ Np0 | Alpgen | 8303.52 | 3462942 | 0.4 |
| $W \to \mu\nu$ Np1 | Alpgen | 1565.04 | 2498593 | 2 |
| $W \to \mu\nu$ Np2 | Alpgen | 453.40 | 3768737 | 8 |
| $W \to \mu\nu$ Np3 | Alpgen | 122.26 | 1008446 | 8 |
| $W \to \mu\nu$ Np4 | Alpgen | 30.90 | 254950 | 8 |
| $W \to \mu\nu$ Np5 | Alpgen | 8.30 | 70000 | 8 |
| $W \to \tau\nu$ Np0 | Alpgen | 8302.32 | 3418296 | 0.4 |
| $W \to \tau\nu$ Np1 | Alpgen | 1563.84 | 2499194 | 2 |
| $W \to \tau\nu$ Np2 | Alpgen | 453.82 | 3750986 | 8 |
| $W \to \tau\nu$ Np3 | Alpgen | 121.81 | 1009946 | 8 |
| $W \to \tau\nu$ Np4 | Alpgen | 30.77 | 249998 | 8 |
| $W \to \tau\nu$ Np5 | Alpgen | 8.45 | 65000 | 8 |
| $W^+W^- \to e\nu e\nu$ | MC@NLO | 0.51 | 199949 | 392 |
| $W^+W^- \to e\nu\mu\nu$ | MC@NLO | 0.51 | 200000 | 392 |
| $W^+W^- \to e\nu\tau\nu$ | MC@NLO | 0.51 | 200000 | 392 |
| $W^+W^- \to \mu\nu\mu\nu$ | MC@NLO | 0.51 | 199000 | 392 |
| $W^+W^- \to \mu\nu e\nu$ | MC@NLO | 0.51 | 199949 | 392 |
| $W^+W^- \to \mu\nu\tau\nu$ | MC@NLO | 0.51 | 200000 | 392 |
| $W^+W^- \to \tau\nu\tau\nu$ | MC@NLO | 0.51 | 199676 | 392 |
| $W^+W^- \to \tau\nu e\nu$ | MC@NLO | 0.51 | 199950 | 392 |
| $W^+W^- \to \tau\nu\mu\nu$ | MC@NLO | 0.51 | 200000 | 392 |

## B.2 Event Selection Details

This section provides additional details on the selection efficiencies of the signal events and summarises a study of the effect of the parton distribution functions on the event acceptance for the $Z/\gamma^*$ background.

**Signal Acceptance** The expected numbers of signal events for the 7 simulated mass points for $\tan\beta = 40$ passing the event selection criteria are shown in Table B.4. As mentioned in Section 6.6 the offline $p_{\mathrm{T}}$ thresholds for muons are chosen rather soft such that the dependence of the selection efficiency on the signal mass is minimal. It can be seen in Table B.4 that the acceptance of the full event selection, i.e. after the $E_{\mathrm{T}}^{\mathrm{miss}}$ cut, increases with $m_A$ from about 60 % to 68 % for the gluon fusion samples and from about 63 % to 69 % for the $b$–quark associated Higgs boson production samples.

This is due to a residual dependence on the muon $p_{\mathrm{T}}$ thresholds and the $p_{\mathrm{T}}$–dependence of the trigger efficiency (see for example Section 5.2.2). The $\eta$ cut on the muons imposes an additional dependence of the signal efficiency on $m_A$ since the muons from Higgs bosons with higher mass are located more centrally in the detector. It can be seen, that the cut on the $\mu^+\mu^-$ invariant mass affecting in principle the low mass tail of the signal resonances has only a minor impact on the selection efficiency.

The selection efficiency for the signal produced in association with $b$ quarks is rather low in the $b$–tagged event category amounting to about 7 %. This is due to the typically low $p_{\mathrm{T}}$ of the $b$ jets and the experimental $b$–tagging efficiency as discussed in Section 6.6. In addition, it can be seen in Table B.4 that the selection efficiency in the $b$–tagged event category is significantly increasing from 5 % for $m_A = 110\,\mathrm{GeV}$ to 10 % for $m_A = 300\,\mathrm{GeV}$ which is due to the fact that the $p_{\mathrm{T}}$ spectrum of the $b$ jets becomes harder for increasing Higgs boson masses allowing for a more efficient tagging of the $b$ jets.

**PDF Reweighting** The expected $Z/\gamma^*$ background in the $h/A/H \to \mu^+\mu^-$ search is generated with the ALPGEN event generator. ALPGEN performs particularly well in the description of the kinematics and multiplicity of hard jets which are produced in association with the $Z/\gamma^*$ bosons. This is important for the analysis since the events are categorised according to the number of tagged $b$ jets. On the other hand, it was found that basic kinematic and fiducial quantities, like the $p_{\mathrm{T}}$, $\eta$ and $\phi$ of the muons from the $Z/\gamma^*$ boson decays are not very well described by ALPGEN. As an example, Figure B.1(a) shows the $\eta$ distribution of events observed in the data compared to the Standard Model background Monte Carlo events passing the $\mu^+\mu^-$ selection described in Section 6.6. At this stage of the selection, the background contains almost exclusively of $Z/\gamma^*$ boson events. It can be seen, that the data is distributed significantly more central than the $Z/\gamma^*$ boson Monte Carlo events..

**Table B.4:** Number of expected $A$ boson signal events produced in gluon fusion and association with $b$ quarks after each analysis cut for the simulated $A$ boson masses and $\tan\beta = 40$ for an integrated luminosity of $4.8\,\mathrm{fb}^{-1}$. The numbers in parentheses represent the statistical uncertainties on the last digit.

| Mass [GeV] | 110 | 130 | 150 | 170 | 200 | 250 | 300 |
|---|---|---|---|---|---|---|---|
| | | | | Gluon fusion for $\tan\beta = 40$ | | | |
| No Cut | 527[4]·10$^{0}$ | 227[2]·10$^{0}$ | 107[2]·10$^{0}$ | 557[4]·10$^{-1}$ | 229[2]·10$^{-1}$ | 638[3]·10$^{-2}$ | 2092[9]·10$^{-3}$ |
| MC weights | 527[4]·10$^{0}$ | 227[2]·10$^{0}$ | 107[2]·10$^{0}$ | 557[4]·10$^{-1}$ | 229[2]·10$^{-1}$ | 638[3]·10$^{-2}$ | 2092[9]·10$^{-3}$ |
| DQ cuts | 527[4]·10$^{0}$ | 227[2]·10$^{0}$ | 108[2]·10$^{0}$ | 557[4]·10$^{-1}$ | 229[2]·10$^{-1}$ | 638[3]·10$^{-2}$ | 2092[9]·10$^{-3}$ |
| Vertex | 526[4]·10$^{0}$ | 227[2]·10$^{0}$ | 108[2]·10$^{0}$ | 556[4]·10$^{-1}$ | 228[2]·10$^{-1}$ | 637[3]·10$^{-2}$ | 2087[9]·10$^{-3}$ |
| Trigger | 438[3]·10$^{0}$ | 192[1]·10$^{0}$ | 93[2]·10$^{0}$ | 480[4]·10$^{-1}$ | 199[2]·10$^{-1}$ | 559[3]·10$^{-2}$ | 1838[9]·10$^{-3}$ |
| 2+ $\mu$ objects | 332[3]·10$^{0}$ | 149[1]·10$^{0}$ | 73[1]·10$^{0}$ | 376[3]·10$^{-1}$ | 158[1]·10$^{-1}$ | 456[2]·10$^{-2}$ | 1509[8]·10$^{-3}$ |
| $\mu^+\mu^-$ pair | 332[3]·10$^{0}$ | 149[1]·10$^{0}$ | 73[1]·10$^{0}$ | 376[3]·10$^{-1}$ | 158[1]·10$^{-1}$ | 456[2]·10$^{-2}$ | 1509[8]·10$^{-3}$ |
| $m_{\mu\mu} > 70$ GeV | 330[3]·10$^{0}$ | 148[1]·10$^{0}$ | 73[1]·10$^{0}$ | 376[3]·10$^{-1}$ | 158[1]·10$^{-1}$ | 455[2]·10$^{-2}$ | 1509[8]·10$^{-3}$ |
| $E_{\mathrm{T}}^{\mathrm{miss}} < 40$ GeV | 318[3]·10$^{0}$ | 143[1]·10$^{0}$ | 70[1]·10$^{0}$ | 358[3]·10$^{-1}$ | 151[1]·10$^{-1}$ | 432[2]·10$^{-2}$ | 1421[8]·10$^{-3}$ |
| $N(b\text{-jet}) = 0$ | 313[3]·10$^{0}$ | 141[1]·10$^{0}$ | 69[1]·10$^{0}$ | 351[3]·10$^{-1}$ | 148[1]·10$^{-1}$ | 421[2]·10$^{-2}$ | 1381[8]·10$^{-3}$ |
| $N(b\text{-jet}) > 0$ | 49[3]·10$^{-1}$ | 23[1]·10$^{-1}$ | 13[1]·10$^{-1}$ | 71[4]·10$^{-2}$ | 31[2]·10$^{-2}$ | 110[4]·10$^{-3}$ | 39[1]·10$^{-3}$ |
| | | | | $b$–quark associated production for $\tan\beta = 40$ | | | |
| No Cut | 685[3]·10$^{0}$ | 391[2]·10$^{0}$ | 236[1]·10$^{0}$ | 1495[7]·10$^{-1}$ | 800[4]·10$^{-1}$ | 321[2]·10$^{-1}$ | 1429[6]·10$^{-2}$ |
| MC weights | 685[3]·10$^{0}$ | 391[2]·10$^{0}$ | 236[1]·10$^{0}$ | 1495[7]·10$^{-1}$ | 800[4]·10$^{-1}$ | 321[2]·10$^{-1}$ | 1429[6]·10$^{-2}$ |
| DQ cuts | 685[3]·10$^{0}$ | 391[2]·10$^{0}$ | 236[1]·10$^{0}$ | 1494[7]·10$^{-1}$ | 800[4]·10$^{-1}$ | 321[2]·10$^{-1}$ | 1428[6]·10$^{-2}$ |
| Vertex | 684[3]·10$^{0}$ | 390[2]·10$^{0}$ | 236[1]·10$^{0}$ | 1493[7]·10$^{-1}$ | 799[4]·10$^{-1}$ | 321[2]·10$^{-1}$ | 1427[6]·10$^{-2}$ |
| Trigger | 570[3]·10$^{0}$ | 332[2]·10$^{0}$ | 202[1]·10$^{0}$ | 1295[6]·10$^{-1}$ | 699[3]·10$^{-1}$ | 281[2]·10$^{-1}$ | 1253[6]·10$^{-2}$ |
| 2+ $\mu$ objects | 456[2]·10$^{0}$ | 270[1]·10$^{0}$ | 1669[9]·10$^{-1}$ | 1069[6]·10$^{-1}$ | 584[3]·10$^{-1}$ | 238[2]·10$^{-1}$ | 1066[5]·10$^{-2}$ |
| $\mu^+\mu^-$ pair | 455[2]·10$^{0}$ | 270[1]·10$^{0}$ | 1669[9]·10$^{-1}$ | 1069[6]·10$^{-1}$ | 584[3]·10$^{-1}$ | 238[2]·10$^{-1}$ | 1066[5]·10$^{-2}$ |
| $m_{\mu\mu} > 70$ GeV | 449[2]·10$^{0}$ | 268[1]·10$^{0}$ | 1661[9]·10$^{-1}$ | 1063[6]·10$^{-1}$ | 582[3]·10$^{-1}$ | 237[2]·10$^{-1}$ | 1063[5]·10$^{-2}$ |
| $E_{\mathrm{T}}^{\mathrm{miss}} < 40$ GeV | 430[2]·10$^{0}$ | 255[1]·10$^{0}$ | 1587[9]·10$^{-1}$ | 1012[5]·10$^{-1}$ | 552[3]·10$^{-1}$ | 223[2]·10$^{-1}$ | 993[5]·10$^{-2}$ |
| $N(b\text{-jet}) = 0$ | 395[2]·10$^{0}$ | 232[1]·10$^{0}$ | 1427[8]·10$^{-1}$ | 901[5]·10$^{-1}$ | 486[3]·10$^{-1}$ | 194[1]·10$^{-1}$ | 849[5]·10$^{-2}$ |
| $N(b\text{-jet}) > 0$ | 343[7]·10$^{-1}$ | 236[4]·10$^{-1}$ | 160[3]·10$^{-1}$ | 111[2]·10$^{-1}$ | 66[1]·10$^{-1}$ | 294[5]·10$^{-2}$ | 144[2]·10$^{-2}$ |

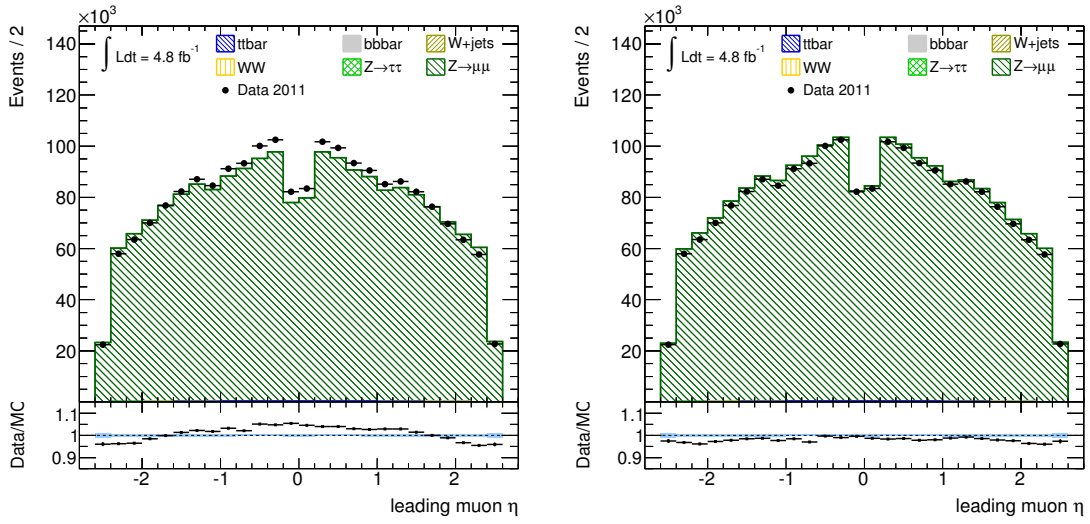


**Figure B.1:** Distributions of the pseudorapidity, $\eta$, of the leading muons in events passing the $\mu^+\mu^-$ selection shown for the data and the simulated background. The simulated $Z/\gamma^*$ background events generated with ALPGEN are shown before (a) and after the reweighting to the MRST2007LO* pdf set.

Comparisons with $Z/\gamma^*$ background events generated with PYTHIA showed that the PYTHIA sample provides a better description of the muon $p_{\mathrm{T}}$ and $\eta$ distributions. The differences in the kinematic and fiducial distributions modelled by the two generators are mainly due to the choice of the sets of parton distribution functions (PDF) for the event generation [222]. In ALPGEN the leading order CTEQ6ll PDF set [186–188] is used while PYTHIA uses MRST2007LO* [189] which is a leading order PDF set with next–to–leading order modifications.

Since ALPGEN performs better than PYTHIA in the description of the hard jets in the $\mu^+\mu^-$ events, the description of the kinematic properties of the muons are corrected for the PDF effects in the generated events. To this end, the initial state kinematics in the ALPGEN events are reweighted according to the more precise MRST2007LO* PDF set applied in PYTHIA using the LHAPDF [223, 224] tool. The weights depend on the flavour, momentum fraction and energy scale of the two interacting partons in the hard scattering.

Figure B.1(b) shows the $\eta$ distribution of events in data compared to the simulated background, where the ALPGEN $Z/\gamma^*$ boson events are reweighted to the MRST2007LO* PDF set. The PDF reweighting clearly improves the agreement with the data. Apart from the shapes of the muon kinematics, also the normalisation of the selected $Z/\gamma^*$ events is improved such that the differences in the acceptances of Monte Carlo and data events decrease from approximately 6 % before PDF reweighting to 2 % after PDF reweighting.

A reason for this is that since the $\eta$ distribution in ALPGEN samples without PDF reweighting is too flat compared to the data the fiducial cut of $|\eta| < 2.5$ rejects more events in the simulation than in data.

Due to the improved agreement in event acceptance the PDF reweighted ALPGEN samples are used to describe the $Z/\gamma^*$ background in the analysis. As mentioned in Section 6.11 the change in acceptance due to PDF reweighting is assigned as systematic uncertainty to the $Z/\gamma^*$ background yields. The effect amount to 3.5 % for the $Z/\gamma^*$+jets sample and 2.9 % for $Z$+$b$ jets sample.

## B.3 Background Model Validation

In order to validate the background model defined in Equation 6.24, function $f_{\mathrm{B}}$ is fitted to the $\mu^+\mu^-$ invariant mass distributions of the total simulated background and of the data in both the $b$–vetoed and $b$–tagged event categories. The validation employs $\chi^2$–based goodness–of–fit tests. The global fit $\chi^2$ value normalised to the number of degrees of freedom, $\chi^2/\mathrm{Ndof}$, as well as the corresponding $\chi^2$ probability, $P(\chi^2, \mathrm{Ndof})$, give good measures of the goodness of the fit.

As described in detail in the following, the $\chi^2$–tests performed on the modelling of the $\mu^+\mu^-$ invariant mass distributions of the simulated Monte Carlo background and of the data are compared with each other and with results of the modelling of pseudo–data generated from the parametrised distributions. Additionally, the background model is extended by Bernstein polynomials of orders 1 to 6 to test the impact of additional degrees of freedom on the $\chi^2$ value of the fit. This in particular tests the flexibility of the model, i.e. whether the model has enough free parameters to describe the actual shape of the $\mu^+\mu^-$ invariant mass distribution. To further cross–check the model flexibility and the stability of the fit, the fit range is varied and the respective fit results are compared. The fit residuals are inspected for systematic shifts or significant local structures. The statistical significances of the residuals are shown to be small. The goodness–of–fit studies show no significant mismodelling of the background above the expected statistical fluctuations in both event categories. Finally, the influence of the signal window size is evaluated for the sideband fits from which the initial background estimate is obtained.

**Background Modelling in the *b*–vetoed Event Category** For the $b$–vetoed event category the background model is fitted in the mass range from 110 GeV to 400 GeV. In order to validate if the background model can describe exactly the shape to the backgrounds in the $h/A/H \to \mu^+\mu^-$ search, a fit to a clean background–only sample needs to be performed. For that purpose, the background model is first fitted to the $\mu^+\mu^-$ invariant mass distribution of the total simulated background, as shown in Figure B.2(a). The pulls and the residuals, $D - B$, show a good compatibility of the background fit with

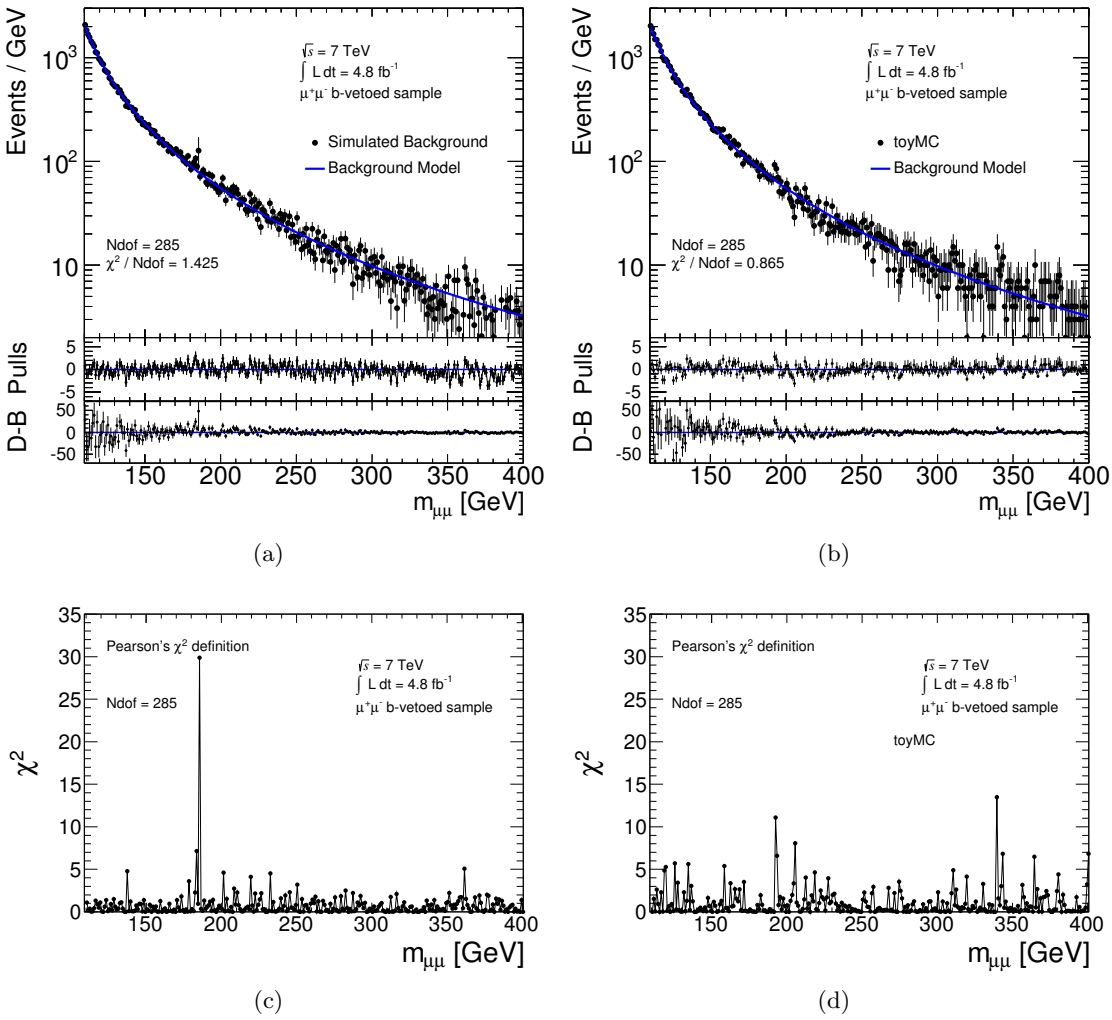


**Figure B.2:** Binned likelihood fits of the background model to the $\mu^+\mu^-$ invariant mass distribution of the total simulated background events (a) and in a Monte Carlo pseudo–data sample generated from the parametrised data (b) for the $b$–vetoed event category. The pulls and the residuals, labelled $D - B$, are also shown. Corresponding distributions of the $\chi^2$ values in each bin of the $\mu^+\mu^-$ invariant mass distribution obtained from the binned likelihood fit of the background model to the $\mu^+\mu^-$ invariant mass distribution of the total simulated background events (c) and in a Monte Carlo pseudo–data sample (d).

the simulation, even though the global $\chi^2$ normalised to the number of degrees of freedom, $\chi^2$/Ndof, is rather high. In the case that the fit residuals are only determined by statistical fluctuations, the $\chi^2$/Ndof is expected to be distributed around 1. On the other hand, this quantity cannot be interpreted straight forward in this application since the different contributions to the total simulated background are scaled by their cross sections to the

recorded instantaneous luminosity. The scaling factors are for some background samples rather large such that the bin–by–bin fluctuations in the $\mu^+\mu^-$ invariant mass distribution are not entirely defined by the Poisson probability.

The global fit $\chi^2$, the residuals and the pulls of the fit to the simulated background are compared with fit results which are expected if the background model is fitted to a distribution which exactly corresponds to the probability density function of the background model. To this end, a Monte Carlo pseudo–data invariant mass distribution is generated from the background function fitted to the simulated background. The pseudo–data sample has the same normalisation as the simulated background and thus has the expected statistical fluctuations given by the Poisson statistics.

The fit of $f_{\mathrm{B}}$ to this pseudo–data distribution is shown in Figure B.2(b). As expected, the global $\chi^2$ value is significantly lower compared to the fit to the simulated background. On the other hand, the distributions of the pulls and residuals do not differ significantly from the case where the background model is fitted to the simulated background. This is a hint that the background modelling performs correctly for the simulated background distribution but only results in a larger global $\chi^2$ value because the individual background distributions are scaled. Nevertheless, a residual mismodeling cannot be excluded at this stage since the pseudo–data distribution is biased with the hypothesis that the background model does describe the shape of the simulated background.

Figures B.2(c) and B.2(d) show the distributions for the bin–wise $\chi^2$ values of the fits for on the simulated background and the Monte Carlo pseudo–data distributions, respectively. These are useful to check if certain regions of the invariant mass distribution cause the increased global $\chi^2$ value of the fit to the simulated background. One significant bin fluctuation is prominent in the simulated background at a $\mu^+\mu^-$ invariant mass of about 190 GeV. This is one bin of the multijet background which has a large scale factor due to the large production cross section of this process. In addition, the mass region from 350 GeV to 400 GeV has a systematically higher local $\chi^2$ values which can also be seen in the pulls in Figure B.2(a).

The shape of the simulated background $\mu^+\mu^-$ invariant mass distribution describes the data reasonably as can be seen in Figure 6.8. Nevertheless, due to the bin–by–bin fluctuations in both distributions a residual mismodeling of the Monte Carlo shape cannot be excluded. Therefore, the background model validation needs also be performed on the data itself.

Considering the expected signal and background rates, the data is clearly dominated by the total background contribution and a possible signal appears only as small and narrow bumps as discussed in Section 6.9. Therefore, fit of function $f_{\mathrm{B}}$ in the complete fit range to the $\mu^+\mu^-$ invariant mass distribution of the data without accounting for signal windows is expected to also give a reliable model validation. In the absence of a signal it provides the most unbiased probe if the shape of the background can be described by the model and

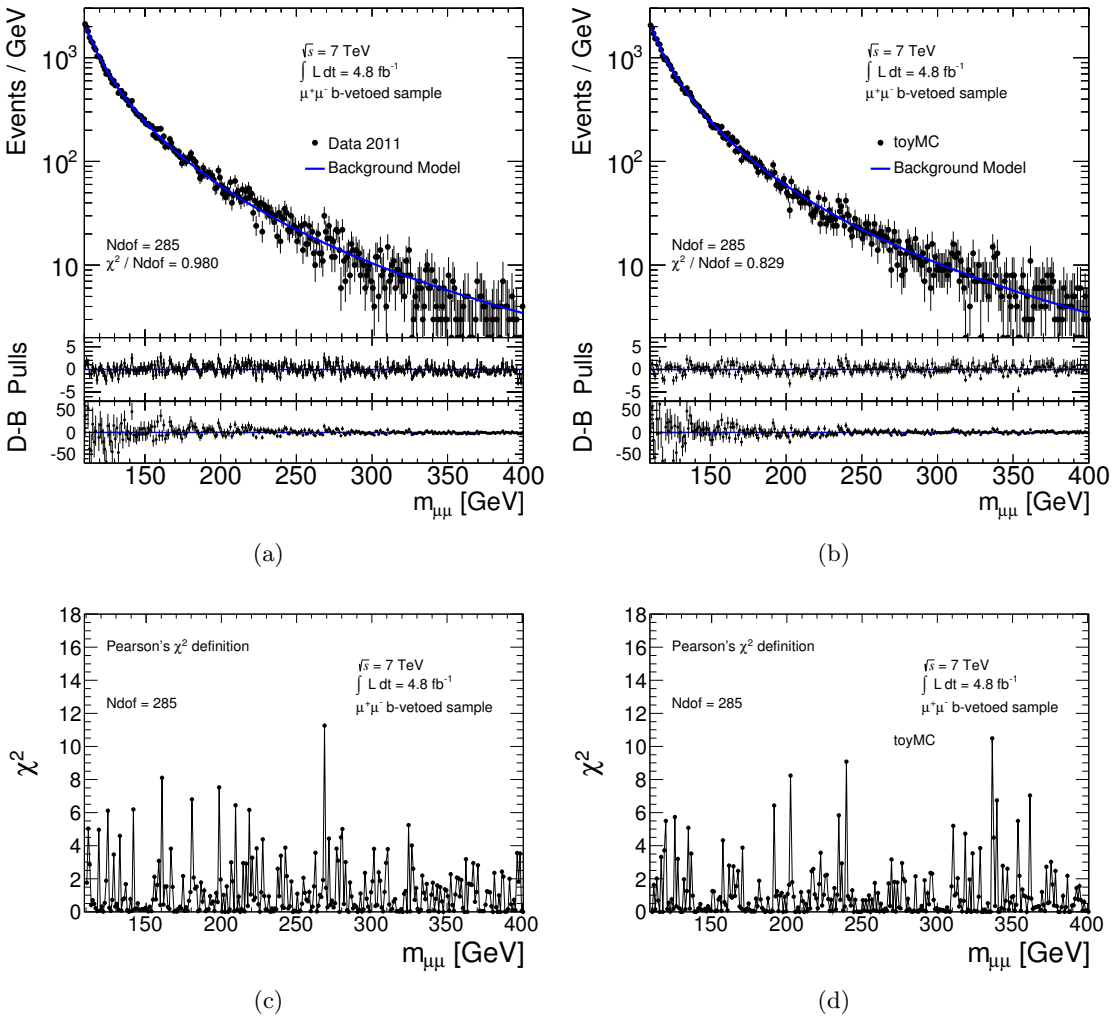


**Figure B.3:** Binned likelihood fits of the background model to the $\mu^+\mu^-$ invariant mass distribution in the data (a) and in a Monte Carlo pseudo–data sample generated from the parametrised data (b) for the $b$–vetoed event category. The pulls and the residuals, labelled $D - B$, are also shown. Corresponding distributions of the $\chi^2$ values in each bin of the $\mu^+\mu^-$ invariant mass distribution obtained from the binned likelihood fit of the background model to the $\mu^+\mu^-$ invariant mass distribution in the data (c) and in a Monte Carlo pseudo–data sample (d).

also the $\chi^2$–based fit results can be interpreted directly as the data is not scaled. In the case of a signal contamination of the data, the effect on the global fit $\chi^2$ value is expected not to be very significant.

Figure B.3(a) shows the results of the binned likelihood fit of function $f_{\mathrm{B}}$ to the data. The $\chi^2$/Ndof of the fit to the data amounts to 0.98 and the corresponding $\chi^2$ probability is

91 % which is significantly better as in the case of the fit to the simulated background. Pulls and residuals of the data compared to the background fit show no significant deviations and are well compatible with 0 given the statistical uncertainties which proves a very good description of the data by the background model.

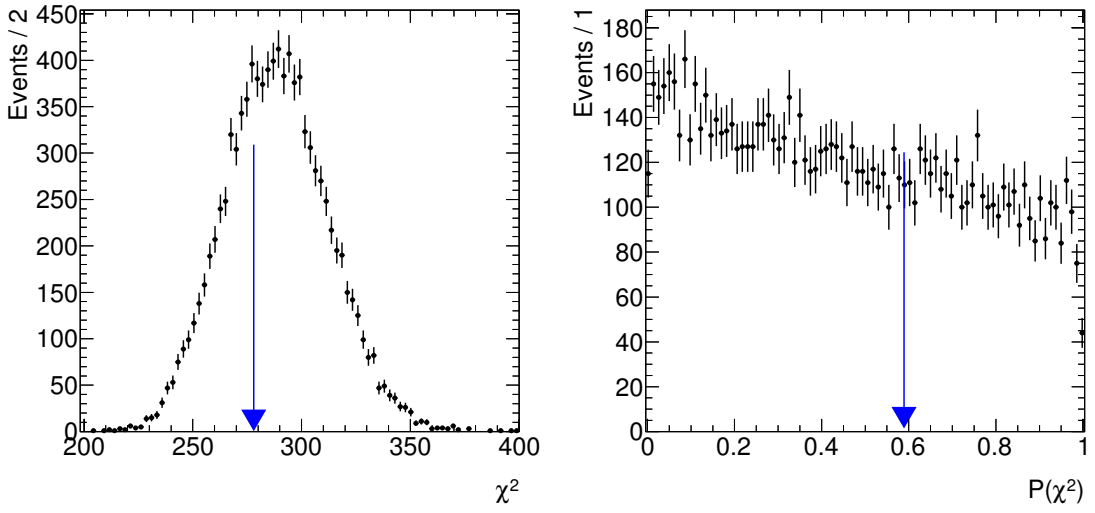


(a) (b)

**Figure B.4:** Distributions of the $\chi^2$ (a) and the $\chi^2$ probability, $P(\chi^2)$, (b) obtained from fitting the background model to distributions from 10000 Monte Carlo pseudo–data samples generated from the parametrised *mumu* invariant mass distribution in the data for the $b$–vetoed event category. The blue arrows indicate the $\chi^2$ and $P(\chi^2)$ obtained from fitting the background model to the respective invariant mass distribution in the data.

Like for the simulated background a Monte Carlo pseudo–data distribution is generated from the data parametrised by the background model. The results from fitting the background model to the Monte Carlo pseudo–data distribution, shown in Figure B.3(b), are very comparable to the results from fitting the background model to the data. The bin–wise local $\chi^2$ values for the two fits, shown in Figures B.3(c) and B.3(d), respectively, also show a very good compatibility.

No tension between the fit results like for the simulated background is observed. These results indicate a correct modelling of the data within the statistical uncertainties. Both the global $\chi^2$ value as well as the fluctuations all over the spectrum can be very well reproduced with the results from the fit to the Monte Carlo pseudo–data distribution.

As a closure test, many Monte Carlo pseudo–data distributions comparable to the one fitted in Figure B.3(b) are generated from the parametrised $\mu^+\mu^-$ invariant mass distribution and fitted with the background function. The distribution of the global $\chi^2$ values and the distribution of the corresponding $\chi^2$ probability, $P(\chi^2, \mathrm{Ndof})$, are shown in

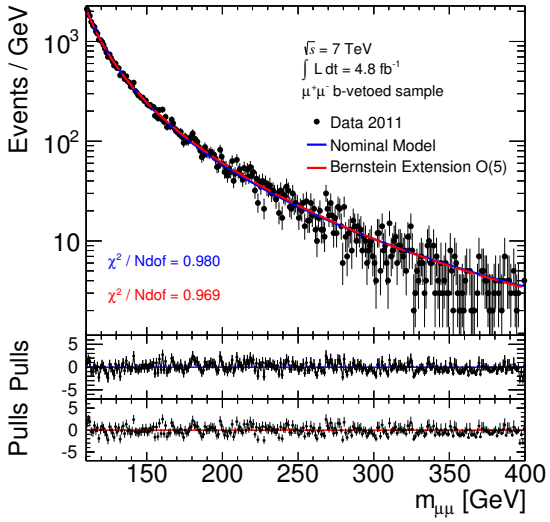


**Figure B.5:** Fits of the nominal background model and the background model extended with a 5th order Bernstein polynomial to the $\mu^+\mu^-$ invariant mass distribution of the $b$–vetoed event category in the data. The pulls for the nominal and extended background models are shown beneath.

Figure B.4. The blue arrows indicate the values for the global $\chi^2$ and $P(\chi^2, \text{Ndof})$ obtained from fitting the background model to the data which assures the validity of the applied background parametrisation.

In order to evaluate, if a background model with more degrees of freedom would result in a better description of the data, the nominal background model is extended with Bernstein polynomials of up to 5 degrees of freedom. Fits of the nominal and an extended model to the data are compared in Figure B.5 for an extension with a 5th degree Bernstein polynomial. It can be seen at most in the pulls for both models that even 5 degrees of freedom more do not result in a significantly better fit.

Sideband fits of function $f_\text{B}$ to the $\mu^+\mu^-$ invariant mass distribution outside the signal windows defined in Section 6.9 provide the initial background estimate for the statistical interpretation of the data of each point in the scanned $m_A$–$\tan\beta$ plane. The stability of the sideband fits with respect to the global fit of the background model to the data needs to be evaluated. Figure B.6 illustrates the result of the background model fitted to the entire $\mu^+\mu^-$ invariant mass distribution compared to the results of the background model fitted to the sidebands of the spectrum outside two different signal window definitions for the mass point $m_A = 150\,\text{GeV}$. The background estimate obtained from the two sideband fits are very compatible, which is indicated by the similar $\chi^2/\text{Ndof}$ values. The two background estimates differ to some extent from the fit to the entire spectrum but is well compatible within the fit parameter uncertainties.

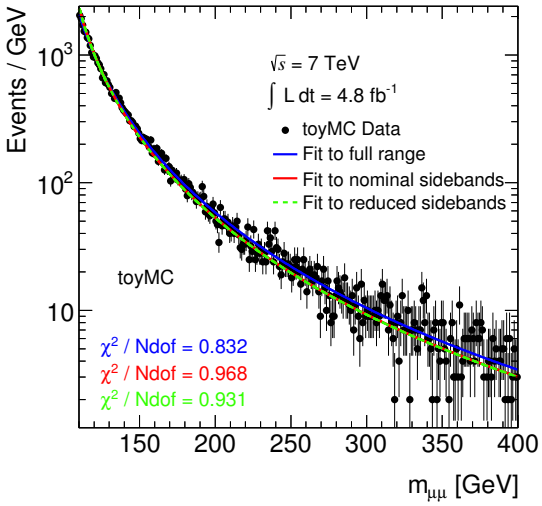


**Figure B.6:** Binned likelihood fits to the distribution of a Monte Carlo pseudo–data sample generated from the parametrised $\mu^+\mu^-$ invariant mass distribution in the data. The fits are performed over the whole visible mass range (blue), the nominal sideband regions (red) and reduced sideband regions (green) to illustrate the dependence of the fit result on the signal window size.

The fit to the reduced sidebands, i.e. outside the larger signal window compared to the definition in Section 6.9 results in a larger background uncertainty. In total, no significant systematic bias is observed when fitting the background model to the sidebands of the nominal signal windows compared to the parametrisation of the full spectrum for any considered point in the $m_A$–$\tan\beta$ plane.

**Table B.5:** Numbers of events in data, $N_{\text{Data}}$, compared to the numbers of events predicted from the background model fit to the data, $N_{\text{Background}}$, within the signal windows around several $m_A$ points in the $b$–vetoed event category. The signal windows correspond to a signal expectation for $\tan\beta = 40$. The relative differences, $(N_{\text{Data}} - N_{\text{Background}})/N_{\text{Background}}$, and pulls, $(N_{\text{Data}} - N_{\text{Background}})/\delta(N_{\text{Background}})$, of data and background prediction are also shown.

| $m_A$ | 130 | 150 | 170 | 200 | 250 | 300 |
|---|---|---|---|---|---|---|
| $N_{\text{Data}}$ | 14865 | 7728 | 4559 | 2586 | 1221 | 684 |
| $N_{\text{Background}}$ | $151[8] \cdot 10^2$ | $76[4] \cdot 10^2$ | $44[3] \cdot 10^2$ | $24[1] \cdot 10^2$ | $121[7] \cdot 10^1$ | $68[4] \cdot 10^1$ |
| $\frac{N_{\text{Data}} - N_{\text{Background}}}{N_{\text{Background}}}$ | −0.02[5] | 0.01[6] | 0.03[6] | 0.06[6] | 0.01[6] | −0.00[6] |
| $\frac{N_{\text{Data}} - N_{\text{Background}}}{\delta(N_{\text{Background}})}$ | −0.31 | 0.21 | 0.51 | 0.99 | 0.12 | −0.05 |

Table B.5 shows the numbers of events observed in the data within the signal windows defined in Section 6.9 around simulated $A$ boson mass points. The numbers are compared to the numbers of expected background events in these mass windows obtained from

the sideband fits. The numbers are well compatible within the uncertainties of the fit parameters. In addition, the quantity $\frac{N_{\text{obs}}-N_{\text{exp}}}{N_{\text{exp}}}$ gives the relative deviation of the observed from the expected background events in the signal window. Within the uncertainties in the predicted background these fluctuations are well consistent with 0. Furthermore, the pulls, $\frac{N_{\text{obs}}-N_{\text{exp}}}{\delta N_{\text{exp}}}$, are expected to fluctuate around 0 with a variation of 1 if the fluctuations in the observation are covered by the background uncertainties. Although there are not enough statistically independent measurements available, the pulls show qualitatively an expected behaviour.

**Background Modelling in the *b*–tagged event category** The background parametrisation defined in Section 6.10 is also used to model the total $\mu^+\mu^-$ background in the $b$–tagged event category. The same validation a presented in the previous paragraph is needed for the $b$–tagged event category since the background in this category is composed differently. The same techniques as demonstrated above are used for the validation applied on the $\mu^+\mu^-$ invariant mass distribution in the $b$–tagged event category for both simulated backgrounds and the data.

For the $b$–tagged event category the background model is fitted in a mass range from 110 to 250 GeV since for higher invariant masses only very few events pass the event selection and no precise characterisation of the spectrum is possible. Figure B.7 shows the results for the binned likelihood fits of function $f_{\text{B}}$ to the data and a Monte Carlo pseudo–data distribution generated from the parametrised data. Like for the results for the $b$–vetoed event category, the result for the fit to the data has a very good global $\chi^2$ value and is very comparable to the result for a fit to a corresponding Monte Carlo pseudo–data distribution. In summary, the validation for the background parametrisation in the $b$–tagged event category shows no significant mismodeling within the statistical uncertainty of this event category.

Table B.6 shows the numbers of events observed in the data in the signal windows defined in Section 6.9 around simulated $A$ boson mass points. Like for the $b$–vetoed event category, the numbers are compared to the numbers of expected background events in these mass windows obtained from the parametrisation of the $\mu^+\mu^-$ invariant mass spectrum. Due to the large statistical uncertainty in this event category the uncertainties of the fit parameters and thus, the background estimate are quite large. Within these uncertainties, the numbers of estimated background events are well compatible with the number of events observed in the data.

## B.4 Model–Independent Search for Excesses and Deficits

The model–dependent approach to the search for the signal or its exclusion as described in the previous section can be complemented by a model–independent approach of evaluating

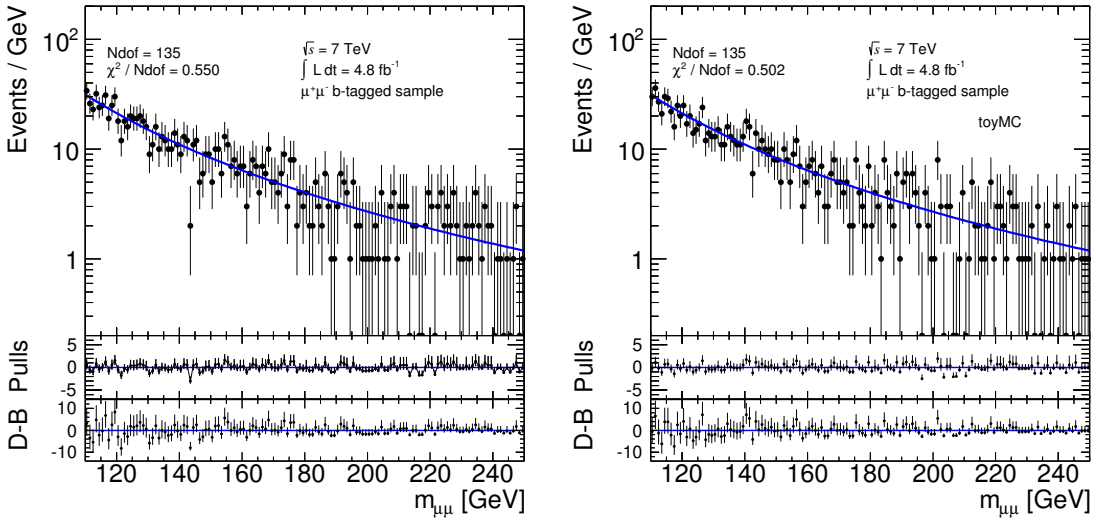


(a) (b)

**Figure B.7:** Binned likelihood fits of the background model to the $\mu^+\mu^-$ invariant mass distribution in the data (a) and in a Monte Carlo pseudo–data sample generated from the parametrised data (b) for the $b$–tagged event category. The pulls and the residuals, labelled $D - B$, are also shown.

the significance of any excess or deficit in the number of observed events compared to the background expectation.

As can be seen in Figure 6.13 the observed data fluctuate around the expected background obtained from the fit of the background function, $f_{\mathrm{B}}$, to the observed $\mu^+\mu^-$ invariant mass distribution. In this section the background model introduced in Section 6.10 is used to search for the most significant local excesses and deficits in the mentioned fluctuations with no restriction to a specific signal expectation. This means that neither any input from simulation nor from the signal model established in Section 6.9 is considered. Consequently, since only one hypothesis — the background–only hypothesis — is tested the statistical procedure to quantify the significance of the local excesses and deficits which are in the following referred to as bumps is somewhat modified with respect to the hypothesis test discussed in the previous section.

Such a model–independent approach is relevant because of two reasons. Firstly, the existence of significantly pronounced bumps can hint for a mismodelling of the background, especially if the bumps are very broad. In that sense this approach can be regarded as an additional validation procedure of the background modelling which allows for a more quantitative interpretation of the bin–by–bin significances shown in Figure 6.13 taking into account the bin correlations rather than only the deviations in each separate bin. Secondly, in the search for new unexpected physics phenomena it is of great interest if a

**Table B.6:** Numbers of events in data, $N_{\text{Data}}$, compared to the numbers of events predicted from the background model fit to the data, $N_{\text{Background}}$, within the signal windows around several $m_A$ points in the $b$–tagged event category. The signal windows correspond to a signal expectation for $\tan\beta = 40$. The relative differences, $(N_{\text{Data}} - N_{\text{Background}})/N_{\text{Background}}$, and pulls, $(N_{\text{Data}} - N_{\text{Background}})/\delta(N_{\text{Background}})$, of data and background prediction are also shown.

| $m_A$ | 130 | 150 | 170 | 200 |
|---|---|---|---|---|
| $N_{\text{Data}}$ | 355 | 248 | 191 | 96 |
| $N_{\text{Background}}$ | $37[6] \cdot 10^1$ | $25[7] \cdot 10^1$ | $17[2] \cdot 10^1$ | $11[7] \cdot 10^1$ |
| $\frac{N_{\text{Data}} - N_{\text{Background}}}{N_{\text{Background}}}$ | $-0.0[2]$ | $-0.0[3]$ | $0.1[1]$ | $-0.1[6]$ |
| $\frac{N_{\text{Data}} - N_{\text{Background}}}{\delta(N_{\text{Background}})}$ | $-0.17$ | $-0.01$ | $0.95$ | $-0.20$ |

significant bump can be observed on top of the background fluctuations which are present over the whole mass spectrum. Even though the search for neutral MSSM Higgs bosons in $h/A/H \to \mu^+\mu^-$ decays profits from the well defined signal expectations as discussed in Section 6.9, a complete signal–model–independent search has the advantage of testing the inconsistency of the data with the background–only hypothesis without any dependence on a specific signal–plus–background hypothesis. This allows for the search for unexpected physics phenomena beyond the Standard Model expectations since the large variety of models can lead to signal resonances of various shapes.

To search for bumps with arbitrary structure, arbitrary widths and at arbitrary positions in the binned $\mu^+\mu^-$ invariant mass distribution the analysis framework called the BumpHunter [192] is used. The BumpHunter algorithm performs a multiple statistical hypothesis test which is introduced briefly in the following based on Reference [192].

**The BumpHunter Hypothesis Test** To search for all possible local excesses and deficits which can appear in the $\mu^+\mu^-$ invariant mass distribution the BumpHunter algorithm combines all individual hypothesis tests which can be performed in the studied mass range without specifying a particular signal model. For that purpose a new test statistic compared to the ones introduced in Section 6.8 is introduced,

$$t = -\log\left(\min_i\left(p_{0,i}\right)\right), \tag{B.1}$$

which uses the smallest local $p_0$–value of the background–only hypothesis found among all local $p_{0,i}$–values in each single hypothesis test, $i$.

The $\mu^+\mu^-$ invariant mass spectrum is scanned using a number of sliding mass windows with varying widths placed at different positions in the mass spectrum. For each of these sliding windows the number of expected background events is compared to the number of events observed in the data. For each observed discrepancy between the data and

background expectation in the considered mass window the local $p_{0,i}$–value is evaluated.

The local $p_{0,i}$–values are at first approximated analytically based on the Poisson probability of observing at least $n_{\mathrm{D}}$ events in the data when $n_{\mathrm{B}}$ background events are expected. The approximation is justified since only the minimum of all local $p_{0,i}$–values is used for the final result and not their exact values. This avoids the need for the sampling of a test statistic of each sliding window over many Monte Carlo pseudo–experiments and allows for a computationally efficient performance of the BumpHunter algorithm, even for a large number of tested mass windows.

A Poisson–based $p_{0,i}$–value is evaluated for each assumed window size at each position in the mass spectrum. Subsequently, the BumpHunter test statistic, $t$, is obtained from the set of Poisson–based $p_{0,i}$–values using Equation B.1. To obtain the final result in terms of a statistical significance of the most pronounced bump, the pdf of the BumpHunter test statistic is sampled by means of Monte Carlo pseudo–experiments based on the background–only hypothesis.

The search for bumps of undefined widths or shapes in the $\mu^+\mu^-$ invariant mass distribution over a wide mass range obviously involves the look–elsewhere effect [180] which is summarised in Section 6.8. However, since the BumpHunter test statistic selects the most significant local bump anywhere in the search range for each generated pseudo–experiment for the background–only hypothesis, the look–elsewhere effect is by construction taken into account.

**Results of the BumpHunter Analysis** The BumpHunter algorithm is used for the scan of the $\mu^+\mu^-$ invariant mass distribution in the $b$–tagged and $b$–vetoed event categories in the mass ranges of 120 GeV to 250 GeV and 120 GeV to 400 GeV, respectively. The width of the considered bumps is a free parameter but constrained by lower and upper bounds. Deviations from the background expectations in the $\mu^+\mu^-$ invariant mass spectrum which are to be considered to originate from new physics processes are required to have a width of at least the $\mu^+\mu^-$ mass resolution at the given position in the mass spectrum. To obtain a conservative lower bound on the width of a physical bump a constant mass resolution of 2.5 % is assumed for the whole spectrum from 120 GeV to 400 GeV. Furthermore, to exclude false bumps from unphysical single bin fluctuations the lower bound on the bump width is additionally restricted to at least two bins of the mass spectrum. The maximum bump width up is chosen to be half of the scanned mass range.

The model for the background–only hypothesis is obtained from the binned extended likelihood fits of the background parametrisation from Equation 6.24 to the data in the scanned invariant mass range. Unlike in the previous sections, the background estimate is not obtained from the sidebands but from the full mass spectrum since no particular signal window can be specified for the scan by the BumpHunter algorithm. However, the validation of the background modelling in Section 6.10 has shown that every possible

physical bump is very small compared to the expected background and therefore not expected to affect the normalisation of the background model significantly. Furthermore, the shape of the background model is also not expected to be affected by a presence of a physical bump since there are no free parameters in the model to describe such a structure.

The results of the BumpHunter scan for the mentioned intervals in the $\mu^+\mu^-$ invariant mass distribution in the $b$–tagged and $b$–vetoed event categories are illustrated in Figure B.8. The size of all bin–by–bin excesses and deficits are quantified in terms of their statistical significance and the bumps found by the BumpHunter algorithm having a local Poisson–based $p_0$–value of less than $10^{-1}$ are visualised by the blue and green areas, respectively. The corresponding mass intervals and Poisson–based $p_0$–values are listed in Table B.7.

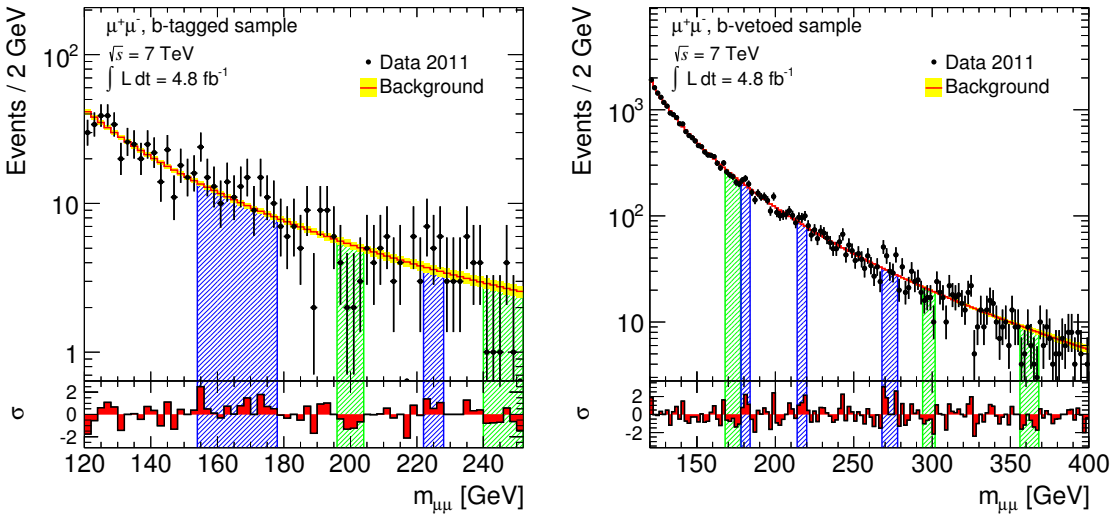


(a) (b)

**Figure B.8:** Results of the BumpHunter analysis of the $\mu^+\mu^-$ invariant mass spectrum in the $b$–tagged (a) and $b$–vetoed event categories (b). Mass ranges with excesses (deficits) having a local Poisson–based $p_0$–values of less than $10^{-1}$ with respect to the background–only hypothesis are indicated by the shaded blue (green) areas. The bin–by–bin significances of the deviations of the data from the background prediction, labelled $\sigma$, are shown beneath.

The most significant excess in the $b$–tagged event category is found in the range of 154 GeV to 178 GeV. The local Poisson–based $p_0$–value of $1.2 \cdot 10^{-2}$ ($2.3\,\sigma$) of this excess corresponds to a global $p_0$–value of $3.6 \cdot 10^{-1}$ ($0.35\,\sigma$) after integrating over the sampled BumpHunter test statistic, $t$, which accounts for the trials factor. The most significant deficit is found in the range of 196 GeV to 204 GeV and has a local Poisson–based $p_0$–value of $1.7 \cdot 10^{-2}$ ($2.1\,\sigma$). The corresponding global $p_0$–value of the BumpHunter test statistic, $t$, is $4.9 \cdot 10^{-1}$ with a Gaussian statistical significance of $0.064\,\sigma$.

In the $b$–vetoed event category the most significant excess is in the $\mu^+\mu^-$ invariant mass

range of 268 GeV to 278 GeV with a local Poisson–based $p_0$–value of $2.6 \cdot 10^{-4}$ ($3.5\,\sigma$). Accounting for the trials factor the corresponding global $p_0$–value amount to $4.6 \cdot 10^{-2}$ corresponding to a statistical significance of $1.7\,\sigma$. The most significant deficit in the $b$–vetoed event category is found in the range of 356 GeV to 368 GeV having a local Poisson–based $p_0$–value of $4.3 \cdot 10^{-3}$ ($2.6\,\sigma$). The corresponding global $p_0$–value amounts to $4.5 \cdot 10^{-1}$ which corresponds to a statistical significance of $0.14\,\sigma$.

**Table B.7:** Most significant excesses and deficits of observed data with respect to the background fit with corresponding $\mu^+\mu^-$ invariant mass intervals and local Poisson–based $p_0$–values as obtained from BumpHunter scans in the $b$–tagged and $b$–vetoed event categories.

| Type | Interval [GeV] | $p$-value |
|---|---|---|
| $b$-tagged event category | | |
| Excess | [154,178] | $1.2 \cdot 10^{-2}$ |
| Excess | [222,228] | $5.4 \cdot 10^{-2}$ |
| Deficit | [196,204] | $1.7 \cdot 10^{-2}$ |
| Deficit | [240,252] | $2.8 \cdot 10^{-2}$ |
| Deficit | [120,124] | $6.5 \cdot 10^{-2}$ |
| $b$-vetoed event category | | |
| Excess | [268,278] | $2.6 \cdot 10^{-4}$ |
| Excess | [214,220] | $5.3 \cdot 10^{-3}$ |
| Excess | [178,184] | $8.5 \cdot 10^{-3}$ |
| Deficit | [354,368] | $4.3 \cdot 10^{-3}$ |
| Deficit | [294,302] | $1.3 \cdot 10^{-2}$ |
| Deficit | [168,178] | $3.0 \cdot 10^{-2}$ |

In summary, no significant excess of data above the background expectation is found in both event categories by the BumpHunter analysis. The most significant excess is found in the $b$–vetoed event category and corresponds to a statistical significance of only $1.7\,\sigma$. Also the structure of this bump is not characteristic for a physical excess. Furthermore, the fact that none of the excesses and deficits are very significant shows the reliability of the applied background model. It is noted that since a large number of hypotheses are tested, the BumpHunter scan is able to spot many anomalous features but consequently involves very high trials factors of up to about 150 which decrease the power of a single hypothesis test. A statistical analysis of the data including specific signal expectations for neutral Higgs bosons predicted by the MSSM presented in Section 6.12 provides a less flexible but statistically more sensitive test.

## B.5 Validation of the Asymptotic Approximation

The exclusion limits presented in Section 6.12 are obtained using asymptotic formulae. In order to validate the application of the asymptotic approximation the results are compared using the approach of sampling the probability density function, $f(\tilde{q}_\mu|\mu)$, with a large number of pseudo–experiments. The Monte Carlo pseudo–data validation is performed for the benchmark point of $m_A = 150\,\text{GeV}$ and $\tan\beta = 40$ in the $b$–vetoed event category. The expected asymptotic limit at 95 % confidence level for this $m_A$–$\tan\beta$ point is $\mu = 0.6346$. For the fixed $\mu$ values of $\mu = 0.58$, 0.60, 0.62, 0.64, 0.66, 0.68 limits are evaluated from the sampling distributions of the test statistic generated with 25000 Monte Carlo pseudo–data samples each. The sampling distributions for the signal–plus–background hypothesis and background–only hypothesis are compared to the respective asymptotic approximations of the probability density functions in Figure B.9 for the six different $\mu$ values. Table B.8 shows the expected $\text{CL}_\text{s}$ values for the corresponding values of $\mu$. From interpolation of the five points an observed limit at 95 % CL is $\mu = 0.6358 \pm 0.0062$. This limit agrees very well with the asymptotic limit $\mu = 0.6346$ and proves the validity of the asymptotic approximation for this application.

**Table B.8:** Expected $\text{CL}_\text{s}$ values for different fixed values of $\mu$ obtained from sampling the distribution of the test statistic, $f(\tilde{q}_\mu|\mu)$, with 25000 Monte Carlo pseudo–experiments.

| $\mu$ | $\text{CL}_\text{s}$ | | |
|---|---|---|---|
| 0.58 | 0.0796 | $\pm$ | 0.0031 |
| 0.60 | 0.0689 | $\pm$ | 0.0029 |
| 0.62 | 0.0570 | $\pm$ | 0.0026 |
| 0.64 | 0.0482 | $\pm$ | 0.0025 |
| 0.66 | 0.0401 | $\pm$ | 0.0022 |
| 0.68 | 0.0389 | $\pm$ | 0.0022 |

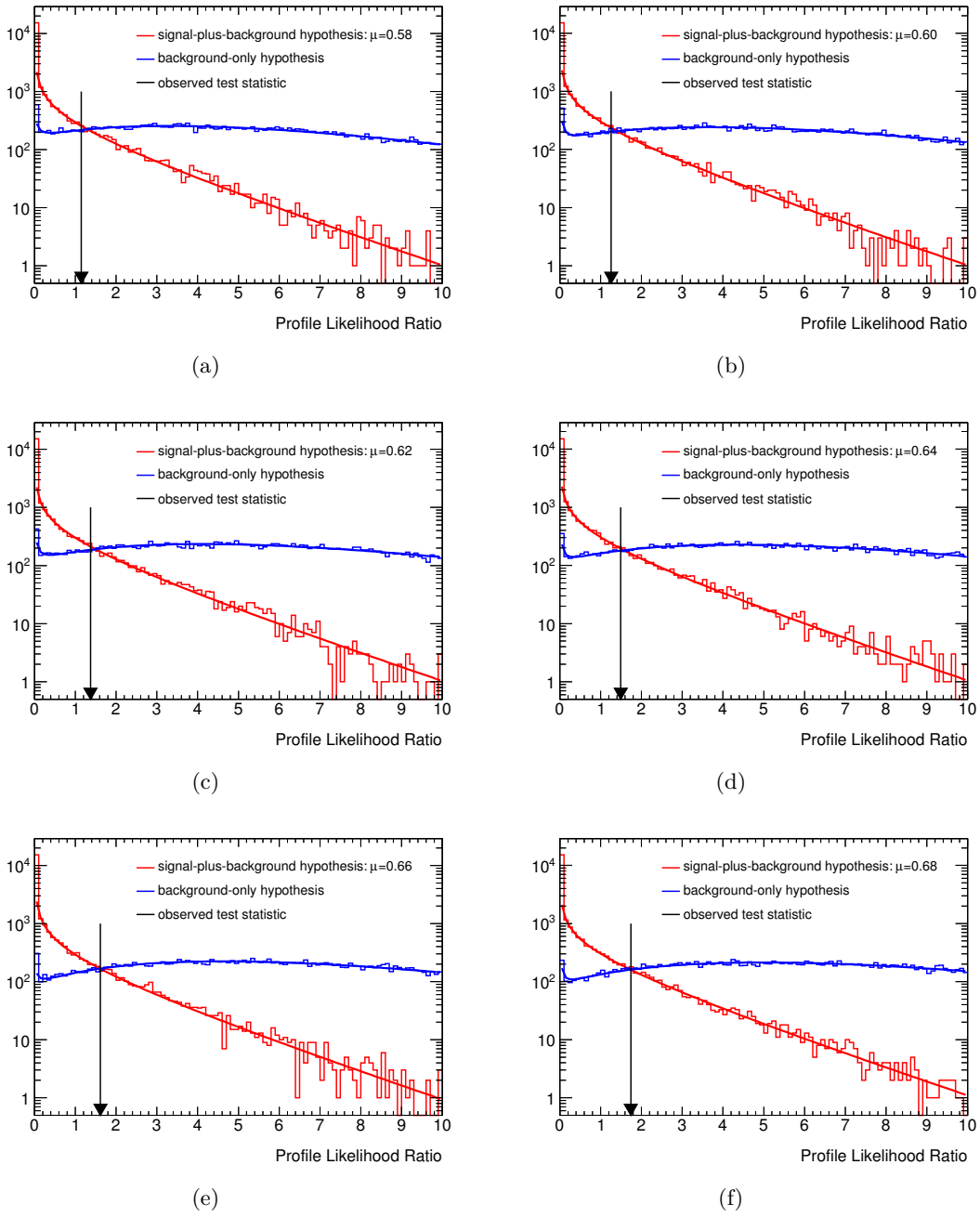


**Figure B.9:** Sampling distributions of the test statistic, $f\,(\tilde{q}_\mu|\mu)$, for signal–plus–background (red) and background–only hypotheses (blue) obtained from 25000 Monte Carlo pseudo–experiments for the benchmark point with $m_A = 150\,\text{GeV}$ and $\tan\beta = 40$ in the $b$–vetoed event category for different $\mu$ values around the asymptotic limit $\mu = 0.6346$. The functions for the asymptotic approximations of the test statistics are also shown.

# List of Figures

# List of Tables

# Bibliography


[1] A. Djouadi, *The Anatomy of Electroweak Symmetry Breaking — Tome I: The Higgs Boson in the Standard Model*, Phys. Rep. **457** (2008) 1.

[2] A. Pich, *The Standard Model of Electroweak Interactions*, `arXiv:0705.4264 [hep-ph]`.

[3] A. Djouadi, *The Anatomy of Electroweak Symmetry Breaking — Tome II: The Higgs Bosons in the Minimal Supersymmetric Model*, Phys. Rep. **459** (2008) 1.

[4] S. P. Martin, *A Supersymmetry Primer*, `arXiv:hep-ph/9709356 [hep-ph]`.

[5] C.-N. Yang and R. L. Mills, *Conservation of Isotopic Spin and Isotopic Gauge Invariance*, Phys. Rev. **96** (1954) 191.

[6] S. L. Glashow, *Partial Symmetries of Weak Interactions*, Nuc. Phys. **22** (1961) 579.

[7] A. Salam, *Weak and Electromagnetic Interactions*, Conf. Proc. **C 680519** (1968) 367. Originally printed in Svartholm: Elementary Particle Theory, proceedings of the Nobel Symposium held 1968 at Lerum, Sweden.

[8] S. Weinberg, *A Model of Leptons*, Phys. Rev. Lett. **19** (1967) 1264.

[9] H. Fritsch, M. Gell-Mann, and H. Leutwyler, *Advantages of the Color Octet Gluon Picture*, Phys. Lett. B **47** (1973) 365.

[10] I. Aitchison and A. Hey, *Gauge Theories in Particle Physics: A Practical Introduction, Vol. 1: From Relativistic Quantum Mechanics to QED*. Inst. of Physics Pub., 2003.

[11] C. S. Wu, E. Ambler, R. W. Hayward, D. D. Hoppes, and R. P. Hudson, *Experimental Test of Parity Conservation in Beta Decay*, Phys. Rev. **105** (1957) 1413.

[12] S. Bethke, *Experimental Tests of Asymptotic Freedom*, Prog. Part. Nucl. Phys. **58** (2007) 351.

[13] P. W. Higgs, *Broken Symmetries, Massless Particles and Gauge Fields*, Phys. Lett. **12** (1964) 132.

[14] F. Englert and R. Brout, *Broken Symmetry and the Mass of Gauge Vector Mesons*, Phys. Rev. Lett. **13** (1964) 321.

[15] P. W. Higgs, *Broken Symmetries and the Masses of Gauge Bosons*, Phys. Rev. Lett. **13** (1964) 508.

[16] G. S. Guralnik, C. R. Hagen, and T. W. B. Kibble, *Global Conservation Laws and Massless Particles*, Phys. Rev. Lett. **13** (1964) 585.

[17] P. W. Higgs, *Spontaneous Symmetry Breakdown without Massless Bosons*, Phys. Rev. **145** (1966) 1156.

[18] T. W. B. Kibble, *Symmetry Breaking in Non–Abelian Gauge Theories*, Phys. Rev. **155** (1967) 1554.

[19] J. Goldstone, *Field Theories with Superconductor Solutions*, Nuovo Cim. **19** (1961) 154.

[20] G. 'tHooft, *Renormalization of Massless Yang–Mills Fields*, Nuc. Phys. B **33** (1971) 173.

[21] C. L. Smith, *High Energy Behaviour and Gauge Symmetry*, Phys. Lett. B **46** (1973) 233.

[22] J. M. Cornwall, D. N. Levin, and G. Tiktopoulos, *Uniqueness of Spontaneously Broken Gauge Theories*, Phys. Rev. Lett. **30** (1973) 1268.

[23] K. Riesselmann, *Limitations of a Standard Model Higgs Boson*, `arXiv:hep-ph/9711456 [hep-ph]`.

[24] A. Arhrib, *Unitarity Constraints on Scalar Parameters of the Standard and two Higgs Doublets Model*, `arXiv:hep-ph/0012353 [hep-ph]`.

[25] W. J. Marciano, G. Valencia, and S. Willenbrock, *Renormalization Group Improved Unitarity Bounds on the Higgs Boson and Top Quark Masses*, Phys. Rev. **D 40** (1989) 1725.

[26] T. Cheng, E. Eichten, and L.-F. Li, *Higgs Phenomena in Asymptotically Free Gauge Theories*, Phys. Rev. **D 9** (1974) 2259.

[27] J. Ellis, J. Espinosa, G. Giudice, A. Hoecker, and A. Riotto, *The Probable Fate of the Standard Model*, Phys. Lett. **B 679** (2009) 369.

[28] N. P. Nilles, *Supersymmetry, Supergravity and Particle Physics*, Phys. Rep. **110** (1984) 1.

[29] H. E. Haber and G. L. Kane, *The Search for Supersymmetry: Probing Physics Beyond the Standard Model*, Phys. Rep. **117** (1985) 75.

[30] W. Hollik, *Standard Model Theory*, `arXiv:hep-ph/9811313 [hep-ph]`.

[31] The ALEPH, CDF, DØ, DELPHI, L3, OPAL and SLD Collaborations, the LEP Electroweak Working Group, Tevatron Working Group and SLD Electroweak and Heavy Flavour Working Groups, *Precision Electroweak Measurements and Constraints on the Standard Model*, `arXiv:1012.2367 [hep-ex]`. Updated for 2012 winter conferences, March 2012, http://www.cern.ch/LEPEWWG.

[32] The Gfitter Group, M. Baak, et al., *Updated Status of the Global Electroweak Fit And constraints on New Physics*, Eur. Phys. J. **C 72** (2012) 2003. Updated for 2012 winter conferences, March 2012, http://gfitter.desy.de.

[33] `http://lepewwg.web.cern.ch/LEPEWWG/plots/winter2012`.

[34] `http://gfitter.desy.de/Standard_Model/2012_05_03_index.html`.

[35] W. Haxton, R. Hamish Robertson, and A. M. Serenelli, *Solar Neutrinos: Status and Prospects*, `arXiv:1208.5723 [astro-ph.SR]`.

[36] M. Gell-Mann, P. Ramond, and R. Slansky, *Complex Spinors and Unified Theories*, Conf. Proc. **C 790927** (1979) 315.

[37] F. Zwicky, *Spectral Displacement of Extra Galactic Nebulae*, Helv. Phys. Acta **6** (1933) 110.

[38] E. W. Kolb and M. S. Turner, *The Early Universe*, Front. Phys. **69** (1990) 1.

[39] The WMAP Collaboration, D. N. Spergel et al., *First Year Wilkinson Microwave Anisotropy Probe (wmap) Observations: Determination of Cosmological Parameters*, Astrophys. J. Suppl. **148** (2003) 175.

[40] H. M. Georgi and S. L. Glashow, *Unity of All Elementary–Particle Forces*, Phys. Rev. Lett. **32** (1974) 438.

[41] J. C. Pati and A. Salam, *Lepton Number as the Fourth "Color"*, Phys. Rev. D **10** (1974) 275.

[42] S. Weinberg, *Gauge Hierarchies*, Phys. Lett. B **82** (1979) 387.

[43] M. Veltman, *The Infrared–Ultraviolet Connection*, Acta Phys. Polon. **B 12** (1981) 437.

[44] C. Smith and G. Ross, *The Real Gauge Hierarchy Problem*, Phys. Lett. B **105** (1981) 38.

[45] J. Wess and B. Zumino, *Supergauge Transformations in Four–Dimensions*, Nucl.Phys. **B70** (1974) 39.

[46] S. R. Coleman and J. Mandula, *All Possible Symmetries of the S Matrix*, Phys.Rev. **159** (1967) 1251.

[47] R. Haag, J. T. Lopuszanski, and M. Sohnius, *All Possible Generators of Supersymmetries of the S Matrix*, Nucl.Phys. **B88** (1975) 257.

[48] P. van Nieuwenhuizen, *Supergravity*, Phys. Rep. **68** (1981) 189.

[49] J. Ellis, J. Hagelin, D. Nanopoulos, K. Olive, and M. Srednicki, *Supersymmetric Relics From the big Bang*, Nuc. Phys. B **238** (1984) 453.

[50] G. Jungman, M. Kamionkowski, and K. Griest, *Supersymmetric Dark Matter*, Phys. Rep. **267** (1996) 195.

[51] J. Ellis, S. Kelley, and D. Nanopoulos, *Probing the Desert Using Gauge Coupling Unification*, Phys. Lett. B **260** (1991) 131.

[52] J. Hisano, H. Murayama, and T. Yanagida, *Nucleon Decay in the Minimal Supersymmetric SU(5) Grand Unification*, Nuc. Phys. B **402** (1993) 46.

[53] E. Witten, *Dynamical Breaking of Supersymmetry*, Nuc. Phys. B **188** (1981) 513.

[54] L. Hall, J. Lykken, and S. Weinberg, *Supergravity as the Messenger of Supersymmetry Breaking*, Phys. Rev. D **27** (1983) 2359.

[55] H. P. Nilles, *Dynamically Broken Supergravity and the Hierarchy Problem*, Phys. Lett. B **115** (1982) 193.

[56] M. Dine and A. E. Nelson, *Dynamical Supersymmetry Breaking at low Energies*, Phys. Rev. D **48** (1993) 1277.

[57] G. Giudice and R. Rattazzi, *Theories with Gauge–Mediated Supersymmetry Breaking*, Phys. Rep. **322** (1999) 419.

[58] L. Ibanez and G. G. Ross, $SU(2)_L$–$U(1)$ *Symmetry Breaking as a Radiative Effect of Supersymmetry Breaking in Guts*, Phys. Lett. B **110** (1982) 215.

[59] S. Heinemeyer, W. Hollik, and G. Weiglein, *The Masses of the Neutral CP–Even Higgs Bosons in the MSSM: Accurate Analysis at the Two–Loop Level*, Eur. Phys. J. **C 9** (1999) 343.

[60] M. Carena, S. Heinemeyer, C. E. M. Wagner, and G. Weiglein, *Suggestions for Benchmark Scenarios for MSSM Higgs Boson Searches at Hadron Colliders*, Eur. Phys. J. **C 26** (2003) 601.

[61] Particle Data Group Collaboration, K. Nakamura et al., *Review of Particle Physics*, J. Phys. G **G37** (2010) 075021.

[62] S. Heinemeyer, W. Hollik, and G. Weiglein, *Feynhiggs: A Program for the Calculation of the Masses of the Neutral CP–Even Higgs Bosons in the MSSM*, Comp. Phys. Comm. **124** (2000) 76.

[63] G. Degrassi, S. Heinemeyer, W. Hollik, P. Slavich, and G. Weiglein, *Towards High–Precision Predictions for the MSSM Higgs Sector*, Eur. Phys. J. **C 28** (2003) 133.

[64] M. Frank et al., *The Higgs Boson Masses and Mixings of the Complex MSSM in the Feynman–Diagrammatic Approach*, JHEP **0702** (2007) 47.

[65] F. Zwirner, *The Quest for Low–Energy Supersymmetry and the Role of High–Energy $e^+e^-$ Colliders*, arXiv:hep-ph/9203204 (1991) .

[66] J. M. Campbell, J. Huston, and W. Stirling, *Hard Interactions of Quarks and Gluons: A Primer for LHC Physics*, Rept. Prog. Phys. **70** (2007) 89.

[67] J. C. Collins and D. E. Soper, *The Theorems of Perturbative QCD*, Ann. Rev. Nucl. Part. Sci. **37** (1987) 383.

[68] S. Drell and T.-M. Yan, *Partons and Their Applications at High–Energies*, Annals Phys. **66** (1971) 578.

[69] The LHC Higgs Cross Section Working Group, S. Dittmaier, C. Mariotti, G. Passarino, and R. Tanaka, *Handbook of LHC Higgs Cross Sections: 1. Inclusive Observables*, CERN–011–02 (2011) .

[70] The LHC Higgs Cross Section Working Group, S. Dittmaier, C. Mariotti, G. Passarino, and R. Tanaka, *Handbook of LHC Higgs Cross Sections: 2. Differential Distributions*, CERN–012–02 (2012) .

[71] A. Djouadi, J. Kalinowski, and M. Spira, *Hdecay: A Program for Higgs Boson Decays in the Standard Model and its Supersymmetric Extension*, Comp. Phys. Comm. **108** (1998) 56.

[72] A. Bredenstein, A. Denner, S. Dittmaier, and M. Weber, *Precise Predictions for the Higgs Boson Decay $H \to Ww/zz \to 4$ Leptons*, Phys. Rev. **D74** (2006) 013004.

[73] A. Bredenstein, A. Denner, S. Dittmaier, and M. Weber, *Radiative Corrections to the Semileptonic and Hadronic Higgs Boson Decays $H \to WW/ZZ \to 4$ Fermions*, JHEP **0702** (2007) 80.

[74] M. Spira, *Higlu: A Program for the Calculation of the Total Higgs Production Cross Section at Hadron Colliders via Gluon Fusion Including QCD Corrections*, `arXiv:hep-ph/9510347`.

[75] R. V. Harlander and W. B. Kilgore, *Next–to–Next–to–Leading Order Higgs Production at Hadron Colliders*, Phys. Rev. Lett. **88** (2002) 201801.

[76] R. V. Harlander and W. B. Kilgore, *Production of a Pseudo–Scalar Higgs Boson at Hadron Colliders at Next–to–Next–to–Leading Order*, JHEP **10** (2002) 17.

[77] R. Harlander, M. Krämer, and M. Schumacher, *Bottom–Quark Associated Higgs–Boson Production: Reconciling the Four– and Five–Flavour Scheme Approach*, `arXiv:1112.3478 [hep-ex]`.

[78] S. Dittmaier, M. Kramer, and M. Spira, *Higgs Radiation off Bottom Quarks at the Tevatron and the LHC*, Phys. Rev. **D70** (2004) 074010.

[79] S. Dawson, C. B. Jackson, L. Reina, and D. Wackeroth, *Exclusive Higgs Boson Production with Bottom Quarks at Hadron Colliders*, Phys. Rev. **D 69** (2004) 074027.

[80] R. V. Harlander and W. B. Kilgore, *Higgs Boson Production in Bottom Quark Fusion at Next–to–Next–to–Leading Order*, Phys. Rev. **D68** (2003) 013001.

[81] The ATLAS Collaboration, G. Aad et al., *Observation of a new Particle in the Search for the Standard Model Higgs Boson with the ATLAS Detector at the LHC*, Phys. Lett. B **716** (2012) 1.

[82] The CMS Collaboration, S. Chatrchyan et al., *Observation of a new Boson at a Mass of 125 GeV with the CMS Experiment at the LHC*, Phys. Lett. B **716** (2012) 30.

[83] The CDF and DØ Collaborations and the Tevatron New Physics and Higgs Working Groups, *Updated Combination of CDF and DØ Searches for Standard Model Higgs Boson Production with up to* $10.0\,fb^{-1}$ *of Data*, `arXiv:1207.0449 [hep-ex]`.

[84] The ATLAS Collaboration, G. Aad et al., *Combined Coupling Measurements of the Higgs–like Boson with the ATLAS Detector Using up to* $25\,fb^{-1}$ *of Proton–Proton Collision Data*, ATLAS–CONF–2013–034 (2013) `http://cds.cern.ch/record/1528170`.

[85] The ATLAS Collaboration, G. Aad et al., *Measurements of the Properties of the Higgs–like Boson in the two Photon Decay Channel with the ATLAS Detector Using* $25\,fb^{-1}$ *of Proton-proton Collision Data*, ATLAS–CONF–2013–012 (2013) `http://cds.cern.ch/record/1523698`.

[86] The ATLAS Collaboration, G. Aad et al., *Measurements of the Properties of the Higgs–like Boson in the Four Lepton Decay Channel with the ATLAS Detector Using* $25\,fb^{-1}$ *of Proton–Proton Collision Data*, ATLAS–CONF–2013–013 (2013) `http://cds.cern.ch/record/1523699`.

[87] The ATLAS Collaboration, G. Aad et al., *Measurements of the Properties of the Higgs–like Boson in the* $WW^{(*)} \to \ell\nu\ell\nu$ *Decay Channel with the ATLAS Detector Using* $25\,fb^{-1}$ *of Proton–Proton Collision Data*, ATLAS–CONF–2013–030 (2013) `http://cds.cern.ch/record/1527126`.

[88] The ATLAS Collaboration, G. Aad et al., *Combined Measurements of the Mass and Signal Strength of the Higgs–like Boson with the ATLAS Detector Using up to* $25\,fb^{-1}$ *of Proton–Proton Collision Data*, ATLAS–CONF–2013–014 (2013) `http://cds.cern.ch/record/1523727`.

[89] The ATLAS Collaboration, G. Aad et al., *Study of the Spin of the new Boson with up to* $25\,fb^{-1}$ *of ATLAS Data*, ATLAS–CONF–2013–040 (2013) `http://cds.cern.ch/record/1542341`.

[90] S. Heinemeyer, O. Stal, and G. Weiglein, *Interpreting the LHC Higgs Search Results in the MSSM*, Phys. Lett. **B 710** (2012) 201.

[91] P. Bechtle, O. Brein, S. Heinemeyer, G. Weiglein, and K. E. Williams, *Higgsbounds: Confronting Arbitrary Higgs Sectors with Exclusion Bounds From LEP and the Tevatron*, Comp. Phys. Comm. **181** (2010) 138.

[92] P. Bechtle, O. Brein, S. Heinemeyer, G. Weiglein, and K. E. Williams, *Higgsbounds 2.0.0: Confronting Neutral and Charged Higgs Sector Predictions with Exclusion Bounds From LEP and the Tevatron*, Comp. Phys. Comm. **182** (2011) 2605.

[93] The CMS Collaboration, S. Chatrchyan et al., *Search for Neutral Higgs Bosons Decaying to Tau Pairs in pp Collisions at* $\sqrt{s} = 7$ *TeV*, CMS–PAS–HIG–11–020 (2011) `http://cds.cern.ch/record/1378096`.

[94] The ATLAS Collaboration, G. Aad et al., *Combination of Higgs Boson Searches with up to* $4.9\,fb^{-1}$ *of pp Collisions Data Taken at a Center–of–Mass Energy of* 7 *TeV with the ATLAS Experiment at the LHC*, ATLAS–CONF–2011–163 (2011) `http://cds.cern.ch/record/1406358`.

[95] The CMS Collaboration, S. Chatrchyan et al., *Combination of SM Higgs Searches*, http://cds.cern.ch/record/1406347.

[96] The ALEPH, the DELPHI, the L3 and the OPAL Collaborations, the LEP Working Group for Higgs Boson Searches, *Search for Neutral MSSM Higgs Bosons at LEP*, Eur. Phys. J. **C 47** (2006) 547.

[97] The MSSM Working Group, A. Djouadi, et al., *The Minimal Supersymmetric Standard Model: Group Summary report*, arXiv:hep-ph/9901246 [hep-ph].

[98] P. Bechtle et al., *MSSM Interpretations of the LHC Discovery: Light or Heavy Higgs?*, arXiv:1211.1955 [hep-ph].

[99] W. Hollik et al., *Precision Observables in the MSSM: W Mass and the Muon Magnetic Moment*, AIP Conf. Proc. **903** (2007) 291.

[100] L. Evans and P. Bryant, *LHC Machine*, JINST **3** (2008) S08001.

[101] The ATLAS Collaboration, G. Aad et al., *The ATLAS Experiment at the CERN Large Hadron Collider*, JINST **3** (2008) S08003.

[102] *LHC Cooldown Status (15 October 2009)*, http://cds.cern.ch/record/1212916, 2009.

[103] The ALICE Collaboration, K. Aamodt et al., *The Alice Experiment at the CERN LHC*, JINST **3** (2008) S08002.

[104] The CMS Collaboration, S. Chatrchyan et al., *The CMS Experiment at the CERN LHC*, JINST **3** (2008) S08004.

[105] The LHCb Collaboration, A. Alves et al., *The LHCb Detector at the LHC*, JINST **3** (2008) S08005.

[106] The LHCf Collaboration, O. Adriani et al., *The LHCf Detector at the CERN Large Hadron Collider*, JINST **3** (2008) S08006.

[107] The MoEDAL Collaboration, J. Pinfold et al., *Technical Design Report of the Moedal Experiment*, CERN-LHCC-2009-006 (2009) .

[108] The TOTEM Collaboration, G. Anelli et al., *The Totem Experiment at the CERN Large Hadron Collider*, JINST **3** (2008) S08007.

[109] The ATLAS Collaboration, G. Aad et al., *ATLAS Forward Detectors for Measurement of Elastic Scattering and Luminosity*, ATLAS-TDR-18, CERN-LHCC-2008-004 (2008) https://cds.cern.ch/record/1095847.

[110] The ATLAS Collaboration, G. Aad et al., *Zero Degree Calorimeters for ATLAS*, Letter of Intent, ATLAS–LHCC–2007–001 (2007) https://cds.cern.ch/record/1009649.

[111] The ATLAS Collaboration, G. Aad et al., *Muon Reconstruction Efficiency and Momentum Resolution of the ATLAS Experiment in Proton-Proton Collisions at* $\sqrt{s} = 7$ *TeV in 2010*, ATL–PERF–2011-01–001 (2013) to be published.

[112] The ATLAS Collaboration, G. Aad et al., *ATLAS Detector and Physics Performance: Technical Design Report 1*, ATLAS-TDR-14, CERN-LHCC-99-014 (1999) https://cds.cern.ch/record/391176.

[113] The ATLAS Collaboration, G. Aad et al., *Luminosity Determination in pp Collisions at* $\sqrt{s} = 7$ *TeV Using the ATLAS Detector at the LHC*, Eur. Phys. J. **C 71** (2011) 1630.

[114] The ATLAS Collaboration, G. Aad et al., *Luminosity Determination in pp Collisions at* $\sqrt{s} = 7$ *TeV Using the ATLAS Detector in 2011*, ATLAS–CONF–2011–116 (2011) http://cds.cern.ch/record/1376384.

[115] S. van der Meer, *Calibration of the Effective Beam Height in the ISR*, CERN–ISR–PO–68–31, ISR–PO–68–31 (1968) http://cds.cern.ch/record/296752.

[116] https://twiki.cern.ch/twiki/bin/view/AtlasPublic/LuminosityPublicResults.

[117] L. Rossi and O. Bruening, *High Luminosity Large Hadron Collider — A Description for the European Strategy Preparatory Group*, CERN–ATS–2012–236 (2012) http://cds.cern.ch/record/1471000.

[118] O. Bruening et al., *High Energy LHC Document Prepared for the European HEP Strategy Update*, CERN–ATS–2012–237 (2012) http://cds.cern.ch/record/1471002.

[119] The ATLAS Collaboration, G. Aad et al., *Expected Performance of the ATLAS Experiment — Detector, Trigger and Physics*, CERN-OPEN-2008-020, arXiv:0901.0512.

[120] T. Cornelissen et al., *Concepts, Design and Implementation of the ATLAS New Tracking (NEWT)*, ATL–SOFT–PUB–2007–007 (2007) .

[121] R. Frühwirth, *Application of Kalman Filtering to Track and Vertex Fitting*, Nucl.Instrum.Meth. **A 262** (1987) 444.

[122] R. Frühwirth, *Track Fitting with Nongaussian Noise*, Comp. Phys. Comm. **100** (1997) 1.

[123] S. Hassani et al., *A Muon Identification and Combined Reconstruction Procedure for the ATLAS Detector at the LHC Using the (Muonboy, Staco, Mutag) Reconstruction Packages*, Nucl. Instrum. Methods Phys. Res., A **572** (2007) 77.

[124] T. Lagouri et al., *A Muon Identification and Combined Reconstruction Procedure for the ATLAS Detector at the LHC at CERN*, IEEE Trans.Nucl.Sci. **51** (2004) 3030.

[125] R. Nicolaidou et al., *Muon Identification Procedure for the ATLAS Detector at the LHC Using Muonboy Reconstruction Package and Tests of its Performance Using Cosmic Rays and Single Beam Data*, Journal of Physics: Conference Series **219** (2010) 032052.

[126] D. Adams et al., *Track Reconstruction in the ATLAS Muon Spectrometer with Moore*, ATL–SOFT–2003–007 (2003) .

[127] K. Nikolopoulos, D. Fassouliotis, C. Kourkoumelis, and A. Poppleton, *Event–by–Event Estimate of Muon Energy Loss in ATLAS*, Nuclear Science, IEEE Transactions on **54** (2007) 1792.

[128] S. Tarem, Z. Tarem, N. Panikashvili, and O. Belkind, *Mugirl – Muon Identification in the ATLAS Detector From the Inside Out*, in *Nuclear Science Symposium Conference Record. IEEE*, vol. 1, p. 617. 2006.

[129] B. Resende on behalf of the ATLAS Collaboration, *Muon Identification Algorithms in ATLAS*, PoS **EPS–HEP2009** (2009) 431.

[130] G. Ordonez Sanz, *Muon Identification in the ATLAS Calorimeters*. PhD thesis, Nijmegen U., Amsterdam, 2009. Presented on 12 Jun 2009.

[131] The ATLAS Collaboration, G. Aad et al., *A Measurement of the ATLAS Muon Reconstruction and Trigger Efficiency Using $J/\psi$ Decays*, ATLAS–CONF–2011–021 (2011) `http://cds.cern.ch/record/1336750`.

[132] The ATLAS Collaboration, G. Aad et al., *Search for the Neutral Higgs Bosons of the Minimal Supersymmetric Standard Model in pp Collisions at $\sqrt{s} = 7$ TeV with the ATLAS Detector*, JHEP **1302** (2013) 095.

[133] The Tevatron New Phenomena and Higgs Working Group, D. Benjamin, et al., *Combined CDF and DØ Upper Limits on MSSM Higgs Boson production in Tau–Tau Final States with up to $2.2\,fb^{-1}$*, `arXiv:1003.3363 [hep-ex]`.

[134] The CMS Collaboration, S. Chatrchyan et al., *Search for MSSM Neutral Higgs Bosons Decaying to Tau Pairs in pp Collisions*, CMS–PAS–HIG–12–050 (2012) `https://cds.cern.ch/record/1493521`.

[135] The CMS Collaboration, S. Chatrchyan et al., *Search for Neutral MSSM Higgs Bosons in the $\mu^+\mu^-$ Final State with the CMS Experiment in pp Collisions at $\sqrt{s} = 7$ TeV*, CMS–PAS–HIG–12–011 (2012) `https://cds.cern.ch/record/1453716`.

[136] The ATLAS Collaboration, G. Aad et al., *Search for the Standard Model Higgs Boson in $H \to \tau\tau$ Decays in Proton–Proton Collisions with the ATLAS Detector*, ATLAS–CONF–2012–160 (2012) `http://cdsweb.cern.ch/record/1493624`.

[137] J. R. Ellis, D. V. Nanopoulos, and K. A. Olive, *Combining the Muon Anomalous Magnetic Moment with other Constraints on the CMSSM*, Phys.Lett. **B508** (2001) 65–73.

[138] The ATLAS Collaboration, G. Aad et al., *Performance of Missing Transverse Momentum Reconstruction in Proton–Proton Collisions at 7 TeV with ATLAS*, Eur. Phys. J. **C 72** (2012) 1844.

[139] S. Alioli, P. Nason, C. Oleari, and E. Re, *NLO Higgs Boson Production via Gluon Fusion Matched with Shower in Powheg*, JHEP **04** (2009) 2.

[140] P. Nason, *A new Method for Combining NLO QCD with Shower Monte Carlo Algorithms*, JHEP **11** (2004) 40.

[141] S. Frixione, P. Nason, and C. Oleari, *Matching NLO QCD Computations with Parton Shower Simulations: the Powheg Method*, JHEP **0711** (2007) 70.

[142] T. Sjostrand, S. Mrenna and P. Skands, *Pythia 6.4 Physics and Manual*, JHEP **05** (2006) 26.

[143] T. Gleisberg et al., *Event Generation with Sherpa 1.1*, JHEP **02** (2009) 7.

[144] M.L. Mangano and M. Moretti and F. Piccinini and R. Pittau and A. Polosa, *Alpgen, a Generator for Hard Multiparton Processes in Hadronic Collisions*, JHEP **07** (2003) 001.

[145] S. Frixione and B. R. Webber, *Matching NLO QCD Computations and Parton Shower Simulations*, JHEP **06** (2002) 29.

[146] S. Frixione, P. Nason, and B. R. Webber, *Matching NLO QCD and Parton Showers in Heavy Flavor Production*, JHEP **0308** (2003) 7.

[147] The ATLAS Collaboration, M. Smizanska, S. P. Baranov, J. Hrivnac, and E. Kneringer, *Overview of Monte Carlo Simulations for ATLAS B–Physics in the Period 1996–1999*, ATL–PHYS–2000–025 (2000) http://cds.cern.ch/record/684060.

[148] C. Anastopoulos et al., *Physics Analysis Tools for Beauty Physics in ATLAS*, Journal of Physics: Conference Series **119** (2008) 032003.

[149] B. P. Kersevan and E. Richter-Was, *The Monte Carlo Event Generator Acermc Version 2.0 with Interfaces to Pythia 6.2 and Herwig 6.5*, arXiv:hep-ph/0405247 [hep-ph].

[150] T. Sjoestrand, *Jet Fragmentation of Multiparton Configurations in a String Framework*, Nuc. Phys. B **248** (1984) 469.

[151] T. Sjoestrand and M. van Zijl, *A Multiple–Interaction Model for the Event Structure in Hadron Collisions*, Phys. Rev. D **36** (1987) 2019.

[152] G. Corcella et al., *Herwig 6: an Event Generator for Hadron Emission Reactions with Interfering Gluons (including Supersymmetric Processes)*, JHEP **01** (2001) 10.

[153] J. M. Butterworth, J. R. Forshaw, and M. H. Seymour, *Multiparton Interactions in Photoproduction at Hera*, Z. Phys. **C 72** (1996) 637.

[154] The ATLAS Collaboration, G. Aad et al., *The ATLAS Simulation Infrastructure*, ATLAS-SOFT-2010-01-004, submitted to Eur. Phys. J. C., arXiv:1005.4568.

[155] The GEANT4 Collaboration, S. Agostinelli et al., *Geant4 — a Simulation Toolkit*, Nucl. Instrum. Meth. **A 506** (2003) 250.

[156] J. Allison et al., *Geant4 Developments and Applications*, IEEE Trans. Nucl. Sci. **53** (2006) 270.

[157] E. Richter-Was, D. Froidevaux, and L. Poggioli, *ATLFAST 2.0 a Fast Simulation Package for ATLAS*, ATL–PHYS–98–131 (1998) http://cds.cern.ch/record/683751.

[158] The ATLFAST–II benchmark group, *The Atlfast–II Performance in Release 14 — Particle Signatures and Selected Benchmark Processes*, ATL–COM–PHYS–2009–554 (2009) internal documentation.

[159] The ATLAS Collaboration, G. Duckeck et al., *ATLAS Computing: Technical Design Report*, CERN-LHCC-2005-022, ATLAS-TRD-017 (2005) https://cds.cern.ch/record/837738.

[160] M. Cacciari, G. P. Salam and G. Soyez, *The Anti–$k_t$ Jet Clustering Algorithm*, JHEP **04** (2008) 63.

[161] W. Lampl et al., *Calorimeter Clustering Algorithms: Description and Performance*, ATL-LARG-PUB-2008-002 (2008) `http://cds.cern.ch/record/1099735`.

[162] The ATLAS Collaboration, G. Aad et al., *Jet Energy Measurement with the ATLAS Detector in Proton–Proton Collisions at* $\sqrt{s} = 7$ *TeV*, Eur.Phys.J. **C 73** (2013) 2304.

[163] The ATLAS Collaboration, G. Aad et al., *Selection of Jets Produced in Proton–Proton Collisions with the ATLAS Detector Using 2011 Data*, ATLAS–CONF–2012–020 (2012) `http://cds.cern.ch/record/1430034`.

[164] The ATLAS Collaboration, G. Aad et al., *Measuring the b-Tag Efficiency in a Top–Pair Sample with* $4.7\,fb^{-1}$ *of Data From the ATLAS Detector*, ATLAS–CONF–2012–097 (2012) `http://cdsweb.cern.ch/record/1460443`.

[165] The ATLAS Collaboration, G. Aad et al., *commissioning of the ATLAS High–Performance b–Tagging Algorithms in the 7 TeV Collision Data*, ATLAS–CONF–2011–102 (2011) `http://cdsweb.cern.ch/record/1369219`.

[166] G. Choudalakis and D. Casadei, *plotting the Differences Between Data and Expectation*, The European Physical Journal Plus **127** (2012) 1.

[167] The ATLAS Collaboration, G. Aad et al., *Measuring the b–Tag Efficiency in a Top–Pair Sample with* $4.7\,fb^{-1}$ *of Data From the ATLAS Detector*, ATLAS–CONF–2012–097 (2012) `http://cdsweb.cern.ch/record/1460443`.

[168] The ATLAS Collaboration, G. Aad et al., *Measurement of the Cross–Section for* $b^-$ *Jets Produced in Association with a Z Boson at* $\sqrt{s} = 7$ *TeV with the ATLAS Detector*, Phys. Lett. **B 706** (2012) 295.

[169] A. Bundock et al., *Measurement of Zb and Zbb Cross Sections with* $4.6\,fb^{-1}$ *of 7 TeV ATLAS Data*, ATL–COM–PHYS–2012–1504 (2012) internal documentation.

[170] G. Cowan, K. Cranmer, E. Gross, and O. Vitells, *Asymptotic Formulae for Likelihood-based Tests of new Physics*, Eur. Phys. J. **C 71** (2011) 1554.

[171] R. Brun et al., *Root: A C++ Framework for Petabyte Data Storage, Statistical Analysis and Visualization*, Comp. Phys. Comm. **182** (2011) 1384.

[172] W. Verkerke and D. P. Kirkby, *The Roofit Toolkit for Data Modeling*, eConf **C0303241** (2003) MOLT007, `arXiv:physics/0306116 [physics.data-an]`.

[173] K. S. Cranmer et al., *The Roostats Project*, PoS **ACAT2010** (2010) 57.

[174] K. Cranmer, G. Lewis, L. Moneta, A. Shibata, and W. Verkerke, *Histfactory: A Tool for Creating Statistical Models for use with Roofit and Roostats*, CERN–OPEN–2012–016 (2012) `http://cds.cern.ch/record/1456844`.

[175] The ATLAS and CMS Collaborations, The LHC Higgs Combination Group, *Procedure for the LHC Higgs Boson Search Combination in Summer 2011*, ATL-PHYS-PUB-2011-011, CMS-NOTE-2011-005 (2011) `http://cds.cern.ch/record/1375842`.

[176] G. J. Feldman and R. D. Cousins, *A Unified Approach to the Classical Statistical Analysis of Small Signals*, Phys. Rev. **D 57** (1998) 3873.

[177] A. L. Read, *Presentation of Search Results: the $CL_s$ Technique*, Journal of Physics G: Nuclear and Particle Physics **28** (2002) 2693.

[178] S. S. Wilks, *The Large–Sample Distribution of the Likelihood Ratio for Testing Composite Hypotheses*, The Annals of Mathematical Statistics **9** (1938) 60.

[179] A. Wald, *Tests of Statistical Hypotheses Concerning Several Parameters When the Number of Observations is Large*, Transactions of the American Mathematical Society **54** (1943) no. 3, 426.

[180] E. Gross and O. Vitells, *Trial Factors for the Look Elsewhere Effect in High Energy Physics*, The European Physical Journal C — Particles and Fields **70** (2010) 525. 10.1140/epjc/s10052-010-1470-8.

[181] O. Vitells and E. Gross, *Estimating the Significance of a Signal in a Multi–Dimensional Search*, Astropart.Phys. **35** (2011) 230.

[182] The ATLAS Collaboration, G. Aad et al., *ATLAS Muon Momentum Resolution in the First Pass Reconstruction of the 2010 p–p Collision Data at $\sqrt{s} = 7$ TeV*, ATLAS–CONF–2011–046 (2011) `http://cdsweb.cern.ch/record/1338575`.

[183] `https://atlas.web.cern.ch/ATLAS/GROUPS/PHYSICS/PAPERS/HIGG-2012-11/`.

[184] The LHC Higgs Cross Section Working Group, S. Dittmaier, C. Mariotti, G. Passarino, and R. Tanaka, *Handbook of LHC Higgs Cross Sections: 1. Inclusive Observables*, CERN-2011-002 (CERN, Geneva, 2011) , `arXiv:1101.0593 [hep-ph]`.

[185] J. Butterworth et al., *Single Boson and Diboson Production Cross Sections in pp Collisions at $\sqrt{s} = 7$ TeV*, ATL–COM–PHYS–2010–695 (2010) internal documentation.

[186] J. Pumplin, *New Generation of Parton Distributions with Uncertainties From Global QCD Analysis*, JHEP **0207** (2002) 012.

[187] P. M. Nadolsky et al., *Implications of CTEQ Global Analysis for Collider Observables*, Phys. Rev. D **78** (2008) 013004.

[188] H.-L. Lai et al., *New Parton Distributions for Collider Physics*, Phys. Rev. **D82** (2010) 074024.

[189] A. Martin, W. Stirling, R. Thorne, and G. Watt, *Parton Distributions for the LHC*, Eur. Phys. J. **C 63** (2009) 189.

[190] The ATLAS Collaboration, G. Aad et al., *Muon Reconstruction Efficiency in Reprocessed 2010 LHC Proton–Proton Collision Data Recorded with the ATLAS Detector*, ATLAS–CONF–2011–063 (2011) `http://cdsweb.cern.ch/record/1345743`.

[191] The ATLAS Collaboration, G. Aad et al., *Calibrating the b–Tag Efficiency and Mistag Rate in 35 $pb^{-1}$ of Data with the ATLAS Detector*, ATLAS–CONF–2011–089 (2011) `http://cdsweb.cern.ch/record/1356198`.

[192] G. Choudalakis, *On Hypothesis Testing, Trials Factor, Hypertests and the Bumphunter*, `arXiv:1101.0390 [physics.data-an]`.

[193] A. Elagin, P. Murat, A. Pranko, and A. Safonov, *A New Mass Reconstruction Technique for Resonances Decaying to di-$\tau$*, Nucl.Instrum.Meth. **A654** (2011) 481.

[194] The ATLAS Collaboration, G. Aad et al., *Performance of the Reconstruction and Identification of Hadronic $\tau$ Decays in ATLAS with 2011 Data*, ATLAS–CONF–2012–142 (2012) `http://cdsweb.cern.ch/record/1485531`.

[195] The ATLAS Collaboration, G. Aad et al., *Search for Neutral MSSM Higgs Bosons Decaying to $\tau\tau$ Pairs in Proton–Proton Collisions at $\sqrt{s} = 7$ TeV with the ATLAS Detector*, Phys. Lett. **B 705** (2011) 174.

[196] The ATLAS Collaboration, G. Aad et al., *Search for a Standard Model Higgs Boson in $H \to \mu\mu$ Decays with the ATLAS Detector*, ATLAS–CONF–2013–010 (2013) `http://cds.cern.ch/record/1523695`.

[197] The ATLAS Collaboration, G. Aad et al., *Physics at a High–Luminosity LHC with ATLAS*, ATL–PHYS–PUB–2012–001 (2012) `http://cds.cern.ch/record/1472518`.

[198] The ATLAS Collaboration, G. Aad et al., *Physics at a High–Luminosity LHC with ATLAS (update)*, ATL–PHYS–PUB–2012–004 (2012) `http://cds.cern.ch/record/1484890`.

[199] The European Strategy for Particle Physics Preparatory Group, R. Aleksan et al. and The Scientific Sectretaries for the Open Symposium in Cracow (Poland), R. Brun et al., *Physics Briefing Book*, http://europeanstrategygroup.web.cern.ch/europeanstrategygroup/Briefing_book.pdf.

[200] D. de Florian, M. Grazzini, and M. Grazzini, *Higgs Production at the LHC: Updated Cross Sections at $\sqrt{s} = 8$ TeV*, arXiv:1206.4133 [hep-ph].

[201] J. M. Campbell and R. Ellis, *Mcfm for the Tevatron and the LHC*, Nucl. Phys. Proc. Suppl. **205-206** (2010) 10.

[202] M. Aliev et al., *Hathor: Hadronic Top and Heavy Quarks Cross Section Calculator*, Comp. Phys. Comm. **182** (2011) 1034.

[203] The LHC Higgs Cross Section Working Group, A. David, et al. https://twiki.cern.ch/twiki/bin/view/LHCPhysics/SMInputParameter.

[204] The ATLAS Collaboration, G. Aad et al., *Performance Assumptions for an Upgraded ATLAS Detector at a High–Luminosity LHC*, ATL–PHYS–PUB–2013–004 (2013) http://cds.cern.ch/record/1527529.

[205] The ATLAS Collaboration, G. Aad, et al., *Letter of Intent for the Phase–I Upgrade of the ATLAS Experiment*, CERN–LHCC–2011–012, LHCC–I–020 (2011) http://cds.cern.ch/record/1502664.

[206] The ATLAS Collaboration, G. Aad, et al., *Letter of Intent for the Phase–II Upgrade of the ATLAS Experiment*, CERN-LHCC-2012-022, LHCC-I-023 (2012) http://cds.cern.ch/record/1502664.

[207] The ATLAS Collaboration, G. Aad et al., *Pile–Up Depedence of the ATLAS Muon Performance*, ATL–COM–PHYS–2011–1640 (2011) https://atlas.web.cern.ch/ATLAS/GROUPS/PHYSICS/MUON/PublicPlots/2011/Dec/index.html.

[208] The LHC Higgs Cross Section Working Group, A. David, et al. https://twiki.cern.ch/twiki/bin/view/LHCPhysics/HiggsEuropeanStrategy2012.

[209] The ATLAS Collaboration, G. Aad et al., *Search for the Standard Model Higgs Boson in $H \to \tau^+\tau^-$ Decays in Proton–Proton Collisions with the ATLAS Detector*, ATLAS–CONF–2012–160 (2012) http://cds.cern.ch/record/1493624.

[210] The LHC Higgs Cross Section Working Group, A. David, et al., *LHC HXSWG Interim Recommendations to Explore the Coupling Structure of a Higgs–like Particle*, arXiv:1209.0040 [hep-ph].

[211] The ATLAS Collaboration, G. Aad et al., *Coupling Properties of the new Higgs–like Boson Observed with the ATLAS Detector at the LHC*, ATLAS–CONF–2012–127 (2012) http://cdsweb.cern.ch/record/1476765.

[212] P. Onyisi on behalf of the ATLAS Collaboration, *Operation of the ATLAS Detector with First Collisions at 7 TeV at the LHC*, PoS **ICHEP2010** (2010) 495.

[213] C. C. Almenar et al., *ATLAS Online Data Quality Monitoring*, Nuc. Phys. B – Proceedings Supplements **215** (2011) 304. Proceedings of the 12th Topical Seminar on Innovative Particle and Radiation Detectors (IPRD10).

[214] J. Adelman et al., *ATLAS Offline Data Quality Monitoring*, Journal of Physics: Conference Series **219** (2010) 042018.

[215] M. Elsing, L. Goossens, A. Nairz, and G. Negri, *The ATLAS Tier–0: Overview and Operational Experience*, Journal of Physics: Conference Series **219** (2010) 072011.

[216] https://atlas-tagservices.cern.ch/tagservices/RunBrowser/index.html.

[217] https://twiki.cern.ch/twiki/bin/view/Persistency/Cool.

[218] M. Verducci on behalf of the ATLAS Collaboration, *ATLAS Conditions Database Experience with the LCG Cool Conditions Database Project*, Journal of Physics: Conference Series **119** (2008) 042031.

[219] I. Bird, *Computing for the Large Hadron Collider*, Ann. Rev. Nucl. Part. Sci. **61** (2011) 99.

[220] C. Eck et al., *LHC Computing Grid: Technical Design Report*, CERN-LHCC-2005-024, LCG-TDR-001 (2005) http://cds.cern.ch/record/840543.

[221] T. Golling, H. Hayward, P. Onyisi, H. Stelzer, and P. Waller, *The ATLAS Data Quality Defect Database System*, Eur. Phys. J. **C 72** (2012) 1960.

[222] A. Sherstnev and R. S. Thorne, *Parton Distributions for Leading Order Generators*, Eur. Phys. J. **C 55** (2008) 553.

[223] M. R. Whalley, D. Bourilkov, and R. C. Group, *The Les Houches Accord Pdfs (LHAPDF) and Lhaglue*, arXiv:hep-ph/0508110 [hep-ph].

[224] *LHAPDF — the Les Houches Accord PDF Interface*, http://hepforge.cedar.ac.uk/lhapdf.